

TECHNISCHE UNIVERSITÄT MÜNCHEN

Lehrstuhl für Numerische Mechanik

A Coupled Finite Element Approach  
for Electrochemical Systems

Georg Josef Bauer

Vollständiger Abdruck der von der Fakultät für Maschinenwesen der  
Technischen Universität München zur Erlangung des akademischen Grades  
eines

Doktor-Ingenieurs (Dr.-Ing.)

genehmigten Dissertation.

Vorsitzender:            Univ.-Prof. Wolfgang H. Polifke, Ph. D.

Prüfer der Dissertation:

1. Univ.-Prof. Dr.-Ing. Wolfgang A. Wall
2. Prof. Antonio Huerta, Ph. D.  
Universitat Politècnica de Catalunya,  
Barcelona/ Spanien

Die Dissertation wurde am 28. Juni 2012 bei der Technischen Universität  
München eingereicht und durch die Fakultät für Maschinenwesen am  
2. Oktober 2012 angenommen.



## Abstract

Electrochemical systems can be found in a large variety of applications. The well-known usage as power sources in form of batteries and fuel cells is particularly relevant in the context of electromobility and renewable energy sources. Electrolytic processes, such as the electrodeposition of metals and alloys, have significant industrial importance. The behavior of an electrochemical system is determined by a complex interplay of thermodynamics, electrode kinetics and ion-transport phenomena. Thus, research and development in the field of electrochemistry are necessarily multidisciplinary tasks involving several scientific disciplines. The use of mathematical modeling and numerical simulation represents one promising approach, which will be instrumental in gaining further insight into these complex systems.

In this work, a comprehensive computational method for the coupled numerical simulation of electrochemical systems is proposed. The present focus is particularly on coupled multi-ion transport in electrolytic cells. As an exemplary application, electrodeposition of metals is considered in this study. Based on a continuum hypothesis, a macroscopic model is established which accounts for all three ion-transport phenomena in dilute electrolyte solutions, that is, convection, diffusion and migration. The latter effect describes the movement of ions caused by an electric field.

One of the key aspects of this work is the consideration of the inherent coupling of ionic transport and complex, often turbulent flow of electrolyte solutions. A challenging two-way coupled problem arises in case of buoyancy-driven flow (natural convection) in an electrochemical cell. For an appropriate modeling of electrode kinetics, nonlinear phenomenological boundary conditions such as the Butler-Volmer law are used at electrode surfaces. A general approach for the simulation of current-controlled (galvanostatic) problems completes the comprehensive model.

A stabilized finite element method is proposed as a unique discretization approach to all governing equations. The stabilization terms are derived from the framework of the residual-based variational multiscale method. It is successfully demonstrated that the proposed stabilization techniques for the coupled ion-transport problem contribute to the robustness of electrochemical simulations when convection plays a significant role. Since the variational multiscale method can also be considered as an approach to large eddy simulation of turbulent flows, the proposed computational framework is capable of simulating coupled multi-ion transport in laminar, transitional and turbulent flow of electrolyte solutions. Moreover, for natural convection phenomena in electrochemical cells, a partitioned solution scheme is proposed in this work.

Various numerical examples demonstrate that the computational method is robust and provides accurate results. Among others, realistic problem configurations with complex three-dimensional geometries are considered. The diversity of numerical examples illustrates the broad spectrum of capabilities.

In summary, the developed computational approach represents an important contribution concerning the development of a predictive tool for industrial electroplating applications in particular and the macroscopic modeling of electrochemical systems in general.

*Abstract*

---

## Zusammenfassung

Elektrochemische Systeme finden sich in einer Vielfalt von technischen Anwendungen. Die Verwendung als Energiequellen in Form von Batterien und Brennstoffzellen ist gerade im Kontext von Elektromobilität und erneuerbaren Energien von besonderer Relevanz. Elektrolytische Prozesse wie zum Beispiel die galvanische Abscheidung von Metallen und Legierungen besitzen eine erhebliche industrielle Bedeutung. Das Verhalten eines elektrochemischen Systems wird durch eine komplexe Wechselwirkung von Thermodynamik, Reaktionskinetik an Elektroden und Ionentransportvorgängen bestimmt. Demzufolge sind Forschung und Entwicklung im Bereich der Elektrochemie notwendigerweise multidisziplinäre Aufgaben, die mehrere verschiedene wissenschaftliche Disziplinen miteinbeziehen. Der Einsatz von mathematischer Modellbildung und numerischer Simulation stellt dabei einen vielversprechenden Ansatz dar, mit Hilfe dessen weitere Einblicke in diese komplexen Systeme erlangt werden können.

In der vorliegenden Arbeit wird ein umfassendes Berechnungsverfahren für die gekoppelte numerische Simulation von elektrochemischen Systemen vorgestellt. Im Fokus ist hierbei insbesondere der gekoppelte Transport von Ionen in elektrolytischen Zellen. Als beispielhafte Anwendung wird die galvanische Abscheidung von Metallen betrachtet. Basierend auf einer Kontinuumshypothese wird ein makroskopisches Modell erstellt, welches alle drei Ionentransportvorgänge in verdünnten Elektrolytlösungen berücksichtigt, d.h. Konvektion, Diffusion und Migration. Der letztere Effekt beschreibt dabei die Bewegung von Ionen, die durch ein elektrisches Feld hervorgerufen wird.

Einer der Schlüsselaspekte dieser Arbeit ist die Betrachtung der inhärenten Kopplung von Ionentransport und komplexer, oftmals turbulenter Strömung von Elektrolytlösungen. Ein anspruchsvolles, beidseitig gekoppeltes Problem muss für den Fall einer auftriebsgetriebenen Strömung (sog. natürliche Konvektion) in einer elektrochemischen Zelle betrachtet werden. Für eine geeignete Modellierung der Reaktionskinetik an Elektroden werden nichtlineare phänomenologische Randbedingungen wie zum Beispiel das Butler-Volmer-Gesetz verwendet. Ein allgemeiner Ansatz für stromkontrollierte (galvanostatische) Probleme vervollständigt das umfassende Modell.

Als einheitliches Diskretisierungsverfahren für alle Bestimmungsgleichungen wird eine neuartige stabilisierte Finite-Element-Methode vorgeschlagen. Die zusätzlichen Stabilisierungsterme werden auf der Grundlage eines residuenbasierten variationellen Mehrskalenansatzes hergeleitet. Es wird gezeigt, dass die vorgeschlagenen Stabilisierungstechniken für das gekoppelte Ionentransportproblem zur Robustheit von elektrochemischen Simulationen beitragen, wenn Konvektion eine erhebliche Rolle spielt. Da die variationelle Mehrskalenmethode ebenfalls eine Möglichkeit zur Großwirbelsimulation turbulenter Strömungen eröffnet, ist die entwickelte Berechnungsumgebung in der Lage, den gekoppelten Transport mehrerer Ionenarten in laminarer, transitioneller und turbulenter Strömung von Elektrolytlösungen zu simulieren. Darüberhinaus wird in dieser Arbeit ein partitionierter Lösungsansatz zur Einbeziehung natürlicher Konvektionsphänomene in elektrochemischen Zellen vorgeschlagen.

Vielfältige numerische Beispiele demonstrieren, dass das neuartige Berechnungsverfahren robust ist und korrekte Ergebnisse liefert. Unter anderem werden dabei verschiedene realistische Problemkonfigurationen mit komplexen dreidimensionalen Geometrien betrachtet. Die Vielseitigkeit der gezeigten numerischen Beispiele veranschaulicht das breite Spektrum an geschaffenen Simulationsmöglichkeiten.

## *Zusammenfassung*

---

Zusammenfassend repräsentiert das entwickelte Berechnungsverfahren einen wichtigen Beitrag zur Entwicklung eines Vorhersagewerkzeugs für industrielle Beschichtungsanwendungen im Besonderen und für die makroskopische Simulation elektrochemischer Systeme im Allgemeinen.

## **Danksagung**

An dieser Stelle möchte ich einen ganz herzlichen Dank an all jene aussprechen, die mich in den Jahren meiner Promotion auf so vielfältige Weise unterstützt haben.

Mein besonderer Dank gilt Herrn Prof. Wolfgang A. Wall sowie Herrn Dr.-Ing. Volker Gravemeier für die hervorragende Betreuung während dieser interessanten und lehrreichen Zeit am Lehrstuhl für Numerische Mechanik. Insbesondere bedanke ich mich für das in mich gesetzte Vertrauen sowie für die exzellenten Rahmenbedingungen, die man hier am Institut vorfindet.

Bei den weiteren Mitgliedern der Prüfungskommission, Herrn Prof. Antonio Huerta und Herrn Prof. Wolfgang H. Polifke, bedanke ich mich für die aufgebrachte Zeit und Mühe im Zusammenhang mit meinem Promotionsverfahren. Der Raumfahrtagentur des Deutschen Zentrums für Luft- und Raumfahrt (DLR) danke ich für die Finanzierung des dreijährigen Forschungsprojektes „Numerische Simulation von galvanischen Beschichtungsvorgängen“, in dessen Rahmen ein Großteil der hier präsentierten Arbeit entstand. Ebenso danke ich dem Industriepartner EADS Astrium für die gute Kooperation in diesem gemeinsamen Projekt.

Meinen Kolleginnen und Kollegen möchte ich für das großartige Arbeitsklima danken, welches den Lehrstuhl in meinen Augen wirklich auszeichnet. Gerne denke ich an die vielen interessanten Gespräche und Erlebnisse zurück, die ich beruflich als auch privat als große Bereicherung empfand. Ich danke allen für die bereitwillige Hilfe, die ich stets erfahren habe, wenn es galt, Probleme gemeinsam anzugehen und zu lösen. Gerade am Anfang der eigenen Promotionsphase ist man über erklärende Worte und helfende Hände erfahrener Mitarbeiter sehr froh. Den fleißigen Korrekturlesern des Manuskripts möchte ich ebenfalls ein großes Dankeschön aussprechen.

Ein herzlicher Dank gilt schließlich auch meiner Familie, insbesondere meiner Frau Anna und meinen Eltern, für die Unterstützung und aufgebrachte Geduld in den vergangenen Jahren.

München, Oktober 2012

Georg Bauer



# Contents

<b>1</b>	<b>Introduction</b>	<b>1</b>
1.1	Overview . . . . .	1
1.2	Basic principles of electrochemical systems . . . . .	1
1.3	Electrodeposition of metals . . . . .	5
1.4	Objectives and outline . . . . .	9
<b>2</b>	<b>Mathematical model</b>	<b>13</b>
2.1	Preliminaries . . . . .	13
2.2	Multi-ion transport in dilute electrolyte solutions . . . . .	14
2.3	Electric field . . . . .	16
2.3.1	Poisson equation . . . . .	17
2.3.2	Electroneutrality condition . . . . .	18
2.3.3	Further constraints derived from electroneutrality . . . . .	19
2.4	Charge conservation . . . . .	20
2.5	Initial and boundary conditions for coupled ion transport . . . . .	22
2.5.1	Initial conditions . . . . .	22
2.5.2	Boundary conditions . . . . .	23
2.5.3	Electrode kinetics . . . . .	25
2.5.4	Current-controlled problems . . . . .	28
2.5.5	Faraday's law and electrode shape changes . . . . .	29
2.6	Simple potential model for electrochemical systems . . . . .	29
2.7	Incompressible flow . . . . .	30
2.7.1	Governing equations . . . . .	31
2.7.2	Constitutive models for the density of electrolyte solutions . . . . .	32
2.7.3	Buoyancy and other types of volume forces . . . . .	32
2.7.4	Initial and boundary conditions . . . . .	33
2.8	Further definitions and remarks . . . . .	34
2.8.1	Analytical results . . . . .	34
2.8.2	Model parameters . . . . .	35
2.8.3	A note on the choice of units . . . . .	35
2.8.4	Categorization of current density distributions . . . . .	35
2.8.5	Dimensionless problem formulation . . . . .	36
<b>3</b>	<b>Computational approach</b>	<b>41</b>
3.1	Survey of existing simulation approaches . . . . .	41
3.1.1	General computational methods for ion transport . . . . .	41
3.1.2	Natural convection in electrochemical cells . . . . .	43
3.1.3	Ion transport in turbulent flow . . . . .	44
3.1.4	Electrodeposition and pulse-plating applications . . . . .	45

3.1.5	Summary and conclusions . . . . .	45
3.2	Time discretization . . . . .	46
3.2.1	Generalized-alpha time-integration scheme . . . . .	46
3.2.2	Semi-discrete form of governing equations . . . . .	48
3.3	Weak formulation of semi-discrete equations . . . . .	50
3.3.1	Multi-ion transport subproblem . . . . .	51
3.3.2	Flow subproblem . . . . .	55
3.3.3	Entire weak form . . . . .	55
3.4	Residual-based variational multiscale finite element method . . . . .	56
3.4.1	Variational multiscale method . . . . .	56
3.4.2	Finite element approximation of resolved-scale quantities . . . . .	58
3.4.3	Standard Galerkin finite element method . . . . .	59
3.4.4	Residual-based subgrid-scale modeling . . . . .	60
3.4.5	Stabilization parameters . . . . .	64
3.4.6	Special case: binary electrolyte solutions . . . . .	65
3.4.7	Simplified model for the electric potential . . . . .	67
3.5	Solution procedure . . . . .	67
3.5.1	Coupling of flow and electrochemistry subproblems . . . . .	67
3.5.2	Current-controlled simulations . . . . .	68
3.5.3	Numerical solution approach for nonlinear equations . . . . .	72
3.5.4	Numerical solution of linear equation systems . . . . .	74
3.5.5	Postprocessing of simulation results . . . . .	76
<b>4</b>	<b>Numerical examples</b>	<b>77</b>
4.1	Basic numerical test cases . . . . .	77
4.1.1	One-dimensional convection-diffusion-migration equation . . . . .	77
4.1.2	One-dimensional transport of three ionic species . . . . .	80
4.1.3	Analysis of a transient diffusion-migration problem in 3D . . . . .	84
4.1.4	Electrolytic cell between two concentric cylinders . . . . .	87
4.2	Oscillating shear flow cell . . . . .	89
4.3	Natural convection in a rectangular electrolytic cell . . . . .	95
4.4	Rotating cylinder electrodes . . . . .	103
4.4.1	Primary and secondary current density distribution . . . . .	104
4.4.2	Natural convection at a rotating cylinder electrode . . . . .	108
4.4.3	Multi-ion transport in turbulent Taylor-Couette flow . . . . .	113
4.5	Copper pulse plating at a rotating disk electrode . . . . .	121
4.6	Numerical simulation of a nickel pulse-reverse plating experiment . . . . .	128
<b>5</b>	<b>Conclusions and outlook</b>	<b>135</b>
5.1	Conclusions . . . . .	135
5.2	Outlook . . . . .	136
<b>A</b>	<b>Binary electrolyte solutions</b>	<b>139</b>
<b>B</b>	<b>Flux calculation for finite element approaches</b>	<b>143</b>
B.1	Consistent boundary-flux calculation . . . . .	143
B.2	Flux approximation in the computational domain . . . . .	145

<b>C Rotationally-symmetric periodic boundary conditions</b>	<b>147</b>
<b>Bibliography</b>	<b>149</b>

*Contents*

---

# Nomenclature

## General symbols

$\mathbb{N}, \mathbb{Z}, \mathbb{R}$	natural, whole and real numbers
$\mathbb{R}_0^+, \mathbb{R}^+$	nonnegative real numbers, positive real numbers
$\mathbb{R}^d$	Euclidean vector space of dimension $d$
$d$	number of space dimensions
$x$	position vector
$t$	time
$T_e$	end time
$I$	unit tensor
$(\cdot)^T$	transposed quantity
$f, y, \psi$	arbitrary functions
$(\cdot)_{\text{ref}}$	reference value, characteristic value
$(\cdot)^*$	dimensionless quantity

## Domains and boundaries

$\Omega$	domain
$\partial\Omega$	boundary of the domain $\Omega$
$\overline{\Omega}$	closure of the domain $\Omega$
$\varphi$	particle motion mapping
$V, \partial V$	arbitrary domain and corresponding boundary
$n$	unit outer normal vector at a boundary
$\Gamma_{D,k}, \Gamma_{N,k}, \Gamma_{E,k}$	Dirichlet, Neumann and electrode boundary part (ionic species $k$ )
$\Gamma_a, \Gamma_c$	anode and cathode boundary part

$\Gamma_D^u, \Gamma_N^u$	Dirichlet and Neumann boundary part for the flow problem
$\Gamma_D^\Phi, \Gamma_N^\Phi, \Gamma_E^\Phi$	Dirichlet, Neumann and electrode boundary part for simple potential model

## Operators

$\frac{d}{dt}$	total time derivative, material time derivative
$\frac{\partial}{\partial t}$	partial time derivative
$\nabla$	spatial gradient operator
$\nabla \cdot$	divergence operator
$\nabla \times$	curl operator
$\text{tr}(\cdot)$	trace operator

## Governing equations

### Multi-ion transport

$m$	number of considered ionic species
$(\cdot)_k$	index of ionic species
$c_k$	molar concentration of ionic species $k$
$c_k^\infty$	bulk concentration of ionic species $k$
$M_k$	molar mass of ionic species $k$
$R_k$	homogeneous reaction term of ionic species $k$
$N_k$	total flux density of ionic species $k$
$N_k^{d+m}$	flux density of ionic species $k$ due to diffusion and migration
$D_k$	diffusion coefficient of ionic species $k$
$z_k$	charge number (valence) of ionic species $k$
$\mu_k$	mobility constant of ionic species $k$
$F$	Faraday's constant ( $F = 96,485.34 \text{ C/mol}$ )
$R$	universal gas constant ( $R = 8.314462 \text{ J K}^{-1} \text{ mol}^{-1}$ )
$T$	temperature
$D$	diffusion coefficient for a binary electrolyte

---

$t_+, t_-$	transference numbers for a binary electrolyte solution
$\tilde{h}$	modified boundary flux for a binary electrolyte solution

### Electric field and charge conservation

$E$	electric field
$D$	electric displacement field
$\rho_e$	electric charge density
$\epsilon$	general permittivity tensor
$\epsilon$	permittivity of a homogeneous, isotropic material
$\epsilon_r$	relative permittivity
$\epsilon_0$	permittivity of vacuum ( $\epsilon_0 = 8.854 \cdot 10^{-12} \text{ F/m}$ )
$\Phi$	electric potential
$r_D$	Debye length
$\sigma$	conductivity
$I$	electric current
$I_{\text{in}}, I_{\text{out}}$	electric current into and out of a given domain
$i$	electric current density

### Boundary-related quantities

$g_k$	prescribed concentration for ionic species $k$
$h_k$	prescribed boundary flux density for ionic species $k$
$j_k$	boundary flux density of ionic species $k$ due to electrode reactions
$i_n$	normal component of the electric current density
$n_{\text{rea}}$	number of electrochemical reactions
$i_n^r$	normal current density due to reaction $r$
$n_r$	number of electrons transferred in reaction $r$
$s_{r,k}$	stoichiometric coefficient of ionic species $k$ in reaction $r$
$\zeta$	sign convention parameter
$(.)_a$	anodic quantity

$(.)_c$	cathodic quantity
$i_0$	exchange current density
$\beta, \alpha_a, \alpha_c$	parameters for Butler-Volmer equation
$U$	cell voltage
$V_E$	electric potential on the metal side of an electrode
$V_a, V_c$	electrode potentials of anode and cathode
$\eta_s$	surface overpotential
$\eta_c$	concentration overpotential
$\Delta\Phi_{\text{ohm}}$	ohmic voltage drop
$E_0$	equilibrium potential/ open-circuit potential
$\mathcal{R}^a, \mathcal{R}^c$	constraints for current-controlled problems
$I_{\text{tot}}$	prescribed total current
$\tilde{u}$	rate of electrode shape change
$\rho_{me}$	density of deposited or dissolved material
$M_{me}$	molar mass of deposited or dissolved material
$\overline{V}_{me}$	molar volume of deposited or dissolved material
$\lambda$	efficiency factor
$\Delta h$	local deposit thickness
$\delta_u$	velocity boundary-layer thickness
$\delta_c$	ionic concentration boundary-layer thickness

### Simple potential model

$\Phi_D$	prescribed electric potential
$h^\Phi$	prescribed normal current density
$i_n(\Phi)$	normal current density due to electrode reactions

### Incompressible flow

$u$	velocity
$p_{\text{dyn}}$	dynamic pressure
$p$	kinematic pressure
$\rho$	fluid density
$\rho^\infty$	reference density
$\mu$	dynamic viscosity
$\nu$	kinematic viscosity
$\tilde{b}$	specific volume force
$b$	volume force term
$\boldsymbol{\varepsilon}(u)$	strain rate tensor
$\alpha_k$	densification coefficient of ionic species $k$
$g$	gravitational acceleration
$u_D$	prescribed velocity
$t$	prescribed traction

### Time discretization

$(.)^{n+1}$	quantity at new time level
$(.)^n$	quantity at previous time level
$(.)^{n+\alpha_f}, (.)^{n+\alpha_m}$	quantity at intermediate time levels
$(.)^0$	initial value, initial field
$\Delta t$	time-step length
$\alpha_f, \alpha_m, \gamma$	parameters of the generalized-alpha scheme
$\theta$	parameter of the generalized trapezoidal rule
$\rho_\infty$	spectral radius for an infinite time step

## Function spaces, inner products, norms

$L^2(\Omega)$	space of square-integrable functions
$H^1(\Omega)$	Sobolev space of order one
$(\cdot, \cdot), (\cdot, \cdot)_\Omega$	inner product of $L^2(\Omega)$
$(\cdot, \cdot)_\Gamma$	inner product of $L^2(\Gamma)$
$\ \cdot\ _{L^2(\Omega)}$	$L^2(\Omega)$ -norm
$\ \cdot\ _{H^1(\Omega)}$	$H^1(\Omega)$ -norm
$\mathcal{S}$	space of trial solution functions
$\mathcal{T}$	space of test (weighting) functions

## Spatial discretization

$\mathcal{B}_k, \mathcal{J}_k, \mathcal{F}_k$	terms within the weak form of the Nernst-Planck equation
$\mathcal{B}_E$	weak form of the electroneutrality condition
$\mathcal{B}_C$	weak form of the alternative closing equation
$(\cdot)^h$	resolved-scale quantity
$(\hat{\cdot})$	subgrid-scale quantity
$n_{el}$	number of elements
$n_{nod}$	number of nodes
$n_{bdry}$	number of boundary nodes
$(\cdot)_e$	element-specific quantity
$\Omega_e$	element domain
$N_a^h$	shape function associated to node $a$
$(\bar{\cdot})$	nodal value
$\mathbf{c}_k, \Phi, \mathbf{u}, \mathbf{p}$	nodal solution vectors
$\tau_M, \tau_C$	stabilization parameters for the flow subproblem
$\tau_k, \tau_E$	stabilization parameters for the multi-ion transport subproblem
$\mathcal{R}_M^h, \mathcal{R}_C^h$	discrete residuals of momentum and continuity equation

---

$\mathcal{R}_k^h$	discrete residual of the transport equation for ionic species $k$
$\mathcal{R}_E^h$	discrete residual of the electroneutrality condition
$\mathbf{u}_{\text{mig}}$	migration velocity
$\sigma_{\text{mig}}$	migration reaction parameter
$\mathbf{v}_k$	effective velocity vector for ionic species $k$
$\mathbf{G}$	metric tensor
$\xi$	coordinate system of reference element
$C$	constant from inverse estimates

## Solution procedure

$\Delta V_c, \Delta V_a$	increments for anodic and cathodic electrode potential
$\Delta\Phi_{\text{bulk}}$	voltage drop in bulk electrolyte solution
$R_{\text{bulk}}$	resistance of bulk electrolyte solution
$L$	length used within galvanostatic control algorithm
$A$	area of an electrode
$\varepsilon_{\text{GCC}}, \varepsilon_R$	tolerances for galvanostatic control algorithm
$\mathbf{F}$	general nonlinear problem
$\mathbf{y}$	general vector of (nodal) unknowns
$\Delta\mathbf{y}$	general increment vector
$\mathbf{F}_F$	nonlinear flow subproblem
$\mathbf{F}_E$	nonlinear multi-ion transport subproblem
$\mathbf{R}_M, \mathbf{R}_C$	discrete residuals of momentum and continuity equation
$\mathbf{R}_{c_k}, \mathbf{R}_\Phi$	discrete residuals of ion-transport and electroneutrality equation

## Dimensionless numbers

Re	Reynolds number
Pe	Peclet number
Sc	Schmidt number
Sh	Sherwood number

## Abbreviations

ALE	Arbitrary Lagrangian Eulerian
AMG	Algebraic Multigrid
BDF2	Backward differentiation formula of order two
CNP	Charge-conservation-Nernst-Planck
DAE	Differential algebraic equation
DC	Direct current
DNS	Direct numerical simulation
ENP	Electroneutrality-Nernst-Planck
FEM	Finite element method
GCC	Galvanostatic constraint condition
GMRES	Generalized minimal residual
IHP	Inner Helmholtz plane
LBB	Ladyzhenskaya-Babuška-Brezzi
LES	Large-eddy simulation
NURBS	Non-uniform rational B-splines
ODE	Ordinary differential equation
OHP	Outer Helmholtz plane
PNP	Poisson-Nernst-Planck
PP	Pulse plating
PRP	Pulse-reverse plating
PSPG	Pressure-stabilizing Petrov-Galerkin
RANS	Reynolds-averaged Navier-Stokes
RCE	Rotating cylinder electrode
RDE	Rotating disk electrode
rms	Root-mean-square value
rpm	Revolutions per minute

SIMPLE	Semi-implicit method for pressure-linked equations
SGFEM	Standard Galerkin finite element method
SUPG	Streamline upwind Petrov-Galerkin
UMFPACK	Unsymmetric multifrontal sparse LU factorization package
VMM	Variational multiscale method



# 1 Introduction

## 1.1 Overview

Electrochemistry denotes a branch of chemical science concerned with the interrelation of electrical and chemical phenomena (Bard et al. [8]). Typically, two categories of electrochemical systems are distinguished. The term *galvanic cells* is used for electrochemical cells where electric current is created due to ongoing electrochemical reactions. Consequently, such cells are commonly used as power sources. Well-known examples are batteries and fuel cells, which are particularly relevant as enabling key technologies in the context of electromobility and renewable energy sources.

The so-called *electrolytic cells* form the second category of electrochemical systems. There, an electric current is externally applied in order to drive desired electrochemical reactions. Electrolytic processes, such as the electrochemical production of various chemicals, electrodeposition of metals and alloys, electrowinning of metals from ores and electrochemical machining applications have significant industrial importance. The charging of a (rechargeable) battery represents a further important electrolytic application. Electrochemical phenomena in general are also the cause for metal corrosion and are fundamental parts of many biological systems.

Electrochemical systems are characterized by a coupling of different physical, chemical and electrical processes. According to Newman and Thomas-Alyea [137], the behavior of an electrochemical system is determined by a complex interplay of thermodynamics, electrode kinetics and ionic transport phenomena. As a consequence, research and development in the field of electrochemistry are necessarily multidisciplinary tasks involving several scientific disciplines. Beside expert knowledge and experimental methods, the use of mathematical modeling and computational methods represents a further promising approach which will be instrumental in gaining further insight into these complex systems, to optimize existing electrochemical configurations and to support the development of future systems.

## 1.2 Basic principles of electrochemical systems

Although the exemplary applications stated above seem to be very different at a first glance, it is important to note that certain principles are common to all electrochemical systems. For an introduction to the scientific field of electrochemistry, the reader is particularly referred to the outstanding book by Newman and Thomas-Alyea [137]. Further adequate references are Bard and Faulkner [7], Bagotsky [4] and Hamann et al. [91]. Ionic transport processes and the related mathematical modeling are addressed by Kontturi et al. [117]. The electrochemical dictionary by Bard et al. [8] can be consulted for clarification and better understanding of electrochemical terminology. Finally, the online platform “Elec-

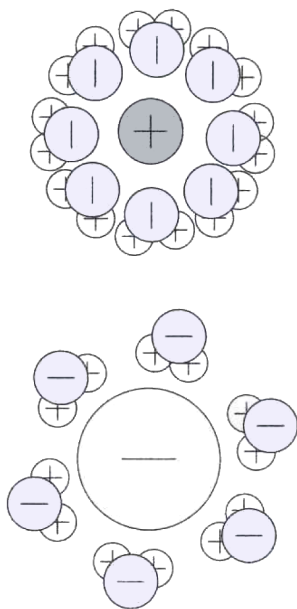


Figure 1.1: Hydration shells (from Kanani [111]).

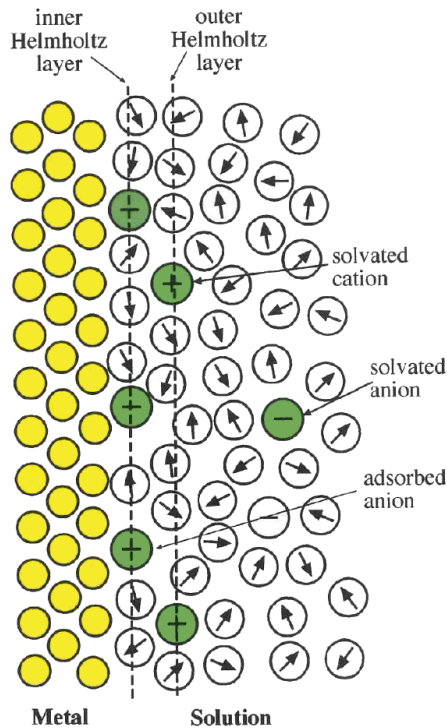


Figure 1.2: Electric double layer (from Bard et al. [8]).

trochemical science and technology information resource (ESTIR)” [59] provides access to numerous online services and information resources related to the broad scientific field of electrochemistry.

In general, an electrochemical cell consists of at least two electron conductors (electrodes) in contact with an ionic conductor (electrolyte). An electrolyte is a chemical compound consisting of ions. Upon dissolution into a solvent or upon melting, an electrolyte dissociates into separate ions. Thus, electrolytes play a fundamental role in electrochemistry, since the ionic conductivity enables the passage of electric current through an electrochemical cell from one electrode to the other. Examples for electrolytes are acids, bases and salts. A chemical compound which is able to act as ionic conductor at solid state is termed solid electrolyte.

For a majority of applications, liquid electrolyte solutions are used. So-called strong electrolytes dissociate completely into ions when dissolved into a solvent such as water, whereas weak electrolytes dissociate only partially. In both cases, the created ions are typically surrounded by a so-called solvation shell. It is caused by electrostatic forces between ions and polar solvent molecules. For aqueous electrolyte solutions, where water is used as a solvent, the solvation shell is also referred to as hydration shell. A schematic representation of hydration shells formed by dipole water molecules around a cation and an anion is provided in Fig. 1.1. A detailed introduction to the important class of aqueous electrolyte solutions is given by Wright [181], for instance.

The dissolved ions are the reason for the electric conductivity of an electrolyte solution.

Furthermore, these ions are the only charge carriers, since there are no free electrons in an electrolyte solution. Often, a so-called supporting electrolyte is added to an electrolyte solution for increasing its conductivity. As a consequence of the reduced electric resistance, undesired ohmic losses are decreased. The ions of a supporting electrolyte are inert and do not participate in electrochemical reactions at the range of potential differences relevant for the particular application. According to Bard et al. [8], typical molar concentration values of supporting electrolyte are within the range  $0.1 - 1.0 \text{ mol/m}^3$ , or even higher. In general, one mole (SI unit: 1 mol) denotes an amount of about  $6.022 \cdot 10^{23}$  molecules. Depending on the application, further additives of organic or inorganic type may be part of an electrolyte solution for chemically influencing its properties. Besides other parameters, the effective conductivity of an electrolyte solution depends on the bath composition, the rate of electrolyte dissociation and the given temperature.

As stated above, two electrodes acting as electron conductors are forming the second fundamental part of every electrochemical cell. According to Bard et al. [8, p. 202], an alternative definition of the term electrode in the sense of a half-cell appears to be reasonable: “*The electrode consists of two or more electrically conducting phases switched in series between which charge carriers (ions or electrons) can be exchanged, one of the terminal phases being an electron conductor and the other an electrolyte.*” Thus, in electrochemistry, the interface between electrode and electrolyte is of primary interest.

When an electrode is in contact with an electrolyte, a so-called electric double layer forms at its surface. This is a general physical phenomenon occurring at the interface between two conducting media. On one side of the interface an excess positive charge is present, which is balanced by the same amount of negative charge accumulating at the opposite side of the interface. Different theoretical models have been developed to describe the formation and the structure of electric double layers. A historical overview of the development of such theories is provided by Damaskin and Petrii [43]. In Fig. 1.2, a basic representation of the electric double layer is provided. The charged layer on the solution side of the interface is typically divided into several substructures. The inner Helmholtz plane (IHP) is characterized as the distance of partially or fully desolvated ions specifically adsorbed to the metal surface. The closest approach of fully solvated ions determines the position of the so-called outer Helmholtz plane (OHP). Adjacent to these two layers, the so-called diffuse layer is located, which denotes a region with nonzero space charge. The electric double layer exhibits a capacitive effect similar to a parallel-plate capacitor (see, e.g., Newman and Thomas-Alyea [137]).

In an electrochemical system, considerable charge separation is observed solely in the electric double layer at the electrode-electrolyte interface and the diffuse layer adjacent to it. Typically, these layers have a combined thickness of 1 - 10 nm, as depicted in Fig. 1.3. Outside of these regions, i.e., in the diffusion layer and the bulk solution, the electrolyte solution is assumed to be electrically neutral. In the diffusion layer, a non-uniform composition of the electrolyte solution is observed, caused by electrochemical surface reactions and ion-transport phenomena. It represents a kind of boundary layer, in which the ionic concentrations vary. As shown in Fig. 1.3, typical boundary-layer thicknesses are in the order of  $\mu\text{m}$ . Finally, in the bulk region, the electrolyte solution is assumed to have uniform composition.

At an electrode surface, electrochemical reactions take place, which typically involve a charge transfer step, where one or more electrons are transferred. According to Bard

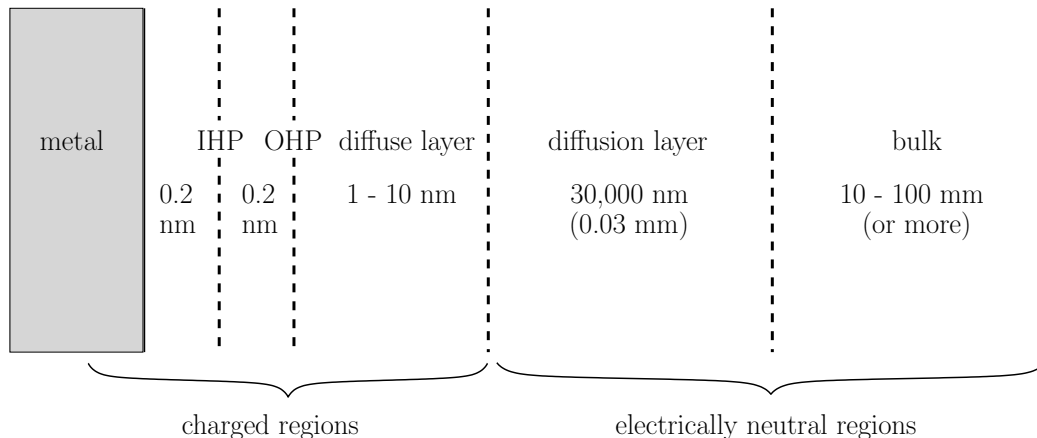


Figure 1.3: Typical dimensions of an electric double layer at a metal-solution interface according to Newman and Thomas-Alyea [137].

and Faulkner [7], an overall electrode reaction is characterized as a reduction-oxidation (red-ox) mechanism of the form



In reaction (1.1), O denotes the dissolved oxidized chemical species, R its reduced form and  $n$  is the number of electrons transferred within the considered reaction. As shown in Fig. 1.4, several processes and phenomena are influencing the reaction rate of (1.1). The first important aspect is ion transport from the bulk solution towards the electrode surface. Typically, three different ion-transport mechanisms are considered in (dilute) electrolyte solutions (see, e.g., Newman and Thomas-Alyea [137]): convection (movement with bulk electrolyte solution), diffusion (movement caused by concentration gradients) and migration (movement caused by the applied electric field). The second important phenomenon is the actual electron transfer at the electrode surface. As depicted in Fig. 1.4, additional chemical reactions or further surface reactions such as adsorption, desorption or crystallization may take place before or after the electron transfer. A characteristic property of electrochemical systems is that the net reaction rate of (1.1) is directly correlated to the arising electric current. Thus, a measurement of the electric current passing an electrochemical cell provides information on the reaction rate of the ongoing electrochemical reactions.

Even in equilibrium, a permanent exchange of charged particles takes place in both directions across the interface between electrode and electrolyte. At equilibrium, the opposing partial currents associated with the ongoing forward and backward partial reactions are balanced. The rate of exchange is associated with the so-called exchange current density  $i_0$ . In the case of a nonzero net current, one of the two opposing reactions is prevalent. As a result, a nonzero net current density in normal direction to the interface is obtained.

The electrode where the reduction reaction is the dominating process is termed cathode. At a cathode, electrons flow from the electrode towards the electrolyte. The opposite electrode, where an oxidation is the prevalent reaction, is called anode. Both electrodes are connected to an external electric circuit. Through this outer connection electrons will

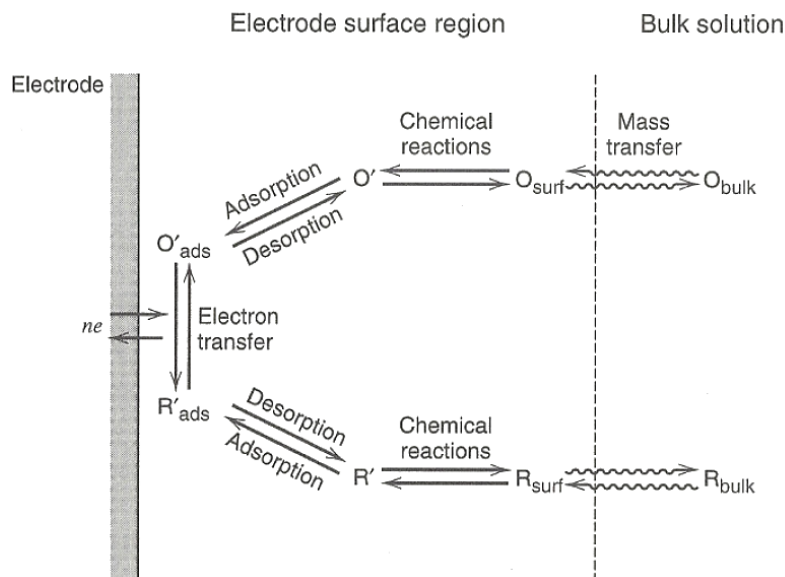
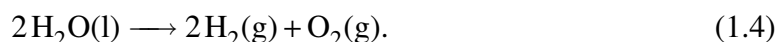
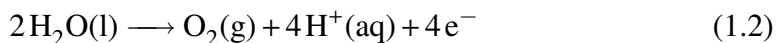


Figure 1.4: General electrode reaction (from Bard and Faulkner [7]).

travel towards or away from the electrodes, while ions are the only charge carriers inside the electrolyte. In the case of an electrolytic cell, usually an external power source is connected to the electrodes, while a galvanic cell is typically connected to some kind of consumer load, e.g., an electric motor.

A well-known electrochemical application is the electrolysis of water, i.e., its decomposition into hydrogen and oxygen gas using electric current. The corresponding reactions are given as



At the anode of a water electrolysis cell, the oxidation reaction (1.2) takes place, while the reduction (1.3) occurs at the cathode. Combining these two half reactions yields the overall reaction stated in (1.4).

A further important electrolytic process is electrodeposition of metals. The basic concepts of this application, which has a high industrial relevance, are explained in the following.

## 1.3 Electrodeposition of metals

In general, electrodeposition denotes an electrolytic process for depositing metal onto a conducting surface using electric current. In literature, also the term electroplating is used as a synonym. Electroplating represents an important and widely-used electrochemical technique for coating electrically conductive objects with metal layers. For an introduction to electrodeposition, the reader is referred to Paunovic and Schlesinger [141], Schlesinger

and Paunovic [155] and Kanani [111], for instance. The ASM handbook [3] on general surface engineering contains also chapters devoted to electroplating techniques. Of course, the reader is also referred to the more general literature on electrochemistry specified previously.

Typical deposit thicknesses produced via electroplating methods are in the order of  $\mu\text{m}$ . Such coatings usually serve functional, decorative or other purposes. Zinc plating, for example, has a high industrial importance for the corrosion protection of metallic components and products. On the other hand, chromium plating is a well-known example for a decorative surface treatment. In semiconductor industries, copper interconnects of integrated circuits are fabricated utilizing electrodeposition techniques. An overview of methods and applications of electrochemical microfabrication is provided by Datta and Landolt [45]. Electroplating techniques also enable the fabrication of special alloys consisting of different metallic compounds and the deposition of multilayered materials. For example, within the manufacturing process of magnetic recording heads, special magnetic materials and magnetoresistant thin films are produced via electrodeposition (see, e.g., Datta and Landolt [45]).

Electroforming techniques even enable the fabrication of very thick metal layers (up to mm-size or more). Via electroforming, even whole parts with complex geometries can be realized with desired shapes and material properties. For example, electroformed components exhibit increased hardness and lower intrinsic stresses compared to the results obtained when using conventional metal cutting procedures. Thus, in aerospace industries such electrochemical techniques are considered as a key technology for an efficient production process of combustion chambers for space propulsion systems. According to Immich et al. [105], most of the present cryogenic high pressure rocket engines have regeneratively cooled, integral combustion chambers made from milled slotted liners of copper alloys surrounded by an electrodeposited outer nickel jacket. Typical examples are the Vulcain 2 rocket engine of the European Ariane 5 launcher and the main engine of the former U.S. space shuttle.

Electrodeposition represents an electrolytic process which takes place in so-called electroplating baths (sometimes also called galvanic baths). In Fig. 1.5, a basic electrolytic system used for electroplating is depicted. The part to be plated acts as cathode of the electrolytic cell. In the context of electrodeposition also the nomenclature “working electrode” for the cathode is found, since there the desired electrochemical process takes place. Metal cations are transported from the bulk electrolyte solution towards the cathode, where a reduction reaction of the form



takes place and the metal plates out. Here, M represents the chemical symbol of the considered metal, z is the number of electrons transferred in the reaction and  $z+$  denotes the valence (charge number) of the corresponding metal cation. In the notation used for the general electrode reaction (1.1), it holds  $O = \text{M}^{z+}$ ,  $R = \text{M}$  and  $n = z$ .

Usually, the same metal M which is intended to be deposited at the cathode is used as anode material. Since, in this case, the reverse reaction of (1.5) is taking place at the anode, the ongoing oxidation of metal ions causes a dissolution process of the anode material. Thus, the (often multiple) anodes act as source for new metal ions which are entering the electrolyte solution.

As stated above, electrodeposition of copper is an important example for electroplating.

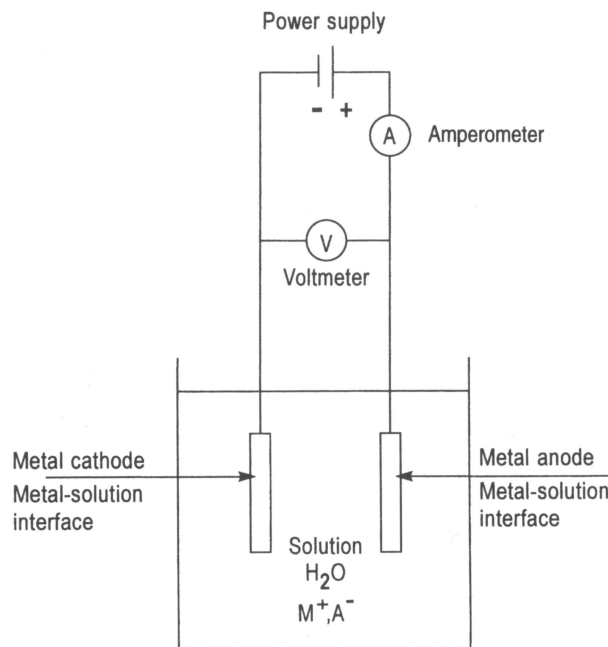
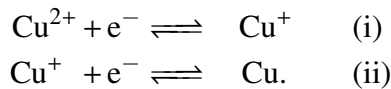


Figure 1.5: Sketch of an electrolytic cell used for electroplating (adapted from Paunovic and Schlesinger [141]).

The corresponding electrochemical reaction is expressed in a simplified form as



Indeed, the copper dissolution and deposition reaction (1.6) is a combination of two elementary charge transfer steps reading



According to, e.g., Newman and Thomas-Alyea [137], elementary step (i) is taking place much faster than the elementary step (ii). Thus, the overall reaction rate for (1.6) is determined by the partial reaction (ii). For copper electroplating usually aqueous  $CuSO_4 - H_2SO_4$  solutions are used, where the ionic conductivity provided from the dissolved copper(II) sulfate is enhanced by additional sulfuric acid acting as supporting electrolyte.

In many industrial electroplating baths, it is aimed at keeping the electrolyte solution well-mixed by using different bath agitation techniques such as jet systems and stirring devices. Rotationally-symmetric parts to be plated are usually also rotated to achieve uniform plating results. As a consequence, quite complex, often turbulent flow conditions arise, directly influencing the ion-transport processes inside the electrolyte solution. Hence, a mathematical model describing such electrochemical systems has to take into account the inherent coupling to fluid flow. As introduced above, diffusion and migration are further ionic transport phenomena that have to be considered besides the convection of ions.

Electrochemical deposition can be performed either voltage-controlled (potentiostatic)

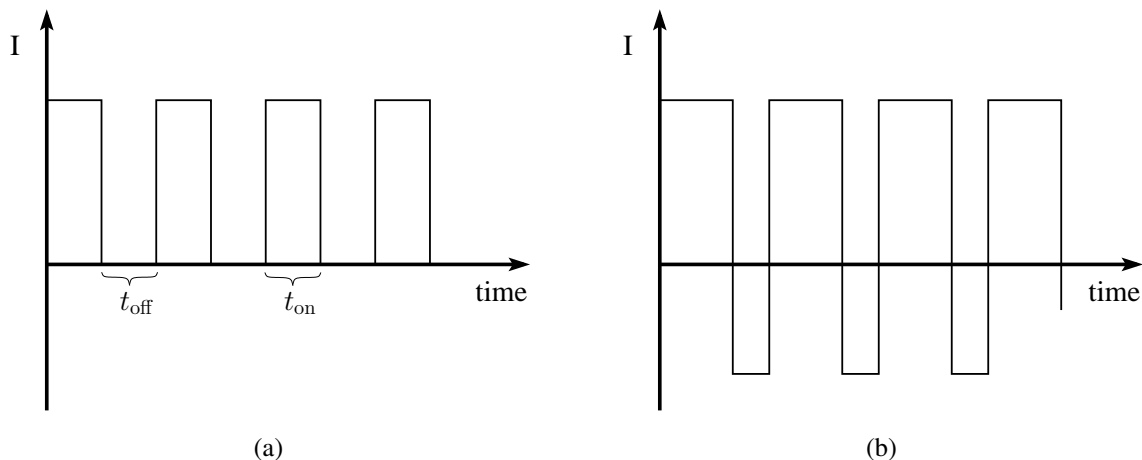


Figure 1.6: Typical current patterns for pulse plating (a) and pulse-reverse plating (b).

or current-controlled (galvanostatic). In the first case, a certain voltage difference is applied to the electrolytic cell. In the second case, the electric current corresponding to the electrochemical rate of reaction is controlled via an external control device (galvanostat). Traditionally, direct current (DC) is used for electroplating processes. However, in the recent decades, plating techniques using non-constant, pulsating current became increasingly important, since they offer more flexibility for the production process and lead to improved plating results. Pulse plating (PP) is a current-controlled technique which is characterized by the usage of a series of direct current pulses separated by periods of zero electric current. The intensity of pulses as well as the “on” and “off” times, which are defining the pulse frequency, are adjustable parameters. A typical current curve for a pulse plating application is depicted in Fig. 1.6(a). An extension of PP is pulse-reverse plating (PRP), where also periods of reverse current are included (see Fig. 1.6(b) for an exemplary current curve).

In general, very different current patterns can be achieved (see, e.g., Puijpe and Leaman [146] for further examples). For each electroplating application, an “optimal” pulse curve has to be determined in order to meet the specific requirements of the considered deposition process. According to Puijpe and Leaman [146] and Chandrasekar and Pushpavanam [32], the main benefits of using PP and PRP methods compared to DC plating methods are:

- improved deposit properties concerning hardness, ductility, porosity, hydrogen content, electric conductivity, roughness and resistance against abrasion
- deposition of special alloys, not producible with other methods
- improvement of the layer thickness distribution due to periodic current reversal (→ more equal coatings)
- allowance for simpler electrolyte compositions, reduction of bath additives
- significantly raised limiting current density (compared to DC methods).

Drawbacks of PP and PRP methods are the higher costs for pulse rectifiers compared to DC units and a decreasing market for selling bath additives. The latter affects mainly the

chemical industry producing such chemicals. In their recent review article, Chandrasekar and Pushpavanam [32, p. 3320] name a further drawback:

*“The technology requires one to think and plan ahead with a series of procedures to follow in order to obtain the best results.”*

The flexibility obtained from the increased amount of process parameters in PP and PRP methods also raises the complexity of the considered systems. Changing the current curve is only one possibility to influence these electroplating processes, which are also influenced by further parameters such as electrolyte composition, temperature, cell geometry, electrode characteristics and flow properties, for instance. Thus, as indicated in the quote above, a rigorous analysis and understanding of a given plating process is required in order to obtain the best results. Numerical simulation provides one approach which can help to analyze existing electroplating facilities and assist in the design process for future bath configurations. The need for an interdisciplinary and comprehensive approach, combining both experimental and numerical analysis, becomes also evident in the following quote from Van den Bossche et al. [169, p. 61]:

*“There is no simple systematic method to establish the practical range of pulse parameters for a given plating process. A reasonable knowledge of the plating reaction mechanism combined with an adequate analytical or numerical solution strategy will always be required to optimize the pulse plating process on a rigorous basis.”*

## 1.4 Objectives and outline

The main objective of this thesis is the development of a novel comprehensive computational approach enabling the coupled numerical simulation of electrochemical systems. As shown above, electrochemical systems can be found in a large variety of applications. In the present work, it is focused on electrolytic cells in general and electrodeposition of metals in particular.

For a sophisticated mathematical modeling and numerical simulation of such electrochemical applications, several coupled physical phenomena have to be considered. These are, among others, multi-ion transport processes inside an electrolyte solution, influenced by an electric field and fluid flow, as well as electrochemical reactions occurring at electrodes. All three ion-transport phenomena in dilute electrolyte solutions, that is, convection, diffusion and migration are accounted for in the macroscopic model presented in this work. It is emphasized that none of these effects is neglected or excluded *a priori*.

One key aspect of the present work is the appropriate consideration of the inherent coupling of ionic transport and incompressible flow due to convection. In addition, it is important to account for buoyancy-driven flow (natural convection) in electrochemical cells, which leads to a two-way coupled problem formulation. Together with an appropriate phenomenological modeling of electrode kinetics, a comprehensive model is proposed in this thesis. In summary, a coupled multiphysics problem with inherent multiscale character (regarding both length and time scales) is obtained, which imposes several numerical challenges.

A further requirement in order to be able to study real laboratory devices and industrial facilities via numerical simulation is the ability to consider complex geometries. To account for this requirement, an appropriate finite element method (FEM) is proposed in this study. Over the last decades, the FEM has been successfully used as a flexible, robust and accurate discretization approach for a large variety of applications such as computational solid mechanics, computational fluid dynamics as well as fluid-structure interaction representing a coupled multi-field problem (see, e.g., Wall [174]). Here, the FEM is utilized as a general approach to the spatial discretization of all governing equations of multi-ion transport and incompressible flow.

In the present work, a novel stabilized finite element approach for the coupled multi-ion transport problem is developed. It is derived from the variational multiscale framework (Hughes [99]). The developed stabilization techniques account for spurious oscillations that arise in convection-dominated cases. The variational multiscale method (VMM) utilized here also allows for developing an approach to large-eddy simulation (LES) of turbulent flows. Thus, the proposed method is capable of considering coupled ionic transport in laminar, transitional and turbulent flows, an important capability required to accurately simulate real electroplating configurations.

Transient simulation approaches are mandatory for considering time-dependent problems such as pulse and pulse-reverse plating applications. Since such electrochemical techniques are typically current-controlled processes, additional algorithmic extensions are necessary to include a galvanostatic control in a general manner.

In summary, an efficient, robust, and accurate computational tool is required to enable the successful numerical simulation of coupled ion transport in realistic geometries. It will be demonstrated that the developed comprehensive methodical approach meets these requirements. To the author's best knowledge, no comparable three-dimensional computational approach has been proposed so far for a comprehensive numerical simulation of coupled multi-ion transport in dilute electrolyte solutions adequately accounting for all of the aforementioned physical phenomena at the same time.

The computational approach was implemented within the multi-purpose parallel computing platform BACI (Wall and Gee [175]). This flexible finite element software environment is continuously developed and maintained by the Institute for Computational Mechanics at the Technische Universität München. The object-oriented code is written in C++ and utilizes powerful open-source libraries provided by the Trilinos project (Heroux et al. [96]). All simulation results presented in the following were obtained using BACI.

Major parts of the work described in this thesis were carried out in the context of the research project "Numerische Simulation von galvanischen Beschichtungsvorgängen", which was supported by the Space Agency of the German Aerospace Center (DLR) under grant 50RL0743 from October 2007 through September 2010. This financial support as well as the successful cooperation with the industrial partner EADS Astrium within this project are gratefully acknowledged.

Parts of the numerical methods and related simulation results presented in this thesis were published in Bauer et al. [9, 10, 11, 12, 13] and Ehrl et al. [56].

The outline of this thesis is as follows. In chapter 2, an appropriate macroscopic model for electrochemical systems is presented. In particular, the governing equations for multi-ion transport in dilute electrolyte solutions, electric field, charge conservation, electrochemical reactions at electrodes and incompressible flow are provided. Afterwards, in

chapter 3, the proposed computational approach is described. The presentation of the developed stabilized finite element method, which is derived from a residual-based variational multiscale framework, constitutes the main part of that chapter. In addition, some important algorithmic aspects of the numerical solution procedure are explained. The proposed computational method is tested for several different numerical examples in chapter 4, demonstrating that it is robust and provides accurate results. Among others, several realistic problem configurations with complex three-dimensional geometries are considered in the context of electroplating. Finally, conclusions are drawn in chapter 5, before ending with an outlook.

Further details are provided in the Appendix. A theoretical analysis for binary electrolyte solutions is provided in Appendix A. The consistent calculation of fluxes in the context of finite element methods is outlined in Appendix B. Finally, in Appendix C, some details concerning rotationally-symmetric periodic boundary conditions are given.



# 2 Mathematical model

This chapter addresses the mathematical modeling of electrochemical systems from a macroscopic point of view. In the following, appropriate modeling approaches based on the continuum hypothesis are presented. The considerations of Newman and Thomas-Alyea [137] form the main basis for the mathematical model described here. Further details regarding the mathematical description of coupled ion transport in electrochemical systems are provided in Kontturi et al. [117] and Rubinstein [152], for instance.

In section 2.1, some continuum-mechanical basics are introduced and fundamental modeling assumptions are presented. Afterwards, the governing equations for multi-ion transport in dilute electrolyte solutions and the electric field are presented in section 2.2 and 2.3, respectively. The fundamental principle of charge conservation is addressed in section 2.4. In section 2.5, initial and boundary conditions for the coupled multi-ion transport problem are specified. Within this section, it is especially focused on the phenomenological modeling of electrochemical reaction kinetics at electrode surfaces. Also the additional requirements for a consideration of current-controlled (galvanostatic) problems are addressed. A simplified modeling approach for electrochemical systems involving solely the electric potential field is derived in section 2.6. The flow of dilute electrolyte solutions is assumed to be governed by the incompressible Navier-Stokes equations, which are introduced in section 2.7. The present chapter concludes with some important remarks regarding the mathematical problem formulation given in section 2.8.

## 2.1 Preliminaries

In the following, the behavior of an electrochemical system is investigated for a time interval  $[0, T_e]$ . In particular, a liquid electrolyte solution is considered, which occupies a bounded domain  $\Omega \subset \mathbb{R}^d$ . As usual, the mathematical term “domain” denotes a non-empty, connected and open set in the  $d$ -dimensional real Euclidean space  $\mathbb{R}^d$ , where  $d \in \{1, 2, 3\}$  is the number of relevant space dimensions. The boundary of  $\Omega$  is denoted by  $\partial\Omega$  and assumed sufficiently smooth. The closure of  $\Omega$  is defined by  $\overline{\Omega} := \Omega \cup \partial\Omega$ . For a macroscopic description of flow, multi-ion transport and electric field, a continuum-mechanical approach is utilized in the following. For the engineering perspective, the continuum-hypothesis represents a commonly accepted approximation for the description of electrochemical systems (see, e.g., Newman and Thomas-Alyea [137]). For a general introduction to continuum mechanics and related mathematical concepts, the reader is referred to Gurtin [87] and Lai et al. [122], for example. More compact introductions in the context of fluid mechanics are given in Spurk [161] and Donea and Huerta [50], for instance. The textbook by Kontturi et al. [117] on ionic transport processes provides also a respective introductory chapter.

Consider now a portion of electrolyte solution which initially occupies a volume  $V_0$ . For

each time  $t \in [0, T_e]$ , a particle motion mapping is defined by

$$\varphi(\cdot, t) : V_0 \rightarrow V_x(t), \quad X \mapsto \mathbf{x} := \varphi(X, t), \quad (2.1)$$

where  $V_x(t)$  denotes the current domain, i.e., the deformed volume occupied by the liquid electrolyte solution at time  $t$ . Since fluids usually undergo quite large deformations, the Eulerian point of view is advantageous for the description of flows (see, e.g., Donea and Huerta [50]). The velocity of the electrolyte solution is given as

$$\mathbf{u} := \frac{\partial \mathbf{x}}{\partial t}. \quad (2.2)$$

The focus of this study is on dilute electrolyte solutions. For this case, ionic concentrations are very low compared to the concentration of the solute. Thus, the ion-solvent interactions are the prevalent effects that have to be accounted for in the model, whereas ion-ion interactions are of minor importance due to the excess of solvent molecules surrounding the dissolved ions. For many electrodeposition applications, aqueous electrolyte solutions are used, with water as the solute. Typically, the dilute solution assumption is a justified model in the context of electroplating. The governing equations for the modeling of ion transport in either moderately dilute solutions or concentrated electrolyte solutions are discussed in Newman and Thomas-Alyea [137] and Kontturi et al. [117], for example, and are not presented here. The dilute-solution theory represents an important subset of these generalized, more complex mathematical modeling approaches.

Furthermore, for the problems studied here, an isothermal system is assumed. This assumption is justified for the applications considered here, since for electroplating the temperature of an electrolyte solution is usually kept constant by some external thermal control. In addition, energy dissipation due to ohmic losses (Joule heating) usually does not cause significant temperature changes for most electrodeposition problems. For these applications, electric currents passing the electrochemical cells are typically low enough to confirm this modeling assumption.

## 2.2 Multi-ion transport in dilute electrolyte solutions

In the following, a dilute electrolyte solution is considered which contains  $m \geq 2$  different ionic species. For each ionic species  $k = 1, \dots, m$  present in the solution, the fundamental principle of mass conservation must hold. Mathematically this property is expressed as

$$\frac{d}{dt} \int_{V(t)} M_k c_k d\mathbf{x} = - \int_{\partial V(t)} M_k \mathbf{N}_k^{d+m} \cdot \mathbf{n} dS + \int_{V(t)} M_k R_k d\mathbf{x}, \quad (2.3)$$

where  $c_k : \overline{\Omega} \times [0, T_e] \rightarrow \mathbb{R}_0^+$ , denotes the unknown molar concentration of ionic species  $k$  (unit: mol/m<sup>3</sup>) and  $M_k$  the corresponding molar mass (g/mol). Consequently, the product  $M_k c_k$  represents a (mass) density distribution. According to (2.3), the temporal change of the mass contained in an arbitrary volume  $V(t) \subset \Omega$  is caused by a mass flux  $M_k \mathbf{N}_k^{d+m} \cdot \mathbf{n}$  across the boundary  $\partial V(t)$  and a source or sink term  $M_k R_k$ . The latter expression accounts for homogeneous chemical reactions within the volume, where ionic species  $k$  is either

produced or consumed. As usual,  $\mathbf{n}$  denotes the unit outer normal at the respective boundary part. The ionic flux due to diffusion (movement caused by concentration gradients) and migration (movement caused by an electric field) is given as

$$\mathbf{N}_k^{\text{d+m}} := \underbrace{-D_k \nabla c_k}_{\text{diffusion}} + \underbrace{z_k \mu_k F c_k \mathbf{E}}_{\text{migration}}. \quad (2.4)$$

In literature, equation (2.4) is also often referred to as Nernst-Planck equation. Here,  $D_k$  is the molecular diffusion coefficient of ionic species  $k$  with respect to the solute,  $z_k$  is the valence (charge number),  $\mu_k$  the mobility constant,  $F$  Faraday's constant (96,485.34 C/mol) and  $\mathbf{E}$  the electric field inside the electrolyte solution. As usual in dilute-solution theory, the mobility constant  $\mu_k$  is assumed to be related to the diffusion coefficient  $D_k$  according to the Nernst-Einstein relation

$$\mu_k = \frac{D_k}{RT}. \quad (2.5)$$

The relation involves the temperature  $T$  (specified in Kelvin (K)) and the universal gas constant  $R$  (8.314462 JK<sup>-1</sup>mol<sup>-1</sup>). However, for brevity of notation, the symbol  $\mu_k$  is kept using in subsequent formulae and is not immediately replaced by (2.5). This also ensures that alternative definitions for the mobility constant can be used within the developed model.

Since  $M_k$  is a substance-specific, constant value, conservation law (2.3) is usually considered in the shorter, but equivalent form

$$\frac{d}{dt} \int_{V(t)} c_k d\mathbf{x} = - \int_{\partial V(t)} \mathbf{N}_k^{\text{d+m}} \cdot \mathbf{n} dS + \int_{V(t)} R_k d\mathbf{x}. \quad (2.6)$$

Application of Reynold's transport theorem (see, e.g., Spurk [161]) to the left-hand side of (2.6) yields

$$\frac{d}{dt} \int_{V(t)} c_k d\mathbf{x} = \int_{V(t)} \frac{\partial c_k}{\partial t} d\mathbf{x} + \int_{\partial V(t)} c_k \mathbf{u} \cdot \mathbf{n} dS. \quad (2.7)$$

The vector field  $\mathbf{u}$  denotes the velocity of the electrolyte solution as introduced in the previous section. Assuming sufficient smoothness of the respective functions, the divergence theorem (Gauss' rule) is used to transform the boundary integrals in (2.6) and (2.7) to integrals over the volume. As a result one obtains

$$\int_{V(t)} \left( \frac{\partial c_k}{\partial t} + \nabla \cdot \mathbf{N}_k - R_k \right) d\mathbf{x} = 0. \quad (2.8)$$

Here, the total ionic flux is given as

$$\mathbf{N}_k := c_k \mathbf{u} + \mathbf{N}_k^{\text{d+m}} = \underbrace{c_k \mathbf{u}}_{\text{convection}} - \underbrace{D_k \nabla c_k}_{\text{diffusion}} + \underbrace{z_k \mu_k F c_k \mathbf{E}}_{\text{migration}}. \quad (2.9)$$

Since relation (2.8) holds for every arbitrary reference volume  $V(t) \subseteq \Omega$ , a partial differential equation is obtained for each ionic species  $k = 1, \dots, m$  present in an electrolyte solution,

describing the temporal and spatial variation of its molar concentration  $c_k$ :

$$\frac{\partial c_k}{\partial t} + \nabla \cdot \mathbf{N}_k - R_k = 0 \quad \text{in } \Omega \times (0, T_e). \quad (2.10)$$

In literature, the term Nernst-Planck equation is also often used to denote the whole partial differential equation (2.10). Note that the arising convective term involving the velocity  $\mathbf{u}$  of the electrolyte solution establishes a one-way coupling of each ion-transport equation (2.10) to the governing equations of fluid motion, which will be described in section 2.7. For a solenoidal velocity field  $\mathbf{u}$ , i.e., it holds  $\nabla \cdot \mathbf{u} = 0$ , equation (2.10) can be converted from the conservative form (2.10) into the following convective form:

$$\frac{\partial c_k}{\partial t} + \mathbf{u} \cdot \nabla c_k + \nabla \cdot \mathbf{N}_k^{d+m} - R_k = 0 \quad \text{in } \Omega \times (0, T_e). \quad (2.11)$$

For the modeling of many electrochemical systems, reactions are typically restricted to electrode surfaces. Thus, no homogeneous chemical reactions inside the bulk solution are taken into account, for the time being. Consequently, for all ionic species  $k = 1, \dots, m$  it holds  $R_k = 0$  in (2.11). The consideration of homogeneous chemical reactions represents a future extension of the present model. First promising results towards such an extension are given by Wittmann [179]. As a consequence, the governing equations

$$\frac{\partial c_k}{\partial t} + \mathbf{u} \cdot \nabla c_k + \nabla \cdot \mathbf{N}_k^{d+m} = 0 \quad \text{in } \Omega \times (0, T_e), \quad k = 1, \dots, m \quad (2.12)$$

are used throughout this work.

Note that for neutral species ( $z_k = 0$ ) the ion-transport equations (2.12) reduce to conventional convection-diffusion equations, since non-charged particles are not influenced by an electric field.

## 2.3 Electric field

The electric field  $\mathbf{E} : \overline{\Omega} \times [0, T_e] \rightarrow \mathbb{R}^d$  (unit: V/m) represents a further unknown physical quantity required for the modeling of an electrochemical system. In general, the physical effects of electrodynamics are mathematically described by the well-known Maxwell equations, a set of partial differential equations relating electric and magnetic fields (see, e.g., Jackson [108]).

For electrochemical systems such as considered here, the electrostatic concept is commonly accepted as a sufficient modeling approach. For that case, the time-dependent coupling terms in the Maxwell equations vanish. As a consequence, electric and magnetic fields become decoupled, allowing a separate consideration of electro- and magnetostatics. The governing equations for electrostatics as obtained from Maxwell's equations read

$$\nabla \times \mathbf{E} = \mathbf{0} \quad \text{in } \Omega \times (0, T_e), \quad (2.13)$$

$$\nabla \cdot \mathbf{D} = \rho_e \quad \text{in } \Omega \times (0, T_e). \quad (2.14)$$

Here,  $\mathbf{D}$  denotes the so-called electric displacement field (unit: C/m<sup>2</sup>) and  $\rho_e$  is the net electric charge density (unit: C/m<sup>3</sup>). Since there are no free electrons in electrolyte so-

solutions such as considered here, ions represent the only charge carriers. Thus, for any  $(\mathbf{x}, t) \in \bar{\Omega} \times [0, T_e]$  the local charge density is computed from the ionic concentrations  $c_k$  according to

$$\rho_e(\mathbf{x}, t) = F \sum_{k=1}^m z_k c_k(\mathbf{x}, t). \quad (2.15)$$

As stated in (2.13), the electric field is always irrotational. Thus, it is possible to express  $\mathbf{E}$  as the gradient of a scalar function, since it holds  $\nabla \times (\nabla \psi) = 0$  for any scalar field  $\psi(\cdot, t) : \Omega \rightarrow \mathbb{R}$  and  $t \in [0, T_e]$ . Hence, the electric field vector is expressed in electrostatics as the negative gradient of the electrostatic potential field  $\Phi$  reading

$$\mathbf{E} = -\nabla \Phi. \quad (2.16)$$

The negative sign originates from the definition that the electric field is directed from locations associated with higher potential towards regions with lower potential. Based on definition (2.16), equation (2.13) is always fulfilled.

The electric displacement field  $\mathbf{D}$  and the electric field  $\mathbf{E}$  are related via a constitutive law, which is usually expressed in the form

$$\mathbf{D} = \epsilon \mathbf{E}. \quad (2.17)$$

The permittivity  $\epsilon$  (unit: F/m) in (2.17) is a second-rank tensor reflecting individual material properties. In general, the material model may account for temperature dependence, anisotropy due to variations in the composition and other properties of the medium. For the most simple case of a homogeneous and isotropic medium, the permittivity is given as  $\epsilon = \epsilon_r \epsilon_0 \mathbf{I}$ , where  $\epsilon_0 = 8.854 \cdot 10^{-12}$  F/m is the permittivity of the vacuum,  $\epsilon_r$  denotes the medium-specific relative permittivity and  $\mathbf{I}$  is the unit tensor. For example, water at 20°C has a relative permittivity of  $\epsilon_r = 80.20$  (see, e.g., Bard et al. [8]).

As a consequence of (2.16), the number of unknowns is reduced, because in the electrostatic case only the single scalar electric potential field  $\Phi$  has to be determined instead of the vector field  $\mathbf{E}$  with its  $d$  components. Since, besides the ionic species concentrations  $c_k$ , the electric potential  $\Phi$  is an additional unknown in the multi-ion transport equations (2.10) and (2.12), one further governing equation is needed to close the system of equations defined by (2.10) or (2.12), respectively. In the following three subsections, different approaches for defining an appropriate closing equation are presented and discussed.

### 2.3.1 Poisson equation

As a direct consequence of the considerations above, a governing equation for the electric potential field is obtained by inserting (2.15), (2.16) and (2.17) into (2.14). This yields the so-called Poisson equation for the electric potential:

$$-\nabla \cdot (\epsilon \nabla \Phi) - F \sum_{k=1}^m z_k c_k = 0 \quad \text{in } \Omega \times (0, T_e). \quad (2.18)$$

In general, equation (2.18) allows for the effect of charge separation, which occurs in the vicinity of electrode surfaces, as explained in section 1.2. Consequently, for simulations

of the electric double layer and the adjacent diffuse layer, the consideration of (2.18) is mandatory. In literature, the coupled system of Poisson equation (2.18) and ion-transport equations (2.12) is often termed Poisson-Nernst-Planck (PNP) equations.

According to Dickinson et al. [48], a normalized form of (2.18) given as

$$2r_D^2 \Delta \Phi^* + \sum_{k=1}^m z_k c_k^* = 0 \quad (2.19)$$

provides further conclusions. Here, the dimensionless potential is given as  $\Phi^* = \Phi \frac{F}{RT}$  and the ionic concentrations are made dimensionless via  $c_k^* = c_k / c_{\text{ref}}$ , where  $c_{\text{ref}}$  denotes an appropriate reference concentration value. For simplicity, a homogeneous and isotropic medium is assumed. The characteristic constant

$$r_D = \sqrt{\frac{RT \epsilon_r \epsilon_0}{2F^2 c_{\text{ref}}}} \quad (2.20)$$

is commonly referred to as Debye length (Dickinson et al. [48]). It serves as an indicator for the distance over which a local charge separation is screened in an electrolyte solution. Typical values for the Debye length are in the order of one nanometer. An explicit consideration of the effects on the nanoscale is usually infeasible for macroscopic models, since the requirements for a proper spatial resolution are linked with prohibitive computational costs. Since the relevant length scales considered in this study are ranging from micrometers up to meters,  $r_D$  vanishes on all significant length scales. An alternative approach to close the system of ion-transport equations is described below and corresponds to the approximation  $r_D \approx 0$ .

### 2.3.2 Electroneutrality condition

For macroscopic models such as considered here, the system of equations is usually closed with the so-called electroneutrality condition instead of using (2.18). This condition is an algebraic constraint originating from the assumption that the electrolyte solution is locally electrically neutral:

$$\rho_e = F \sum_{k=1}^m z_k c_k = 0 \quad \text{in } \bar{\Omega} \times [0, T_e]. \quad (2.21)$$

As pointed out by Newman and Thomas-Alyea [137], the condition of electroneutrality is not a fundamental law of nature, but represents an “accurate approximation”, which is generally accepted for a macroscopic description of electrochemical systems. Regions with considerable charge separation are solely the electric double layers in the vicinity of electrode-solution interfaces. Since these regions have typical thicknesses of 1 – 10 nm (cf. section 1.2), a consideration using (2.18) is infeasible, as explained above. Consequently, the electrode-solution interface is not explicitly considered as done in the PNP model, but the corresponding effects of the electric double layer region are accounted for in appropriate phenomenological boundary conditions, which will be introduced below in the sections 2.5.2 and 2.5.3.

A recent review on the use of the electroneutrality approximation in electrochemistry

is provided by Dickinson et al. [48]. Therein, the authors state that notable differences in simulation results are only observed when physical effects on spatial length scales of nanometers and/or time scales of nanoseconds are studied. However, nanoscale effects are not in the focus of the present modeling approach. Feldberg [63] demonstrated that solving ion-transport problems coupled to the electroneutrality constraint is equivalent to invoking the corresponding limit of the exact PNP model when certain charge-density-related terms become negligibly small. A division of (2.21) by  $F$  transforms the electroneutrality condition into the form

$$\sum_{k=1}^m z_k c_k = 0, \quad (2.22)$$

which is usually used as closing equation.

As a general consequence, always at least two ionic species with opposite charges are required for modeling electrochemical systems. The special case  $m = 2$  corresponds to the dissociation of a single salt into its ion pair and is usually referred to as binary electrolyte. For binary electrolyte solutions, the electroneutrality condition enables further analytical analysis of the coupled ion transport problem, as described in Appendix A. In general, the electroneutrality condition (2.22) facilitates analytical considerations of electrochemical problem formulations due to its nature as a simple algebraic constraint. A further advantage is that no additional material or other physical parameters are required for imposing electroneutrality. In the following, the coupled system of electroneutrality condition (2.22) and ion-transport equations (2.12) is referred to as Electroneutrality-Nernst-Planck (ENP) model.

### 2.3.3 Further constraints derived from electroneutrality

Although the electric potential does not appear in an explicit way in (2.22), the electroneutrality condition represents the governing equation for  $\Phi$ . This becomes more evident when transforming the electroneutrality condition as described in the following. First, a partial derivative with respect to time is applied to the algebraic constraint equation (2.21). The ion-transport equations (2.12) are then utilized to replace the time derivatives of each ionic species concentration. Owing to electroneutrality, the convective terms cancel out. After inserting (2.16), the partial differential equation

$$-\nabla \cdot \left[ \left( \sum_{k=1}^m z_k^2 F^2 \mu_k c_k \right) \nabla \Phi \right] - F \nabla \cdot \left[ \sum_{k=1}^m z_k D_k \nabla c_k \right] = 0 \quad (2.23)$$

is obtained as a result. In the context of differential-algebraic equations (DAEs) so-called hidden constraints are revealed from the original algebraic constraint by differentiating it with respect to time (see, e.g., Hairer and Wanner [90]). Thus, equation (2.23) represents the hidden constraint of the present problem formulation, which is derived from the algebraic electroneutrality constraint.

Alternatively, formula (2.23) can be obtained by multiplication of each transport equation with  $z_k F$  and summing them over all  $k$ . Owing to the electroneutrality condition, temporal derivatives and convective terms cancel out and (2.23) remains as a result. This second method to derive (2.23) is merely based on forming a linear combination of all ion-transport equations. An inherent problem arises when a steady-state situation is reached,

where all time derivatives become negligible small. Then, the equation system closed with (2.23) becomes linearly dependent. In that case, singular system matrices are obtained within numerical solution approaches. As a consequence, it is refrained from using (2.23) as an alternative to the electroneutrality condition (2.22).

However, it is possible to eliminate one ionic concentration from the system of equations based on the electroneutrality condition. Without loss of generality concentration  $c_m$  is eliminated from (2.23) using

$$c_m = -\frac{1}{z_m} \sum_{k=1}^{m-1} z_k c_k, \quad (2.24)$$

and assuming  $z_m \neq 0$ . The resulting equation reads

$$-\nabla \cdot \left[ \left( \sum_{k=1}^{m-1} z_k F^2 (z_k \mu_k - z_m \mu_m) c_k \right) \nabla \Phi \right] - F \nabla \cdot \left[ \sum_{k=1}^{m-1} z_k (D_k - D_m) \nabla c_k \right] = 0. \quad (2.25)$$

In addition, the ion-transport equation for species  $m$  can be dropped from the system of equations, because  $c_m$  is now simply determined by the algebraic relation (2.24). However, the effect of ionic species  $m$  still enters the problem formulation, since the material properties  $z_m$ ,  $\mu_m$  and  $D_m$  are still present in (2.25). This reformulation of (2.23) is usually sufficient for solving the problem of linear dependency explained above. Thus, equation (2.25) represents a further alternative to define a closing equation for the multi-ion transport problem. Furthermore, the system of partial differential equations was reduced by one due to the elimination of  $c_m$ . In the following, the coupled system of (2.25) and the Nernst-Planck equations (2.12) is referred to as Charge-conservation-Nernst-Planck (CNP) model. The reason for this nomenclature becomes more evident in the subsequent section.

It is important to note that the concentration-dependent factor in front of the gradient of the electric potential in (2.23) and (2.25) can be interpreted as a specific ionic conductivity of the electrolyte solution given as

$$\sigma = \sum_{k=1}^m z_k^2 F^2 \mu_k c_k = \sum_{k=1}^{m-1} z_k F^2 (z_k \mu_k - z_m \mu_m) c_k. \quad (2.26)$$

As obvious from (2.26), local variations in the molar ion concentrations  $c_k$ , that is, variations in the electrolyte composition, will cause local variations in the ionic conductivity  $\sigma$ . In general, conductivity values are specified in the unit S/m.

As a summary, only two options for the governing equation of the electric potential field appear to be appropriate in the present context of macroscopic modeling. Thus, in the following, only (2.22) and (2.25) are considered as possible closing equations, yielding the ENP and CNP systems of equations. The main focus of this work is on the ENP problem formulation, but remarks concerning the CNP model will be given at several appropriate places.

## 2.4 Charge conservation

A fundamental physical principle is charge conservation. Any modeling approach for electrochemical systems has to fulfill this elementary physical concept. The corresponding

conservation law given as

$$\frac{\partial \rho_e}{\partial t} + \nabla \cdot \mathbf{i} = 0 \quad \text{in } \Omega \times (0, T_e) \quad (2.27)$$

is a direct consequence of the four Maxwell equations of electrodynamics (see, e.g., Jackson [108]). In (2.27),  $\rho_e$  denotes the local net charge density in the medium and  $\mathbf{i}$  is the local current density. For electrolyte solutions,  $\rho_e$  is governed by the local ion concentrations via relation (2.15), as stated above. The current density depends on the ionic mass flux densities via

$$\mathbf{i} = F \sum_{k=1}^m z_k \mathbf{N}_k, \quad (2.28)$$

since ions are both mass and charge carriers. The unit of the current density expressed in SI base units is A/m<sup>2</sup>, but in the context of electrochemistry the choice mA/cm<sup>2</sup> is more common. Note that equation (2.28) matches the convention for the direction of (conventional) current defined arbitrarily to be the direction of the flow of positive charges. The total electric current  $I$  through a given surface  $A$  can be calculated by integrating the normal component of  $\mathbf{i}$  according to

$$I = \int_A \mathbf{i} \cdot \mathbf{n} \, dS. \quad (2.29)$$

In the following, a simple proof is given that (2.27) holds for the ion-transport model introduced in section 2.2. After multiplying each ion-transport equation (2.10) for species  $k$  with the corresponding valence  $z_k$  and the Faraday constant  $F$ , the equations are summed up. Introducing the relationships (2.15) and (2.28) into the arising terms immediately reveals that conservation law (2.27) is fulfilled. Thus, conservation of mass for each ionic species automatically implies conservation of charge. This is reflecting the fact that ions are carrying mass and charge at the same time and are the only charge carriers inside the electrolyte solution. It is important to point out that charge conservation is not affected by the actual choice for the governing equation for the electric potential field (cf. section 2.3).

For ion-transport models coupled to the electroneutrality condition (2.22), i.e., the ENP system of equations in the present case, it holds  $\rho_e \equiv 0$  in (2.27). In addition, convection does not contribute to the current density in (2.28) due to electroneutrality. Consequently, it holds

$$\mathbf{i} = F \sum_{k=1}^m z_k \mathbf{N}_k^{d+m} \quad (2.30)$$

in this case. Insertion of the definition (2.4) of the ionic flux due to diffusion and migration into (2.30) and subsequent rearrangement yields

$$-\sigma \nabla \Phi = \mathbf{i} + F \sum_{k=1}^m z_k D_k \nabla c_k. \quad (2.31)$$

As a result, the gradient of the electric potential field is governed by three different effects. First, the ionic conductivity  $\sigma$  defined in (2.26) is concentration-dependent and may thus exhibit local variations. Second, the passage of an electric current through the electrochem-

ical system will cause a corresponding ohmic voltage drop. Finally, arising concentration gradients may cause a so-called diffusion potential, which builds up in order to maintain electroneutrality.

In case of absent space charge, the current density  $\mathbf{i}$  is solenoidal, i.e., it holds

$$0 = \nabla \cdot \left( F \sum_k z_k N_k^{d+m} \right) = \nabla \cdot \mathbf{i}. \quad (2.32)$$

When inserting the definition for  $N_k^{d+m}$  (2.4) into (2.32), it becomes obvious that (2.32) is identical to the hidden constraint (2.23), which was derived from the electroneutrality condition, as presented above. Thus, the derived constraints (2.23) and (2.25) actually have a physical meaning, since they are simply enforcing charge conservation. This explains also the terminology Charge-conservation-Nernst-Planck (CNP), which was introduced in section 2.3.

The integral form of (2.32) reveals a further important implication when it is converted to a boundary integral using the divergence theorem:

$$0 = \int_{\Omega} \nabla \cdot \mathbf{i} \, d\mathbf{x} = \int_{\partial\Omega} \mathbf{i} \cdot \mathbf{n} \, dS \quad (2.33)$$

$$= \int_{\Gamma_{\text{insul}}} \underbrace{\mathbf{i} \cdot \mathbf{n}}_{=0} \, dS + \int_{\Gamma_{\text{in}}} \underbrace{\mathbf{i} \cdot \mathbf{n}}_{<0} \, dS + \int_{\Gamma_{\text{out}}} \underbrace{\mathbf{i} \cdot \mathbf{n}}_{>0} \, dS = I_{\text{in}} + I_{\text{out}}. \quad (2.34)$$

Here, a subdivision of the boundary into three disjoint parts reading  $\partial\Omega = \Gamma_{\text{insul}} \cup \Gamma_{\text{in}} \cup \Gamma_{\text{out}}$  is considered, which is based on the sign of the normal current density  $\mathbf{i} \cdot \mathbf{n}$ . No electric current is passing through the insulating boundary part denoted by  $\Gamma_{\text{insul}}$ . Since the electrolyte solution is assumed to be electrically neutral, the amount of electric current  $I_{\text{in}}$  directed into the domain  $\Omega$  is always in exact balance with the amount of electric current  $I_{\text{out}}$  flowing out of the considered electrochemical system. This property is mathematically expressed in (2.34). For an electrochemical cell, the boundary parts  $\Gamma_{\text{in}}$  and  $\Gamma_{\text{out}}$  typically coincide with the electrode surfaces, since there the electric current is passing through.

## 2.5 Initial and boundary conditions for coupled ion transport

Appropriate initial and boundary conditions are required for the coupled system of partial differential equations describing multi-ion transport and electric potential field. Suitable choices for such conditions are presented below, completing the formulation of the considered initial-boundary value problem.

### 2.5.1 Initial conditions

For the transient case, initial conditions for each ionic species  $k = 1, \dots, m$  of the form

$$c_k = c_k^0 \quad \text{in } \overline{\Omega} \times \{0\} \quad (2.35)$$

have to be specified, where  $c_k^0$  denotes the initial concentration field of ionic species  $k$ . For many applications, constant initial fields  $c_k^0$ , which obey the electroneutrality condition, are used to represent an electrolyte solution which is initially in equilibrium.

Based on the initial concentration fields prescribed in (2.35), a consistent representation of the corresponding electric potential field  $\Phi^0$  can be computed from (2.23). Thus, in general, the second-order partial differential equation (2.23) has to be solved for the consistent representation of  $\Phi^0$ . Of course, also (2.25) can be utilized as an alternative. More often, however, the cell voltage is initially zero and no concentration gradients are present in the beginning. In this case,  $\Phi^0$  is a simple constant function, which can be deduced directly without solving (2.23) or (2.25).

## 2.5.2 Boundary conditions

To specify boundary conditions for each ionic species  $k$ , a partition of the boundary given as  $\partial\Omega = \Gamma_{D,k} \cup \Gamma_{N,k} \cup \Gamma_{E,k}$  is considered. The three boundary regions are assumed to be pairwise disjoint. It is important to note that the partitions do not have to be the same for each species  $k = 1, \dots, m$ .

On  $\Gamma_{D,k}$ , essential (or Dirichlet) boundary conditions reading

$$c_k = g_k \quad \text{on } \Gamma_{D,k} \times (0, T_e) \quad (2.36)$$

are applied. A typical example for (2.36) is an inflow boundary, where the composition of the electrolyte solution entering the domain due to convection is known. For that case, the prescribed values  $g_k$  fulfill the electroneutrality condition in order to represent an electrolyte solution in equilibrium. It is emphasized that initial condition (2.35) and boundary condition (2.36) have to be consistent for the initial time  $t = 0$ .

On the Neumann boundary part  $\Gamma_{N,k}$ , the negative normal flux caused by migration and diffusion is prescribed:

$$-N_k^{d+m} \cdot \mathbf{n} = h_k \quad \text{on } \Gamma_{N,k} \times (0, T_e). \quad (2.37)$$

As introduced above,  $\mathbf{n}$  denotes the unit outer normal vector on the respective boundary part. The prescribed flux distribution for the ionic species  $k$  is denoted by  $h_k$ . At insulating boundaries for example, all ionic species  $k = 1, \dots, m$  have zero mass flux. Thus, it holds  $h_k = 0$  at such boundary parts. For the modeling of outflow boundaries, where the electrolyte solution is leaving the considered domain  $\Omega$ , homogeneous Neumann conditions are usually applied, too.

Finally, electrode surfaces are represented by the boundary part  $\Gamma_{E,k}$ , which can be further subdivided into any number of anodic and cathodic parts. On  $\Gamma_{E,k}$ , electrochemical reaction models for reactive ionic species are included into the mathematical problem formulation. At electrode surfaces, the normal component of the current density introduced in (2.28) is of special interest, since it corresponds to the rate of electrochemical reaction. The entire normal current density  $i_n$  is determined by

$$i_n = \sum_{r=1}^{n_{rea}} i_n^r, \quad (2.38)$$

where  $n_{\text{rea}}$  denotes the number of considered electrochemical reactions and  $i_n^r$  is the reaction current density caused by the reaction  $r = 1, \dots, n_{\text{rea}}$ . Each respective electrochemical reaction  $r$  can be expressed in the general form

$$\sum_{k=1}^m s_{r,k} M_k^{z_k} \rightleftharpoons n_r e^- , \quad (2.39)$$

where  $n_r$  denotes the number of transferred electrons  $e^-$ ,  $s_{r,k}$  is the stoichiometric coefficient of ionic species  $k$  in reaction  $r$  and  $M_k^{z_k}$  is the symbol for the chemical formula of species  $k$  with the valence  $z_k$ . In general, the boundary condition for electrode surfaces reads

$$-N_k^{\text{d+m}} \cdot \mathbf{n} = j_k := \sum_{r=1}^{n_{\text{rea}}} \zeta \frac{s_{r,k} i_n^r}{n_r F} . \quad (2.40)$$

The factor  $s_{r,k}/n_r F$  in (2.40) is used to determine the respective contributions to the ionic mass flux density of species  $k$  from the electric current density  $i_n^r$ . If an ionic species  $k$  does not take part in an electrochemical reaction  $r$ , the related stoichiometric coefficient is simply zero, i.e., it holds  $s_{r,k} = 0$ . The additional parameter  $\zeta = -1$  in (2.40) has been introduced in order to account for a different sign convention that is typically used for  $i_n$  and  $i_n^r$  in electrochemical literature.

Since in the present study the focus is on electroplating, the consideration of a single electrochemical reaction as given in (1.5) provides already a sufficient model for a large variety of electrodeposition applications. Thus, in the following, it holds  $n_{\text{rea}} = 1$  and the index  $r$  is dropped. According to the convention used in (2.39), such an electrochemical reaction can be written as

$$-M^{z_k} + M \rightleftharpoons z_k e^- , \quad (2.41)$$

where  $M$  denotes the chemical symbol for the considered metal and  $z_k > 0$  is the number of transferred electrons. The metal cation  $M^{z_k}$  in (2.41) represents the only reacting species in the multi-ion transport model, since the solid metal  $M$  is part of the electrode surface and thus not present in the electrolyte solution. All other ionic species are inert and have zero mass flux at the electrode boundaries. Thus, the general boundary condition (2.40) simplifies to

$$-N_k^{\text{d+m}} \cdot \mathbf{n} = j_k := \begin{cases} 0 & : \text{inert ionic species} \\ \frac{i_n}{z_k F} & : \text{reactive ionic species.} \end{cases} \quad (2.42)$$

Without loss of generality, the reacting species is usually considered the first one ( $k = 1$ ) in the numerical examples presented below. For electroplating applications,  $i_n$  is directly proportional to the deposition rate at the cathode and the rate of dissolution at the anode, respectively.

However, it has to be emphasized that the consideration of multiple electrode reactions represents an important future extension of the computational framework presented in this work. First promising results towards this aim are presented in the work by Wittmann [179].

### 2.5.3 Electrode kinetics

The normal current density  $i_n$  at an associated boundary part is determined by some (often nonlinear) kinetic model that in general depends on the solution variables:

$$i_n = f(\eta_s, c_1, \dots, c_m). \quad (2.43)$$

The so-called surface overpotential defined as  $\eta_s = V_E - \Phi$  is the driving force for electrochemical reactions. Here, the potential applied on the metal side of the electrode is denoted by  $V_E$  and the electric potential on the solution side of the electric double layer is  $\Phi$ . It is assumed that each electrode surface represents an equipotential surface on the metal side of the corresponding metal-solution interface. The surface overpotential models the strong variation of the electric potential field within the electric double layer region as a “jump” in the potential field at the electrode-electrolyte interface. In general, the surface overpotential varies in time as well as in space, i.e., along the electrode surface, depending on the local reaction rate. For a historic overview of the fundamental steps in the development of models describing electrode kinetics, the reader is referred to the recent review article by Inzelt [107].

An important example for (2.43) is the Butler-Volmer law in the form specified in Newman and Thomas-Alyea [137]:

$$i_n(\eta_s, c_k) = i_0 \left( \frac{c_k}{c_k^\infty} \right)^\beta \left[ \exp\left( \frac{\alpha_a F}{RT} \eta_s \right) - \exp\left( \frac{-\alpha_c F}{RT} \eta_s \right) \right]. \quad (2.44)$$

The additional parameters involved are the exchange current density  $i_0$  (cf. section 1), some reference concentration for the reactive ionic species  $c_k^\infty$ , an exponent  $\beta$  for weighting the concentration dependency, an anodic constant  $\alpha_a$  and a cathodic constant  $\alpha_c$ . Further formulations of the Butler-Volmer law are given in Bard and Faulkner [7], for example.

Two limiting cases of the Butler-Volmer law are worth mentioning. On the one hand, for the case of very small surface overpotentials, the expression (2.44) can be linearized around the equilibrium point  $\eta_s = 0 \text{ V}$  using standard Taylor series expansion of the exponential function. The concentration-dependent factor can be assumed to be one, since concentration gradients are negligible for low current densities. As a result, a linear kinetic law reading

$$i_n = i_0 (\alpha_a + \alpha_c) \eta_s \quad (2.45)$$

is obtained, which holds for very small values of the surface overpotential  $\eta_s$ .

On the other hand, for sufficiently large absolute values of the surface overpotential  $\eta_s$ , either the anodic or the cathodic part in (2.44) is dominating. Solely consideration of the dominant term results in the famous Tafel law for describing electrode kinetics (see, e.g., Newman and Thomas-Alyea [137]). For a cathodic reaction, the relationship

$$i_n = -i_0 \left( \frac{c_k}{c_k^\infty} \right)^\beta \exp\left( \frac{-\alpha_c F}{RT} \eta_s \right) \quad (2.46)$$

is obtained from (2.44). For the classical Tafel law, the concentration-dependent term in (2.46) has to be omitted. Alternatively, the simple parameter choice  $\beta = 0$  can be used to obtain the identical effect.

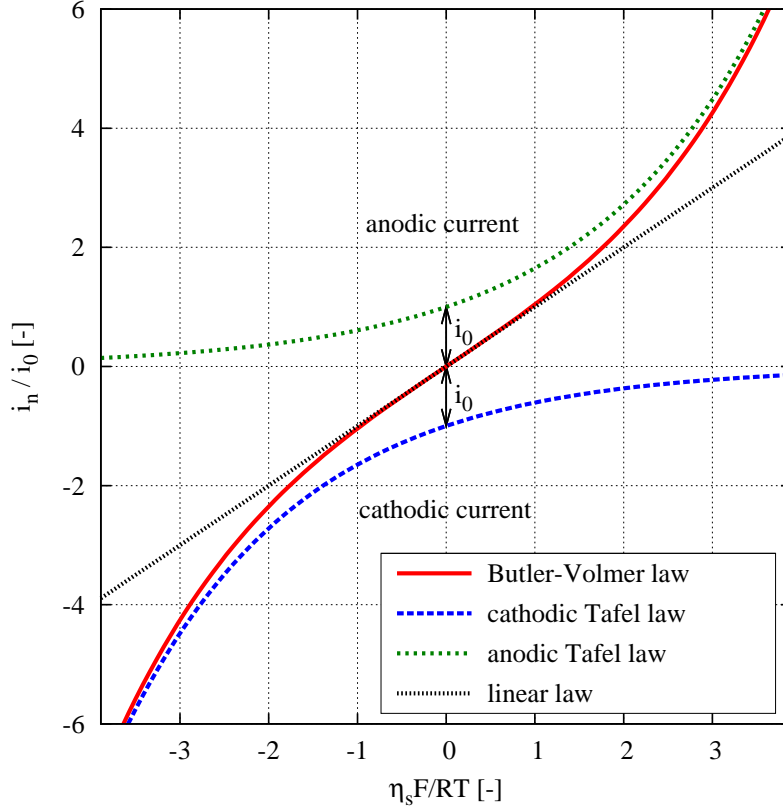


Figure 2.1: Characteristic profiles for different electrode kinetics laws (symmetric case with parameters  $\beta = 0.0$ ,  $\alpha_a = 0.5$ ,  $\alpha_c = 0.5$ ).

For further illustration, typical profiles for the different electrode kinetics laws introduced above are depicted in Fig. 2.1. The asymptotic behavior of both the linear and the Tafel law with respect to the Butler-Volmer curve are clearly visible. In general, the required parameters of the phenomenological electrode kinetics laws have to be determined from experiments. Each problem setup necessitates an individual characterization, including electrode material, composition of electrolyte solution, temperature and considered electrochemical reaction. It is emphasized that the mathematical model and the computational approach developed below is not restricted to any specific electrode kinetics law. In principal, any general function (2.43) which represents the experimentally observed dependencies can be used.

For most cases, one cathode and one anode surface is considered. This results in a partition given as  $\Gamma_{E,k} = \Gamma_c \cup \Gamma_a$ , with  $\Gamma_c \cap \Gamma_a = \emptyset$ . The electric potential  $V_E$  on the metal side of the cathode is denoted by  $V_c$  and the corresponding anode potential is termed  $V_a$ , respectively. When the two electrode potentials  $V_a$  and  $V_c$  are prescribed, either set as constant parameters or following a specified time-dependent curve, a voltage-controlled operation mode of an electrolytic cell is modeled. The overall cell voltage is given by the difference  $U(t) = V_a(t) - V_c(t)$ . When a certain cell voltage  $U$  is prescribed, the considered electrolytic system is also said to be under potentiostatic control. In numerical simulations, usually a reference value for the electric potential is defined by setting  $V_a = 0\text{ V}$ . A typical profile of the electric potential field for a one-dimensional problem setting is depicted in

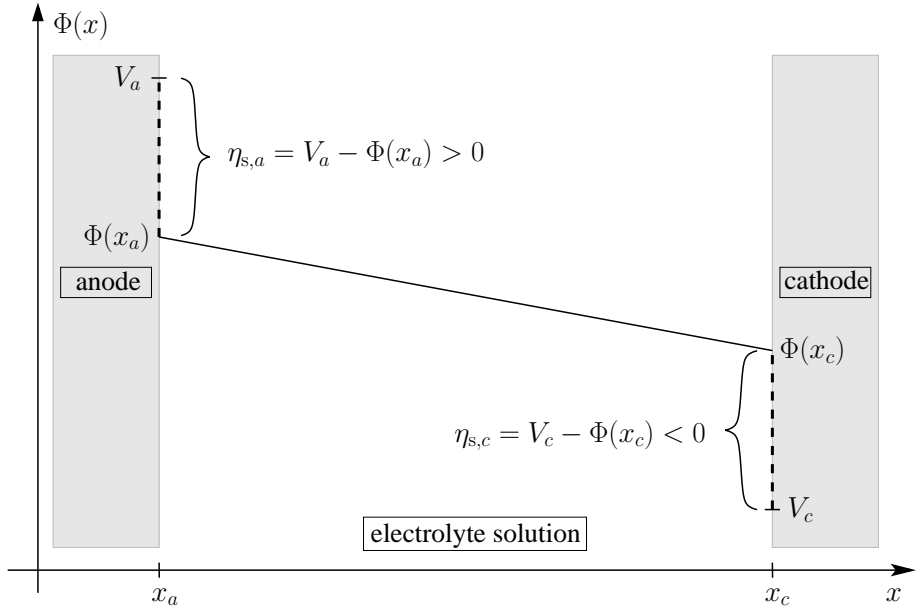


Figure 2.2: Typical profile of the electric potential field.

Fig. 2.2. Using the nomenclature introduced in Fig. 2.2, the cell voltage  $U$  can be further split up into several characteristic contributions reading

$$\begin{aligned} U &= V_a - V_c \\ &= (V_a - \Phi(x_a)) + (\Phi(x_a) - \Phi(x_c)) - (V_c - \Phi(x_c)) \\ &= \eta_{s,a} + (\eta_{c,a} + \Delta\Phi_{\text{ohm}} + E_0 - \eta_{c,c}) - \eta_{s,c}. \end{aligned} \quad (2.47)$$

In (2.47), the explicit dependency on the time has been dropped for the sake of a shorter notation. All relevant dissipative effects in an electrochemical cell are given in (2.47). As introduced above, surface overpotentials at anode and cathode are denoted by  $\eta_{s,a}$  and  $\eta_{s,c}$ , respectively. As shown in Fig. 2.2, the anodic surface overpotential  $\eta_{s,a}$  has a positive value, while the cathodic surface overpotential  $\eta_{s,c}$  is negative. The dissipative losses inside the electrolyte solution are due to concentration overpotentials  $\eta_{c,a}$ ,  $\eta_{c,c}$  in the vicinity of each electrode, ohmic losses denoted by  $\Delta\Phi_{\text{ohm}}$  and the open-circuit potential termed  $E_0$ . For further explanations of the different contributions as well as the modeling of electrode reactions in general, the reader is referred to, e.g., Newman and Thomas-Alyea [137]. Note that in Fig. 2.2 only the surface overpotentials and the ohmic drop are depicted. For simplicity, possible concentration overpotentials are omitted.

An exemplary potential-current curve (polarization curve) is provided in Fig. 2.3. Therein, the different contributions to the cell potential  $U$  are shown. The anodic contributions are negligible small for the investigated electrochemical system considered in Fig. 2.3 and are therefore not shown. The horizontal current plateau denoted by (I), which is observed for a high applied cell voltage difference, indicates the region of the so-called limiting current. For this case, the reaction rate at the electrode is fully controlled by ionic mass transfer. In particular, the surface concentration of the reacting ion drops down to zero at the cathode and the ionic flux towards the electrode is limited by diffusion. For a further increase of the applied cell voltage  $U$ , additional electrode reactions are triggered and a

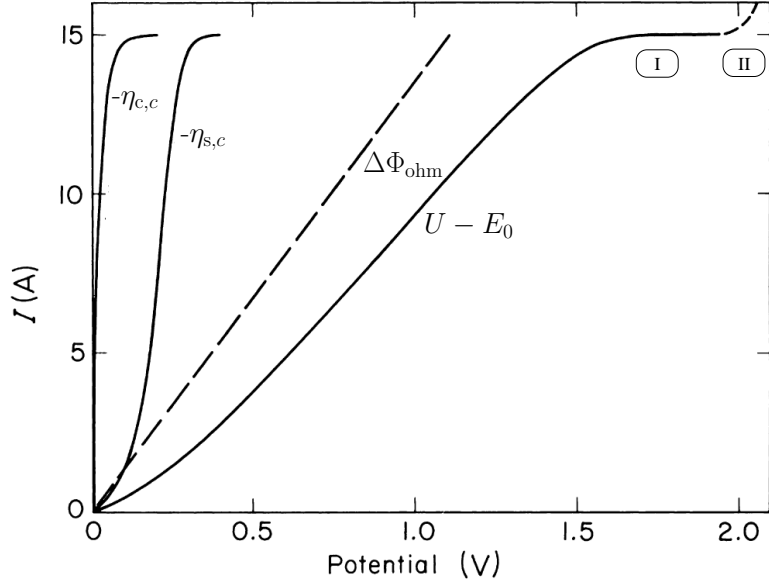


Figure 2.3: Exemplary potential-current curve and corresponding overpotential contributions (adapted from Newman and Thomas-Alyea [137]).

further increase of the electric current beyond the limiting current is observed (see region II in Fig. 2.3). It is emphasized that the concentration-dependent terms in (2.44) and (2.46) are required to model the limiting current.

#### 2.5.4 Current-controlled problems

For current-controlled problems, the total current  $I_{\text{tot}}(t)$  passing an electrolytic cell is prescribed. In experiments, an external control device is used to continually adjust the applied cell voltage to the prescribed current curve. Examples for applications utilizing a time-varying total current  $I_{\text{tot}}(t)$  are pulse-plating and pulse-reverse-plating methods with prescribed time-dependent current curves (cf. section 1.3). For the classical galvanostatic mode of cell operation, the total current  $I_{\text{tot}}$  is a simple direct current, which is kept constant over time.

The continuous adjustment of the cell voltage also has to be realized numerically within the computational approach. At each time  $t \in [0, T_e]$ , the current  $I(t)$  passing an electrochemical system has to follow the prescribed current  $I_{\text{tot}}(t)$ , which requires a corresponding adaptation of the overall cell voltage  $U(t) = V_a(t) - V_c(t)$ . Thus, the following equations have to be satisfied both at the cathode and anode surface, respectively:

$$\mathcal{R}^c(V_c) := I_{\text{tot}} - I_c = I_{\text{tot}} - \int_{\Gamma_c} i_n^c dS = 0, \quad (2.48)$$

$$\mathcal{R}^a(V_a) := I_{\text{tot}} - I_a = I_{\text{tot}} - \int_{\Gamma_a} i_n^a dS = 0, \quad (2.49)$$

whereas it holds  $I = I_c = I_a$  due to charge conservation (see section 2.4). For the case

of only one reactive ionic species and a single electrochemical reaction process, the net faradaic current densities  $i_n^c, i_n^a$  normal to an electrode surface are given by a reaction model, such as the Butler-Volmer law (2.44). The values of the current densities  $i_n^c, i_n^a$  depend on all solution variables and are typically varying along the electrode surfaces  $\Gamma_c$  and  $\Gamma_a$ . Equations (2.48) and (2.49) are nonlinear and strongly coupled, since  $i_n^c, i_n^a$  (and, consequently, also  $I$ ) result from all governing equations for the electrochemical problem, including nonlinear bulk and boundary equations.

### 2.5.5 Faraday's law and electrode shape changes

According to Faraday's law (see, e.g., Bard et al. [8]), the amount of substance consumed or produced during an electrochemical reaction at an electrode is proportional to the electric charge which passed the corresponding electrode-solution interface. In case of an electrodeposition reaction (2.41), this fundamental dependency enables the computation of a local cathode surface growth rate  $\tilde{u}$  from the normal component of the local current density via

$$\tilde{u} = \lambda \frac{M_{me}}{\rho_{me}} \frac{1}{nF} \mathbf{i} \cdot \mathbf{n}. \quad (2.50)$$

Here,  $n$  represents the number of electrons transferred in the reaction,  $F$  is Faraday's constant,  $M_{me}$  denotes the molar mass of the deposited metal and  $\rho_{me}$  the corresponding density. The ratio of these two values is often termed molar volume  $\bar{V}_{me} = M_{me}/\rho_{me}$ , since the corresponding unit is  $\text{m}^3/\text{mol}$ . The additional parameter  $\lambda \in (0, 1]$  in (2.50) is an efficiency factor, which is used to reflect the non-ideal plating behavior observed in reality, where a minor percentage of the total current is consumed by other electrode reactions. The local deposit thickness  $\Delta h$  achieved during a time interval  $[t_0, t_1]$  can be computed by integrating (2.50) over the corresponding time interval. For a simple plating process on a flat surface and a known current density distribution which remains constant over time, a simple formula of the form

$$\Delta h = \lambda \bar{V}_{me} \frac{t_1 - t_0}{nF} \mathbf{i} \cdot \mathbf{n} \quad (2.51)$$

is obtained. As shown here, a detailed knowledge of the current-density distribution is important for a sophisticated prediction of plating results in electrodeposition. This inherent dependency becomes also evident in the following quote from Dukovic [54, p. 694]:

*„... the challenge of deposit uniformity can be posed as a problem of current-density distribution: How can one distribute the electrolytic current evenly over the surface of the cathode?“*

## 2.6 Simple potential model for electrochemical systems

When gradients of ionic concentrations are negligible small, the problem formulation presented above can be drastically simplified. This situation is often encountered when the electric current passing an electrolytic cell remains far below the limiting current. Then, mass transfer due to convection and diffusion are negligible effects, and migration is the

prevalent ion-transport phenomenon. Since in this case the composition of the electrolyte solution is assumed to remain uniform, no ion-transport equations have to be solved anymore. As a further consequence, there is also no need for solving the flow problem. The only remaining unknown physical quantity is the electric potential field. Equation (2.23) represents a suitable choice for deriving a governing equation for the electric potential  $\Phi$ . Neglecting all concentration gradients in (2.23) yields

$$-\nabla \cdot \left[ \underbrace{\left( \sum_{k=1}^m z_k^2 F^2 \mu_k c_k \right)}_{=\sigma} \nabla \Phi \right] = 0. \quad (2.52)$$

Since the bath composition remains uniform, the ionic conductivity  $\sigma$  as defined in (2.26) is a constant value. Thus, the electric potential  $\Phi$  is governed by the Laplace equation reading

$$-\nabla \cdot (\sigma \nabla \Phi) = 0. \quad (2.53)$$

Typically, a measured value is used in (2.53) for the conductivity of the electrolyte solution. The current density is simply computed from Ohm's law reading

$$\mathbf{i} = -\sigma \nabla \Phi. \quad (2.54)$$

In general, appropriate boundary conditions for the simplified potential model (2.53) are given as

$$\Phi = \Phi_D \quad \text{on } \Gamma_D^\Phi \times (0, T_e), \quad (2.55)$$

$$\sigma \nabla \Phi \cdot \mathbf{n} = h_\Phi \quad \text{on } \Gamma_N^\Phi \times (0, T_e), \quad (2.56)$$

$$\sigma \nabla \Phi \cdot \mathbf{n} = i_n(\Phi) \quad \text{on } \Gamma_E^\Phi \times (0, T_e). \quad (2.57)$$

On the Dirichlet boundary part  $\Gamma_D^\Phi$ , a value  $\Phi_D$  for the electric potential is prescribed, while  $h_\Phi$  is an applied value for the negative current density in normal direction at the Neumann boundary  $\Gamma_N^\Phi$ . Insulating surfaces belong to the latter type of boundaries since the condition  $\sigma \nabla \Phi \cdot \mathbf{n} = 0$  is usually used to model these. At the boundary  $\Gamma_E^\Phi$ , the current density is linked to some model for electrode kinetics (see section 2.5.3), which yields in general a nonlinear term  $i_n(\Phi)$ .

## 2.7 Incompressible flow

The incompressible Navier-Stokes equations provide an adequate model to describe the flow of a dilute electrolyte solution in an electrochemical cell at a macroscopic scale (see, e.g., Newman and Thomas-Alyea [137]). For dilute solutions, as considered here, concentrations of contained ionic species are very low compared to the solute. As a result, values for density and viscosity are typically similar to those of the pure solute, but may depend on the local bath composition. For electroplating applications, typically water is used as a solvent, which is governing the flow behavior of the whole electrolyte solution. For a detailed derivation of the Navier-Stokes equations in particular, and the field of fluid mechanics in general, the reader is referred to Spurk [161] and Kundu and Cohen [118],

for instance. Further detailed introductions to the modeling of incompressible flows are provided by Wall [174], Gravemeier [78] and Gamnitzer [69].

### 2.7.1 Governing equations

The viscous flow of a Newtonian fluid is mathematically described by the Navier-Stokes equations reading

$$\frac{\partial(\rho\mathbf{u})}{\partial t} + (\mathbf{u} \cdot \nabla)\rho\mathbf{u} - 2\mu\nabla \cdot \boldsymbol{\varepsilon}(\mathbf{u}) + \nabla p_{\text{dyn}} = \rho\tilde{\mathbf{b}} \quad \text{in } \Omega \times (0, T_e), \quad (2.58)$$

$$\frac{\partial\rho}{\partial t} + \nabla \cdot (\rho\mathbf{u}) = 0 \quad \text{in } \Omega \times (0, T_e). \quad (2.59)$$

Here, equation (2.58) is derived from the principle of conservation of linear momentum, while (2.59) is deduced from mass conservation. Usually, (2.58) is referred to as momentum equation and (2.59) is termed the continuity equation. The involved physical quantities are the velocity field  $\mathbf{u} : \overline{\Omega} \times [0, T_e] \rightarrow \mathbb{R}^d$ , the (dynamic) pressure  $p_{\text{dyn}} : \overline{\Omega} \times [0, T_e] \rightarrow \mathbb{R}$  and the density field  $\rho : \overline{\Omega} \times [0, T_e] \rightarrow \mathbb{R}^+$ . Furthermore,  $\mu$  denotes the dynamic viscosity of the Newtonian fluid,  $\boldsymbol{\varepsilon}(\mathbf{u})$  the symmetric strain rate tensor given by

$$\boldsymbol{\varepsilon}(\mathbf{u}) = \frac{1}{2}(\nabla\mathbf{u} + (\nabla\mathbf{u})^\top), \quad (2.60)$$

and  $\tilde{\mathbf{b}}$  the specific volume force.

As emphasized by Newman and Thomas-Alyea [137], a divergence-free velocity field is a valid approximation for dilute electrolytes, where only small density variations occur at the electrodes. Therefore, the so-called Boussinesq approximation (see, e.g., Kundu and Cohen [118]) is also valid for the electrolyte solutions considered here. Consequently, the influence of density variations is neglected in all terms of the momentum equation (2.58), except for the volume force term on the right-hand side. Thus, in all terms on the left-hand side of (2.58),  $\rho$  is replaced by the constant reference density of the bulk electrolyte solution denoted by  $\rho^\infty$ . As a second step, the momentum equation (2.58) is divided by  $\rho^\infty$ . Since the flow of an electrolyte solution is assumed to be incompressible, equation (2.59) reduces to the usual incompressibility constraint  $\nabla \cdot \mathbf{u} = 0$ .

As a result of all these considerations, one obtains the following set of partial differential equations:

$$\frac{\partial\mathbf{u}}{\partial t} + (\mathbf{u} \cdot \nabla)\mathbf{u} - 2\nu\nabla \cdot \boldsymbol{\varepsilon}(\mathbf{u}) + \nabla p = \mathbf{b} \quad \text{in } \Omega \times (0, T_e), \quad (2.61)$$

$$\nabla \cdot \mathbf{u} = 0 \quad \text{in } \Omega \times (0, T_e). \quad (2.62)$$

Here, the kinematic pressure  $p = p_{\text{dyn}}/\rho^\infty$  and the kinematic viscosity  $\nu = \mu/\rho^\infty$  were introduced in (2.61). In addition, the right-hand side of (2.61) reads

$$\mathbf{b} = \frac{\rho}{\rho^\infty} \tilde{\mathbf{b}}. \quad (2.63)$$

### 2.7.2 Constitutive models for the density of electrolyte solutions

It is emphasized that for the coupled multi-ion transport problem the density field  $\rho$  does not appear as a solution variable since it can be directly expressed in terms of ionic concentrations via a constitutive law

$$\rho = f(c_1, \dots, c_m). \quad (2.64)$$

Usually, a linear relationship of the form

$$\rho = \rho^\infty \left( 1 + \sum_{k=1}^m \alpha_k (c_k - c_k^\infty) \right) \quad (2.65)$$

provides already a sufficient model. Here,  $\alpha_k$  denotes the so-called densification factor and  $c_k^\infty$  the bulk concentration value of ionic species  $k$ . A common choice for the densification coefficients is given by  $\alpha_k = M_k / \rho^\infty$ , where  $M_k$  denotes the molar mass of ionic species  $k$ .

When ionic species  $m$  is eliminated from the problem formulation by means of electroneutrality as described in section 2.3.3, the formula for the density (2.65) changes to

$$\rho = \rho^\infty \left( 1 + \sum_{k=1}^{m-1} \left( \alpha_k - z_k \frac{\alpha_m}{z_m} \right) (c_k - c_k^\infty) \right). \quad (2.66)$$

It is emphasized that (2.65) and (2.66) yield identical values for the density, since the effect of species  $m$  is still present in (2.66).

Besides the density, also the viscosity of an electrolyte solution depends in general on the local bath composition. In this work, such a dependency is not considered. Buoyancy forces due to density variations are usually estimated to be much more important for a successful modeling of the flow than a concentration-dependent viscosity. Thus, the viscosity is assumed to be a constant throughout this work. Nevertheless, the computational approach presented below can be extended accordingly to account for a concentration-dependent viscosity as well. Numerical simulations considering a concentration-dependent viscosity of an electrolyte solution were presented by Mangiavacchi et al. [133], Barcia et al. [6] and Pontes et al. [143], for instance.

### 2.7.3 Buoyancy and other types of volume forces

When local variations in the ionic concentrations occur, corresponding variations of the density arise according to (2.64). Consequently, buoyancy forces are present, which are causing so-called natural convection in an electrochemical cell. To account for such buoyancy effects, the specific volume force term is given as  $\bar{\mathbf{b}} = \mathbf{g}$ , where  $\mathbf{g}$  represents the gravitational acceleration. For numerical simulations it is usually convenient to remove the hydrostatic pressure contribution by including  $-\rho^\infty \mathbf{g}$  in the volume force term  $\mathbf{b}$ . Consequently, the right-hand-side in (2.61) reads

$$\mathbf{b} := \frac{\rho - \rho^\infty}{\rho^\infty} \mathbf{g}. \quad (2.67)$$

Thus, the pressure  $p$  in (2.61) does not contain the hydrostatic pressure part. If needed, the latter can always be computed in a postprocessing step. This approach is utilized throughout this work. As a result, a challenging two-way coupled problem has to be considered, since ion transport is influenced by convection and buoyancy effects depend on the local ionic concentrations.

However, for many electrochemical configurations natural convection phenomena can be considered as negligible small. For such situations,  $\rho = \rho^\infty$  can be assumed. Since (2.67) is zero in this case, the dependency of the flow solution on the local ionic concentrations vanishes completely. Consequently, the consideration of a one-way coupling of ionic transport to the flow field via convection is sufficient.

In general, besides the gravitational force, other types of forces may contribute to the volume force term in the momentum equation. An overview of further physical effects which can be important in the context of electrochemistry is provided by Hinds et al. [97]. Therein, also rough estimates for the relative importance of each force term are given. One contribution in the context of electrochemical systems is the effect of the electric field on the electrolyte solution (see, e.g., Rubinstein [152]). However, the arising force is negligible small for the considered length scales of the present macroscopic model, as shown in the textbook by Newman and Thomas-Alyea [137]. When an electrochemical system is superposed by a strong external magnetic field, physical effects such as the Lorentz force (see Hinds et al. [97]) have to be accounted for in the mathematical model. For the applications considered in this work no magnetic fields are imposed. Thus, magnetic effects are not considered in the proposed model for the moment.

### 2.7.4 Initial and boundary conditions

Based on the partition  $\partial\Omega = \Gamma_D^u \cup \Gamma_N^u$  with  $\Gamma_D^u \cap \Gamma_N^u = \emptyset$ , appropriate boundary conditions for the flow problem are given as:

$$\mathbf{u} = \mathbf{u}_D \quad \text{on } \Gamma_D^u \times (0, T_e), \quad (2.68)$$

$$(-p\mathbf{I} + 2\nu\boldsymbol{\varepsilon}(\mathbf{u})) \cdot \mathbf{n} = \mathbf{t} \quad \text{on } \Gamma_N^u \times (0, T_e). \quad (2.69)$$

Here,  $\mathbf{u}_D$  is the velocity prescribed at the Dirichlet boundary part  $\Gamma_D^u$ ,  $\mathbf{n}$  the unit outer normal to the boundary and  $\mathbf{t}$  the prescribed boundary traction at the Neumann boundary part  $\Gamma_N^u$ . At walls, typically a so-called no-slip condition with  $\mathbf{u}_D = 0$  is applied. In case of free-slip conditions, the fluid may not penetrate the boundary (i.e.,  $\mathbf{u}_D \cdot \mathbf{n} = 0$ ), but can move in tangential direction along the boundary. Outflows are typically regarded as a part of  $\Gamma_N^u$ , demanding a zero traction vector  $\mathbf{t} = \mathbf{0}$ . A general overview and discussion of possible boundary conditions for the incompressible Navier-Stokes equations can be found in Gresho and Sani [85].

Finally, an initial condition in the form

$$\mathbf{u} = \mathbf{u}^0 \quad \text{in } \overline{\Omega} \times \{0\} \quad (2.70)$$

is required for time-dependent flow problems, with  $\mathbf{u}^0$  being a solenoidal initial velocity field. Often, an electrolyte solution is considered, which is initially at rest. In this case,  $\mathbf{u}^0 = \mathbf{0}$  is used in (2.70).

## 2.8 Further definitions and remarks

This section provides some further definitions of important electrochemical terms and concepts, which will be required within the subsequent parts of this work. In addition, the current chapter on the mathematical model is completed by giving some additional remarks.

### 2.8.1 Analytical results

The coupled system of multi-ion transport equations (Nernst-Planck equations) subject to the electroneutrality constraint was also investigated theoretically in the past. In the following, some exemplary references regarding this ambitious task are given. The provided collection of publications is certainly not complete, but provides at least an overview of available theoretical results. From a mathematical point of view, questions regarding the existence and uniqueness of solutions have to be answered.

The uniqueness of steady-state solutions for an electrochemistry model with multiple species was proved by Choi and Lui [35] considering one spatial dimension. In a subsequent publication, Choi and Lui [36] investigated the global stability of solutions for this problem formulation. In Choi and Lui [37], it was shown that the results presented in Choi and Lui [35, 36] hold also for the two- and three-dimensional case. The global existence of solutions of a strongly coupled quasilinear parabolic system with applications to electrochemistry was addressed by Choi et al. [34].

Besides these more fundamental investigations, analytical solution formulae can be derived for simple problem setups in rather basic geometries. Such exact solutions are important in the context of numerical methods, since they enable code verification and numerical convergence studies based on error calculations.

Exact solutions for one-dimensional ion transport in a binary electrolyte subject to electroneutrality were presented by Choi and Chan [33]. The analytical solution of the problem considered in that work was the basis for a more general extension to two spatial dimensions performed by Kwok and Wu [119]. Using similar methods, the logical extension to three space dimensions was provided recently by Bauer et al. [11]. A steady-state solution for electroplating was derived by Choi and Yu [38] considering a one-dimensional binary system with Butler-Volmer boundary conditions. Sokirko and Bark [160] derived an exact solution for ionic transport governed by diffusion and migration coupled to Butler-Volmer kinetics. They considered electrolyte solutions containing two and three ionic species in one-dimensional domains. Steady-state solutions for an electrochemistry model with non-linear diffusion were derived by Fang and Ito [61]. A stationary analytical solution for one-dimensional ion transport governed by diffusion and migration was presented by Bortels et al. [21]. In a subsequent publication, Bortels et al. [22] used this result to identify the parameters of a Butler-Volmer law. Molina et al. [135] presented an analytical solution for reverse pulse voltammetry at spherical electrodes. Exact solutions for ion transport in binary electrolyte solutions were also provided by Bauer et al. [11, 12], which were utilized for the validation of developed computational approaches.

Recently, a theoretical investigation for a strong binary electrolyte governed by the Poisson-Nernst-Planck (PNP) system of equations was performed by Ghosal and Chen [77]. Qualitative properties of steady-state PNP systems were investigated by Park and Jerome [139]. An analytical solution for a PNP system of equations coupled to Stokes

flow in cylindrical channels was presented by Berg and Findlay [18].

The three-dimensional incompressible Navier-Stokes equations are already stating a challenging mathematical problem themselves. It is still not known whether they possess unique smooth (continuously differentiable) solutions at high Reynolds numbers. The interested reader is referred to Doering [49] for a recent review on the related mathematical theory and the encountered difficulties.

## 2.8.2 Model parameters

The proposed mathematical model contains several parameters, which need to be determined before any numerical simulation can be performed. In general, the properties of a considered electrolyte solution need to be characterized in a laboratory by experimental techniques. The parameters of the different electrode kinetics laws addressed in section 2.5.3 are typically determined by fitting an appropriate law to measured polarization curves. Consequently, a combined experimental and numerical approach is necessary for a sophisticated investigation of a given electrochemical problem setup. For certain common electrolyte solutions data collections are available in literature, providing the required parameter values. For example, data for typical copper electrolytes are provided by Subbaiah and Das [162] and Price and Davenport [144], for example. Therein, values for density, viscosity and electrical conductivity are specified for varying temperatures and different electrolyte compositions. The effect of bath composition and temperature on copper diffusion coefficients was investigated by Moats et al. [134]. Nickel electrolytes have been investigated by Imamura and Toguri [104], for instance. In general, the experimental determination of parameters such as the required diffusion constants of ionic species is a difficult task. Uncertainties in the model parameters may also affect the prediction capabilities of numerical simulations. This is an important fact one should always be aware of.

## 2.8.3 A note on the choice of units

It is important to point out that the choice of units for all involved model variables is not completely free. A fundamental dependency is revealed when the Volt unit is expressed in terms of SI base units, reading

$$1 \text{ V} = 1 \frac{\text{kg m}^2}{\text{As}^3}. \quad (2.71)$$

In practice, usually appropriate units for time, spatial length, current and electric potential are chosen. Thus, the unit for mass is fixed due to (2.71). One has to be aware of this fact when specifying a value for the electrolyte density. In case of natural convection caused by local density variations, a correct specification of the corresponding constitutive law such as (2.65) is even more important in order to obtain correct simulation results.

## 2.8.4 Categorization of current density distributions

A very important terminology often encountered in electrochemical literature is the following classification of current density distributions. To be more precise, the local distribution

of normal current density at electrode surfaces is of special interest, since it is directly related to the rate of electrochemical reaction (see section 2.5). Depending on the importance of certain interfacial phenomena, the following three categories are defined (see, e.g., Bard et al. [8]):

### Primary current density distribution

The so-called primary current density distribution is observed when the resistivity of the bulk electrolyte solution is the dominating effect. Interfacial phenomena such as surface overpotentials are of negligible importance as well as mass transfer by diffusion and convection. Thus, the most simple mathematical model is applicable in this case, where the Laplace equation (2.53) is solved for the electric potential field. For the primary current density distribution, only boundary conditions of type (2.55) and (2.56) are considered. Typically, Dirichlet conditions (2.55) are used at the electrode surfaces, where  $\Phi = V_a$  is set at the anode and  $\Phi = V_c$  is prescribed at the cathode. As a consequence, only geometric effects determine the current density distribution at the electrode surfaces.

### Secondary current density distribution

The secondary current density distribution corresponds to the situation that interfacial phenomena lead to surface overpotentials which are of comparable order to the ohmic drop across the bulk volume of the electrolyte solution. As a consequence, the consideration of (nonlinear) electrode kinetics models as introduced in section 2.5 is required. Since still no concentration-dependent effects have to be considered, the Laplace equation (2.53) is the governing equation here as well. But in contrast to the primary current density distribution, it holds  $\Gamma_E^\Phi \neq \emptyset$ . Thus, all three types of boundary conditions (2.55)-(2.57) are considered. In general, the use of (2.57) requires the solution of a nonlinear problem.

### Tertiary current density distribution

Finally, a tertiary current density distribution is encountered when concentration overpotentials become important quantities as a result of significant variations in the ionic concentrations. For this case, mass transport phenomena such as convection, diffusion and migration are considerably influencing the behavior of a respective electrochemical system. Consequently, the full multi-ion transport model introduced in the previous sections has to be considered, including the inherent coupling to incompressible flow.

## 2.8.5 Dimensionless problem formulation

By introducing appropriate reference values (marked with an index  $(\cdot)_{\text{ref}}$ ) for the involved quantities, all presented governing equations can be reformulated in dimensionless quantities (marked with an asterisk). For an incompressible flow problem, dimensionless variables for length, time, velocity and pressure are introduced via

$$\mathbf{x}^* = \frac{\mathbf{x}}{L_{\text{ref}}}, \quad t^* = \frac{t}{t_{\text{ref}}}, \quad \mathbf{u}^* = \frac{\mathbf{u}}{u_{\text{ref}}}, \quad p^* = \frac{p}{p_{\text{ref}}}. \quad (2.72)$$

The specific choice  $t_{\text{ref}} = L_{\text{ref}}/u_{\text{ref}}$ ,  $p_{\text{ref}} = \rho^{\infty} u_{\text{ref}}^2$  yields the following dimensionless representation of the incompressible Navier-Stokes equations (2.61), (2.62):

$$\frac{\partial \mathbf{u}^*}{\partial t^*} + (\mathbf{u}^* \cdot \nabla^*) \mathbf{u}^* - \frac{2}{\text{Re}} \nabla^* \cdot \boldsymbol{\varepsilon}^*(\mathbf{u}^*) + \nabla^* p^* - \mathbf{b}^* = \mathbf{0} \quad \text{in } \Omega^* \times (0, T_e^*), \quad (2.73)$$

$$\nabla^* \cdot \mathbf{u}^* = 0 \quad \text{in } \Omega^* \times (0, T_e^*). \quad (2.74)$$

In (2.73), the dimensionless body force is defined as  $\mathbf{b}^* = (L_{\text{ref}}/u_{\text{ref}}^2) \mathbf{b}$ . Note that the differential operators  $\nabla^*(.)$  and  $\nabla^* \cdot (.)$  in (2.73), (2.74) are referring to the new spatial coordinate  $\mathbf{x}^*$ . The Reynolds number arising in (2.73) is defined as

$$\text{Re} = \frac{u_{\text{ref}} L_{\text{ref}}}{\nu}. \quad (2.75)$$

It is an important dimensionless quantity for characterizing the flow, representing a measure for the ratio of inertial to viscous forces.

Dimensionless quantities for each ionic concentration  $c_k$  and the electric potential  $\Phi$  are introduced by

$$c_k^* = \frac{c_k}{c_{\text{ref}}}, \quad \Phi^* = \frac{\Phi}{\Phi_{\text{ref}}}, \quad (2.76)$$

where  $c_{\text{ref}}$  denotes an appropriate reference concentration used for all ionic species  $k = 1, \dots, m$ . As a reference value for the electric potential, often  $\Phi_{\text{ref}} = RT/F$  is used. This represents a natural choice for a reference potential, because the factor  $F/RT$  (unit: 1/V) appears in all terms containing the electric potential, i.e., in the migration term of the ion-transport equation as well as in electrode kinetics boundary conditions.

Based on (2.72) and (2.76), a dimensionless form of the ion-transport equations (2.12) in combination with (2.5) and (2.16) is obtained as

$$\frac{\partial c_k^*}{\partial t^*} + \mathbf{u}^* \cdot \nabla^* c_k^* - \frac{1}{\text{Pe}_k} \nabla^* \cdot (\nabla^* c_k^* + z_k c_k^* \nabla^* \Phi^*) = 0 \quad \text{in } \Omega^* \times (0, T_e^*). \quad (2.77)$$

The corresponding dimensionless form of the electroneutrality condition (2.22) reads

$$\sum_{k=1}^m z_k c_k^* = 0, \quad (2.78)$$

while the alternative closing equation (2.25) is reformulated as

$$-\nabla^* \cdot \left[ \left( \sum_{k=1}^{m-1} z_k \left( \frac{z_k}{\text{Pe}_k} - \frac{z_m}{\text{Pe}_m} \right) c_k^* \right) \nabla^* \Phi^* \right] - \nabla^* \cdot \left[ \sum_{k=1}^{m-1} z_k \left( \frac{1}{\text{Pe}_k} - \frac{1}{\text{Pe}_m} \right) \nabla^* c_k^* \right] = 0. \quad (2.79)$$

In (2.77) and (2.79), the individual Peclet numbers for the ionic species  $k = 1, \dots, m$  are defined as

$$\text{Pe}_k = \frac{u_{\text{ref}} L_{\text{ref}}}{D_k} = \text{Sc}_k \cdot \text{Re}. \quad (2.80)$$

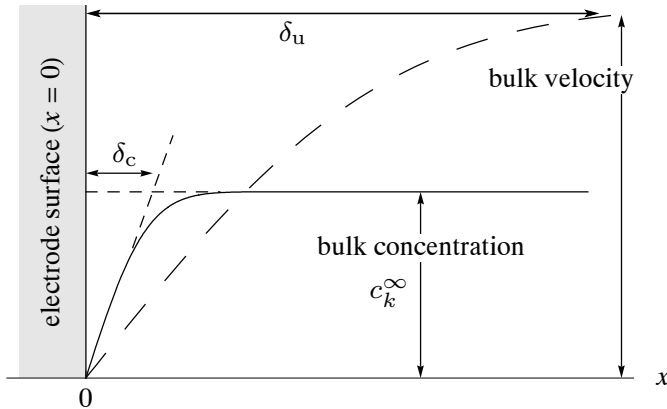


Figure 2.4: Typical boundary layer profiles for velocity and ionic concentrations at an electrode surface (adapted from Kontturi et al. [117]).

The dimensionless Schmidt number in (2.80) is computed as

$$\text{Sc}_k = \frac{\nu}{D_k}, \quad (2.81)$$

and relates the kinematic viscosity of the considered fluid to the diffusivity of ionic species  $k$ . For ionic mass transport, typical Schmidt numbers are in the order of 1000 or higher (see, e.g., Newman and Thomas-Alyea [137]). Consequently, the modeling of ionic transport in electrochemical systems yields a high-Schmidt-number problem. According to Incropera and DeWitt [106], for most applications a scaling law reading

$$\frac{\delta_u}{\delta_c} \approx \text{Sc}^{1/3} \quad (2.82)$$

is reasonable for the ratio of velocity boundary-layer thickness  $\delta_u$  and concentration boundary-layer thickness  $\delta_c$  of a reactive ionic species. This scaling law is also observed for mass transfer in turbulent channel flow (see, e.g., Calmet and Magnaudet [30]). As a consequence of (2.82) and the high Schmidt numbers which are typically encountered for ionic mass transport in electrolyte solutions, the boundary layer of the ionic species concentration is usually located completely within the boundary layer of the flow. This characteristic situation is also sketched in Fig. 2.4. Consequently, the consideration of ion-transport phenomena is very challenging from a numerical point of view, since the required spatial resolution for resolving concentration boundary layers in the vicinity of electrode surfaces leads to even higher computational costs than encountered for pure flow problems.

The Sherwood number represents a dimensionless quantification for the mass transfer rate at a surface. For specific problem setups, often correlations of the form

$$\text{Sh} = f(\text{Re}, \text{Sc}) \quad (2.83)$$

are specified in literature, where the mass transfer rate depends on the flow characterized by the Reynolds number and the electrolyte solution characterized by the Schmidt number.

One example for such an empirically determined relation is the Eisenberg correlation for rotating cylinder electrodes (see Eisenberg et al. [58] and the numerical example 4.4.3). Owing to the analogy between mass and heat transfer (see, e.g., Incropera and DeWitt [106]), the nomenclature used in the context of heat transfer problems is also often employed in literature devoted to electrochemistry. The Prandtl number is the analogon of the Schmidt number and the Nusselt number the analogous definition of the Sherwood number. A comprehensive overview of dimensionless parameters in the context of heat and mass transfer is provided by Incropera and DeWitt [106], for instance.

The fundamental structure of the dimensionless problem formulation is identical to the governing equations formulated in dimensional quantities. Thus, for convenience, the non-dimensional problem formulation is not considered in a separate way in the following chapters. The developed numerical methods can also be applied to the dimensionless formulation without any further modifications.



# 3 Computational approach

In this chapter, the developed computational approach is described. First, an overview of existing simulation approaches is provided in section 3.1. This literature survey demonstrates the novelty and significance of the computational method presented in the subsequent sections. In section 3.2, the time discretization of the governing equations is addressed. Afterwards, in section 3.3, the weak formulation of the semi-discrete equations is presented. This weak problem formulation represents the basis of the residual-based variational multiscale finite element formulation proposed in section 3.4. Finally, the solution procedure for the fully-discretized problem is explained in section 3.5.

## 3.1 Survey of existing simulation approaches

According to Britz [25], the article by Feldberg and Auerbach [64] published in 1969 can be seen as the pioneering work regarding numerical simulation in electrochemistry. Over the last decades, various numerical methods for the simulation of ion transport in electrolyte solutions have been developed. Some of these computational methods will be addressed in the following in order to provide an overview of existing simulation approaches. The focus is on the macroscopic modeling of ion transport in electrolytic systems in general, and electroplating applications in particular. Hence, computational approaches proposed for numerical simulation of galvanic cells, such as batteries and fuel cells, are not addressed in the following. Also numerical methods for simulating electrochemical phenomena at the micro- or even nanoscale are not in the scope of this work. Examples for such methods are Monte Carlo techniques for molecular dynamics simulations or atomistic simulation approaches.

### 3.1.1 General computational methods for ion transport

Traditionally, finite difference approaches are widely used in the context of electrochemistry (see, e.g., Britz [25], Newman and Thomas-Alyea [137]), since they are easy to implement and usually sufficient for simple geometries. However, they often lack the necessary flexibility for considering complex realistic geometries. A fractional-step algorithm using a finite-difference scheme for spatial discretization was developed by Kwok and Wu [119]. One-dimensional electrochemical diffusion-migration problems with reaction at electrodes were simulated by Kwok and Wu [120] utilizing a solution procedure which decouples the calculations of ionic concentrations and electric potential. A finite-difference method with upwinding was developed by Georgiadou [74] for the simulation of convection-dominated multi-ion transport. Using that method, various two-dimensional electrochemical systems including convection, e.g., parallel-plate electrochemical reactors (Georgiadou [74, 75]), a backward-facing step (Georgiadou [74]) and cavities in laminar shear flow (Georgiadou et al. [76]) were studied.

### 3 Computational approach

---

A Lattice-Boltzmann model for studying electrochemical processes influenced by all three transport mechanisms was proposed by He and Li [93] for two-dimensional problems. Mesh-free numerical schemes were used by La Rocca and Power [121]. A multi-dimensional upwinding method for the analysis of multi-ion electrolytes controlled by diffusion, convection and migration was proposed by Bortels et al. [20]. This computational method was used to perform steady-state studies for a two-dimensional flow channel.

Recently, a fractional-step method proposed by Buoni and Petzold [27] for solving two-dimensional diffusion-migration problems on irregular domains with moving boundaries was extended to three space dimensions in Buoni and Petzold [28]. The resulting method is first-order accurate in time and second-order accurate in space using a finite volume approach for the spatial discretization. Convection was neglected there, since their focus was on semiconductor applications with very small length scales below 1  $\mu\text{m}$ . Transient mass-transfer processes in a 3D-model of an electrochemical sensor were investigated by Barak-Shinar et al. [5] using a finite-volume approach. All of the three ion-transport mechanisms were addressed in that study, but only the concentration field of one single reactive species was considered. In all investigations, the species concentration at the electrode surface was assumed to be zero. The electric potential was computed by solving a Poisson-Boltzmann equation.

The finite element method (FEM) has also been used already for the spatial discretization of different electrochemical problems including ionic mass transport. Henley and Fisher [94] used a FEM to simulate current-density distributions in three-dimensional microchannels. However, their model did not account for migration, and a constant conductivity of the electrolyte solution was assumed. Ion-diffusion mechanisms in porous media were modeled by Samson et al. [154], using the PNP system of equations. Only diffusion and migration were considered in the ion-transport model. The governing equations were discretized in space using a FEM. Applying a commercial finite element software, a rotating cylinder Hull cell was investigated by Low et al. [127]. Steady-state current distributions assuming Tafel kinetics at the working electrode for a 2D axial-symmetric model were computed. Only the concentration of a single ionic species was considered, and no flow field was computed, since the corresponding mass transport model was based on a Nernstian diffusion layer expression with prescribed concentration boundary-layer thickness. An adaptive multilevel finite element algorithm was proposed by Ludwig et al. [128] and applied for solving various electrochemical experiments with controlled current in one spatial dimension. Finite element discretizations for a Navier-Stokes-Nernst-Planck-Poisson system were investigated theoretically by Prohl and Schmuck [145]. A stabilized finite element approach for ionic transport was proposed in Ganjoo and Tezduyar [71] for the simulation of electrophoresis separation in one and two space dimensions.

It is well-known that a standard Galerkin finite element method (SGFEM) applied to convection-diffusion equations with a dominating convective term can lead to oscillations. To account for this, stabilized finite element methods were developed for the numerical solution of convection-diffusion-reaction equations and the incompressible Navier-Stokes equations, e.g., the Streamline-upwind Petrov/Galerkin (SUPG) method by Brooks and Hughes [26]. For an overview on existing methods, the reader is referred to, for instance, Hughes et al. [102]. Stabilized methods may be considered particular methods derived from the more general framework of the variational multiscale method (VMM) as originally introduced by Hughes [99].

Concerning electrochemistry, particularly coupled multi-ion transport problems, very few publications addressing stabilized finite element methods exist. In Ganjoo et al. [72], a mixed finite element method for the numerical simulation of electrophoresis separation phenomena was proposed. Therein, different ion-separation processes in one- and two-dimensional configurations were studied. An SUPG approach was proposed as the stabilizing technique. However, no coupling to the Navier-Stokes equations was included in that solution approach, and no boundary conditions for modeling electrochemical reactions at electrode surfaces were considered in the mathematical model.

The popular drift-diffusion model for describing the transport of charge carriers within semiconductor devices exhibits also similarities to the governing equations of multi-ion transport in dilute electrolyte solutions. A stabilized finite element method was proposed for the spatial discretization of drift-diffusion equations by Hennigan et al. [95], Lin et al. [125]. The large-scale parallel performance of an algebraic multigrid preconditioner for the numerical solution of such problems was investigated by Lin et al. [126].

### 3.1.2 Natural convection in electrochemical cells

In recent years, natural convection phenomena in electrochemical cells have also been investigated numerically. The influence of natural convection on the current density and the ionic concentration at the electrode was investigated, e.g., by Kawai et al. [113]. Therein, the Laplace (electric potential field), the ion-transport (excluding migration effects), and the fluid equations were solved individually by a finite difference scheme. A galvanostatic boundary condition was introduced to keep the electric current flow at the electrodes constant over time. The numerical results were experimentally validated by Kawai et al. [114]. In Kawai et al. [115], the Butler-Volmer law was added as a kinetic boundary-condition model.

The importance of including density gradients for modeling rotating cylinder electrodes was emphasized by Mandin et al. [130]. The steady state ion-transport (excluding migration effects) and fluid equations were solved using a commercial software. A finite difference scheme to simulate ionic transport (including the migration effect) under the influence of natural convection was proposed by Volgin et al. [173]. A review on natural-convective instabilities in electrochemical systems was provided by Volgin and Davydov [172]. In Chung [40], the tertiary current density distribution in the case of electrodeposition from a multi-ion electrolyte solution was studied for two-dimensional high-aspect-ratio cells including convection, diffusion and migration. Therein, the flow, the ionic concentration and the potential field were strongly coupled by an iterative (two-dimensional) finite volume scheme. Natural convection phenomena were also investigated in Wallgren et al. [176] using a finite volume scheme, including an ion-transport equation for binary electrolyte solutions, an equation for the electric potential and a Butler-Volmer law as a kinetic boundary condition. Further references on theoretical, experimental and numerical considerations of natural convection in electrochemical cells are provided by Ehrl et al. [56]. The computational approach presented in the latter publication has emerged from the previous work by Ehrl [55].

#### 3.1.3 Ion transport in turbulent flow

If convection was accounted for in the computational approaches referenced above at all, mostly laminar flow regimes were addressed. Although comprehensive numerical methods considering ionic mass transport coupled to turbulent flow are still rare in literature, a few approaches can be found. For instance, multi-ion transport and electrochemical reactions in turbulent parallel plate flow were studied by Nelissen et al. [136], considering a two-dimensional problem setup. A Reynolds-averaged Navier-Stokes (RANS) method was used for modeling the turbulent flow, including a low-Reynolds number  $k-\omega$  model. Utilizing a similar RANS approach, turbulent fluid flow and electrochemical mass transfer in an annular duct with an obstruction were studied numerically by Weyns et al. [177] considering a ferri-ferrocyanide system.

In general, turbulent mass transfer in electrochemical systems is a challenging topic due to the usually high Schmidt numbers involved. As introduced in section 2.8.5, the Schmidt number is defined as  $Sc = \nu/D$ , relating kinematic viscosity to molecular diffusivity. Typically, only a single passive scalar field governed by convection and diffusion is considered. DNS data for passive scalar transport in turbulent channel flow with low Reynolds number at Schmidt numbers up to  $Sc = 49$  were provided by Schwertfirm and Manhart [156]. Large-eddy simulations of high-Schmidt-number mass transfer in a turbulent channel flow were reported in Calmet and Magnaudet [30] and Dong et al. [53], for instance. In both studies, numerical results up to  $Sc = 200$  were provided. A nonlinear large-eddy simulation (nLES) method was proposed in Burton [29] for studying turbulent mixing of passive scalars for Schmidt numbers in the range  $Sc \in [1; 8192]$ .

In the special context of electrochemistry, simplified modeling approaches are often utilized, such as the ones used in Lee and Talbot [123], Low et al. [127] and Mandin et al. [131]. Therein, the ionic boundary-layer thickness is prescribed *a priori* based on the Nernst diffusion-layer expression, rather than obtaining it as a result of the simulations. However, this approach requires some *a priori* knowledge in the form of empirical formulae for each electrochemical cell configuration. As a consequence, general applicability is rather limited. Owing to complex geometries regarding both the parts to be plated and the bath itself, a more universal solution approach is needed, in general.

The configuration of a rotating cylinder electrode (RCE), which is used to validate the formulation presented in this work, received continuous attention in research as documented in a series of review papers Gabe [66], Gabe and Walsh [67] and Gabe et al. [68]. In particular, empirical mass-transfer correlations valid for limiting current and turbulent flow conditions have been known for long time (see, e.g., Eisenberg et al. [58]). Since configurations of this type obviously without the electrochemistry part were investigated, e.g., by Direct Numerical Simulation (DNS) in Dong [52], and LES in Bazilevs and Akkerman [15], valuable literature data for the turbulent flow behavior exist, at least for such a 'pure' flow problem. Therefore, this setup was preferred to the one proposed in Hwang et al. [103], for example, where a DNS of turbulent flow around a single rotating circular cylinder was performed, and no outer cylinder surface was considered. Recently, turbulent mass transfer studies for the cases  $Sc=1, 10$  and  $100$  were presented in Yoon et al. [184] for that single-cylinder configuration using direct numerical simulation. Further references regarding experimental work and computational flow results regarding Taylor-Couette flow between two concentric cylinders were provided in Dong [52] and Bazilevs and Akkerman [15], for instance.

### 3.1.4 Electrodeposition and pulse-plating applications

Many of the aforementioned references are concerned with the simulation of electrolytic processes such as electroplating. In the following some further references dedicated to this topic are provided.

Transient electrochemical techniques such as pulse plating (PP) and pulse-reverse plating (PRP) applications (see section 1.3) were also already addressed by means of numerical simulation. A one-dimensional computational model for PP on a rotating disk electrode was proposed by Yin and White [183]. Varadarajan et al. [171] presented a modeling approach for computing tertiary current distribution for PP of copper into high aspect ratio trenches. However, the proposed two-dimensional model did not account for migration. Steady-state and pulsed current multi-ion simulations for a thallium electrodeposition process were carried out by Van den Bossche et al. [169] based on the computational approach proposed by Bortels et al. [20]. Therein a (quasi-) one-dimensional model perpendicular to the surface of a rotating disk electrode was considered. Lee and West [124] used a numerical method to study the impact of pulse parameters on the current distribution. A one-dimensional model for copper PP at a rotating disk electrode was utilized by Tsai et al. [168] to investigate the effect of additives and the influence of the electric double layer. Copper PP and PRP methods were addressed by Tantavichet and Pritzker [163]. Dan et al. [44] simulated transient current responses in dilute electrochemical systems. It is important to note that all of the computational approaches listed above use the electroneutrality condition to close the system of ion-transport equations. Hence, the ENP system of equations focused on in this work provides also a justified approach to the modeling of PP and PRP applications.

A second aspect in the context of electrodeposition is the simulation of electrode shape changes. For many applications the computation of a current density distribution is already sufficient and allows a prediction of the deposit thickness distribution according to (2.51). Numerical simulation approaches including electrode shape changes were primarily developed for numerical simulations in the context of copper electrodeposition in semiconductor manufacturing. Methods for such moving-boundary problems in the context of electrodeposition were proposed by Purcar et al. [148], Buoni and Petzold [27], Sethian and Shan [157] and Hughes et al. [98] for example. Owing to the need to account for large deformations and even self-contact of electrodeposited copper layers, level-set-based techniques are commonly proposed in this context. Note that computational methods capable of simulating large electrode shape changes are also of importance in the context of electrochemical machining applications (see, e.g. Purcar et al. [147]).

### 3.1.5 Summary and conclusions

In summary, the consideration of multi-ion transport in three-dimensional complex geometries represents still a challenging task. As a result of the literature survey presented above, only some recent publications actually consider such complex problems. Often, computational methods were specifically developed for single applications and do therefore not include for all of the physical phenomena in the model. In contrast, a general and comprehensive computational approach is presented in this work, which accounts for all three ion-transport phenomena, electrode kinetics and coupling to incompressible flow at the same time. Especially the coupling of ion-transport to laminar and turbulent flow is one of

the key aspects of this work. The framework of the finite element method introduced below provides also the necessary flexibility for the consideration of complex three-dimensional geometries. In the following sections 3.2-3.5 this novel computational approach will be presented in detail.

## 3.2 Time discretization

As a general discretization procedure, Rothe's method (also known as "horizontal method of lines") is utilized for the developed computational approach. Thus, discretization in time is performed prior to discretization in space. As a result, a sequence of boundary value problems has to be solved. In this study, the so-called generalized-alpha time-integration scheme is utilized for discretizing the governing equations in time, as presented below.

### 3.2.1 Generalized-alpha time-integration scheme

The generalized-alpha method was originally proposed by Chung and Hulbert [39] as a time-integration algorithm with improved dissipative damping for structural dynamics simulations. It provides user-defined adjustment of high frequency damping and includes several well-known and popular discretization schemes as special cases. In the publication by Jansen et al. [110] the original method was developed further to be applicable for first-order systems such as those arising in fluid dynamics. In particular, Jansen et al. [110] addressed the temporal discretization of the compressible Navier-Stokes equations. Generalized-alpha methods for the large-eddy simulation of turbulent incompressible flows were considered by Bazilevs et al. [16], Gamnitzer et al. [70], Gamnitzer [69] and Gravemeier et al. [80], for instance. Recently, the generalized-alpha method was also utilized for turbulent variable-density flow at low Mach number by Gravemeier and Wall [82, 83]. Since the present problem formulation introduced in chapter 2 represents a first-order system with respect to time, the formulation originally proposed by Jansen et al. [110] is taken as a basis for the following considerations.

The time period of interest  $[0, T_e]$  is divided into a series of uniform time steps with constant length  $\Delta t$ . For time step  $n + 1$ , the previous time is denoted by  $t^n$  and the new time level is given by  $t^{n+1} = t^n + \Delta t$ . For the generalized-alpha time-integration scheme two further intermediate time levels are introduced by

$$t^{n+\alpha_f} = (1 - \alpha_f) t^n + \alpha_f t^{n+1}, \quad (3.1)$$

$$t^{n+\alpha_m} = (1 - \alpha_m) t^n + \alpha_m t^{n+1}, \quad (3.2)$$

where  $\alpha_f$  and  $\alpha_m$  are two parameters of the method. Adaptive methods with non-uniform time stepping combined with appropriate error estimation techniques are not considered in the present study. However, adaptivity in time represents a possible future extension of the current computational approach.

In the following, an initial-value problem for a general ordinary differential equation

(ODE) of the form

$$\begin{aligned}\frac{d}{dt}y(t) &= f(y(t), t), \\ y(0) &= y^0\end{aligned}\tag{3.3}$$

is considered. The corresponding discretized form of (3.3) obtained from the generalized-alpha method reads

$$\dot{y}^{n+\alpha_m} = f(y^{n+\alpha_f}, t^{n+\alpha_f}),\tag{3.4}$$

$$\dot{y}^{n+\alpha_m} = (1 - \alpha_m)\dot{y}^n + \alpha_m\dot{y}^{n+1},\tag{3.5}$$

$$y^{n+\alpha_f} = (1 - \alpha_f)y^n + \alpha_f y^{n+1},\tag{3.6}$$

$$y^{n+1} = y^n + \Delta t((1 - \gamma)\dot{y}^n + \gamma\dot{y}^{n+1}).\tag{3.7}$$

Note that a third parameter of the method denoted by  $\gamma$  has been introduced in (3.7). According to Jansen et al. [110], a stable method is only obtained when the relation

$$\alpha_m \geq \alpha_f \geq \frac{1}{2}\tag{3.8}$$

is fulfilled. To accomplish second-order accuracy, the three parameters of the method must additionally satisfy the condition

$$\gamma = \frac{1}{2} + \alpha_m - \alpha_f.\tag{3.9}$$

Several well-known time-integration schemes can be represented with the generalized-alpha method. These are simply obtained by different choices for the three parameters  $\alpha_f$ ,  $\alpha_m$  and  $\gamma$ . In the following, only the methods actually used in this study are addressed.

### Generalized trapezoidal rule (one-step-theta scheme)

The well-known generalized trapezoidal rule (also termed one-step-theta scheme) is obtained for the choice  $\alpha_m = \alpha_f = 1$  and  $\gamma \in [0; 1]$ . By introducing  $\theta := \gamma$ , the perhaps more familiar form of the generalized trapezoidal rule given as

$$y^{n+1} = y^n + \Delta t(\theta f(y^{n+1}, t^{n+1}) + (1 - \theta)f(y^n, t^n))\tag{3.10}$$

is obtained from (3.4)-(3.7).

Unconditionally stable, fully implicit schemes such as desired here, are only obtained for the parameter choice  $\theta \in [0.5; 1]$ . Most prominent examples are the first-order accurate backward Euler scheme ( $\theta = 1$ ) and the second-order accurate classical trapezoidal rule ( $\theta = 0.5$ ). The latter method is sometimes also termed Crank-Nicolson scheme. For the generalized trapezoidal rule it holds  $\dot{y}^0 = f(y^0, 0)$ , due to (3.4) and  $\alpha_m = \alpha_f = 1$ . Consequently, the value of  $\dot{y}^0$  is not independent, but has to be computed in a consistent manner from (3.4) based on the initial value  $y^0$ .

### $\rho_\infty$ -scheme

According to Jansen et al. [110], a second-order accurate, one-parameter family of methods with a specified high frequency damping is defined by the parameter setting

$$\alpha_f = \frac{1}{1+\rho_\infty}, \quad \alpha_m = \frac{1}{2} \left( \frac{3-\rho_\infty}{1+\rho_\infty} \right), \quad \gamma = \frac{1}{2} + \alpha_m - \alpha_f. \quad (3.11)$$

Here, the parameter  $\gamma$  is determined by condition (3.9), which ensures the desired second-order accuracy. The new parameter  $\rho_\infty \in [0; 1]$  can be interpreted as spectral radius for an infinite time step (see Jansen et al. [110] for details). For the choice  $\rho_\infty = 1$ , the implicit midpoint rule is obtained, while the choice  $\rho_\infty = 0$  (i.e.,  $\alpha_m = 3/2$ ,  $\alpha_f = 1$ ,  $\gamma = 1$ ) yields the second-order accurate BDF2 method, which is addressed below. Based on the investigations carried out by Jansen et al. [110],  $\rho_\infty = 0.5$  represents a common choice in the context of fluid dynamics simulations.

### BDF2 (backward differentiation formula of order 2)

The BDF2 method represents a very popular A-stable method (see, e.g., Hairer et al. [89], Hairer and Wanner [90] for further details on the stability of numerical solution schemes for ODEs). Using the corresponding parameter choice  $\alpha_m = 3/2$ ,  $\alpha_f = 1$  and  $\gamma = 1$ , equations (3.4)-(3.7) can be combined to

$$\frac{3}{2}y^{n+1} - 2y^n + \frac{1}{2}y^{n-1} = \Delta t f(y^{n+1}, t^{n+1}). \quad (3.12)$$

This clearly demonstrates that BDF2 is actually a two-step method, which is less obvious in the general generalized-alpha notation. For multistep methods such as BDF2 or other certain variants of the generalized-alpha scheme, a start-up procedure is needed until the required number of history values is completely available. In case of a two-step method, a single-step method such as the generalized trapezoidal rule has to be used for the first time step, where the initial value  $y^0$  represents the only available history value. After this starting step, values for the two required quantities  $y^n$ ,  $y^{n-1}$  are available in the subsequent time steps.

### 3.2.2 Semi-discrete form of governing equations

The semi-discrete problem formulation is obtained by applying the generalized-alpha time-integration scheme to the governing equations introduced in chapter 2. In this work, an identical time discretization approach is used for both subproblems, i.e., the multi-ion transport and the incompressible flow problem.

#### Multi-ion transport

According to the generalized-alpha method, the semi-discrete form of each ion-transport equation (2.12) for species  $k = 1, \dots, m$  reads

$$c_k^{n+\alpha_m} + \mathbf{u}^{n+\alpha_f} \cdot \nabla c_k^{n+\alpha_f} + \nabla \cdot N_k^{d+m} (c_k^{n+\alpha_f}, \Phi^{n+\alpha_f}) = 0. \quad (3.13)$$

The third term on the left-hand side of (3.13) reads

$$\nabla \cdot \mathbf{N}_k^{d+m} (c_k^{n+\alpha_f}, \Phi^{n+\alpha_f}) = -D_k \nabla c_k^{n+\alpha_f} - z_k \mu_k F c_k^{n+\alpha_f} \nabla \Phi^{n+\alpha_f}. \quad (3.14)$$

In accordance to the previous subsection, the required solution variables at intermediate time levels are defined as

$$\dot{c}_k^{n+\alpha_m} = (1 - \alpha_m) \dot{c}_k^n + \alpha_m \dot{c}_k^{n+1}, \quad (3.15)$$

$$c_k^{n+\alpha_f} = (1 - \alpha_f) c_k^n + \alpha_f c_k^{n+1}, \quad (3.16)$$

$$\Phi^{n+\alpha_f} = (1 - \alpha_f) \Phi^n + \alpha_f \Phi^{n+1}, \quad (3.17)$$

and the relation (3.7) reads for the present case

$$c_k^{n+1} = c_k^n + \Delta t ((1 - \gamma) \dot{c}_k^n + \gamma \dot{c}_k^{n+1}). \quad (3.18)$$

Note that both alternatives (2.22), (2.25) for closing the system of equations do not include a time derivative. In the present work, these constraints are enforced to hold at the intermediate time level  $t^{n+\alpha_f}$ . An alternative to this choice will be discussed below. The corresponding form of the electroneutrality condition (2.22) reads

$$\sum_{k=1}^m z_k c_k^{n+\alpha_f} = 0, \quad (3.19)$$

while the semi-discrete form of the alternative closing equation for the electric potential (2.25) is given as

$$-\nabla \cdot \left[ \left( \sum_{k=1}^{m-1} z_k F (z_k \mu_k - z_m \mu_m) c_k^{n+\alpha_f} \right) \nabla \Phi^{n+\alpha_f} \right] - \nabla \cdot \left[ \sum_{k=1}^{m-1} z_k (D_k - D_m) \nabla c_k^{n+\alpha_f} \right] = 0. \quad (3.20)$$

For the latter equation, a division by  $F$  was performed in order to obtain similar order of magnitudes for the individual terms compared to (3.13).

### Incompressible flow

The time-discretized form of the incompressible Navier-Stokes equations (2.61)-(2.62) reads

$$\dot{\mathbf{u}}^{n+\alpha_m} + (\mathbf{u}^{n+\alpha_f} \cdot \nabla) \mathbf{u}^{n+\alpha_f} - 2\nu \nabla \cdot \boldsymbol{\varepsilon}(\mathbf{u}^{n+\alpha_f}) + \nabla p^{n+\alpha_f} - \mathbf{b}^{n+\alpha_f} = \mathbf{0}, \quad (3.21)$$

$$\nabla \cdot \mathbf{u}^{n+\alpha_f} = 0. \quad (3.22)$$

The arising quantities at intermediate time levels are computed according to

$$\dot{\mathbf{u}}^{n+\alpha_m} = (1 - \alpha_m) \dot{\mathbf{u}}^n + \alpha_m \dot{\mathbf{u}}^{n+1}, \quad (3.23)$$

$$\mathbf{u}^{n+\alpha_f} = (1 - \alpha_f) \mathbf{u}^n + \alpha_f \mathbf{u}^{n+1}, \quad (3.24)$$

$$p^{n+\alpha_f} = (1 - \alpha_f) p^n + \alpha_f p^{n+1}, \quad (3.25)$$

together with

$$\mathbf{u}^{n+1} = \mathbf{u}^n + \Delta t \left( (1 - \gamma) \dot{\mathbf{u}}^n + \gamma \dot{\mathbf{u}}^{n+1} \right). \quad (3.26)$$

Note that the incompressibility constraint (3.22) is enforced here at the intermediate time level  $t^{n+\alpha_f}$ . This choice can be interpreted as the incompressible limit of the semi-discrete form of the general continuity equation (2.59), which reads

$$\dot{\rho}^{n+\alpha_m} + \nabla \cdot (\rho^{n+\alpha_f} \mathbf{u}^{n+\alpha_f}) = 0. \quad (3.27)$$

The semi-discrete formulation (3.21)-(3.22) was used by Gravemeier et al. [80] in the context of large-eddy simulation of turbulent incompressible flow. Recently, Kang et al. [112] used the present semi-discrete formulation within their numerical investigations devoted to fluid-structure interaction and the use of generalized-alpha methods for this coupled multifield field problem.

An alternative to (3.22) is to demand

$$\nabla \cdot \mathbf{u}^{n+1} = 0, \quad (3.28)$$

that is, the incompressibility is enforced at the time level  $t^{n+1}$ . This choice is typically combined with an evaluation of the pressure gradient in (3.21) at time  $t^{n+1}$  instead of  $t^{n+\alpha_f}$ . For further details on this alternative approach, the reader is referred to, e.g., Calo [31], Gamnitzer [69] and Gamnitzer et al. [70]. Both discussed variants are available within the current implementation of the flow solver. However, only the first approach will be considered in the following.

It is emphasized that both presented options (3.22), (3.28) to treat the continuity equation w.r.t. time ensure that  $\nabla \cdot \mathbf{u}^{n+\alpha_f} = 0$  is fulfilled. In the case of (3.28) this follows directly from  $\nabla \cdot \mathbf{u}^n = 0$ , relation (3.24) and the linearity of the divergence operator. As a consequence, the conversion of the ion-transport equation from its convective form (3.13) to its conservative form, and vice versa, is not affected by the employed time-discretization scheme. An alternative enforcement of the constraints (3.19) and (3.20) at time level  $t^{n+1}$  represents an option which certainly deserves future investigation. For the time being, the formulation introduced above is used. Since for most of the numerical examples presented in this work, time-integration schemes with the parameter choice  $\alpha_f = 1$  are used, the distinction between both options is insignificant anyway.

### 3.3 Weak formulation of semi-discrete equations

A so-called weak formulation of the governing equations is the basis for the spatial discretization procedure performed in this study. As a first step, the semi-discrete equations derived in the previous section are multiplied with appropriate weighting (or test) functions and an integration over the computational domain  $\Omega$  is performed. This establishes a weighted residual formulation of each equation in an integral sense. As a second step, by using integration by parts on terms where appropriate, the requirements regarding the differentiability of the solution functions are decreased. As a result, the so-called weak problem formulation is obtained.

In the following, appropriate function spaces for the weighting and the trial solution functions are provided for the present problem formulation. As usual,  $L^2(\Omega)$  represents

the space of square-integrable functions defined on  $\Omega$ . The Hilbert space  $L^2(\Omega)$  is equipped with an inner product given as

$$(\cdot, \cdot)_\Omega : L^2(\Omega) \times L^2(\Omega) \rightarrow \mathbb{R}, \quad (f_1, f_2) \mapsto (f_1, f_2)_\Omega := \int_{\Omega} f_1 f_2 \, dx. \quad (3.29)$$

This inner product induces a corresponding norm, which is given by

$$\|f\|_{L^2(\Omega)} = \sqrt{(f, f)_\Omega} \quad \text{for } f \in L^2(\Omega). \quad (3.30)$$

The subspace  $H^1(\Omega) \subset L^2(\Omega)$  denotes the usual Sobolev space of  $L^2(\Omega)$ -functions that possess a weak first derivative:

$$H^1(\Omega) := \left\{ f \in L^2(\Omega) \mid \frac{\partial f}{\partial x_i} \in L^2(\Omega), i = 1, \dots, d \right\}. \quad (3.31)$$

Further details on the underlying concepts of functional analysis in general and Sobolev spaces in particular can be found in Adams and Fournier [1], for instance.

### 3.3.1 Multi-ion transport subproblem

With respect to each ionic species concentration  $c_k$ , the space

$$\mathcal{S}_{c_k} := \left\{ c_k \in H^1(\Omega) \mid c_k = g_k \text{ on } \Gamma_{D,k} \right\} \quad (3.32)$$

of admissible trial solutions satisfying the Dirichlet boundary conditions (2.36) is defined. The corresponding spaces of weighting (or test) functions for  $k = 1, \dots, m$  are given by

$$\mathcal{T}_{c_k} := \left\{ w_k \in H^1(\Omega) \mid w_k = 0 \text{ on } \Gamma_{D,k} \right\}. \quad (3.33)$$

With respect to the electric potential  $\Phi$  two spaces of functions,

$$\mathcal{S}_\Phi := \left\{ \Phi \in H^1(\Omega) \right\} \quad (3.34)$$

and

$$\mathcal{T}_\Phi := \left\{ \varphi \in H^1(\Omega) \right\}, \quad (3.35)$$

are introduced for admissible trial solutions and test functions, respectively. Note that both spaces coincide, since typically no Dirichlet boundary conditions for the electric potential are applied. However, when only boundary conditions of type (2.36) and (2.37) are considered, the electric potential  $\Phi$  is only defined up to a constant. For getting a unique solution, a point in  $\Omega$  has to be chosen where a reference value for the electric potential is prescribed. In that case, formally, the quotient spaces  $\mathcal{S}_\Phi/\mathbb{R}$  and  $\mathcal{T}_\Phi/\mathbb{R}$  have to be used instead, where all functions that differ only by a constant are grouped together in corresponding equivalence classes. Hence, two functions that differ only by a constant are interpreted as the same function in these quotient spaces.

### Weak form of Nernst-Planck equation

Now, each semi-discrete ion-transport equation (3.13) for  $k = 1, \dots, m$  is considered. Multiplication with an arbitrary weighting function  $w_k \in \mathcal{T}_{c_k}$  and integration over  $\Omega$  yields the weighted residual formulation reading

$$\int_{\Omega} w_k \dot{c}_k^{n+\alpha_m} dx + \int_{\Omega} w_k \mathbf{u}^{n+\alpha_f} \cdot \nabla c_k^{n+\alpha_f} dx + \int_{\Omega} w_k \nabla \cdot \mathbf{N}_k^{d+m}(c_k^{n+\alpha_f}, \Phi^{n+\alpha_f}) dx = 0. \quad (3.36)$$

After application of integration by parts to the third term on the left-hand side, one obtains

$$\begin{aligned} & (w_k, \dot{c}_k^{n+\alpha_m}) + (w_k, \mathbf{u}^{n+\alpha_f} \cdot \nabla c_k^{n+\alpha_f}) - (\nabla w_k, \mathbf{N}_k^{d+m}(c_k^{n+\alpha_f}, \Phi^{n+\alpha_f})) \\ & + (w_k, \mathbf{N}_k^{d+m}(c_k^{n+\alpha_f}, \Phi^{n+\alpha_f}) \cdot \mathbf{n})_{\partial\Omega} = 0 \quad \forall w_k \in \mathcal{T}_{c_k}. \end{aligned} \quad (3.37)$$

Here, a more compact notation is introduced, where  $(\cdot, \cdot) := (\cdot, \cdot)_{\Omega}$  denotes the  $L^2(\Omega)$ -inner product as introduced in (3.29). The  $L^2$ -inner product w.r.t.  $\partial\Omega$  is denoted by  $(\cdot, \cdot)_{\partial\Omega}$ . Note that in the third term of (3.37) actually a generalization of the inner product (3.29) for vector-valued quantities is used (see, e.g., Gamnitzer [69] for further details). For simplicity of notation, the nomenclature  $(., .)$  is used for such terms as well.

Based on the boundary partition  $\partial\Omega = \Gamma_{D,k} \cup \Gamma_{N,k} \cup \Gamma_{E,k}$  introduced in section 2.5.2, the boundary conditions (2.37) and (2.40) are inserted and the property  $w_k = 0$  on  $\Gamma_{D,k}$  is used. The final weak formulation of the semi-discrete Nernst-Planck equation for ionic species  $k = 1, \dots, m$  reads

$$\begin{aligned} & (w_k, \dot{c}_k^{n+\alpha_m}) + (w_k, \mathbf{u}^{n+\alpha_f} \cdot \nabla c_k^{n+\alpha_f}) - (\nabla w_k, \mathbf{N}_k^{d+m}(c_k^{n+\alpha_f}, \Phi^{n+\alpha_f})) \\ & - (w_k, j_k^{n+\alpha_f})_{\Gamma_{E,k}} = (w_k, h_k^{n+\alpha_f})_{\Gamma_{N,k}} \quad \forall w_k \in \mathcal{T}_{c_k}. \end{aligned} \quad (3.38)$$

In accordance to the nomenclature introduced above, the  $L^2$ -inner products w.r.t.  $\Gamma_{N,k}$  and  $\Gamma_{E,k}$  are denoted by  $(\cdot, \cdot)_{\Gamma_{N,k}}$  and  $(\cdot, \cdot)_{\Gamma_{E,k}}$ , respectively. The third term on the left-hand side of (3.38) reads

$$- (\nabla w_k, \mathbf{N}_k^{d+m}(c_k^{n+\alpha_f}, \Phi^{n+\alpha_f})) = D_k (\nabla w_k, \nabla c_k^{n+\alpha_f}) + z_k \mu_k F (\nabla w_k, c_k^{n+\alpha_f} \nabla \Phi^{n+\alpha_f}). \quad (3.39)$$

At this point it is worth mentioning that the boundary conditions (2.37), (2.40) are automatically embedded into the weak form (3.38). Assuming sufficient smoothness of the solution functions, another integration by parts on (3.37) can be performed. This yields

$$\begin{aligned} & (w_k, \dot{c}_k^{n+\alpha_m} + \mathbf{u}^{n+\alpha_f} \cdot \nabla c_k^{n+\alpha_f} + \nabla \cdot \mathbf{N}_k^{d+m}(c_k^{n+\alpha_f}, \Phi^{n+\alpha_f})) \\ & - (w_k, \mathbf{N}_k^{d+m}(c_k^{n+\alpha_f}, \Phi^{n+\alpha_f}) \cdot \mathbf{n} + j_k^{n+\alpha_f})_{\Gamma_{E,k}} = (w_k, \mathbf{N}_k^{d+m}(c_k^{n+\alpha_f}, \Phi^{n+\alpha_f}) \cdot \mathbf{n} + h_k^{n+\alpha_f})_{\Gamma_{N,k}}, \end{aligned}$$

which has to hold for all  $w_k \in \mathcal{T}_{c_k}$ . Thus, when the solutions  $c_k$  and  $\Phi$  of the weak form are smooth enough to fulfill the original partial differential equation, the flux boundary conditions (2.37) and (2.40) are naturally fulfilled.

The velocity of the electrolyte solution is typically set to zero at an impermeable wall using a no-slip boundary condition. Consequently, there is no mass flux due to convection across such a boundary part, since it holds  $\mathbf{u} \cdot \mathbf{n} = 0$ . In that case, a prescribed normal flux

$N_k^{d+m} \cdot \mathbf{n}$  caused by diffusion and migration is identical to the total ionic mass flux. If a zero flux in normal direction is demanded due to either (2.37) or (2.42), the respective boundary integral w.r.t.  $\Gamma_{N,k}$  or  $\Gamma_{E,k}$  simply vanishes in (3.38). Thus, actually no boundary integral has to be computed resulting in simple “doing nothing” conditions in that case. Such conditions are usually also used at outflow boundaries, which are again fulfilled by the method in a natural way. As a consequence, only Dirichlet boundary conditions and boundary parts with  $h_k \neq 0$  or  $j_k \neq 0$  require to be explicitly accounted for in the computational framework. For typical electrochemical problem configurations, “doing nothing” conditions are quite common, since major parts of the whole boundary are usually representing the insulating walls of an electrochemical cell. In addition, inert species have zero mass flux at electrode surfaces as well.

### Weak form of electroneutrality condition

In case of the ENP system of equations, the electroneutrality condition (2.22) is the equation for the electric potential (although it does not explicitly contain  $\Phi$ ). Thus, it is multiplied with a corresponding test function  $\varphi \in \mathcal{T}_\Phi$ . This approach is consistent with the performed weighting of the ion-transport residuals as well as with the treatment of other closing equations for the electric potential within a finite element formulation (see, e.g., Ganjoo and Tezduyar [71], Samson et al. [154]). After integration over the computational domain the weak form of (2.22) reads:

$$\mathcal{B}_E(\varphi, c_1^{n+1}, \dots, c_m^{n+1}) := \left( \varphi, \sum_{k=1}^m z_k c_k^{n+\alpha_f} \right) = \sum_{k=1}^m z_k (\varphi, c_k^{n+\alpha_f}) = 0 \quad \forall \varphi \in \mathcal{T}_\Phi. \quad (3.40)$$

### Weak form of alternative closing equation

When equation (3.20) is used to close the system of equations, i.e., the CNP system of equations is considered, an additional integration by parts is performed after multiplication of (3.20) with a test function  $\varphi$  and integration over the domain  $\Omega$ . Since  $\varphi \in \mathcal{T}_\Phi \subset H^1(\Omega)$ , the integration by parts is admissible. As a result of this procedure, one obtains

$$\begin{aligned} & \left( \nabla \varphi, \sum_{k=1}^{m-1} z_k F(z_k \mu_k - z_m \mu_m) c_k^{n+\alpha_f} \nabla \Phi^{n+\alpha_f} \right) + \left( \nabla \varphi, \sum_{k=1}^{m-1} z_k (D_k - D_m) \nabla c_k^{n+\alpha_f} \right) \\ & - \left( \varphi, \sum_{k=1}^{m-1} z_k \underbrace{(z_k \mu_k F c_k^{n+\alpha_f} \nabla \Phi^{n+\alpha_f} + D_k \nabla c_k^{n+\alpha_f}) \cdot \mathbf{n}}_{= -N_k^{d+m}(c_k^{n+\alpha_f}, \Phi^{n+\alpha_f}) \cdot \mathbf{n}} \right)_{\partial\Omega} \\ & - \left( \varphi, \underbrace{(-z_m \mu_m F c_m^{n+\alpha_f} \nabla \Phi^{n+\alpha_f} - D_m \nabla c_m^{n+\alpha_f}) \cdot \mathbf{n}}_{= N_m^{d+m}(c_m^{n+\alpha_f}, \Phi^{n+\alpha_f}) \cdot \mathbf{n}} \right)_{\partial\Omega} = 0 \quad \forall \varphi \in \mathcal{T}_\Phi. \end{aligned} \quad (3.41)$$

As stated above, typically no Dirichlet boundary conditions are applied for the electric potential field  $\Phi$ . Consequently, the boundary integrals in (3.41) arising from the integration by parts are referring to the complete boundary  $\partial\Omega$  of the domain. These boundary

terms were already rearranged in (3.41) to reveal the dependency on the normal ionic mass fluxes. As a next step, the boundary partition  $\partial\Omega = \Gamma_{D,k} \cup \Gamma_{N,k} \cup \Gamma_{E,k}$  introduced in section 2.5.2 is considered. By inserting the boundary conditions (2.37), (2.40) into (3.41) the following weak form is obtained as a result:

$$\begin{aligned} \mathcal{B}_C(\varphi, c_1^{n+1}, \dots, c_{m-1}^{n+1}, \Phi^{n+1}) := & \left( \nabla \varphi, \sum_{k=1}^{m-1} z_k F(z_k \mu_k - z_m \mu_m) c_k^{n+\alpha_f} \nabla \Phi^{n+\alpha_f} \right) \\ & + \left( \nabla \varphi, \sum_{k=1}^{m-1} z_k (D_k - D_m) \nabla c_k^{n+\alpha_f} \right) - \sum_{k=1}^m (\varphi, z_k N_k^{d+m}(c_k^{n+\alpha_f}, \Phi^{n+\alpha_f}) \cdot \mathbf{n})_{\Gamma_{D,k}} \\ & - \sum_{k=1}^m (\varphi, z_k j_k^{n+\alpha_f})_{\Gamma_{E,k}} - \sum_{k=1}^m (\varphi, z_k h_k^{n+\alpha_f})_{\Gamma_{N,k}} = 0 \quad \forall \varphi \in \mathcal{T}_\Phi. \end{aligned} \quad (3.42)$$

Concerning the weak form (3.42) several important remarks have to be made:

1. It is an important observation that the flux boundary conditions (2.37), (2.40) of all ionic species  $k = 1, \dots, m$  enter the weak form (3.42). As explained in section 2.4, this is a consequence of the fact that ions are mass and charge carriers at the same time and (3.42) enforces charge conservation.
2. As a further consequence, the CNP formulation appears to be applicable only in situations where an inert, i.e., non-reacting ionic species  $m$  is eliminated from the system of ion-transport equations. Then, it holds  $N_m^{d+m}(c_m^{n+\alpha_f}, \Phi^{n+\alpha_f}) \cdot \mathbf{n} = 0$  on the complete boundary  $\partial\Omega$ . In particular,  $h_m = 0$  and  $j_m = 0$  holds in this case. Otherwise, an unknown flux contribution arises for  $k = m$  which prevents the elimination of species  $m$  in this case. However, since at least one inert ionic species is present in all multi-ion transport models of practical relevance, the general usability of the CNP model is *de facto* not limited.
3. For problem setups with  $\Gamma_{D,k} \neq \emptyset$ , the *a priori* unknown mass fluxes at the Dirichlet boundaries have to be specified in (3.42). For the moment, the CNP formulation is only applied to electrochemical problem setups subjected only to boundary conditions of type (2.37) and (2.40). Nevertheless, it is emphasized that the ideas outlined in the Appendix B will be instrumental for a future extension of the CNP model, since the normal ionic mass flux at  $\Gamma_{D,k}$  can essentially be replaced by the residual of the ion-transport equation as shown in equation (B.1).
4. In comparison to the weak form of the electroneutrality condition (3.40) considerably more terms have to be evaluated in (3.42). This leads to increased computational cost within an implementation. However, a careful comparison of (3.42) with (3.38) reveals that a major part of the first two and the last two terms in (3.42) arise also in (3.38). Within an implementation of the CNP approach, these readily evaluated terms can be multiplied with  $z_k$  and simply reused in (3.42). Hence, only the terms with respect to ionic species  $m$  have actually to be calculated. Note that this advantage can only be used when the constraint condition is enforced to hold at the intermediate time level  $t^{n+\alpha_f}$ , as it is done in this work.

### 3.3.2 Flow subproblem

A detailed derivation of the weak form of the incompressible flow problem is not presented here. It follows the general procedure outlined at the beginning of this section. For details, the reader can consult the textbooks by Gresho and Sani [85], Zienkiewicz and Taylor [186] or Donea and Huerta [50], for example. The required trial solution and test function spaces for velocity and pressure are defined as

$$\mathcal{S}_u := \left\{ \mathbf{u} \in \left[ H^1(\Omega) \right]^d \mid \mathbf{u} = \mathbf{u}_D \text{ on } \Gamma_D^u \right\}, \quad \mathcal{T}_u := \left\{ \mathbf{u} \in \left[ H^1(\Omega) \right]^d \mid \mathbf{u} = \mathbf{0} \text{ on } \Gamma_D^u \right\}, \quad (3.43)$$

$$\mathcal{S}_p := \left\{ p \in L^2(\Omega) \right\}, \quad \mathcal{T}_p := \left\{ p \in L^2(\Omega) \right\}. \quad (3.44)$$

In case of a full Dirichlet problem, i.e.  $\partial\Omega \equiv \Gamma_D$ , or a full Neumann problem, i.e.  $\partial\Omega \equiv \Gamma_N$ , the pressure is only defined up to a constant. Formally, the quotient spaces  $\mathcal{S}_p/\mathbb{R}$  and  $\mathcal{T}_p/\mathbb{R}$  have to be considered instead, as discussed above for the electric potential field. For practical computations, the pressure value is often simply prescribed at an appropriate position. An alternative method to obtain a unique solution was proposed by Bochev and Lehoucq [19], where a discrete projection is performed during the numerical solution process (see also Gamnitzer [69] for further details).

### 3.3.3 Entire weak form

In summary, the weak form of the semi-discrete system of equations of the ENP model reads as follows: for each discrete time level  $t^{n+1}$ , find  $c_1^{n+1} \in \mathcal{S}_{c_1}, \dots, c_m^{n+1} \in \mathcal{S}_{c_m}, \Phi^{n+1} \in \mathcal{S}_\Phi, \mathbf{u}^{n+1} \in \mathcal{S}_u$  and  $p^{n+1} \in \mathcal{S}_p$ , such that

$$\mathcal{B}_k(w_k, c_k^{n+1}, \Phi^{n+1}, \mathbf{u}^{n+1}) + \mathcal{J}_k(w_k, c_k^{n+1}, \Phi^{n+1}) = \mathcal{F}_k(w_k) \quad \forall w_k \in \mathcal{T}_{c_k}, k = 1, \dots, m, \quad (3.45)$$

$$\mathcal{B}_E(\varphi, c_1^{n+1}, \dots, c_m^{n+1}) = 0 \quad \forall \varphi \in \mathcal{T}_\Phi, \quad (3.46)$$

$$\begin{aligned} & (\mathbf{v}, \dot{\mathbf{u}}^{n+\alpha_m}) + (\mathbf{v}, (\mathbf{u}^{n+\alpha_f} \cdot \nabla) \mathbf{u}^{n+\alpha_f}) - (\nabla \cdot \mathbf{v}, p^{n+\alpha_f}) + (\boldsymbol{\varepsilon}(\mathbf{v}), 2\nu \boldsymbol{\varepsilon}(\mathbf{u}^{n+\alpha_f})) \\ &= (\mathbf{v}, \mathbf{b}^{n+\alpha_f}) + (\mathbf{v}, \mathbf{t}^{n+\alpha_f})_{\Gamma_N^u} \quad \forall \mathbf{v} \in \mathcal{T}_u, \end{aligned} \quad (3.47)$$

$$(q, \nabla \cdot \mathbf{u}^{n+\alpha_f}) = 0 \quad \forall q \in \mathcal{T}_p. \quad (3.48)$$

In (3.45), the following additional abbreviations were introduced to obtain a more compact notation:

$$\begin{aligned} \mathcal{B}_k(w_k, c_k^{n+1}, \Phi^{n+1}, \mathbf{u}^{n+1}) &:= (w_k, \dot{c}_k^{n+\alpha_m}) + (w_k, \mathbf{u}^{n+\alpha_f} \cdot \nabla c_k^{n+\alpha_f}) \\ &\quad + D_k(\nabla w_k, \nabla c_k^{n+\alpha_f}) + z_k \mu_k F(\nabla w_k, c_k^{n+\alpha_f} \nabla \Phi^{n+\alpha_f}), \end{aligned} \quad (3.49)$$

$$\mathcal{J}_k(w_k, c_k^{n+1}, \Phi^{n+1}) := - (w_k, j_k(c_k^{n+\alpha_f}, \Phi^{n+\alpha_f}))_{\Gamma_{E,k}}, \quad (3.50)$$

and

$$\mathcal{F}_k(w_k) := (w_k, h_k^{n+\alpha_f})_{\Gamma_{N,k}}. \quad (3.51)$$

This notation additionally emphasizes that the quantities at time level  $t^{n+1}$  are the unknowns which have to be determined at time step  $n + 1$ .

Note that in the case of the CNP system of equations, (3.45) is only considered for the ionic species  $k = 1, \dots, m - 1$ . In summary, the equations (3.45)-(3.46) have to be replaced by the alternative formulation

$$\mathcal{B}_k(w_k, c_k^{n+1}, \Phi^{n+1}, \mathbf{u}^{n+1}) + \mathcal{J}_k(w_k, c_k^{n+1}, \Phi^{n+1}) = \mathcal{F}_k(w_k) \quad (3.52)$$

$$\forall w_k \in \mathcal{T}_{c_k}, k = 1, \dots, m - 1,$$

$$\mathcal{B}_C(\varphi, c_1^{n+1}, \dots, c_{m-1}^{n+1}, \Phi^{n+1}) = 0 \quad \forall \varphi \in \mathcal{T}_\Phi. \quad (3.53)$$

## 3.4 Residual-based variational multiscale finite element method

In this section, the spatial discretization of the weak semi-discrete problem formulation is explained. Throughout this work, the finite element method (FEM) is used as a unique spatial discretization approach to all governing equations. For a general introduction to the FEM, the reader is referred to, e.g., Hughes [100], Brenner and Scott [24], Zienkiewicz and Taylor [185]. Finite element methods for flow problems are addressed by Gresho and Sani [85], Zienkiewicz and Taylor [186] as well as Donea and Huerta [50], for instance. In the subsequent sections, a stabilized finite element formulation for all governing equations is derived from the framework of the so-called Variational Multiscale Method (VMM).

For this purpose, the VMM is introduced in section 3.4.1, and applied to the weak problem formulation. Within the obtained model, so-called resolved-scale and subgrid-scale quantities have to be approximated. The finite element approximation of resolved-scale quantities is outlined in section 3.4.2. Afterwards, two options to account for the unknown subgrid-scale contributions are presented. The standard Galerkin FEM is addressed in 3.4.3, and a residual-based subgrid-scale modeling approach is proposed in 3.4.4. Appropriate stabilization parameters required for the latter method are specified in section 3.4.5. The special case of a binary electrolyte solution is considered in section 3.4.6. Finally, the finite element formulation of the simplified modeling approach involving solely the electric potential field is provided in section 3.4.7.

### 3.4.1 Variational multiscale method

The VMM was originally proposed by Hughes [99] as a general framework for multiscale modeling in computational mechanics; see, e.g., Gravemeier et al. [81] for a categorization of multiscale methods including the VMM. The VMM for Large-Eddy-Simulation (LES) of turbulent flow was reported for the first time by Hughes et al. [101]. For an overview article on the VMM method for laminar and turbulent flow, the reader is referred to Gravemeier [79]. By variational projection, the VMM provides an *a priori* scale separation into (large and small) resolved scales and unresolved (subgrid) scales. An equation for the resolved scales is solved, while the effect of the more universal subgrid scales is modeled.

In this original VMM for LES, which is more elaborately described as a three-level approach, e.g., by Collis [42], Gravemeier [79], the model effect is confined to the small resolved scales, preserving consistency for the large resolved scales. A recent three-level

approach in the form of an algebraic variational multiscale-multigrid method (AVM<sup>3</sup>), using level-transfer operators from plain aggregation algebraic multigrid methods for scale separation, was proposed for turbulent incompressible flow, e.g., by Gravemeier et al. [80] and for turbulent variable-density flow at low Mach number by Gravemeier and Wall [82].

Alternatively, as will be done in this study, a two-level VMM can be used for LES, which is usually referred to as a residual-based VMM; see, e.g., Calo [31], Bazilevs et al. [16] for the residual-based VMM for turbulent incompressible flow and Gravemeier and Wall [83] for the residual-based VMM for turbulent variable-density flow at low Mach number. The residual-based VMM can be considered as a variationally consistent extension of stabilized finite element methods, as presented, for instance, in Hughes et al. [102]. Stabilized finite element methods for flow problems are addressed by, e.g., Braack et al. [23] and Hachem et al. [88].

As stated above, resolved and unresolved scales are separated by a variational projection. The basis for this separation is a direct sum decomposition of each involved trial solution and test function space into a (finite-dimensional) subspace of resolved scales and an (infinite-dimensional) space of subgrid-scale parts of the solution variables:

$$\begin{aligned} \mathcal{S}_u &= \mathcal{S}_u^h \oplus \hat{\mathcal{S}}_u, & \mathcal{T}_u &= \mathcal{T}_u^h \oplus \hat{\mathcal{T}}_u, \\ \mathcal{S}_p &= \mathcal{S}_p^h \oplus \hat{\mathcal{S}}_p, & \mathcal{T}_p &= \mathcal{T}_p^h \oplus \hat{\mathcal{T}}_p, \\ \mathcal{S}_{c_k} &= \mathcal{S}_{c_k}^h \oplus \hat{\mathcal{S}}_{c_k}, & \mathcal{T}_{c_k} &= \mathcal{T}_{c_k}^h \oplus \hat{\mathcal{T}}_{c_k}, & \text{for } k = 1, \dots, m, \\ \mathcal{S}_\Phi &= \mathcal{S}_\Phi^h \oplus \hat{\mathcal{S}}_\Phi, & \mathcal{T}_\Phi &= \mathcal{T}_\Phi^h \oplus \hat{\mathcal{T}}_\Phi. \end{aligned}$$

Consequently, this implies a decomposition of all solution and test functions into a resolved-scale part denoted by  $(.)^h$  and a subgrid-scale part marked with  $(\hat{.})$ :

$$\mathbf{u} = \mathbf{u}^h + \hat{\mathbf{u}}, \quad p = p^h + \hat{p}, \quad c_k = c_k^h + \hat{c}_k, \quad \Phi = \Phi^h + \hat{\Phi}, \quad (3.54)$$

$$\mathbf{v} = \mathbf{v}^h + \hat{\mathbf{v}}, \quad q = q^h + \hat{q}, \quad w_k = w_k^h + \hat{w}_k, \quad \varphi = \varphi^h + \hat{\varphi}. \quad (3.55)$$

Owing to the finite sum decomposition of test function spaces, a coupled system of resolved-scale and subgrid-scale equations arises. For the resolved-scale equations, the test function spaces are restricted to the corresponding resolved-scale subspaces  $\mathcal{T}_k^h, \mathcal{T}_\Phi^h, \mathcal{T}_u^h$  and  $\mathcal{T}_p^h$ . The resolved-scale equations for the multi-ion transport problem are then obtained by introducing (3.54), (3.55) into (3.45)-(3.46) and read

$$\begin{aligned} \mathcal{B}_k(w_k^h, c_k^{h,n+1}, \Phi^{h,n+1}, \mathbf{u}^{h,n+1} + \hat{\mathbf{u}}^{n+1}) + \mathcal{J}_k(w_k^h, c_k^{h,n+1} + \hat{c}_k^{n+1}, \Phi^{h,n+1} + \hat{\Phi}^{n+1}) \\ + (w_k^h, (\mathbf{u}^{h,n+\alpha_f} + \hat{\mathbf{u}}^{n+\alpha_f}) \cdot \nabla \hat{c}_k^{n+\alpha_f}) + D_k(\nabla w_k^h, \nabla \hat{c}_k^{n+\alpha_f}) \\ + z_k \mu_k F(\nabla w_k^h, \hat{c}_k^{n+\alpha_f} \nabla (\Phi^{h,n+\alpha_f} + \hat{\Phi}^{n+\alpha_f}) + c_k^{h,n+\alpha_f} \nabla \hat{\Phi}^{n+\alpha_f}) \\ = \mathcal{F}_k(w_k^h) \quad \forall w_k^h \in \mathcal{T}_k^h, \quad k = 1, \dots, m, \end{aligned} \quad (3.56)$$

$$\mathcal{B}_E(\varphi^h, c_1^{h,n+1} + \hat{c}_1^{n+1}, \dots, c_m^{h,n+1} + \hat{c}_m^{n+1}) = 0 \quad \forall \varphi^h \in \mathcal{T}_\Phi^h. \quad (3.57)$$

Analogously, the resolved-scale equations of the incompressible flow problem as obtained

from (3.47)-(3.48) are given as

$$\begin{aligned} & (\mathbf{v}^h, \dot{\mathbf{u}}^{n+\alpha_m}) + (\mathbf{v}^h, (\mathbf{u}^{h,n+\alpha_f} \cdot \nabla) \mathbf{u}^{h,n+\alpha_f}) - (\nabla \cdot \mathbf{v}^h, p^{h,n+\alpha_f}) + (\boldsymbol{\varepsilon}(\mathbf{v}^h), 2\nu \boldsymbol{\varepsilon}(\mathbf{u}^{h,n+\alpha_f})) \\ & + (\mathbf{v}^h, (\mathbf{u}^{h,n+\alpha_f} \cdot \nabla) \hat{\mathbf{u}}^{n+\alpha_f}) + (\mathbf{v}^h, (\hat{\mathbf{u}}^{n+\alpha_f} \cdot \nabla) \mathbf{u}^{h,n+\alpha_f}) + (\mathbf{v}^h, (\hat{\mathbf{u}}^{n+\alpha_f} \cdot \nabla) \hat{\mathbf{u}}^{n+\alpha_f}) \\ & - (\nabla \cdot \mathbf{v}^h, \hat{p}^{n+\alpha_f}) + (\boldsymbol{\varepsilon}(\mathbf{v}^h), 2\nu \boldsymbol{\varepsilon}(\hat{\mathbf{u}}^{n+\alpha_f})) = (\mathbf{v}^h, \mathbf{b}^{h,n+\alpha_f}) + (\mathbf{v}^h, \mathbf{t}^{h,n+\alpha_f})_{\Gamma_N^u} \quad \forall \mathbf{v}^h \in \mathcal{T}_u^h, \end{aligned} \quad (3.58)$$

$$(\mathbf{q}^h, \nabla \cdot \mathbf{u}^{h,n+\alpha_f}) + (\mathbf{q}^h, \nabla \cdot \hat{\mathbf{u}}^{n+\alpha_f}) = 0 \quad \forall \mathbf{q}^h \in \mathcal{T}_p^h. \quad (3.59)$$

In (3.56) and (3.58), potential time derivatives of subgrid-scale concentrations and subgrid-scale velocity are neglected. This corresponds to a “quasi-static” modeling approach of subgrid-scale quantities. Further remarks on this assumption will be given below.

In case of the CNP system of equations, only the ion-transport equations (3.56) for  $k = 1, \dots, m-1$  have to be considered. In addition, (3.57) has to be replaced by

$$\mathcal{B}_C(\varphi^h, c_1^{h,n+1} + \hat{c}_k^{n+1}, \dots, c_{m-1}^{h,n+1} + \hat{c}_{m-1}^{n+1}, \Phi^{h,n+1} + \hat{\Phi}^{n+1}) = 0 \quad \forall \varphi^h \in \mathcal{T}_\Phi^h. \quad (3.60)$$

The resolved-scale equations (3.56)-(3.59) are solved for the resolved-scale quantities  $c_k^{h,n+1}$ ,  $\Phi^{h,n+1}$ ,  $\mathbf{u}^{h,n+1}$  and  $p^{h,n+1}$ , which represent the discrete approximations to the unknown solution fields. For this purpose, the unknown subgrid-scale contributions present in the resolved-scale equation system have to be modeled in an appropriate way. Two different approaches for subgrid-scale closures are presented and discussed in the sections 3.4.3 and 3.4.4. For the resolved-scale quantities, a finite element approximation is utilized as described in the following section 3.4.2.

### 3.4.2 Finite element approximation of resolved-scale quantities

The computational domain  $\Omega$  is discretized into  $n_{el}$  non-overlapping finite elements denoted by  $\Omega_e$ . Thus, it holds

$$\bar{\Omega} \approx \bigcup_{e=1}^{n_{el}} \bar{\Omega}_e \quad \text{with } \Omega_e \cap \Omega_f = \emptyset \quad \forall e \neq f. \quad (3.61)$$

By using a nodal basis  $\{N_a^h, a = 1, \dots, n_{\text{nod}}\}$ , where  $N_a^h$  denotes the shape function associated to node  $a$ , the finite-element approximation  $c_k^{h,n+1} \in \mathcal{S}_{c_k}^h$  to the concentration  $c_k^{n+1} \in \mathcal{S}_{c_k}$  reads

$$c_k^{h,n+1}(\mathbf{x}) = \sum_{a=1}^{n_{\text{nod}}} N_a^h(\mathbf{x}) \bar{c}_{k,a}^{n+1}. \quad (3.62)$$

Here,  $\bar{c}_{k,a}^{n+1}$  denotes the unknown concentration value of ionic species  $k$  at node  $a$  for the discrete time  $t^{n+1}$ . The latter are arranged in the nodal solution vector  $\mathbf{c}_k^{n+1}$ . The same shape functions are also used to express  $\Phi^{h,n+1}$ ,  $\mathbf{u}^{h,n+1}$  and  $p^{h,n+1}$  in terms of basis functions and nodal unknowns in the form

$$\Phi^{h,n+1}(\mathbf{x}) = \sum_{a=1}^{n_{\text{nod}}} N_a^h(\mathbf{x}) \bar{\Phi}_a^{n+1}, \quad \mathbf{u}(\mathbf{x}) = \sum_{a=1}^{n_{\text{nod}}} N_a^h(\mathbf{x}) \bar{\mathbf{u}}_a^{n+1}, \quad p(\mathbf{x}) = \sum_{a=1}^{n_{\text{nod}}} N_a^h(\mathbf{x}) \bar{p}_a^{n+1}. \quad (3.63)$$

The corresponding solution vectors are denoted by  $\Phi^{n+1}$ ,  $\mathbf{u}^{n+1}$  and  $\mathbf{p}^{n+1}$ , respectively. As obvious from (3.62)-(3.63), identical spatial discretizations for all unknown fields are used within the present computational approach. In this work, the isoparametric concept is utilized, where the same ansatz functions are used for the spatial representation and the approximation of the unknown fields.

For the “classical” FEM, piecewise polynomial approximations of the resolved-scale quantities are constructed (see, e.g., Hughes [100]). In the present implementation of the computational approach, (bi-,tri-)linear and (bi-,tri-)quadratic shape functions can be used. This classical choice of basis functions is used for most cases studied here and yields a piecewise polynomial representation of each unknown physical field.

One alternative approach is a so-called isogeometric discretization. The spatial discretization in isogeometric approaches is also based on the isoparametric concept. The shape functions used for representing both the geometry and the solution are rational functions of weighted B-spline basis polynomials. For a given degree, these B-spline basis polynomials are defined recursively by the values of a knot vector. The latter allows for controlling the support of the basis polynomials as well as the level of smoothness and interpolation properties of the arising B-splines and NURBS (non-uniform rational B-splines). The weights required in the definition of the NURBS basis are defined by control points, which also contain coordinate information for one point per basis function to complete the geometry definition. NURBS can be refined by knot insertion and degree elevation without a change in geometry. A more thorough definition of these terms can be found, e.g., in Farin [62], Piegl and Tiller [142]. A detailed description of isogeometric concepts in the context of large-eddy simulation of turbulent incompressible flow is provided by Gamnitzer [69].

Advantages of an isogeometric discretization in the present context are that curved boundaries can be represented exactly and the variation-diminishing property of NURBS is beneficial for a proper resolution of turbulent boundary layers. The latter is especially useful in the context of electrochemistry, where very thin ionic concentration boundary layers have to be considered due to the high Schmidt numbers associated with ion-transport problems (cf. section 2.8.5).

It is noted that also other methods have been developed that are able to represent a curved geometry exactly. For example, the NURBS-enhanced finite element method proposed by Sevilla et al. [158, 159] combines a NURBS approach for an exact boundary representation with the effectiveness of classical FEM used in the interior of the computational domain.

### 3.4.3 Standard Galerkin finite element method

Completely neglecting any contributions due to unresolved scales in (3.56)-(3.59) results in a Bubnov-Galerkin approach, denoted as Standard Galerkin Finite Element Method (SGFEM) in the following. This is certainly the simplest approach to account for the unknown subgrid-scale contributions.

The SGFEM for the multi-ion transport equations coupled via electroneutrality was elaborated on in Bauer et al. [11] and used there in combination with a stabilized finite element flow solver. In this work, it is accounted for both options of possible closing equations for the electric potential, i.e., the ENP and CNP system of equations. Thus, the SGFEM formulation of (3.56)-(3.57) reads: for each discrete time level  $t^{n+1}$ , find

$c_1^{h,n+1} \in \mathcal{S}_{c_1}^h, \dots, c_m^{h,n+1} \in \mathcal{S}_{c_m}^h$  and  $\Phi^{h,n+1} \in \mathcal{S}_\Phi^h$ , such that for all  $w_k^h \in \mathcal{T}_k^h, \varphi^h \in \mathcal{T}_\Phi^h$

$$\mathcal{B}_k(w_k^h, c_k^{h,n+1}, \Phi^{h,n+1}, \mathbf{u}^{h,n+1}) + \mathcal{J}_k(w_k^h, c_k^{h,n+1}, \Phi^{h,n+1}) = \mathcal{F}_k(w_k^h) \quad k = 1, \dots, m, \quad (3.64)$$

$$\mathcal{B}_E(\varphi^h, c_1^{h,n+1}, \dots, c_m^{h,n+1}) = 0. \quad (3.65)$$

Here, the resolved-scale velocity field  $\mathbf{u}^{h,n+1}$  is supposed to be given, e.g., as a result of the flow computation. In case of the CNP system of equations, the corresponding SGFEM formulation reads

$$\mathcal{B}_k(w_k^h, c_k^{h,n+1}, \Phi^{h,n+1}, \mathbf{u}^{h,n+1}) + \mathcal{J}_k(w_k^h, c_k^{h,n+1}, \Phi^{h,n+1}) = \mathcal{F}_k(w_k^h) \quad k = 1, \dots, m-1, \quad (3.66)$$

$$\mathcal{B}_C(\varphi^h, c_1^{h,n+1}, \dots, c_{m-1}^{h,n+1}, \Phi^{h,n+1}) = 0. \quad (3.67)$$

It is well-known that the SGFEM is potentially unstable for convection-diffusion-reaction problems when convection dominates. Such instabilities might be avoided by using (very) fine spatial resolutions, as done by Bauer et al. [11], for instance. However, such a strategy will usually become prohibitively expensive in terms of computational costs for most examples. Since kinematic diffusion constants of ionic species are typically very small  $O(10^{-9}\text{m}^2/\text{s})$  compared to usual kinematic viscosity values  $O(10^{-6}\text{m}^2/\text{s})$ , extremely fine meshes are required in regions where concentration gradients occur. As an alternative to (very often unfeasible) mesh refinement, a strategy for modeling the subgrid scales is proposed in the subsequent section 3.4.4.

For the incompressible flow problem, the numerical difficulties caused by local convection dominance arise, too. As a result, spurious “wiggles” might be observed in a computed velocity field (see, e.g., Wall [174]). Besides, it is well-known that equal-order interpolation of velocity and pressure fields is unstable. The reason is the violation of the so-called Ladyzhenskaya-Babuška-Brezzi (LBB) condition (cf. Brenner and Scott [24], Gresho and Sani [85]), which reads in the “inf-sup” form

$$\inf_{0 \neq q^h \in \mathcal{T}_p^h} \sup_{\mathbf{0} \neq \mathbf{v}^h \in \mathcal{T}_u^h} \frac{|\langle \nabla \cdot \mathbf{v}^h, q^h \rangle_\Omega|}{\|\mathbf{v}^h\|_{H^1(\Omega)} \cdot \|q^h\|_{L^2(\Omega)}} \geq c > 0, \quad (3.68)$$

where  $c \in \mathbb{R}^+$  denotes a positive constant. When (3.68) is violated by a chosen set of function spaces for velocity and pressure, spurious pressure oscillations (pressure modes) are observed in the numerical solution. Thus, the SGFEM is especially problematic for the flow subproblem, since equal-order discretizations for velocity and pressure are used here as introduced in (3.63). As a remedy, either the function spaces for pressure and velocity have to be chosen in such a way that the LBB condition is fulfilled, or, as performed here, additional pressure stabilization terms have to be added to the problem formulation in order to circumvent the LBB condition. Such stabilization techniques can be derived on the basis of the VMM as performed in the following.

### 3.4.4 Residual-based subgrid-scale modeling

In residual-based variational multiscale approaches, the subgrid-scale parts of the solution fields are typically modeled using an elementwise, algebraic approximation, which is

based on the residual of the strong form of the resolved-scale equations. For a detailed description of residual-based multiscale approximations leading to stabilized methods, the reader is referred to, e.g., Hughes et al. [102].

In each element  $\Omega_e$ , the subgrid-scale parts introduced in (3.54) are modeled as

$$\hat{\mathbf{u}} = -\tau_M \mathcal{R}_M^h, \quad \hat{p} = -\tau_C \mathcal{R}_C^h, \quad \hat{c}_k = -\tau_k \mathcal{R}_k^h, \quad \hat{\Phi} = -\tau_E \mathcal{R}_E^h, \quad (3.69)$$

using respective stabilization parameters  $\tau$ , which will be defined below. In case of the ENP model, which is in the focus of this work, the corresponding discrete residuals of fluid momentum conservation, fluid mass conservation (continuity equation), ionic mass conservation and electroneutrality condition are given as

$$\mathcal{R}_M^h = \dot{\mathbf{u}}^{h,n+\alpha_m} + (\mathbf{u}^{h,n+\alpha_f} \cdot \nabla) \mathbf{u}^{h,n+\alpha_f} - 2\nu \nabla \cdot \boldsymbol{\varepsilon}(\mathbf{u}^{h,n+\alpha_f}) + \nabla p^{h,n+\alpha_f} - \mathbf{b}^{h,n+\alpha_f}, \quad (3.70)$$

$$\mathcal{R}_C^h = \nabla \cdot \mathbf{u}^{h,n+\alpha_f}, \quad (3.71)$$

$$\mathcal{R}_k^h = \dot{c}_k^{n+\alpha_m} + \mathbf{u}^{h,n+\alpha_f} \cdot \nabla c_k^{h,n+\alpha_f} - \nabla \cdot (z_k \mu_k F c_k^{h,n+\alpha_f} \nabla \Phi^{h,n+\alpha_f}) - \nabla \cdot (D_k \nabla c_k^{h,n+\alpha_f}), \quad (3.72)$$

$$\mathcal{R}_E^h = \sum_{k=1}^m z_k c_k^{h,n+\alpha_f}. \quad (3.73)$$

Formally, consistency of the method for  $h \rightarrow 0$  is ensured, since residual-based subgrid-scale modeling as given in (3.69) is used, and residuals obviously vanish in this limiting case. The complete variational multiscale finite element formulation is obtained by introducing the subgrid-scale approximations (3.69) into the resolved-scale equations (3.56)-(3.59). Owing to the consideration of subgrid-scale contributions on each element interior  $\Omega_e$ , a sum over all elements is introduced. In order to circumvent the presence of unknown gradients of subgrid-scale quantities, integration by parts is applied to the element-specific terms, where needed. For this procedure, the usual assumption of vanishing subgrid contributions at element boundaries is used. Thus, no terms with respect to the element boundaries  $\partial\Omega_e$  appear in the final formulation.

The complete residual-based variational multiscale formulation, which is obtained as a result, reads in case of the ENP system of equations: find  $c_1^{h,n+1} \in \mathcal{S}_{c_1}^h, \dots, c_m^{h,n+1} \in \mathcal{S}_{c_m}^h, \Phi^{h,n+1} \in \mathcal{S}_\Phi^h, \mathbf{u}^{h,n+1} \in \mathcal{S}_u^h$  and  $p^{h,n+1} \in \mathcal{S}_p^h$ , such that

$$\begin{aligned} & \mathcal{B}_k(w_k^h, c_k^{h,n+1}, \Phi^{h,n+1}, \mathbf{u}^{h,n+1}) + \mathcal{J}_k(w_k^h, c_k^{h,n+1} - \tau_k^{n+\alpha_f} \mathcal{R}_k^h, \Phi^{h,n+1} - \tau_E \mathcal{R}_E^h) \\ & - \sum_{e=1}^{n_{el}} (w_k^h \tau_M^{n+\alpha_f} \mathcal{R}_M^h, \nabla c_k^{h,n+\alpha_f})_{\Omega_e} + \sum_{e=1}^{n_{el}} ((\mathbf{u}^{h,n+\alpha_f} - z_k \mu_k F \nabla \Phi^{h,n+\alpha_f}) \cdot \nabla w_k^h, \tau_k^{n+\alpha_f} \mathcal{R}_k^h)_{\Omega_e} \\ & - \sum_{e=1}^{n_{el}} (\tau_M^{n+\alpha_f} \mathcal{R}_M^h \cdot \nabla w_k^h, \tau_k^{n+\alpha_f} \mathcal{R}_k^h)_{\Omega_e} - \sum_{e=1}^{n_{el}} (z_k \mu_k F (c_k^{h,n+\alpha_f} - \tau_k^{n+\alpha_f} \mathcal{R}_k^h) \nabla w_k^h, \nabla (\tau_E^{n+\alpha_f} \mathcal{R}_E^h))_{\Omega_e} \\ & + \sum_{e=1}^{n_{el}} (D_k \Delta w_k^h, \tau_k^{n+\alpha_f} \mathcal{R}_k^h)_{\Omega_e} = \mathcal{F}_k(w_k^h) \quad \forall w_k^h \in \mathcal{T}_{c_k}^h, k = 1, \dots, m, \end{aligned} \quad (3.74)$$

$$\mathcal{B}_E(\varphi^h, c_1^{h,n+1}, \dots, c_m^{h,n+1}) - \sum_{e=1}^{n_{el}} \left( \varphi^h, \sum_{k=1}^m \tau_k^{n+\alpha_f} \mathcal{R}_k^h \right)_{\Omega_e} = 0 \quad \forall \varphi^h \in \mathcal{T}_\phi^h. \quad (3.75)$$

together with

$$\begin{aligned}
& (\mathbf{v}^h, \hat{\mathbf{u}}^{n+\alpha_m}) + (\mathbf{v}^h, (\mathbf{u}^{h,n+\alpha_f} \cdot \nabla) \mathbf{u}^{h,n+\alpha_f}) - (\nabla \cdot \mathbf{v}^h, p^{h,n+\alpha_f}) + (\boldsymbol{\varepsilon}(\mathbf{v}^h), 2\nu \boldsymbol{\varepsilon}(\mathbf{u}^{h,n+\alpha_f})) \\
& + \sum_{e=1}^{n_{el}} ((\mathbf{u}^{h,n+\alpha_f} \cdot \nabla) \mathbf{v}^h, \tau_M^{n+\alpha_f} \mathcal{R}_M^h)_{\Omega_e} + \sum_{e=1}^{n_{el}} (\nabla \cdot \mathbf{v}^h, \tau_C^{n+\alpha_f} \mathcal{R}_C^h)_{\Omega_e} \\
& - \sum_{e=1}^{n_{el}} (\mathbf{v}^h, (\tau_M^{n+\alpha_f} \mathcal{R}_M^h \cdot \nabla) \mathbf{u}^{h,n+\alpha_f})_{\Omega_e} - \sum_{e=1}^{n_{el}} ((\tau_M^{n+\alpha_f} \mathcal{R}_M^h \cdot \nabla) \mathbf{v}^h, \tau_M^{n+\alpha_f} \mathcal{R}_M^h)_{\Omega_e} \\
& = (\mathbf{v}^h, \mathbf{b}^{h,n+\alpha_f}) + (\mathbf{v}^h, \mathbf{t}^{h,n+\alpha_f})_{\Gamma_N^u} \quad \forall \mathbf{v}^h \in \mathcal{T}_{\mathbf{u}}^h,
\end{aligned} \tag{3.76}$$

$$(q^h, \nabla \cdot \mathbf{u}^{h,n+\alpha_f}) + \sum_{e=1}^{n_{el}} (\nabla q^h, \tau_M^{n+\alpha_f} \mathcal{R}_M^h)_{\Omega_e} = 0 \quad \forall q^h \in \mathcal{T}_p^h. \tag{3.77}$$

The first line in (3.76) constitutes the standard Galerkin part of the equation, followed by a Streamline-Upwind Petrov-Galerkin (SUPG) term,  $((\mathbf{u}^h \cdot \nabla) \mathbf{v}^h, \tau_M \mathcal{R}_M^h)_{\Omega_e}$  as proposed by Brooks and Hughes [26], a grad-div (or bulk viscosity) term,  $(\nabla \cdot \mathbf{v}^h, \tau_C \mathcal{R}_C^h)_{\Omega_e}$  as addressed, e.g., by De Mulder [47], and cross- and Reynolds-stress stabilization terms in the third line, respectively. If not stated otherwise, the latter two stabilization terms are neglected in the numerical examples studied in this work. The stabilization term introduced into the continuity equation (3.77) is a Pressure-Stabilizing Petrov-Galerkin (PSPG) term,  $(\nabla q^h, \tau_M \mathcal{R}_M^h)_{\Omega_e}$ , as proposed, e.g., by Tezduyar [166]. The PSPG term is utilized here to circumvent the LBB condition and allows for the use of equal-order discretizations for velocity and pressure such as considered here.

The electrochemical part (3.74)-(3.75) of the complete variational multiscale formulation is further simplified according to the following five steps:

1. Based on the usual assumption of vanishing subgrid contributions at element boundaries, potential subgrid-scale contributions are also zero along the discretized domain boundary  $\partial\Omega$ . As a consequence, subgrid-scale contributions to (nonlinear) electrode kinetics boundary conditions are neglected. Thus, only the term  $\mathcal{J}_k(w_k^h, c_k^h, \Phi^h)$  based on resolved scales is considered in the following.
2. Neglecting subgrid-scale velocity contributions  $\hat{\mathbf{u}} = -\tau_M \mathcal{R}_M^h$  in (3.74) leads to a rather “standard” stabilized formulation. The consideration of the subgrid-scale velocity represents a potential extension of the computational approach. However, the inclusion of the subgrid-scale part of the velocity has not turned out to provide relevant improvement to the results in other investigations, e.g., for turbulent variable-density flow at low Mach number as presented by Gravemeier and Wall [82]. Hence, it is refrained from taking it into account, for the time being.
3. As usually done, subgrid-scale terms arising from transient and diffusive terms will be neglected. As already stated above, the first assumption yields a so-called “quasi-static” subgrid-scale approximation (see Codina et al. [41] for the original idea of including time-dependent subgrid scales and Gamnitzer et al. [70] for comparative evaluations of time-dependent and quasi-static subgrid-scale approximations in the context of turbulent channel flow). The diffusive terms are anyway insignificant

when linearly-interpolated elements are used. For higher-order discretizations using at least quadratic ansatz functions, the effect of these terms might be investigated in the future.

4. Applying the product rule to the migration term reveals a convective and reactive effect of the migration operator:

$$\nabla \cdot (-z_k \mu_k F c_k \nabla \Phi) = \mathbf{u}_{\text{mig},k} \cdot \nabla c_k + \sigma_{\text{mig},k} c_k,$$

with a “migration velocity”  $\mathbf{u}_{\text{mig},k} := -z_k \mu_k F \nabla \Phi$  and a reaction parameter  $\sigma_{\text{mig},k} := -z_k \mu_k F \Delta \Phi$ , both depending on  $\Phi$ . Thus, for a known or prescribed electric potential, each ion-transport equation (2.12) may be interpreted as a convection-diffusion-reaction equation for  $c_k$ :

$$\frac{\partial c_k}{\partial t} + \mathbf{v}_k \cdot \nabla c_k - D_k \Delta c_k + \sigma_{\text{mig},k} c_k = 0, \quad (3.78)$$

with

$$\mathbf{v}_k := \mathbf{u} + \mathbf{u}_{\text{mig},k} = \mathbf{u} - z_k \mu_k F \nabla \Phi. \quad (3.79)$$

The analogous definition for the discretized form reads

$$\mathbf{v}_k^h := \mathbf{u}^h + \mathbf{u}_{\text{mig},k}^h = \mathbf{u}^h - z_k \mu_k F \nabla \Phi^h, \quad (3.80)$$

with  $\mathbf{u}_{\text{mig},k}^h := -z_k \mu_k F \nabla \Phi^h$  and  $\sigma_{\text{mig},k}^h := -z_k \mu_k F \Delta \Phi^h$ . Note that  $\sigma_{\text{mig},k}^h$  can only be represented when higher-order (i.e., at least quadratic) shape functions are used.

5. As an assumption, electroneutrality is already enforced for the resolved-scale concentration fields, such that  $\mathcal{R}_E^h = 0$ , consequently. Owing to (3.69), subgrid-scale contributions to the electric potential field are zero, i.e.,  $\hat{\Phi} = 0$  is assumed throughout this work. The case of non-vanishing subgrid-scale contributions to electroneutrality is certainly an interesting aspect, which deserves a more detailed analysis in a future study.

In summary, the final stabilized finite element formulation for the coupled ion-transport subproblem reads:

$$\begin{aligned} & \mathcal{B}_k(w_k^h, c_k^{h,n+1}, \Phi^{h,n+1}, \mathbf{u}^{h,n+1}) + \mathcal{J}_k(w_k^h, c_k^{h,n+1}, \Phi^{h,n+1}) \\ & + \sum_{e=1}^{n_{\text{el}}} (\mathbf{v}_k^{h,\alpha} \cdot \nabla w_k^h, \tau_k^{h,\alpha} \mathcal{R}_E^h)_{\Omega_e} = \mathcal{F}_k(w_k^h) \quad \forall w_k^h \in \mathcal{T}_{c_k}^h, k = 1, \dots, m, \end{aligned} \quad (3.81)$$

$$\mathcal{B}_E(\varphi^h, c_1^{h,n+1}, \dots, c_m^{h,n+1}) = 0 \quad \forall \varphi^h \in \mathcal{T}_\phi^h. \quad (3.82)$$

As done in Bauer et al. [12], only the convective subgrid-scale terms are considered in the present formulation (3.81)-(3.82). The stabilization term in (3.81) accounts for convection due to fluid flow and migration.

For completeness, a stabilized finite element formulation is also provided for the CNP system of equations. Since the following formulation was implemented quite recently, the thorough numerical investigation regarding the CNP model is still an ongoing task.

However, in the opinion of the author, the CNP forms a promising alternative to the ENP model that is in the focus of this work. Here, it is suggested to replace (3.81)-(3.82) by

$$\begin{aligned} & \mathcal{B}_k(w_k^h, c_k^{h,n+1}, \Phi^{h,n+1}, \mathbf{u}^{h,n+1}) + \mathcal{J}_k(w_k^h, c_k^{h,n+1}, \Phi^{h,n+1}) \\ & + \sum_{e=1}^{n_{\text{el}}} (\mathbf{v}_k^{h,n+\alpha_f} \cdot \nabla w_k^h, \tau_k^{n+\alpha_f} \mathcal{R}_k^h)_{\Omega_e} = \mathcal{F}_k(w_k^h) \quad \forall w_k^h \in \mathcal{T}_{c_k}^h, k = 1, \dots, m-1, \end{aligned} \quad (3.83)$$

$$\mathcal{B}_C(\varphi^h, c_1^{h,n+1}, \dots, c_{m-1}^{h,n+1}, \Phi^{h,n+1}) = 0 \quad \forall \varphi^h \in \mathcal{T}_\phi^h. \quad (3.84)$$

In order to be consistent with the treatment of the ENP system of equations presented above,  $\mathcal{R}_E^h = 0$  is assumed also here. Additionally, this assumption is in accordance with equation (2.24), which is used to compute the eliminated ionic concentration  $c_m$ . Thus, potential subgrid-scale contributions to the electric potential field are neglected in (3.83)-(3.84). Furthermore, no subgrid-scale concentrations are considered within (3.84) at the moment. Since the CNP model was developed quite recently, and is therefore still under development, the formulation presented above has to be understood as a first suggestion. The proposed stabilized finite element formulation (3.83)-(3.84) is consistent with the ENP case, but certainly deserves further investigation in the near future.

#### 3.4.5 Stabilization parameters

The stabilization parameters as originally proposed by Taylor et al. [164] and Whiting and Jansen [178] are used within the flow solver. Thus, the definitions

$$\tau_M = \frac{1}{\sqrt{\left(\frac{2}{\Delta t}\right)^2 + \mathbf{u}^h \cdot \mathbf{G} \mathbf{u}^h + C \nu^2 \mathbf{G} : \mathbf{G}}}, \quad (3.85)$$

and

$$\tau_C = \frac{1}{\tau_M \operatorname{tr} \mathbf{G}}. \quad (3.86)$$

are used. Here,  $\mathbf{G}$  is the second-rank metric tensor, given as

$$\mathbf{G} = \left( \frac{\partial \xi}{\partial \mathbf{x}} \right)^T \frac{\partial \xi}{\partial \mathbf{x}}, \quad (3.87)$$

which is defined based on the inverse Jacobian  $\partial \xi / \partial \mathbf{x}$  of the element mapping between the reference (unit) element and the physical domain; see, e.g., Hughes [100] for elaboration. The coordinate system of the reference element is denoted by  $\xi$ . In (3.85), the time-step length of the temporal discretization of the problem formulation is denoted by  $\Delta t$ , and  $C$  is a positive constant independent of the characteristic element length. For those numerical examples of this study, for which linearly-interpolated finite elements are used, this constant is chosen to be  $C = 36$ . For quadratic polynomials a value of  $C = 144$  is used in accordance to Gamnitzer [69]. Of course, a broad variety of other stabilization parameter definitions is found in literature. For an overview of different stabilization techniques and corresponding parameter definitions the interested reader is referred to, e.g., Wall [174],

Förster [65] and Gamnitzer [69].

For the present problem formulation including convection due to fluid flow as well as migration, the stabilization parameter (3.85) is adopted as proposed by Bauer et al. [12] reading

$$\tau_k = \frac{1}{\sqrt{\left(\frac{2}{\Delta t} + |\sigma_{\text{mig},k}^h|\right)^2 + \mathbf{v}_k^h \cdot \mathbf{G} \mathbf{v}_k^h + CD_k^2 \mathbf{G} : \mathbf{G}}}, \quad (3.88)$$

with  $\mathbf{v}_k^h$  as defined in (3.80). Here, the reactive contribution  $\sigma_{\text{mig},k}^h = -z_k \mu_k F \Delta \Phi^h$  is included in accordance to Hauke [92], Gravemeier and Wall [84]. The value for the constant  $C$  in (3.88) is chosen as explained above.

An alternative closure taking into account the temporal variation of the unresolved scales was proposed by Codina et al. [41] and later studied for turbulent incompressible flow by Gamnitzer et al. [70]. The results of that study indicated, however, that the closure by quasi-static subgrid scales as given in (3.69) appears to be sufficient for the type of problems considered in this paper.

Since modeling of semiconductor devices involves similar governing equations for the transport of charge-carriers as discussed here, the reader is also referred to Lin et al. [125], Hennigan et al. [95] for a stabilized finite element formulation used for such applications.

### 3.4.6 Special case: binary electrolyte solutions

Additional analytical results exist for the most simple case of a binary electrolyte ( $m = 2$ ). It is worth considering these for the construction of stabilization terms. Solutions for both concentration fields  $c_1$  and  $c_2$  of a binary electrolyte system coupled by electroneutrality are also fulfilling the same linear convection-diffusion equation given as

$$\frac{\partial c_{\{1,2\}}}{\partial t} + \mathbf{u} \cdot \nabla c_{\{1,2\}} - D \Delta c_{\{1,2\}} = 0 \quad \text{in } \Omega \times (0, T_e). \quad (3.89)$$

Here, the effective diffusion coefficient for the binary electrolyte is defined as

$$D := \frac{z_1 \mu_1 D_2 - z_2 \mu_2 D_1}{z_1 \mu_1 - z_2 \mu_2}. \quad (3.90)$$

It is emphasized that  $D$  non-trivially depends on the material parameters of *both* ionic species. Details on the derivation of (3.89) are provided in Appendix A. Further details are also given in Bauer et al. [11], Newman and Thomas-Alyea [137], for example.

The following conclusions can be drawn from (3.89)-(3.90). For a binary electrolyte solution, migration causes a change in the diffusion behavior of both ionic species, but does not contribute to the convective term. Thus, oscillations can not occur when diffusion and migration are the only transport effects, since migration contributes to the diffusion term. Convection is caused by the fluid velocity field only. This behavior is indeed also observed in numerical simulations. Consequently, in such a case, a stabilization with respect to the migration velocity  $\mathbf{u}_{\text{mig},k}$  is *not* necessary.

Based on this observation, the convective stabilization term in the second row of (3.81) should consider the fluid velocity field only. Consequently, the effective diffusion coefficient  $D$  defined in (3.90) instead of  $D_k$  has to be used in the stabilization parameter

definitions for correctly reflecting the migration effect. Additionally, no migration velocity or migration-reaction parameter has to be accounted for. Thus, for a binary electrolyte, it holds  $\tau_1 = \tau_2$ , which reflects the fact that the actual movement of both species is not independent, but subject to the electroneutrality constraint. As a summary of these consequences, in case of a binary electrolyte solution, it is suggested to replace (3.81) for the two ionic species  $k = 1, 2$  by

$$\begin{aligned} & \mathcal{B}_k(w_k^h, c_k^{h,n+1}, \Phi^{h,n+1}, \mathbf{u}^{h,n+1}) + \mathcal{J}_k(w_k^h, c_k^{h,n+1}, \Phi^{h,n+1}) \\ & + \sum_{e=1}^{n_{\text{el}}} (\mathbf{u}^{h,n+\alpha_f} \cdot \nabla w_k^{h,n+\alpha_f}, \tau_k^{n+\alpha_f} \mathcal{R}_k^h)_{\Omega_e} = \mathcal{F}_k(w_k^h) \quad \forall w_k^h \in \mathcal{T}_{c_k}, \quad k = 1, \dots, m, \end{aligned} \quad (3.91)$$

and (3.88) by

$$\tau_1 = \tau_2 = \frac{1}{\sqrt{\left(\frac{2}{\Delta t}\right)^2 + \mathbf{u}^h \cdot \mathbf{G} \mathbf{u}^h + CD^2 \mathbf{G} : \mathbf{G}}}. \quad (3.92)$$

Thus, only the stabilization terms are adapted, leaving the SGFEM part unchanged. For binary electrolyte solutions, the use of the effective diffusion coefficient  $D$  defined in (3.90) is one of the keys for improved stabilization parameter design. It is emphasized that in (3.92) basically any other stabilization parameter definition developed for conventional convection-diffusion equations can be used as long as the effective diffusion coefficient  $D$  is used for computing both  $\tau_1$  and  $\tau_2$ . For an overview of other stabilization parameter definitions the reader is referred to Donea and Huerta [50], for instance. The corresponding modification of the CNP system of equations is straight-forward and follows directly from (3.91). Thus, it is not explicitly shown here.

It is well-known that the element Peclet number serves as an indicator for estimating local convection dominance. Another consequence from the considerations above is that the element Peclet number for *both* ionic species is identical for  $k = 1$  and  $k = 2$  and reads

$$\text{Pe}_e^k = \frac{h \|\mathbf{u}\|_2}{2D}, \quad (3.93)$$

with  $h$  denoting a characteristic element length. This is a clear contrast to the interpretation

$$\text{Pe}_e^k = \frac{h \|\mathbf{u} + \mathbf{u}_{\text{mig},k}\|_2}{2D_k}, \quad k = 1, 2,$$

that might have been concluded from (3.78). Based on the interpretation given in (3.78) the migration velocity  $\mathbf{u}_{\text{mig},k}^h$  should be included as a potential convective effect of migration into the stabilization term. This approach is perfectly correct for any externally prescribed potential field  $\Phi$  that is *not* depending on the solution variables  $c_k$ . However, this is not the case in the present context, since  $\Phi$  is an additional unknown field which couples all ion-transport equations due to the migration term. As seen above, an isolated consideration of each transport equation as implied by (3.78) is not always admissible, and the coupled problem has to be considered as a whole.

For all cases with  $m > 2$ , no analytical relationship is known that can be used as for the binary case above. For these problem classes, the general formulations introduced in the

preceding sections are used for the time being.

### 3.4.7 Simplified model for the electric potential

For completeness, the finite element discretization of the simplified model presented in section 2.6 is briefly summarized here. For the elliptic problem (2.53) the SGFEM provides an already sufficient discretization approach. Since the Laplace equation (2.53) is addressed in nearly every textbook on finite element methods, details can be neglected here. Thus, the reader is referred to, e.g., Hughes [100], Zienkiewicz and Taylor [185]. The discrete finite element formulation of (2.53) reads

$$\left( \nabla \varphi^h, \sigma \nabla \Phi^h \right)_\Omega - \left( \varphi^h, i_n(\Phi^h) \right)_{\Gamma_E^\Phi} = \left( \varphi^h, h_\Phi \right)_{\Gamma_N^\Phi} \quad \varphi^h \in T_\Phi^h, \quad (3.94)$$

where the boundary conditions (2.56)-(2.57) have been inserted into the weak form. When modeling a secondary current distribution at electrode surfaces, it holds  $i_n(\Phi^h) \neq 0$  and the problem formulation (3.94) is in general nonlinear due to the electrode kinetics boundary condition (2.57). When addressing the primary current density distribution, the influence of electrode kinetics is neglected. As a result, a simple linear problem has to be solved for  $\Phi^h$ .

## 3.5 Solution procedure

This section is devoted to the numerical solution procedure, which is applied to the fully-discretized problem formulation derived above. Different algorithmic aspects are addressed in the following. The numerical treatment of the coupling of flow and electrochemistry subproblems is explained in section 3.5.1. In section 3.5.2, required extensions for current-controlled (galvanostatic) electrochemical problems are presented. Afterwards, the numerical solution approach for nonlinear equation systems is explained in 3.5.3. Appropriate solution methods for the arising linear equation systems are presented in section 3.5.4. Finally, several important remarks on the postprocessing of simulation results are given in section 3.5.5.

### 3.5.1 Coupling of flow and electrochemistry subproblems

If convection has to be accounted for, an appropriate treatment of the coupling of fluid flow and multi-ion transport is required. In general, a two-way-coupled problem has to be solved. On the one hand, multi-ion transport is influenced by the flow field due to convection. On the other hand, the flow solution depends on the local bath composition, since material properties such as the density and the viscosity of an electrolyte solution typically depend on the local ion concentrations. Variations of the ionic concentrations primarily occur close to the electrode surfaces as a result of electrochemical reactions. Arising buoyancy forces due to the induced density variations cause natural convection phenomena in electrochemical cells. In the following, only the more important case of a concentration-dependent density is considered. Local variations of the viscosity can be accounted for in the same manner as presented below for the case of natural convection.

For electrochemical problems with natural convection, a two-way-coupled partitioned scheme is proposed in this study. A sketch of the coupling algorithm is provided in Fig. 3.1(a). The discrete forms of the fluid and ion-transport subproblems are solved separately from each other representing the inner iteration loops. Within an outer iteration loop, required data, such as velocity and density values are exchanged. As presented above, matching discretizations for both the fluid and the electrochemical system based on the same shape function order and identical time-integration schemes are utilized in the present approach. As a consequence, a simple transfer of nodal values is sufficient. The consideration of non-matching discretizations represents a possible future extension and generalization of the present scheme. For that purpose, mesh tying methods (see, e.g., Wohlmuth [180]) may be also utilized to construct a general framework applicable for volume-coupled problems such as the one considered here.

In the first outer iteration ( $i = 1$ ) for each new time level  $t^{n+1}$ , first approximations for the velocity  $\mathbf{u}_1^{n+1}$  and the pressure  $p_1^{n+1}$  are computed by the nonlinear flow solver based on the density value of the preceding time step (i.e.,  $\rho_0^{n+1} = \rho^n$ ). For further iterations  $i > 1$ , the most recent computed density  $\rho_{i-1}^{n+1}$  is used to solve the discretized Navier-Stokes equations for  $\mathbf{u}_i^{n+1}$  and  $p_i^{n+1}$ . After each flow solver call, the velocity vector  $\mathbf{u}_i^{n+\alpha_f}$  for the intermediate time level can be computed and is provided for solving the nonlinear multi-ion transport subproblem. As a result, updated values for concentration  $c_{k,i}^{n+1}$  and  $\Phi_i^{n+1}$  are obtained. The new density field  $\rho_i^{n+1}$  is then calculated from a constitutive law such as (2.65). The outer iteration loop is terminated as soon as the relative norms of the solution increments for concentration, potential and velocity field are all smaller than a predefined tolerance. Furthermore, inner iterations of the fluid and ion-transport subproblems are performed, which are also terminated based on a predefined tolerance; this tolerance may be similar or different to the tolerance for the outer iteration loop. This procedure ensures that all physical fields are in equilibrium before proceeding to the next time step. In all simulations presented in this contribution, both tolerances are set to be  $10^{-5}$  in order to ensure a fully converged solution. Thus, although partitioned scheme is used, a fully-implicit time discretization scheme is retained. According to Ehrl et al. [56], for most numerical examples typically about three outer iteration loops are required for achieving convergence.

For problem settings, where the effect of natural convection is negligible small, an outer iteration loop is not necessary. A one-way coupled scheme as depicted in Fig. 3.1(b) is sufficient in this case (see Bauer et al. [11] for further details). In many situations, the so-called “forced convection” induced by a rotation of electrodes or other bath agitation techniques is the dominant convective effect. In addition, when the electric current passing an electrochemical cell is far below the limiting current, concentration gradients become usually negligible small, and buoyancy forces can be neglected. The methodology presented here is also applicable for solving stationary problem formulations without proceeding in time. Of course, for simple models for the electric potential field (see section 2.6) no coupling to a flow field has to be considered at all.

#### 3.5.2 Current-controlled simulations

For current-controlled (galvanostatic) electrochemical systems, an additional constraint on the total electric current passing a cell arises (see section 2.5.4). For such situations an

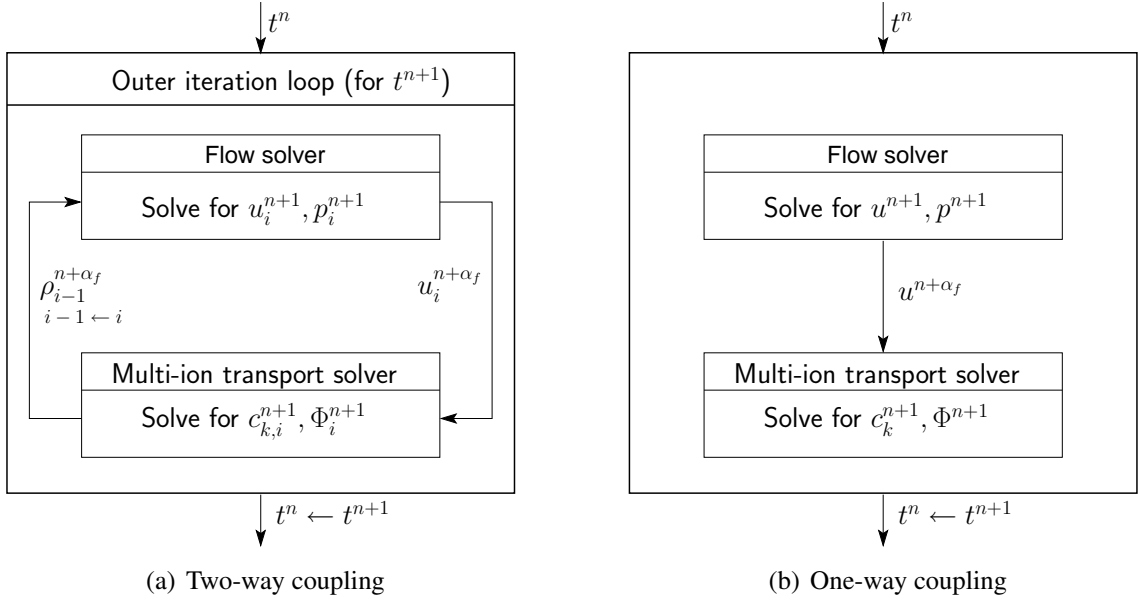


Figure 3.1: Partitioned solution schemes for the coupled simulation of electrochemical systems.

appropriate extension of the basic computational approach is required for continuously adjusting the cell potential difference  $U = V_a - V_c$  in order to follow the prescribed current curve. In the following, a cathode surface  $\Gamma_c$  and an anode surface  $\Gamma_a$  are considered as introduced in section 2.5.4. However, it is emphasized that the consideration of any number of electrode surfaces does not pose a problem for the computational approach presented below.

From a computational point of view it is convenient to set  $V_a = 0\text{ V}$  to define a reference level for the electric potential. Given that,  $U = -V_c$  represents the only additional degree of freedom within the considered Galvanostatic Constraint Condition (GCC). Based on a Newton-Raphson scheme, increments  $\Delta V_c^{i,j+1}$ ,  $\Delta V_a^{i,j+1}$  and  $\Delta \Phi_{\text{bulk}}^{i,j+1}$  are computed iteratively, yielding the new cell voltage

$$U_{i,j+1} = -V_c^{i,j+1} = \underbrace{-V_c^{i,j}}_{=:U_{i,j}} + \underbrace{\Delta V_a^{i,j+1} + \Delta \Phi_{\text{bulk}}^{i,j+1}}_{=: \Delta V_{i,j+1}}, \quad (3.95)$$

until convergence is achieved, as shown in Algorithm 3.1. After solving the ion-transport system, the new overall cell potential needs to be evaluated. Therefore, the potential increments  $\Delta V_c^{i,j+1}$  and  $\Delta V_a^{i,j+1}$  depending on the results of the ion-transport solver in GCC iteration  $j$  are determined via (3.96) and (3.97).

An additional potential increment  $\Delta \Phi_{\text{bulk}}^{i,j+1}$  accounting for the potential drop due to ohmic resistance in the electrolyte solution is also necessary to preserve a fast convergence rate of the applied cell voltage  $U_{i,j+1}$ . This predictor step is particularly important for electrolyte solutions with a rather low conductivity, since the overall resistive losses are dominated by the ohmic resistance. The electrical resistance of an electrolyte solution is here approximated by Ohm's law, including a one-dimensional projection of the two-dimensional or

### 3 Computational approach

---

**Algorithm 3.1** Galvanostatic constraint condition.

---

#### Solve ion-transport system

**Compute**  $\Delta V_c^{i,j+1}, \Delta V_a^{i,j+1}$  **and**  $\Delta \Phi_{\text{bulk}}^{i,j+1}$ :

$$\frac{\partial \mathcal{R}^c(V_c^{i,j})}{\partial V_c} \Bigg|_{V_{i,j}^C} \Delta V_c^{i,j+1} = -\mathcal{R}^c(V_c^{i,j}) \quad (3.96)$$

$$\frac{\partial \mathcal{R}^a(V_a^{i,j})}{\partial V_a} \Bigg|_{V_{i,j}^A} \Delta V_a^{i,j+1} = -\mathcal{R}^a(V_a^{i,j}) \quad (3.97)$$

$$\Delta \Phi_{\text{bulk}}^{i,j+1} \approx R_{\text{bulk}} \Delta I_{i,j}$$

**Check convergence:**

$$\begin{aligned} |\Delta V_c^{i,j+1} + \Delta V_a^{i,j+1} + \Delta \Phi_{\text{bulk}}^{i,j+1}| &\leq \varepsilon_{\text{GCC}} \\ |\mathcal{R}^c(V_c^{i,j})| &\leq \varepsilon_R \\ |\mathcal{R}^a(V_a^{i,j})| &\leq \varepsilon_R \end{aligned} \quad (3.98)$$

**Update:**

$$U_{i,j+1} = U_{i,j} + \Delta V_{i,j+1} \quad (3.99)$$


---

three-dimensional domain:

$$\Delta \Phi_{\text{bulk}}^{i,j+1} \approx \underbrace{\frac{1}{\sigma A} L}_{R_{\text{bulk}}} \underbrace{(-I_{\text{tot}} + I_{i,j})}_{\Delta I_{i,j}}. \quad (3.100)$$

Here,  $\sigma$  is the specific conductivity of the bulk electrolyte solution,  $R_{\text{bulk}}$  the electrical resistance,  $A$  the area of an electrode, and generally,  $L$  the average length of the electric field lines (for simple geometries with parallel electrodes,  $L$  is essentially the inter-electrode distance). The conductivity is computed once in the beginning according to (2.26) assuming a uniform concentration level. Conductivity variations of the electrolyte solution due to concentration variations in the vicinity of the electrode are neglected in this simple approximation. After determining  $U_{i,j+1}$  in the update step (3.99) and if not converged, the multi-ion-transport system has to be solved again to compute the new current  $I_{i,j+1}$  and the resulting variations in all solution variables caused by the new cell voltage  $U_{i,j+1}$ . If the GCC loop has reached convergence, the current density calculated from the ionic concentrations field  $\mathbf{c}_{k,i,j}$  is transferred to the fluid solver to compute the new velocity and pressure field.

The GCC iteration is terminated when the absolute value of the computed voltage increment falls below a user-specified tolerance  $\varepsilon_{\text{GCC}}$  or the absolute value of the scalar residuals  $|\mathcal{R}^c(V_c^{i,j})|$  and  $|\mathcal{R}^a(V_a^{i,j})|$  is smaller than  $\varepsilon_R$ , where  $\varepsilon_R$  denotes the tolerance for

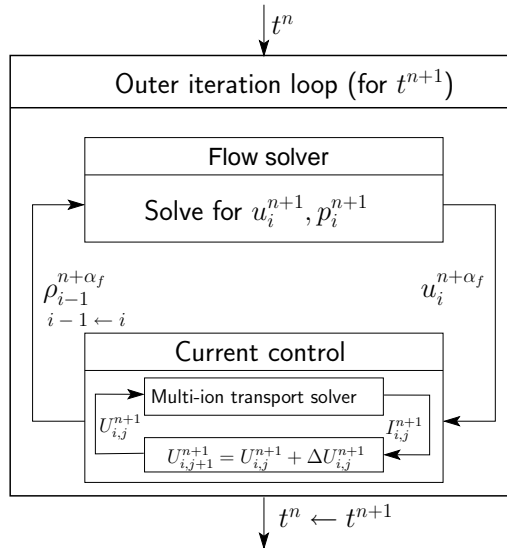


Figure 3.2: Algorithmic extension for the consideration of current-controlled electrolytic cells.

the residual norm. In the numerical examples presented below the tolerances are usually chosen to be  $\varepsilon_{\text{GCC}} = 1 \cdot 10^{-6}$  and  $\varepsilon_R = 1 \cdot 10^{-3}$ . To proceed to the next time step, both the criteria for terminating the outer iteration loop and the GCC have to be fulfilled. The iterative scheme for a computation including the GCC in the two-way-coupled partitioned scheme is shown in Fig. 3.2.

The proposed methodology works also for simpler cases, for example, when neglecting contributions due to anode overpotential  $\Delta V_a^{i,j}$  and ohmic drop  $\Delta \Phi_{\text{bulk}}^{i,j+1}$ . However, very slow convergence can be observed for particular configurations, since the computed voltage increment is considerably underestimated if not all potential increments are computed. In the presented method, no temporal or spatial distribution of the local current density is assumed; only the total amount of current is controlled. The actual current density distribution at the electrode surfaces is part of the unknown solution. This general current-control algorithm can be easily added to already existing electrochemical solution schemes, just introducing a GCC loop. The evaluation of the total current  $I$  and its derivative represent the only additional evaluations which are required within the galvanostatic solution procedure. Thus, the actual electrochemistry model enclosed inside the galvanostatic constraint loop may be of any kind as long as it provides the required information about the electric current. Besides the multi-ion transport model considered above, also simpler models for the electric potential (see section 2.6) can be enclosed inside the proposed GCC loop. Thus, secondary current distributions under current-controlled situations can be computed with the proposed algorithm as well.

A potential future extension would be a simultaneous solution of the equation for  $U$  and all governing equations of the electrochemical problem. This would result in a monolithic solution approach for galvanostatic applications with  $U$  as an additional degree of freedom. In that case, no nested solution loops would be required.

### 3.5.3 Numerical solution approach for nonlinear equations

The discretized formulations of both the flow and the multi-ion transport subproblem are representing discrete nonlinear equation systems. In this work, each of these problems is solved numerically by a Newton-Raphson methodology. This iterative procedure for solving the nonlinear subproblems represents the inner iteration loops within the outer loop of the two-way coupled scheme presented above. For a general nonlinear problem given as

$$\mathbf{F}(\mathbf{y}) = \mathbf{0}, \quad (3.101)$$

the iteration procedure of the Newton-Raphson method reads as follows:

$$\frac{\partial \mathbf{F}(\mathbf{y})}{\partial \mathbf{y}} \Big|_{\mathbf{y}_l} \Delta \mathbf{y}_l = -\mathbf{F}(\mathbf{y}_l), \quad (3.102)$$

$$\mathbf{y}_{l+1} = \mathbf{y}_l + \Delta \mathbf{y}_l. \quad (3.103)$$

Thus, in each iteration step  $l$  a linear equation system (3.102) has to be solved to determine the next increment vector  $\Delta \mathbf{y}_l$ , which is required for the subsequent update step (3.103). The iteration is terminated when either a user-defined convergence criterion is fulfilled or a maximum number of iterations is reached, which would indicate potential divergence of the method. This basic strategy (3.102)-(3.103) is now applied to each of the nonlinear subproblems that arise within the coupling schemes presented above.

#### Flow subproblem

The discrete nonlinear formulation of the incompressible Navier-Stokes equations obtained from the generalized-alpha time-integration scheme and the stabilized finite element method can be expressed as

$$\mathbf{F}_F^{n+1}(\mathbf{y}_F^{n+1}) = \frac{\gamma \Delta t}{\alpha_m} \begin{bmatrix} \mathbf{R}_M^{n+1}(\mathbf{u}^{n+1}, \mathbf{p}^{n+1}) \\ \mathbf{R}_C^{n+1}(\mathbf{u}^{n+1}, \mathbf{p}^{n+1}) \end{bmatrix} = \begin{bmatrix} \mathbf{0} \\ \mathbf{0} \end{bmatrix} \quad \text{with } \mathbf{y}_F^{n+1} := \begin{bmatrix} \mathbf{u}^{n+1} \\ \mathbf{p}^{n+1} \end{bmatrix}. \quad (3.104)$$

In accordance to Gravemeier et al. [80], an additional scaling factor  $\gamma \Delta t / \alpha_m$  is introduced in (3.104). The discrete residuals of momentum and continuity equation are denoted by  $\mathbf{R}_M^{n+1}$  and  $\mathbf{R}_C^{n+1}$ , respectively. For details concerning this discrete formulation of the incompressible Navier-Stokes equations the reader is referred to Gravemeier et al. [80].

The arising linear equation system (3.102) to be solved at iteration step  $l$  of the Newton-Raphson iteration has the form

$$\begin{bmatrix} \mathbf{M} + \frac{\alpha_f}{\alpha_m} \gamma \Delta t \mathbf{K}_{vu}^{n+\alpha_f, l} & \frac{\alpha_f}{\alpha_m} \gamma \Delta t \mathbf{K}_{vp}^{n+\alpha_f, l} \\ \frac{\alpha_f}{\alpha_m} \gamma \Delta t \mathbf{K}_{qu}^{n+\alpha_f, l} & \frac{\alpha_f}{\alpha_m} \gamma \Delta t \mathbf{K}_{qp}^{n+\alpha_f, l} \end{bmatrix} \begin{bmatrix} \Delta \mathbf{u}^{n+1, l} \\ \Delta \mathbf{p}^{n+1, l} \end{bmatrix} = -\frac{\gamma \Delta t}{\alpha_m} \begin{bmatrix} \mathbf{R}_M^{n+1, l} \\ \mathbf{R}_C^{n+1, l} \end{bmatrix}. \quad (3.105)$$

Here, the matrix  $\mathbf{M}$  emanates from the transient term in the momentum equation and the matrices  $\mathbf{K}_{vu}$ ,  $\mathbf{K}_{vp}$  are a result of the linearization of all remaining terms in  $\mathbf{R}_M^{n+1}(\mathbf{u}^{n+1}, \mathbf{p}^{n+1})$ . For the discrete continuity equation  $\mathbf{R}_C^{n+1}(\mathbf{u}^{n+1}, \mathbf{p}^{n+1})$ , respective submatrices  $\mathbf{K}_{vu}$ ,  $\mathbf{K}_{vp}$  are obtained. Note that the factors  $\alpha_f$  in (3.105) arise from the fact that  $\partial \mathbf{u}^{n+\alpha_f} / \partial \mathbf{u}^{n+1} = \alpha_f$  and  $\partial \mathbf{p}^{n+\alpha_f} / \partial \mathbf{p}^{n+1} = \alpha_f$ . Since  $\partial \dot{\mathbf{u}}^{n+\alpha_m} / \partial \mathbf{u}^{n+1} = \alpha_m / (\gamma \Delta t)$ , the performed scaling of the nonlin-

ear problem with  $\gamma\Delta t/\alpha_m$  ensures that no actual factor appears in front of the matrix  $\mathbf{M}$  (cf. Gravemeier et al. [80]).

### Multi-ion transport subproblem

For the multi-ion transport subproblem, the resulting nonlinear equation system for all nodal unknowns at time  $t^{n+1}$  is given by

$$\mathbf{F}_E^{n+1}(\mathbf{y}_E^{n+1}) = \begin{bmatrix} \frac{\gamma\Delta t}{\alpha_m} \mathbf{R}_{c_1}^{n+1}(\mathbf{c}_1^{n+1}, \Phi^{n+1}) \\ \vdots \\ \frac{\gamma\Delta t}{\alpha_m} \mathbf{R}_{c_m}^{n+1}(\mathbf{c}_m^{n+1}, \Phi^{n+1}) \\ \mathbf{R}_\Phi^{n+1}(\mathbf{c}_1^{n+1}, \dots, \mathbf{c}_m^{n+1}) \end{bmatrix} = \begin{bmatrix} \mathbf{0} \\ \vdots \\ \mathbf{0} \\ \mathbf{0} \end{bmatrix} \quad \text{with } \mathbf{y}_E^{n+1} := \begin{bmatrix} \mathbf{c}_1^{n+1} \\ \vdots \\ \mathbf{c}_m^{n+1} \\ \Phi^{n+1} \end{bmatrix}. \quad (3.106)$$

The corresponding discrete residuals of the ENP system of equations are defined as

$$\begin{aligned} \mathbf{R}_{c_k}^{n+1}(\mathbf{c}_k^{n+1}, \Phi^{n+1}) &= \mathbf{M}\dot{\mathbf{c}}_k^{n+\alpha_m} + (\mathbf{C}(\mathbf{u}^{n+\alpha_f}) + \mathbf{K}_k)\mathbf{c}_k^{n+\alpha_f} + \mathbf{E}_k(\mathbf{c}_k^{n+\alpha_f}, \Phi^{n+\alpha_f}) \\ &\quad + \mathbf{S}_k(\dot{\mathbf{c}}_k^{n+\alpha_m}, \mathbf{c}_k^{n+\alpha_f}, \Phi^{n+\alpha_f}, \mathbf{u}^{n+\alpha_f}) + \mathbf{I}_k(\mathbf{c}_k^{n+\alpha_f}, \Phi^{n+\alpha_f}) - \mathbf{f}_{N,k}^{n+\alpha_f}, \end{aligned} \quad (3.107)$$

$$\mathbf{R}_\Phi^{n+1}(\mathbf{c}_1^{n+1}, \dots, \mathbf{c}_m^{n+1}) = \sum_{k=1}^m z_k \mathbf{M}\mathbf{c}_k^{n+\alpha_f}. \quad (3.108)$$

Here,  $\mathbf{M}$  denotes the mass matrix,  $\mathbf{C}(\mathbf{u}^{n+\alpha_f})$  the matrix arising from the discretization of the convective term,  $\mathbf{K}_k$  the matrix emanating from the diffusive term, and  $\mathbf{E}_k(\mathbf{c}^{n+\alpha_f}, \Phi^{n+\alpha_f})$  represents the nonlinear migration term in its discretized form. Potential stabilization terms are represented by  $\mathbf{S}_k(\dot{\mathbf{c}}_k^{n+\alpha_m}, \mathbf{c}_k^{n+\alpha_f}, \Phi^{n+\alpha_f}, \mathbf{u}^{n+\alpha_f})$ . Contributions due to mass-flux boundary conditions (2.37) and (2.40) are denoted by  $\mathbf{f}_{N,k}^{n+\alpha_f}$  and  $\mathbf{I}_k(\mathbf{c}_k^{n+\alpha_f}, \Phi^{n+\alpha_f})$ , respectively. In a similar manner as performed for the flow problem above, the residuals  $\mathbf{R}_{c_k}^{n+1}$  of the ion-transport equations are scaled with  $\gamma\Delta t/\alpha_m$ .

As shown by Bauer et al. [11], the weak enforcement of the algebraic electroneutrality constraint leading to (3.108) is equivalent to a nodewise enforcement of electroneutrality, since the mass matrix  $\mathbf{M}$  is regular.

The nonlinear problem (3.106) is solved via Newton's method for all nodal unknowns collected in the vector  $\mathbf{y}_E^{n+1}$ . The simultaneous solution for ion concentrations and electric potential results in a monolithic solution approach for the electrochemistry subproblem. In each iteration step  $l$  of the nonlinear solution algorithm, a sparse linear equation system (3.102) has to be solved for the solution increment  $\Delta\mathbf{y}_E^{n+1,l}$ . Owing to the electroneutrality condition, the tangent matrix in (3.102) exhibits a saddle-point structure of the form

$$\begin{bmatrix} A_1^{n+\alpha_f,l} & \mathbf{0} & \dots & \mathbf{0} & B_1^{n+\alpha_f,l} \\ \mathbf{0} & A_2^{n+\alpha_f,l} & \ddots & \vdots & B_2^{n+\alpha_f,l} \\ \vdots & \ddots & \ddots & \mathbf{0} & \vdots \\ \mathbf{0} & \dots & \mathbf{0} & A_m^{n+\alpha_f,l} & B_m^{n+\alpha_f,l} \\ C_1 & C_2 & \dots & C_m & \mathbf{0} \end{bmatrix} \begin{bmatrix} \Delta\mathbf{c}_1^{n+1,l} \\ \Delta\mathbf{c}_2^{n+1,l} \\ \vdots \\ \Delta\mathbf{c}_m^{n+1,l} \\ \Delta\Phi^{n+1,l} \end{bmatrix} = - \begin{bmatrix} r_1^{n+1,l} \\ r_2^{n+1,l} \\ \vdots \\ r_m^{n+1,l} \\ r_\Phi^{n+1,l} \end{bmatrix}. \quad (3.109)$$

Here, the individual contributions to the block matrix are defined as

$$\mathbf{A}_k^{n+\alpha_f,l} = \partial \mathbf{R}_{c_k}^{n+1}(\mathbf{c}_k^{n+1,l}, \boldsymbol{\Phi}^{n+1,l}) / \partial \mathbf{c}_k^{n+1}, \quad (3.110)$$

$$\mathbf{B}_k^{n+\alpha_f,l} = \partial \mathbf{R}_{c_k}^{n+1}(\mathbf{c}_k^{n+1,l}, \boldsymbol{\Phi}^{n+1,l}) / \partial \boldsymbol{\Phi}^{n+1}, \quad (3.111)$$

$$\mathbf{C}_k = \alpha_f z_k \mathbf{M}. \quad (3.112)$$

The contributions to the right-hand side of (3.109) read  $\mathbf{r}_k^{n+1,l} = \frac{\gamma \Delta t}{\alpha_m} \mathbf{R}_{c_1}^{n+1}(\mathbf{c}_k^{n+1,l}, \boldsymbol{\Phi}^{n+1,l})$  and  $\mathbf{r}_\Phi^{n+1,l} = \sum_{k=1}^m z_k \mathbf{M} \mathbf{c}_k^{n+\alpha_f}$ . Note that the zero block in the unsymmetric saddle-point matrix (3.109) is challenging for the numerical solution of this linear system, as will be explained in the subsequent section.

In case of the CNP system of equations the solution procedure utilizing Newton's method remains basically the same. Only the properties of the arising linear system given as

$$\begin{bmatrix} \mathbf{A}_1^{n+\alpha_f,l} & \mathbf{0} & \cdots & \mathbf{0} & \mathbf{B}_1^{n+\alpha_f,l} \\ \mathbf{0} & \mathbf{A}_2^{n+\alpha_f,l} & \ddots & \vdots & \mathbf{B}_2^{n+\alpha_f,l} \\ \vdots & \ddots & \ddots & \mathbf{0} & \vdots \\ \mathbf{0} & \cdots & \mathbf{0} & \mathbf{A}_{m-1}^{n+\alpha_f,l} & \mathbf{B}_{m-1}^{n+\alpha_f,l} \\ \mathbf{D}_1^{n+\alpha_f,l} & \mathbf{D}_2^{n+\alpha_f,l} & \cdots & \mathbf{D}_{m-1}^{n+\alpha_f,l} & \mathbf{E}^{n+\alpha_f,l} \end{bmatrix} \begin{bmatrix} \Delta \mathbf{c}_1^{n+1,l} \\ \Delta \mathbf{c}_2^{n+1,l} \\ \vdots \\ \Delta \mathbf{c}_{m-1}^{n+1,l} \\ \Delta \boldsymbol{\Phi}^{n+1,l} \end{bmatrix} = - \begin{bmatrix} \mathbf{r}_1^{n+1,l} \\ \mathbf{r}_2^{n+1,l} \\ \vdots \\ \mathbf{r}_{m-1}^{n+1,l} \\ \tilde{\mathbf{r}}_\Phi^{n+1,l} \end{bmatrix}. \quad (3.113)$$

are different compared to the ENP model. For the ion-transport equations of ionic species  $k = 1, \dots, m-1$ , the matrix entries and right-hand terms are identical to those in (3.109). Thus, the same matrix blocks  $\mathbf{A}_k^{n+\alpha_f,l}$  and  $\mathbf{B}_k^{n+\alpha_f,l}$  are present in (3.113). Also the right-hand-side contributions  $-\mathbf{r}_k^{n+\alpha_f,l}$  are identical to the ENP model (3.109). Since ionic species concentration  $\mathbf{c}_m$  is eliminated by means of electroneutrality, the corresponding line from (3.109) does not appear in (3.113). The alternative closing equation for the electric potential leads to different matrix entries denoted by  $\mathbf{D}_k^{n+\alpha_f,l}$ ,  $\mathbf{E}^{n+\alpha_f,l}$  and the corresponding right-hand-side  $-\tilde{\mathbf{r}}_\Phi^{n+\alpha_f,l}$  in the last row of the linear block system. The main differences of (3.113) compared to (3.109) are the reduced size of the linear problem and the nonzero submatrix  $\mathbf{E}$ , which replaces the zero block in (3.109).

### 3.5.4 Numerical solution of linear equation systems

As stated above, in each iteration step of Newton's method a linear system of equations has to be solved in order to determine the new increment vector. For problems with a relatively small number of degrees of freedom, direct sparse solvers can be used for this purpose. For the numerical examples in the present study, the UMFPACK package by Davis [46] is utilized whenever a direct solution approach is applicable. When considering large systems w.r.t. the number of unknowns, iterative solution strategies in combination with efficient preconditioning techniques are mandatory. The GMRES method by Saad and Schultz [153] is used as the basic iterative procedure for such situations. For improving the condition number of the Jacobian matrix, and thus, the convergence rate of the GMRES method, appropriate preconditioning of the linear system is required. Libraries from the Trilinos package (Heroux et al. [96]) provide a broad variety of preconditioning methods. Typically, Algebraic Multigrid (AMG) methods with smoothed aggregation exhibit

good numerical performance as preconditioner for linear systems within Newton-Krylov schemes.

### **ENP system of equations**

In the case of the ENP system of equations, the saddle-point structure of the matrix in (3.109) is challenging from a numerical point of view. If the problem size in terms of degrees of freedom is still small, a direct solution approach can be used without any limitations. However, problems arise in the context of iterative solution approaches required for large-scale problems. Standard preconditioning techniques typically utilize the inverse value of the main diagonal entries. Unfortunately, the zero entries on the main diagonal in (3.109) prevent the usage of these methods. A comprehensive overview of solution techniques for general saddle-point problems is provided by Benzi et al. [17].

In this work, a block-preconditioning technique of the popular SIMPLE (Semi-implicit method for pressure-linked equations) type is used in combination with GMRES. Originally, SIMPLE was proposed by Patankar and Spalding [140] as a solution approach for solving the discretized incompressible Navier-Stokes equations. SIMPLE and its variants can be utilized as block-preconditioners (see, e.g., Elman et al. [60], Rehman et al. [151]) or smoothers in multigrid methods (Benzi et al. [17]). In the present computational approach, the first of these two options is applied. For performance reasons, actually a cheaper approximative version of SIMPLE is used as a preconditioner. Although the usage of this SIMPLE-like preconditioner enables the parallel solution of large-scale electrochemical problems, difficulties may be experienced in practice in finding appropriate parameters.

Recently, AMG techniques with a special focus on electrochemical problems were proposed by Thum et al. [167]. Since the drift-diffusion equations used in the context of semiconductor device modeling lead to similar problem structures as considered here, also the investigations by Lin et al. [125, 126] are worth considering in the present context. Therein, the performance of a parallel algebraic multilevel preconditioner was studied for these types of problems.

### **CNP system of equations**

Considering the CNP system of equations, an explicit dependency on the electric potential is given in the closing equation for the electric potential. Thus, the lower right block of the matrix in (3.113) is nonzero, and the full spectrum of preconditioning (e.g., AMG, ILU) and linear solution techniques is applicable to solve (3.113). Furthermore, due to the elimination of the ionic species concentration  $c_m$  from the system of equations, the system size is reduced by one from  $m + 1$  degrees of freedom per node to  $m$  degrees of freedom per node. For a binary electrolyte ( $m = 2$ ), the relative difference is maximal. Then, the CNP formulation leads to a system size which is only 2/3 of the size of the corresponding linear problems obtained from the ENP model.

This illustrates the enormous numerical potential provided by the CNP system of equations. Since often the time spent for solving linear equation systems is (much) higher than the time spent in evaluation of element contribution and assembly of those into the system matrix, the benefits of the CNP model are obvious. For smaller problems the saved computational time might be negligible, but for parallel large-scale problems a substantial

improvement can be obtained. However, a more detailed investigation on solver techniques for electrochemical problems in general and a comparison of ENP and CNP formulation in particular, will be required in the future.

#### **3.5.5 Postprocessing of simulation results**

The present chapter on the computational approach is ended with a brief comment on the postprocessing of numerical simulations. Of course, the primary simulation results are the approximations to the unknown physical fields. In the present case these are velocity, pressure, ionic concentrations and electric potential field. The proposed computational approach enables the investigation of their spatial and temporal behavior as well as their interaction.

In the context of electrochemistry, some secondary results are of even greater importance. One of the main objectives is the computation of current density distributions at electrode surfaces. This value directly corresponds to the rate of electrochemical reaction at the electrodes. For electroplating applications, a prediction of deposit thickness distributions is possible based on these data (see section 2.5.5). A categorization of current density distributions into primary, secondary and tertiary distributions is given in section 2.6. For an actual calculation of these boundary-related quantities, it is strongly recommended to use consistent flux-calculation methods such as the one presented by Gresho et al. [86]. For the present context of electrochemical systems the method is adapted accordingly as outlined in the Appendix B. Besides current density distributions, also ionic mass flux densities at boundaries can be computed.

Sometimes, a vector-field representation of the current or the individual mass fluxes in the whole computational domain is required for visualization purposes. An appropriate method to obtain these data from finite element solutions in a consistent manner is proposed in Appendix B. An  $L^2$ -projection is utilized to compute the desired nodewise approximations from finite element results.

The open-source software ParaView developed by Kitware Inc. was used for the visualization of the simulation results presented in this work.

# 4 Numerical examples

In this chapter, the proposed computational method is tested for several different numerical examples, demonstrating that it is robust and provides accurate results. Among others, several realistic problem configurations with complex three-dimensional geometries are considered in the context of electroplating. Each numerical example focuses on quite different aspects of both the mathematical modeling and the computational approach. Regarding the coupling of ionic transport and incompressible flow, both laminar and turbulent flow regimes are considered. Also the two-way-coupled case of natural convection in electrochemical cells is investigated. The variety of considered examples demonstrates the broad spectrum of capabilities. Some of the following numerical examples have been published in Bauer et al. [9, 11, 12] and Ehrl et al. [56]. Further simulation results obtained with the present computational approach can also be found in these references.

The remainder of this chapter is as follows. In section 4.1, several simpler problem setups are considered that enable a detailed study of the computational approach and its properties. After these rather fundamental numerical investigations, coupled multi-ion transport within an oscillating shear flow cell is simulated in section 4.2. Natural convection in a copper electroplating cell under galvanostatic control is addressed in numerical example 4.3. A collection of three different examples considering the modeling of rotating cylinder electrodes is provided in section 4.4. In particular, simple potential-based models, natural convection phenomena and multi-ion transport in turbulent flow are considered in the context of this electrochemical configuration. A three-dimensional model for copper pulse plating at a rotating disk electrode is presented in section 4.5. Finally, a summary of simulation results for a nickel pulse-reverse plating experiment within a realistic galvanic bath is given in 4.6.

## 4.1 Basic numerical test cases

Within this first subsection, some simpler numerical test cases are considered, demonstrating that the developed computational approach is correct and provides accurate results. Since for most of the following model problems even analytical solutions are available, numerical convergence studies are presented as well. In addition, the positive effect of the proposed stabilization terms on both stability and accuracy for convection-dominated regimes is highlighted. Note that all quantities in this subsection have to be interpreted as dimensionless values. For simplicity of notation, the additional asterisk introduced in section 2.8.5 for denoting dimensionless quantities is neglected below.

### 4.1.1 One-dimensional convection-diffusion-migration equation

A one-dimensional model problem including convection, diffusion and migration is studied first. The computational domain is given as  $\Omega := ]0, L[$  with  $L = 1$ . A binary electrolyte

solution based on cation concentration  $c_1$  and anion concentration  $c_2$  is considered. The corresponding valences are given as  $z_1 = +1$  and  $z_2 = -1$ . Diffusion constants are chosen to be  $D_1 = 1/150$  and  $D_2 = 1/50$ . The ENP system of equations is considered here, where ion transport is subjected to the electroneutrality constraint. Dirichlet boundary conditions in the form  $c_1(0) = c_2(0) = g_0$  with  $g_0 = 1$  are applied at the left boundary located at  $x = 0$ . In addition, a reference level for the (dimensionless) electric potential is set via  $\frac{F}{RT}\Phi(0) = 0$ . At the right boundary, located at  $x = L$ , the condition  $c_1(L) = g_L = 0.1$  is prescribed. Defining no explicit boundary condition for the anion concentration  $c_2$  results in a zero-flux condition on the right boundary. A constant convective velocity of  $u = 2$  is assumed. The corresponding Peclet number of the problem is given as  $\text{Pe} = uL/D = 200$ , where  $D = 1/100$  denotes the effective diffusion constant for the binary electrolyte as defined in (3.90).

In Bauer et al. [12], an analytical solution for this simple model problem is provided. The equilibrium concentration profiles for both ionic species in the case  $\text{Pe} > 0$  read:

$$c_1(x) = c_2(x) = g_0 \frac{e^{\text{Pe}} - e^{\text{Pe} \frac{x}{L}}}{e^{\text{Pe}} - 1} + g_L \frac{e^{\text{Pe} \frac{x}{L}} - 1}{e^{\text{Pe}} - 1}. \quad (4.1)$$

The corresponding electric potential field is determined by

$$\frac{F}{RT}\Phi(x) = \frac{F}{RT}\Phi(0) - \frac{1}{z_2} \ln\left(\frac{c_1(x)}{c_1(0)}\right) + \frac{u}{z_2 D_2} (x - g_L G(x)), \quad (4.2)$$

together with

$$G(x) = \frac{e^{\text{Pe}} - 1}{g_0 e^{\text{Pe}} - g_L} \left( x - \frac{L}{\text{Pe}} \ln\left(g_0 e^{\text{Pe}} - g_L + (g_L - g_0) e^{\text{Pe} \frac{x}{L}}\right) + \frac{L}{\text{Pe}} \ln\left(g_0 (e^{\text{Pe}} - 1)\right) \right). \quad (4.3)$$

For discretizing the one-dimensional computational domain, 10 linear elements with constant element length  $h = 0.1$  are used. For one-dimensional convection-diffusion problems, utilizing linear shape functions, a stabilization parameter definition exists that gives nodally exact finite element solutions for stationary problems (see, e.g., Brooks and Hughes [26]). The formula involves a value for the local element Peclet number. For a binary electrolyte solution, this well-known definition is adopted as explained in section 3.4.6. Thus, for both  $\tau_1$  and  $\tau_2$ , the definition

$$\tau_{\text{ana}} = \frac{h}{2|u|} \left( \frac{1}{\tanh \text{Pe}_e^{\text{eff}}} - \frac{1}{\text{Pe}_e^{\text{eff}}} \right) \quad (4.4)$$

is used. Here, the effective element Peclet number, as defined for a binary electrolyte solution in (3.91), is  $\text{Pe}_e^{\text{eff}} = uh/(2D) = 10$ , indicating local convection dominance, since the value is greater than one.

The results from the steady-state simulations are depicted in Fig. 4.1, showing the calculated cation concentration  $c_1$ . The analytical solution is given as a reference, and it can be clearly seen that the chosen mesh is too coarse to resolve the strong concentration gradient evolving near the right boundary. The SGFEM solution is highly oscillatory in the whole domain. With the additional stabilization terms in (3.93), the spurious oscillations are removed. Only when using the effective element Peclet number  $\text{Pe}_e^{\text{eff}}$  for calculating

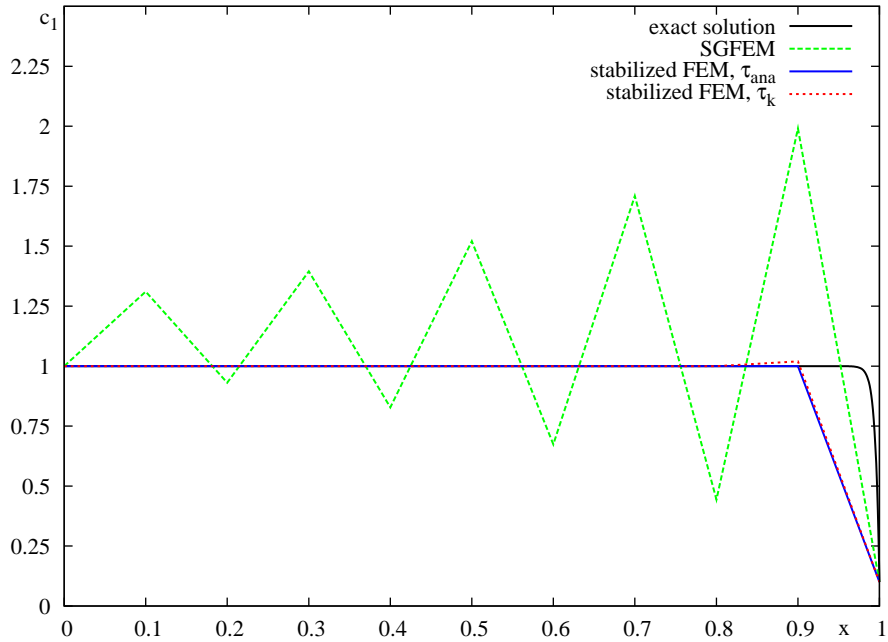


Figure 4.1: Stationary concentration profiles of  $c_1$  for the convection-dominated case with  $\text{Pe}_e^{\text{eff}} = 10$ .

the stabilization parameter  $\tau_{\text{ana}}$  defined in (4.4), the nodally exact finite element solution is obtained as depicted in Fig. 4.1. For comparison, also the results obtained when using the more general formulation of  $\tau_k$ , as specified in (3.92) for the case of a binary electrolyte solution, are shown. Of course, a nodally exact solution cannot be achieved in this case. However, spurious oscillations in the cation concentration are removed as shown in Fig. 4.1.

Oscillations in computed ionic concentration fields also cause oscillations in the electric potential field due to the inherent coupling of all physical fields. This can be clearly seen in Fig. 4.2 for the SGFEM case. Again, the additional usage of a stabilization technique substantially improves the situation compared to the analytical potential curve. For the current example, both choices for the stabilization parameter considered here lead to very similar results for the electric potential. Thus, both curves almost coincide in Fig. 4.2.

Since a 1-D problem is considered, total mass fluxes of ionic species as well as the current passing the cell are constant along  $[0, L]$ . The exact value for the cation flux can be computed using (4.1), (4.2) and definition (2.4). For the right boundary, a value of

$$N_{1,\text{exact}}^{\text{d+m}}(L) = \frac{12}{5} = 2.4 \quad (4.5)$$

is obtained. However, when computing fluxes based on a simple evaluation of the gradient of the finite element solution that is nodally exact for the concentration field, one obtains  $N_{1,\text{FEM}}^{\text{d+m}}(L) \approx 0.1205$ . Comparison with the exact value (4.5) reveals a dramatic difference, even for the nodally exact stabilized finite element solution.

Such a simple flux evaluation approach is a common mistake, since for a consistent calculation of fluxes, the additional subgrid-scale terms present in the problem formulation

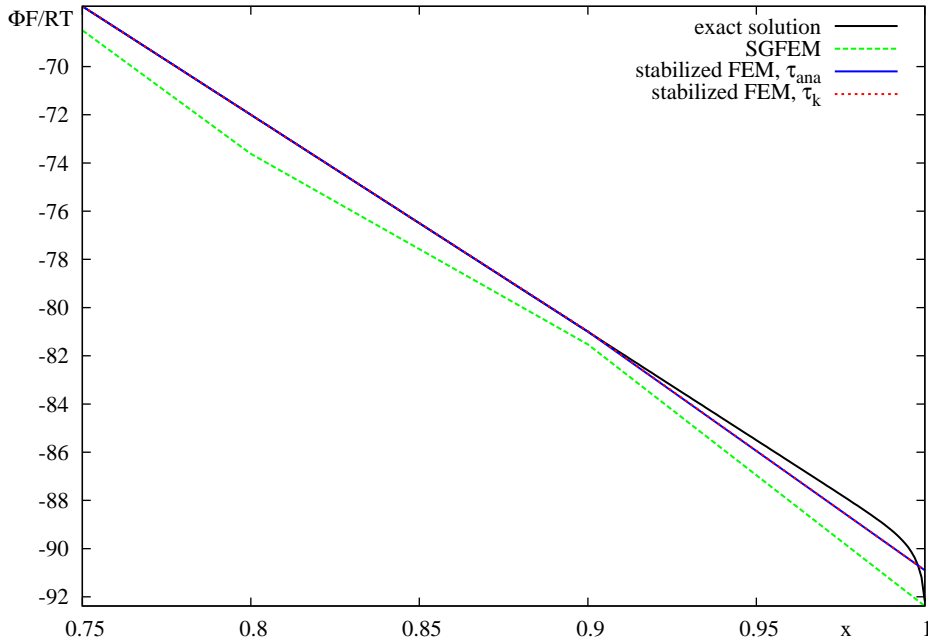


Figure 4.2: Results for the dimensionless electric potential  $\Phi F/RT$  near the right boundary (convection-dominated case with  $\text{Pe}_e^{\text{eff}} = 10$ ).

have to be accounted for. Furthermore, differentiating the finite element solution requires a well-resolved boundary layer to produce acceptable results. Especially in the context of stabilized methods, this requirement is often not fulfilled. In fact, the fluxes already contained in the weak problem formulation are the consistent values that have to be extracted. Since predicting mass fluxes and particularly current densities at electrode surfaces is crucial for electrochemical applications, it is strongly recommended using consistent flux calculation methods such as the one specified by Gresho et al. [86], for instance. Its derivation within the present context of electrochemical systems is briefly outlined in Appendix B.

For the present 1-D problem, merely the residual of the weak form has to be evaluated at the boundary node of interest, after the nonlinear solution procedure has converged. Note that this has to be performed prior to imposing any boundary conditions to the residual vector. From the nodally exact simulation results,  $N_2^{\text{d+m}}(L) = 4.3 \cdot 10^{-15}$  is obtained, clearly showing that the zero flux condition is numerically fulfilled for the anion species. The computed value for the cation mass flux is  $N_1^{\text{d+m}}(L) = 2.4$  and matches the analytical value given in (4.5). In summary, although the concentration boundary layer at the right boundary was not adequately resolved, the cation flux at the right boundary can be computed correctly in a consistent manner using the recommended method.

### 4.1.2 One-dimensional transport of three ionic species

This example is similar to the first example, but now an electrolyte solution containing three different ionic species is considered. The geometrical problem settings are identical to the previous numerical example. The valences are set as  $z_1 = +2$ ,  $z_2 = -2$ ,  $z_3 = +1$ , while for the diffusion coefficients the values  $D_1 = 1/150$ ,  $D_2 = 1/50$ ,  $D_3 = 3/1000$  are used.

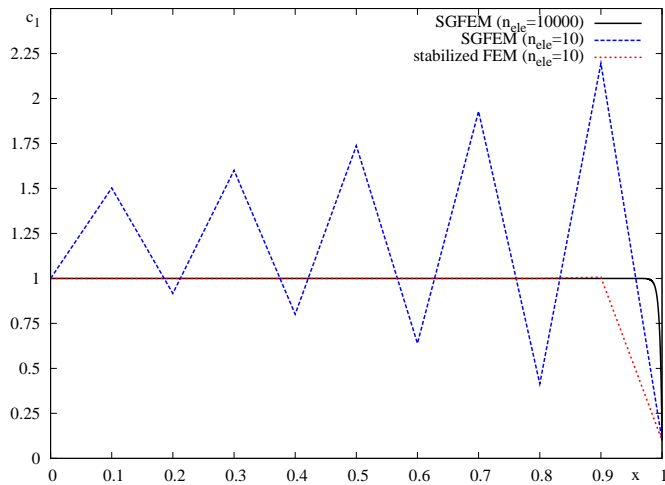


Figure 4.3: Stationary concentration profiles of  $c_1$  for the 3-ion system and  $u = 2.0$ .

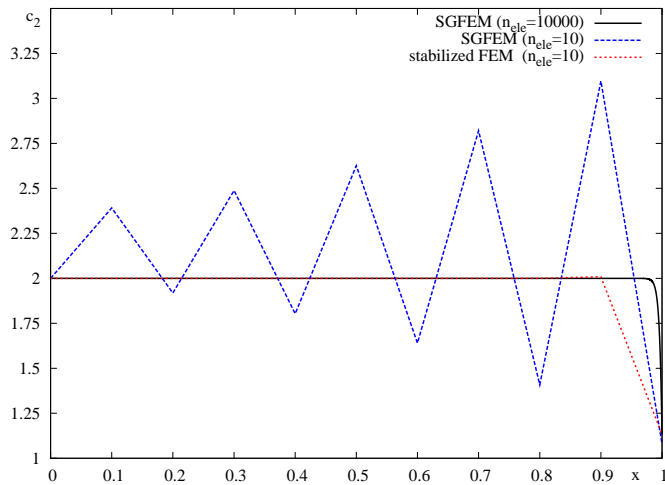


Figure 4.4: Stationary concentration profiles of  $c_2$  for the 3-ion system and  $u = 2.0$ .

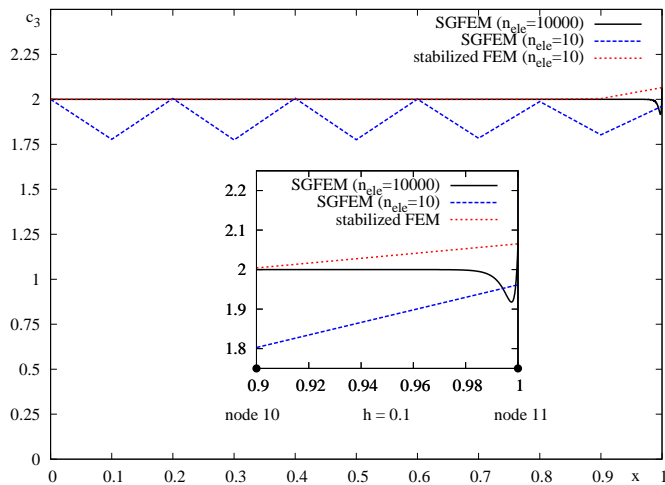


Figure 4.5: Stationary concentration profiles of  $c_3$  for the 3-ion system and  $u = 2.0$ .

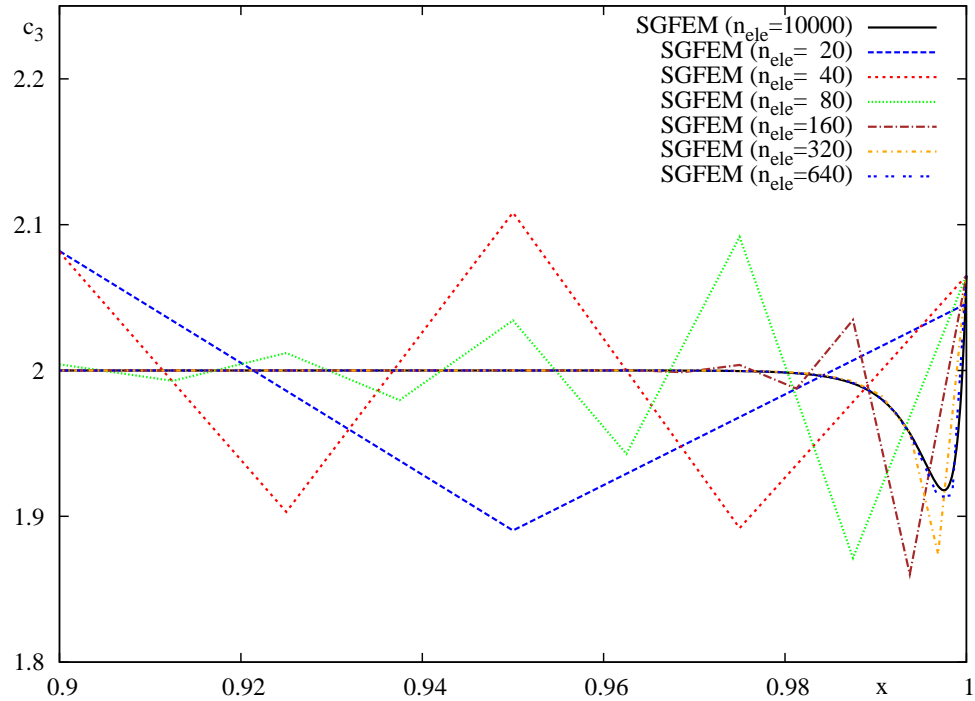


Figure 4.6: Mesh refinement study for the stationary concentration profiles of  $c_3$  for the 3-ion system and  $u = 2.0$  obtained with SGFEM.

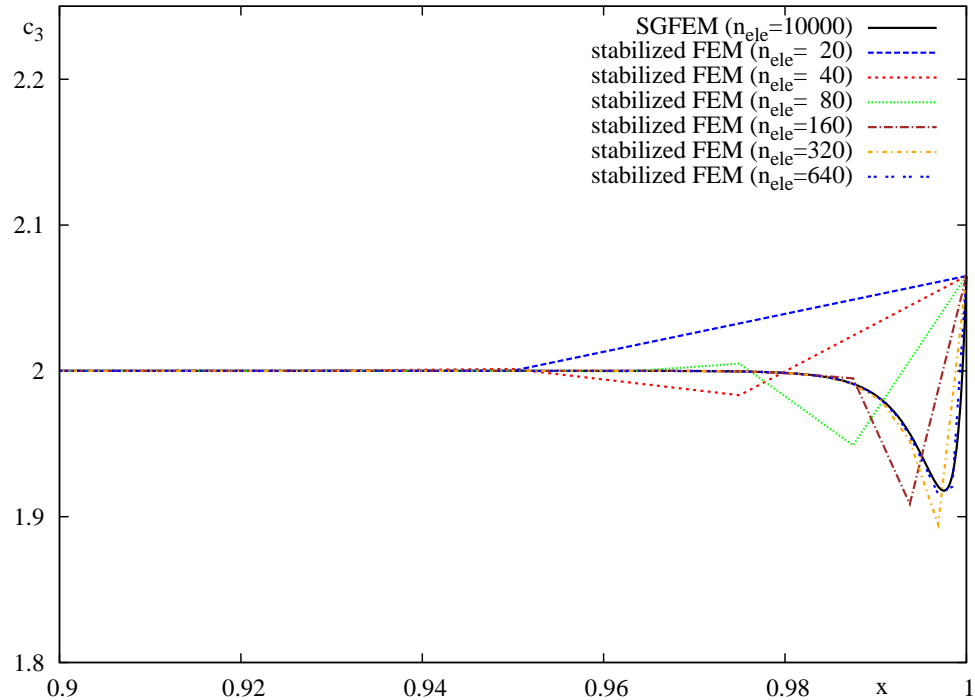


Figure 4.7: Mesh refinement study for the stationary concentration profiles of  $c_3$  for the 3-ion system and  $u = 2.0$  obtained with stabilized FEM.

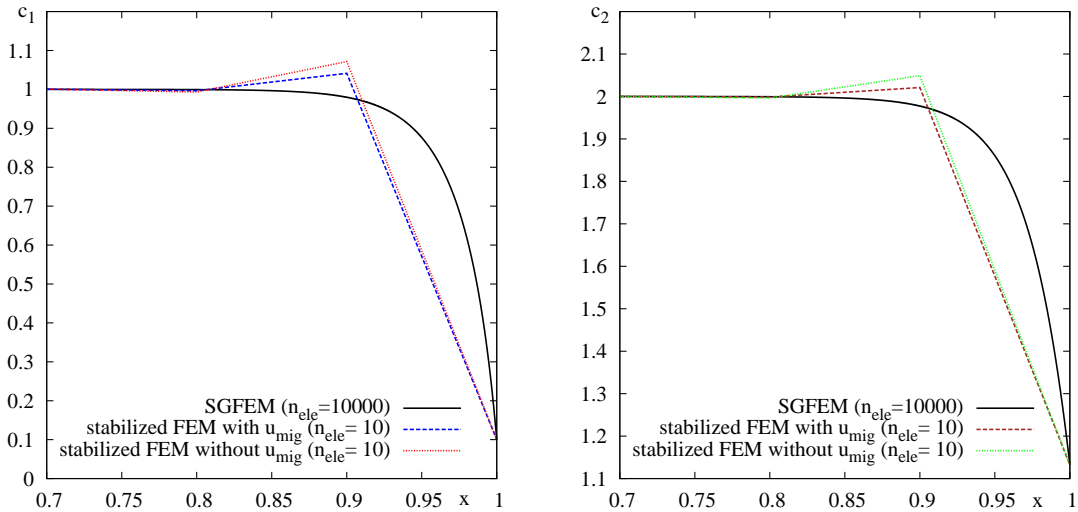


Figure 4.8: Stationary concentration profiles of  $c_1$  (left) and  $c_2$  (right) for the 3-ion system and  $u = 0.3$  obtained with different stabilization approaches.

At the left boundary,  $x = 0$ , the following conditions are prescribed:  $c_1 = 1.0$ ,  $c_2 = 2.0$ ,  $c_3 = 2.0$  and  $F\Phi(0)/RT = 0$ . At the right boundary,  $x = L$ , only  $c_1 = 0.1$  is prescribed. As a consequence, the natural boundary conditions  $N_2^{d+m}(L) = N_3^{d+m}(L) = 0$  hold at the right boundary without specifying them in an explicit way. The velocity range  $u = 0$  up to  $u = 2.0$  is studied in this example, which corresponds to  $\text{Pe}_1 = uL/D_1 \in [0; 300]$ . The results obtained for the stationary version of the SGFEM formulation (3.64)-(3.65) are compared with the results of the stationary form of the stabilized finite element model stated in (3.81)-(3.82) in combination with (3.88).

Computed concentration profiles for the case  $\text{Pe}_1 = 300$  are depicted in Figs. 4.3-4.5. For comparison, results obtained for a very fine spatial resolution (SGFEM with 10,000 linear elements) are shown, which represent very good approximations to the (unknown) exact concentration profiles. Oscillations in the concentration profiles for all three ionic species are observed when using only 10 linear elements for the SGFEM. In contrast, results for the stabilized FEM with stabilization parameter as defined in (3.88), do not exhibit oscillations and agree well with the reference solution. In particular, the good prediction of  $c_3$  in Fig. 4.5 is emphasized, which is nearly optimal when considering the given coarse mesh of only 10 elements. Of course, none of the arising concentration boundary layers are properly resolved based on the present spatial discretization.

In addition, a mesh-refinement study for this problem setting is performed. For this purpose, further uniform discretizations using 20, 40, 80, 160, 320 and 640 linear finite elements are considered. As a result, with decreasing element size  $h$ , convergence of each of the unknown fields towards the respective reference solution is observed. As an exemplary result, the different numerical approximations obtained for  $c_3$  are compared. For better illustration, only the region close to the right boundary is shown. SGFEM results for  $c_3$  are provided in Fig. 4.6, while Fig. 4.7 shows results obtained with the stabilized finite element approach. It is obvious from the results that both finite element formulations converge towards the same reference solution. As expected, the boundary layer is more and more resolved with decreasing element size.

The large benefit of the proposed stabilization is especially visible for mesh sizes, which do not yet resolve the boundary layer. Then the stabilization technique considerably removes spurious oscillations caused by apparent convection dominance. In comparison to the SGFEM results, this leads to very good and smooth approximations in the bulk solution.

Finally, the numerical results obtained with the proposed method including and excluding the migration velocity, respectively, in both stabilization term and parameter, are compared. As can be seen in Fig. 4.8, both approaches lead to numerical approximations of the reference solution without spurious oscillations. However, the inclusion of the migration velocity, as proposed in this study, leads to slightly improved results. This is exemplarily depicted in Fig. 4.8 for the concentration profiles  $c_1$  and  $c_2$  obtained for  $u = 0.3$ .

#### 4.1.3 Analysis of a transient diffusion-migration problem in 3D

To demonstrate that the computational approach performs well for transient problems, ion transport governed by diffusion and migration is simulated in the following for a time interval  $[0, T_e]$ . A binary system with two ionic species is considered. In the following, the SGFEM version of the ENP system of equations is utilized.

The computational domain is the three-dimensional unit cube  $\Omega = (0, 1)^3$ . At all boundaries, zero flux conditions for both ionic species are prescribed, i.e., it holds  $\partial\Omega = \Gamma_{N,1} = \Gamma_{N,2}$  and  $h_1 = h_2 = 0$ . The material parameters are set to be  $z_1 = 1$ ,  $z_2 = -2$ ,  $D_1 = 0.008$  and  $D_2 = 0.005$ . The initial concentration fields, fulfilling the electroneutrality condition at  $t = 0$ , are given as:

$$c_1^0(x, y, z) = 2.0 + \cos(\pi x) \cos(2\pi y) \cos(3\pi z), \quad (4.6)$$

$$c_2^0(x, y, z) = -\frac{z_1}{z_2} c_1^0(x, y, z). \quad (4.7)$$

Visualizations of the initial field  $c_1^0$  and the corresponding potential field  $\Phi^0$  are provided in Fig. 4.9.

A similar configuration was investigated by Choi and Chan [33] as a 1-D problem. The analytical solution of the problem considered in that work was the basis for a more general extension to two spatial dimensions performed by Kwok and Wu [119]. Using similar methods, the logical extension to three space dimensions was provided recently by Bauer et al. [11] as a special case of a more general analysis. Parts of the following numerical results were published in Bauer et al. [11], too. The exact solution for the specified initial boundary value problem reads:

$$c_1(x, y, z, t) = 2.0 + \cos(\pi x) \cos(2\pi y) \cos(3\pi z) e^{-14D\pi^2 t}, \quad (4.8)$$

$$c_2(x, y, z, t) = -\frac{z_1}{z_2} c_1(x, y, z, t), \quad (4.9)$$

$$\frac{F}{RT} \Phi(x, y, z, t) = \frac{D_2 - D_1}{z_1 D_1 - z_2 D_2} \ln \left( \frac{c_1(x, y, z, t)}{c_1(0, 0, 0, t)} \right), \quad (4.10)$$

where  $\Phi(0, 0, 0, t) = 0$  is fixed to define a reference level for the electric potential  $\Phi$ . The factor  $F/RT$  remains arbitrary and is assumed to be 1.0 in this example.

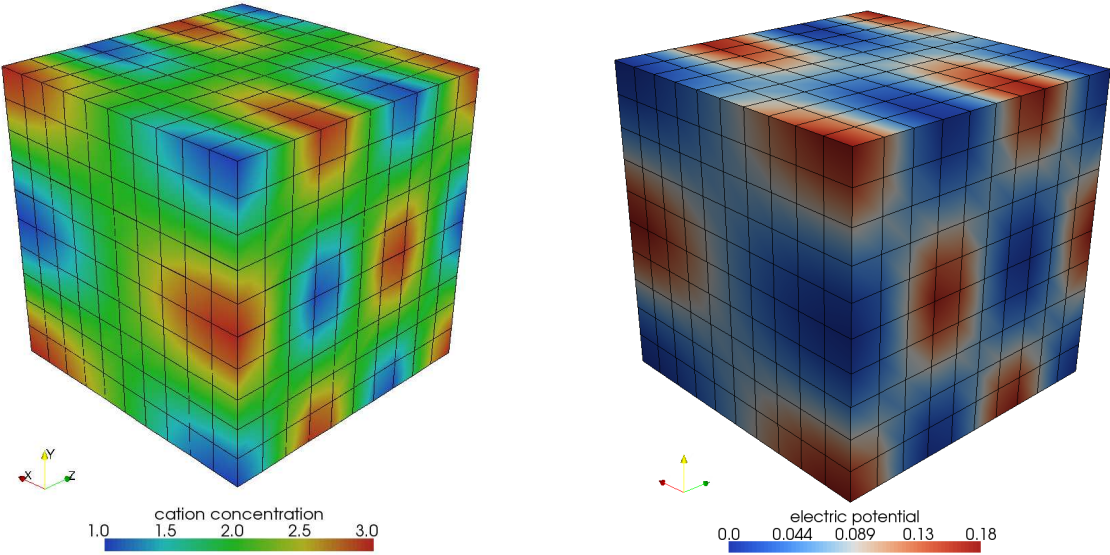


Figure 4.9: Initial cation concentration field  $c_1^0$  (left) and potential field  $\Phi^0$  (right) for the transient three-dimensional diffusion-migration problem depicted on the discretization with element edge length  $h = 0.1$ .

For studying the convergence behavior in space and time, the absolute errors

$$\varepsilon_k := \|c_k^h - c_k\|_{L^2(\Omega)} \quad \text{for } k \in \{1, 2\}, \quad (4.11)$$

$$\varepsilon_\Phi := \|\Phi^h - \Phi\|_{L^2(\Omega)}, \quad (4.12)$$

are computed for each of the three unknown fields at the time of interest using the  $L^2$ -norm as defined in (3.30). In the following, hexahedral elements with trilinear shape functions are used. A series of four uniform discretizations with characteristic element edge lengths  $h = 0.2, h = 0.1, h = 0.05$  and  $h = 0.025$  are considered. For the temporal error being negligible compared to the error introduced by the spatial discretization, a small (constant) time-step size  $\Delta t = 0.005$  is used. Using the Crank-Nicolson scheme ( $\theta = 0.5$ ), 20 time steps are performed until  $T_e = 0.1$  is reached. The computed errors depicted in Fig. 4.10 show second-order convergence in space for both ionic species concentrations as well as for the electric potential. Note that (4.9) is reflected in the computed values for the absolute errors, leading to  $\varepsilon_1 = 2\varepsilon_2$  for the given valences. When depicting relative instead of absolute errors, the curves for cation and anion concentration would coincide.

For investigating the temporal accuracy of the computational approach, the spatial error contributions have to be minimized. Owing to the approximation of cosine functions with trilinear shape functions, the spatial error is dominating in this example. Hence, a very fine uniform discretization with  $h = 0.01$  has to be used for revealing the error contribution due to time discretization. Consequently, a spatial resolution of  $100 \times 100 \times 100$  elements is utilized for this investigation. Different numbers of constant time steps are used to reach  $T_e = 2.0$ , where the error measures introduced above are evaluated. Note that the end time  $T_e$  has a different value compared to the choice used above. The results for the Crank-Nicolson scheme ( $\theta = 0.5$ ) are shown in Fig. 4.11. As expected, second-order

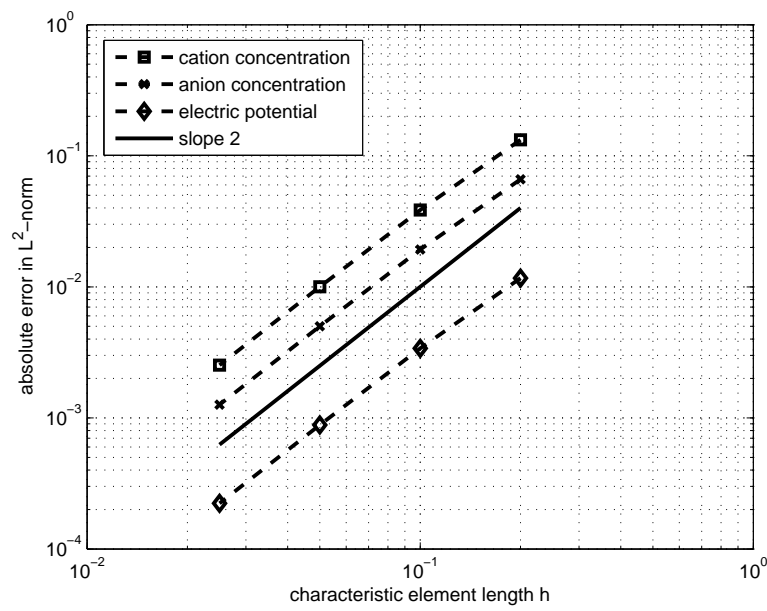


Figure 4.10: Spatial convergence for cation concentration  $c_1$ , anion concentration  $c_2$  and electric potential  $\Phi$ .

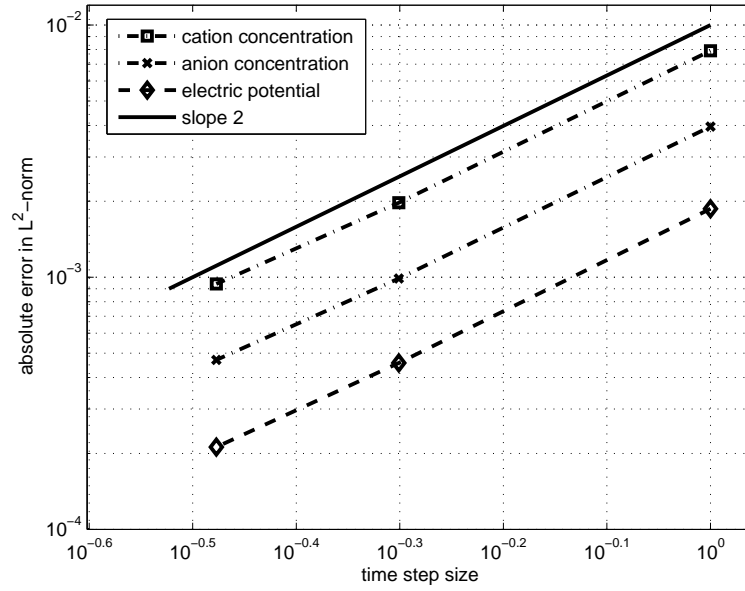


Figure 4.11: Temporal convergence for cation concentration  $c_1$ , anion concentration  $c_2$  and electric potential  $\Phi$  using the Crank-Nicolson scheme.

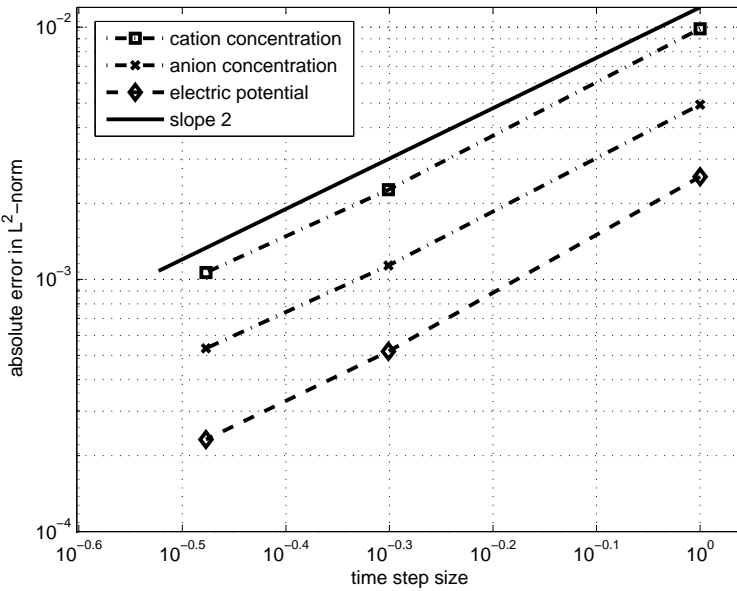


Figure 4.12: Temporal convergence for cation concentration  $c_1$ , anion concentration  $c_2$  and electric potential  $\Phi$  using the generalized-alpha scheme with  $\rho_\infty = 0.5$ .

accuracy in time is observed for all physical fields. This second-order convergence rate is also observed for the generalized-alpha method with  $\rho_\infty = 0.5$  (i.e.,  $\alpha_m = 5/6$ ,  $\alpha_f = 2/3$ ,  $\gamma = 2/3$ ) as illustrated in Fig. 4.12.

When the CNP system of equations (3.66)-(3.67) is utilized for the latter simulations instead of the standard ENP model, a considerably increase in computational efficiency is observed. For the CNP model the inert ionic species  $k = 2$  is eliminated from the system of equations by means of electroneutrality. Consequently, it has only to be solved for the nodal values of  $c_1$  and  $\Phi$ . For the structured mesh with  $10^6$  hexahedral elements considered here, the corresponding number of nodes reads  $n_{\text{nod}} = 1,030,301$ . Thus, for the CNP model only  $2n_{\text{nod}}$  degrees of freedom arise, while a number of  $3n_{\text{nod}}$  degrees of freedom have to be determined in the usual formulation. As a consequence, the sparse system matrix has  $2n_{\text{nod}}$  rows in case of the CNP model and  $3n_{\text{nod}}$  rows in case of the ENP problem formulation. The number of nonzero entries into the sparse matrix are  $1.09 \cdot 10^9$ (CNP) and  $2.45 \cdot 10^9$ (ENP), respectively. For this specific example the simulations are carried out in parallel using four processors. As a rough estimate, a reduction of about 40% in required simulation time is observed. This demonstrates the benefit of the CNP formulation and encourages further investigations of this modeling approach in the future. Finally, it has to be emphasized that identical results for all unknown fields are obtained with both the CNP and the ENP model.

#### 4.1.4 Electrolytic cell between two concentric cylinders

In the following numerical example, a model problem for an electrolyte solution confined between two concentric cylinder surfaces is considered (see Bauer et al. [11]). The inner cylinder with radius  $r_i = 1$  is forming the cathode surface, while the outer cylinder with

parameter	$c_1^\infty$	$\beta$	$\alpha_a$	$\alpha_c$	$i_0$	$V_E$
anode	1.0	1.0	1.0	0.0	1.0	5.0( $V_A$ )
cathode	1.0	1.0	0.0	1.0	1.0	0.0( $V_C$ )

Table 4.1: Parameters for the Butler-Volmer law used for the concentric cylinder example.

radius  $r_o = 2$  is defining the anode surface. The height of the computational domain is given as  $H = 1$ . Material properties and boundary conditions are set identical as specified in Bauer et al. [11]. Thus, the values  $z_1 = 1$ ,  $z_2 = -1$ ,  $D_1 = 5.0$  and  $D_2 = 10.0$  are used in the following. In this example, the ionic species  $k = 1$  is reacting, while species  $k = 2$  is inert. At both cylinder surfaces, the Butler-Volmer law (2.44) is used for modeling electrode kinetics. The corresponding parameters are listed in Table 4.1. Here, the SGFEM for the ENP systems of equations is considered. According to Bauer et al. [11], the rotationally-symmetric exact solution to this problem is given as

$$c_1^{\text{exact}}(r) = c_1^i + \frac{\ln r - \ln r_i}{\ln r_o - \ln r_i} (c_1^o - c_1^i), \quad (4.13)$$

$$\Phi^{\text{exact}}(r) = \Phi^i + \ln(c_1(r)/c_1^i), \quad (4.14)$$

and again  $c_2^{\text{exact}}(r) = -z_1 c_1^{\text{exact}}(r)/z_2$  due to the electroneutrality condition. Since the two cylinder surfaces are aligned with the  $z$ -axis, the cylinder radius is defined as  $r(\mathbf{x}) = \sqrt{x^2 + y^2}$ . The problem-specific constants  $c_1^i$  (cation concentration at inner cylinder surface),  $c_1^o$  (cation concentration at outer cylinder surface) and  $\Phi^i$  (electric potential at inner cylinder surface) are obtained from simulation results using a very fine spatial resolution ( $h = 0.01$ ).

A backward Euler time-integration scheme ( $\theta = 1$ ) is used to compute the stationary solution. This procedure ensures that the total amount of inert ions contained is fixed, so that the computed solution fulfills

$$\int_{\Omega} c_2(\mathbf{x}) d\mathbf{x} = \pi(r_o^2 - r_i^2)H = 3\pi, \quad (4.15)$$

corresponding to an average anion concentration value of one. When the stationary form of the ENP system of equations is considered instead, (4.15) must be explicitly added as an additional constraint in order to obtain a unique solution. In contrast, the pseudo-transient approach utilized here automatically ensures (4.15) given appropriate initial fields for the ionic concentrations.

Successive, simultaneous mesh refinement in each spatial direction is performed. The coarsest mesh uses two elements in radial as well as axial direction and twelve elements in the circumferential direction. A characteristic element length  $h$  is defined by the gap size  $r_o - r_i$  divided by the number of elements in radial direction. Fig. 4.13 depicts computed solutions for  $c_1$  and  $\Phi$  based on a mesh with  $h = 0.125$ . As can be seen in Fig. 4.14, a second-order convergence rate is also obtained for the current setting including nonlinear Butler-Volmer kinetics and curved boundaries.

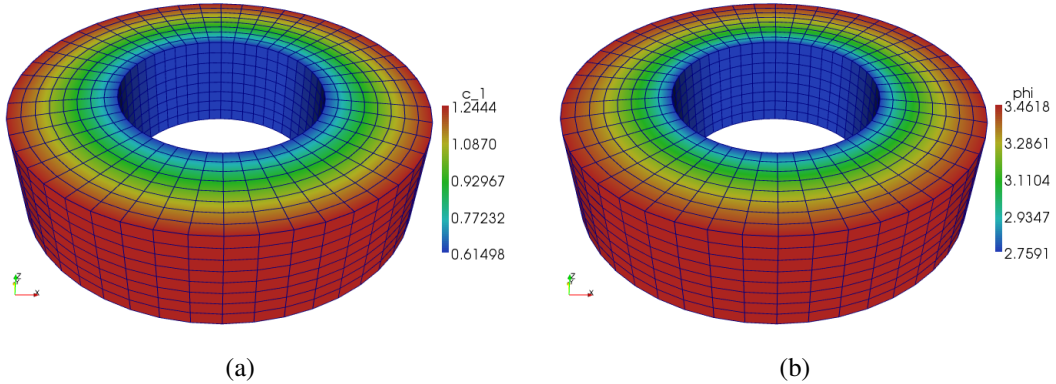


Figure 4.13: Numerical results for cation concentration  $c_1$  (a) and electric potential field  $\Phi$  (b) at steady state obtained for a mesh with  $h = 0.125$ .

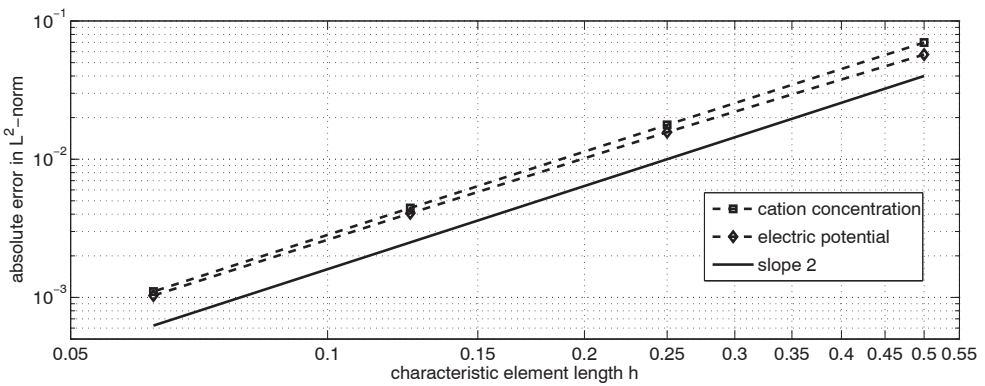


Figure 4.14: Spatial convergence for cation concentration  $c_1$  and electric potential  $\Phi$  obtained for an electroplating problem including Butler-Volmer electrode kinetics.

## 4.2 Oscillating shear flow cell

As an example for unsteady tertiary current density distributions a configuration governed by an oscillating shear flow is considered. In the following a summary of the results presented in Bauer et al. [11] is given. The setup of the problem investigated below is originally described in detail by Yang and West [182]. A two-dimensional sketch of the cell configuration is provided in Fig. 4.15.

Here, the cathode with length  $2L$  is part of the bottom plane that is oscillating in its own plane. The counter electrode (anode) is placed above the working electrode in a distance  $H$ . In the following it holds  $L = 0.125$  mm and  $H = 16$  mm. In the experiments carried out by Yang and West [182], the anode of size 20 cm  $\times$  13 cm and the bottom plane are very large compared to the line-shaped cathode ( $2L \times 2$  cm). Thus, the planes at top and bottom can be assumed infinitely long. However, the computational domain has to be limited by two artificial boundaries located at  $x_1 = -(D+L)$  and  $x_1 = D+L$ . The value for  $D$  has to be chosen sufficiently large for not introducing errors due to these artificial boundaries. Here, a value of  $D = 20$  mm is used. Dimensional input parameters were derived from the non-

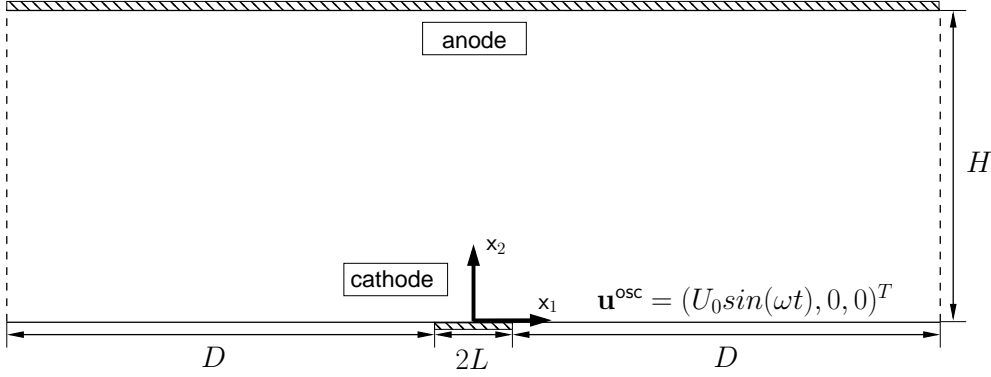


Figure 4.15: Two-dimensional sketch of the oscillating shear flow cell (not drawn to scale).

dimensional data specified by Yang and West [182]. The velocity of the bottom boundary plane at  $x_2 = 0$  is given as

$$\mathbf{u}^{\text{osc}}(x_1, 0, x_3, t) = (U_0 \sin(\omega t), 0, 0)^T, \quad (4.16)$$

where  $U_0 = 32.6 \text{ mm/s}$  and  $\omega = 0.645 \text{ s}^{-1}$ . Consequently, the periodic time is  $T_p = 9.74 \text{ s}$ .

This example is especially interesting, since the one-way coupling of multi-ion transport to fluid flow is tested for an unsteady problem including all three mechanisms of ion transport. In addition, the usage of nonlinear kinetic models at the cathode surface is emphasized. Depending on the applied cell potential, situations far below and also near the limiting current density are investigated. In Yang and West [182], two-dimensional simulations using finite-difference schemes were performed. Here, an appropriate three-dimensional “slice” with thickness  $L/20$  is used as computational domain for testing the present three-dimensional implementation and proving that the computational approach can also deal with essentially two-dimensional problem setups. In Yang and West [182], a linear approximation to the convective velocity field was used in the vicinity of the cathode, which was derived analytically. In contrast, the time-dependent incompressible Navier-Stokes equations are actually solved at every time step to provide the current flow field. This way, the proposed one-way coupling algorithm is tested within this example as well. For the incompressible flow problem, the proposed stabilized finite element formulation is used. In accordance to Bauer et al. [11], the SGFEM formulation of the ENP system of equations is utilized for modeling the present multi-ion transport problem.

A zero initial velocity field is used to start computing the flow of electrolyte solution. For this purpose, a sinus function is used in (4.16) instead of a cosine curve as done by Yang and West [182]. However, this merely amounts to a simple shift in time, redefining the origin of the time axis  $t = 0$ . The kinematic viscosity of the dilute electrolyte solution is assumed to be  $\nu = 1.0 \text{ mm}^2/\text{s}$ . The degrees of freedom located at the nodes of the artificial left and right boundary representations are connected by periodic boundary conditions. This enables the computation of unsteady shear flow between two infinitely long plates, where the lower one is oscillating in its own plane with velocity  $\mathbf{u}^{\text{osc}}$ . At the top boundary, a zero velocity boundary condition is prescribed, and the pressure reference level is set to zero. The  $x_3$ -component of the velocity vector is set to zero at the front and back boundary of the three-dimensional computational domain.

Copper deposition from an aqueous 0.003 M CuSO<sub>4</sub> – 0.1 M H<sub>2</sub>SO<sub>4</sub> electrolyte solution under potentiostatic conditions is considered. As done by Yang and West [182], complete dissociation is assumed resulting in a multi-ion transport problem involving three different ionic species: Cu<sup>2+</sup> ( $k=1$ ), SO<sub>4</sub><sup>2-</sup> ( $k=2$ ) and H<sup>+</sup> ( $k=3$ ). The specific properties and bulk concentration values are listed in Table 4.2. The electrode kinetics boundary condition for the cathode is based on the following relationship for the normal current density:

$$i_n = i_0 \left[ \exp\left(\frac{\alpha_a F}{RT} (V_c - \Phi)\right) - \left(\frac{c_1}{c_1^\infty}\right)^\beta \exp\left(\frac{-\alpha_c F}{RT} (V_c - \Phi)\right) \right]. \quad (4.17)$$

Note that here the concentration-dependency is only present at the cathodic term. The parameter values are  $i_0 = 4.0 \mu\text{A}/\text{mm}^2$ ,  $\beta = 0.5$ ,  $\alpha_a = 1.5$  and  $\alpha_c = 0.5$ . The anode potential defines the reference level for  $\Phi$  and is set to zero ( $V_a = 0 \text{ V}$ ). No overpotential is considered at the anode. The potential  $V_c$  at the metal side of the cathode is  $V_c = -0.095 \text{ V}$  in the first experiment, corresponding to 45% of limiting current density, and  $V_c = -0.245 \text{ V}$  in the second one. According to Yang and West [182], the latter corresponds to 97% of limiting current density. The applied cell potential differences are the same as those used in the reference, but a different reference level for the electric potential is used here.

Since the temperature of the electrolyte solution is not explicitly given in the reference, a reasonable value of  $T = 298 \text{ K}$  is assumed. At left, right and top boundary, being far away from the cathode, the boundary conditions are set as  $c_k = c_k^\infty$  and  $\Phi = 0 \text{ V}$ . At all other boundary parts not yet discussed, zero mass flux is assumed for all concentrations. It is beneficial to solve the electrochemistry equations in a frame of reference where the cathode and its associated boundary part are at rest. Thus, the relative motion of electrolyte solution with respect to the origin is required for solving the electrochemistry problem. Consequently, the velocity of the origin has to be subtracted from the velocity field  $\mathbf{u}^f$  computed from the Navier-Stokes solver. Thus, the relative convective velocity to be used in the ion-transport equations reads

$$\mathbf{u}(\mathbf{x}, t) = \mathbf{u}^f(\mathbf{x}, t) - \mathbf{u}^{\text{osc}}(\mathbf{0}, t), \quad (4.18)$$

being zero all along the bottom boundary plane. Since fluid flow and ionic transport are considered in the complete area between the parallel planes, one can choose  $H/2$  as characteristic length and a time-averaged velocity value of  $2U_0/\pi$  as characteristic velocity. The corresponding Reynolds number is  $\text{Re} = U_0 H / (\nu \pi) = 166$  and the according value for the Peclet number is  $\text{Pe} = \text{Re} \cdot \text{Sc} = 230,609$  with a Schmidt number of  $\text{Sc} = \nu/D_1 = 1389$ . A particular definition of a Peclet number was given by Yang and West [182], reading  $\text{Pe} = (\omega/\nu)^{0.5} U_0 L^2 / D_1 = 568$ .

ionic species	Cu <sup>2+</sup>	SO <sub>4</sub> <sup>2-</sup>	H <sup>+</sup>
$z_k$	+2	-2	+1
$D_k [10^{-3} \text{ mm}^2/\text{s}]$	0.721	0.0659	0.312
$c_k^\infty [\mu\text{mol}/\text{mm}^3]$	0.003	0.103	0.2

Table 4.2: Material parameters and electrolyte bulk concentrations of ionic species.

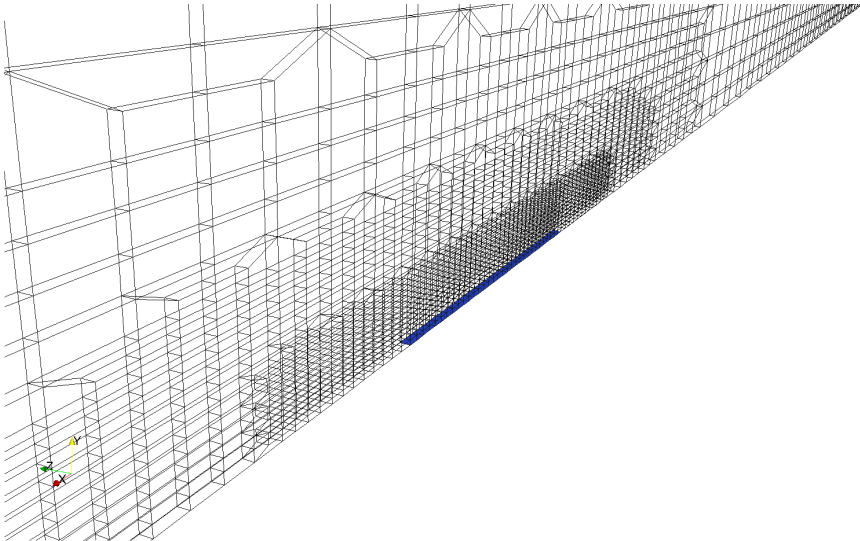


Figure 4.16: Locally refined mesh near the cathode surface.

The computational domain is discretized using a symmetric mesh with 184 elements in  $x_1$ -direction and 60 in  $x_2$ -direction. The considered three-dimensional slice is discretized with one element in  $x_3$ -direction. Refinement towards the bottom plane is realized with mesh grading using a bias factor of 1.065. The elements next to the bottom plane exhibit a height of about 24.3  $\mu\text{m}$ . Near the cathode surface an additional local refinement is applied (see Fig. 4.16). Thus, the minimum edge length in  $x_2$ -direction of elements adjacent to the cathode is locally reduced to 3.041  $\mu\text{m}$ . In total, the mesh consists of 12,296 hexahedral elements with trilinear shape functions and 25,148 nodes.

Here, a generalized trapezoidal rule with  $\theta = 0.5$  is utilized for time integration. A constant time-step length of  $\Delta t = T_p/100$  is used in all simulations. For the start-up phase of each simulation, an appropriate smooth ramp function is applied for changing  $V_c$  from zero to its final value within one period of oscillation. With four degrees of freedom per node for the fluid problem (velocity  $\mathbf{u}^f$ , pressure  $p$ ) and four degrees of freedom per node for the electrochemistry fields ( $c_1, c_2, c_3, \Phi$ ), in total, more than 200,000 degrees of freedom have to be determined within each time step.

At least 15 periodic cycles (1500 time steps) are computed before any data evaluation is performed. This ensures that initial transients have vanished and the quasi-static periodic solution has been reached. In Fig. 4.17, the computed copper cation concentration profiles near the cathode are depicted for the case  $V_c = -0.245$  V. Snapshots at four different times are provided which clearly reveal the influence of the oscillating shear flow on the shape of the concentration boundary layer. The periodic changes in the boundary-layer thickness cause the observed oscillatory behavior of mass flux and current density at the cathode surface. In Fig. 4.18, the temporal evolution of the spatially averaged current density at the cathode surface is shown over two periods of oscillation. The comparison with the experimental data from Yang and West [182] shows excellent agreement for both investigated values of applied cell voltages. The computed evolution of copper cation concentration at the cathode surface relative to the bulk value is depicted in Fig. 4.19. These data are also space-averaged along the electrode surface. Oscillation of concentration due to periodic shear flow is observed here as well. For  $V_c = -0.245$  V the  $\text{Cu}^{2+}$ -concentration is varying

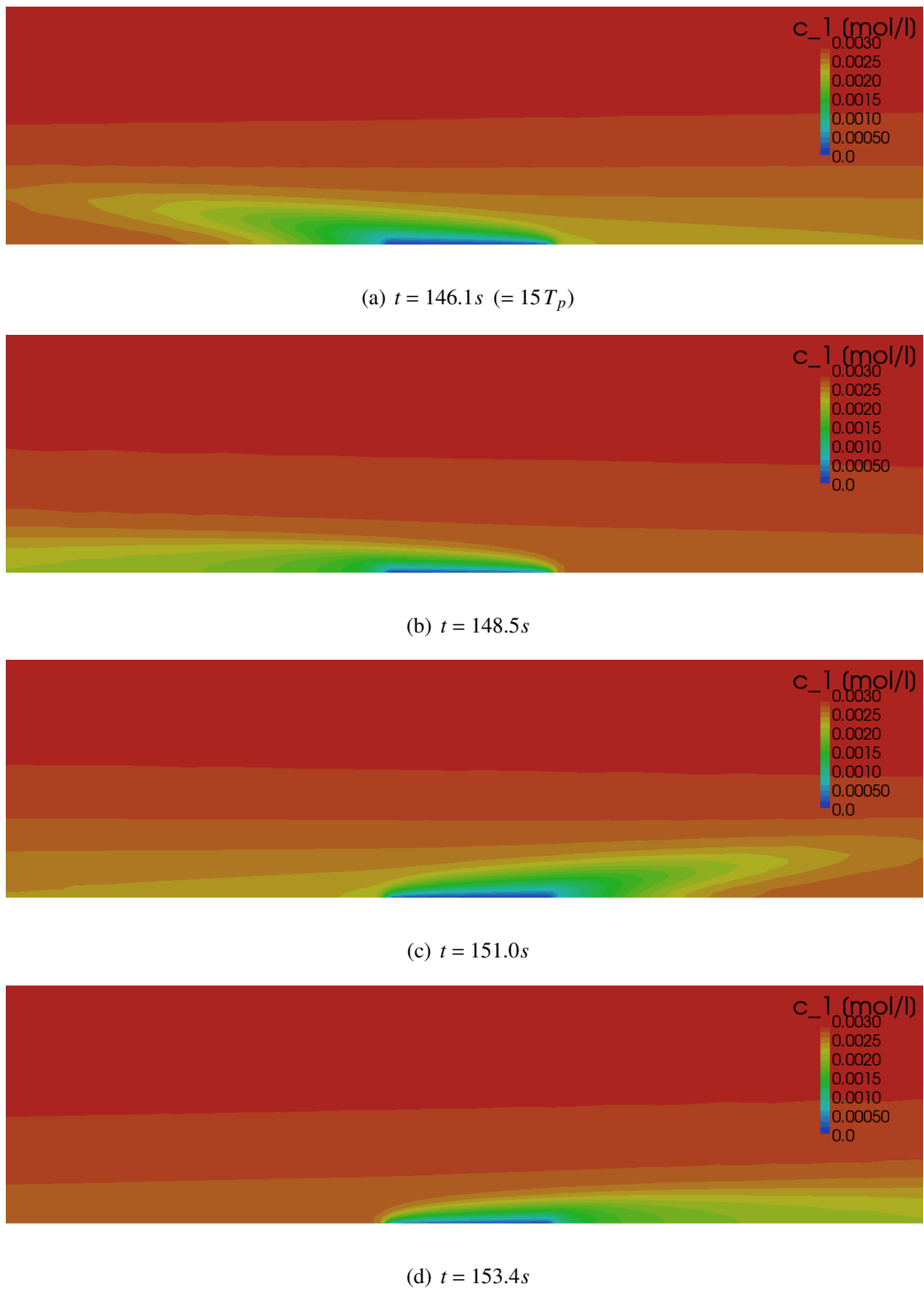


Figure 4.17: Concentration boundary layer of  $\text{Cu}^{2+}$  forming near the cathode surface: snapshots at various times within one oscillation period ( $T_p = 9.74\text{s}$ ).

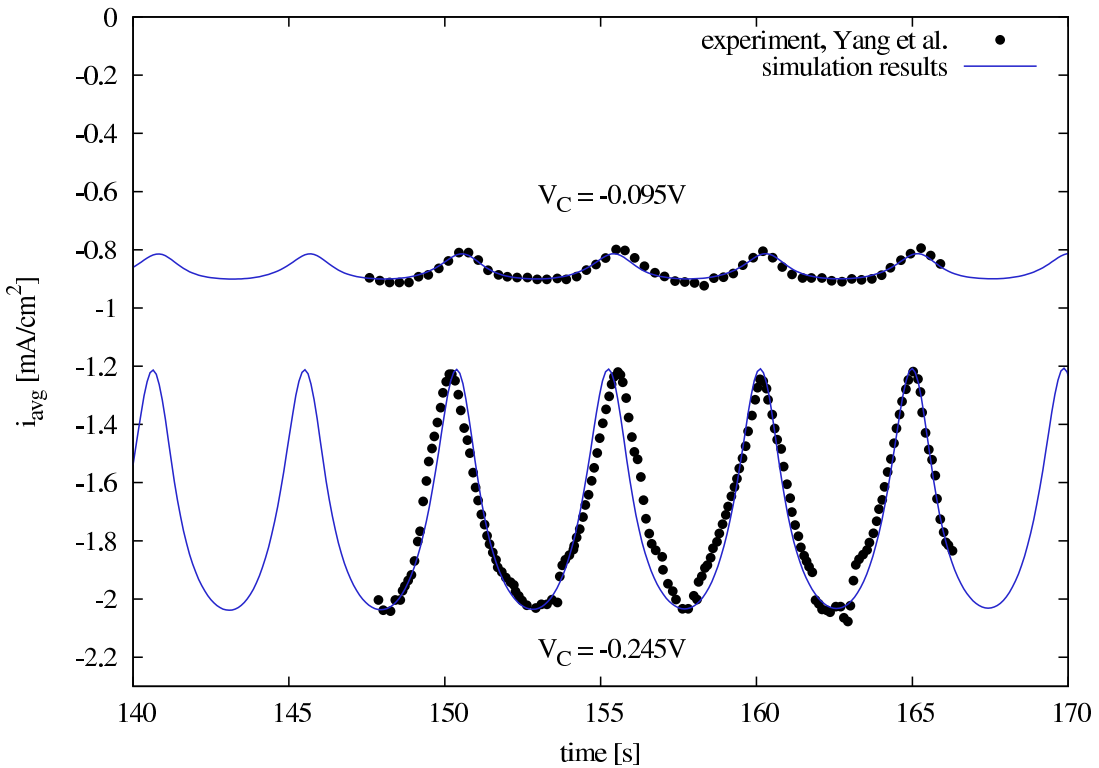


Figure 4.18: Temporal evolution of space-averaged cathodic current density. Comparison of computed results with experimental data provided in Yang and West [182].

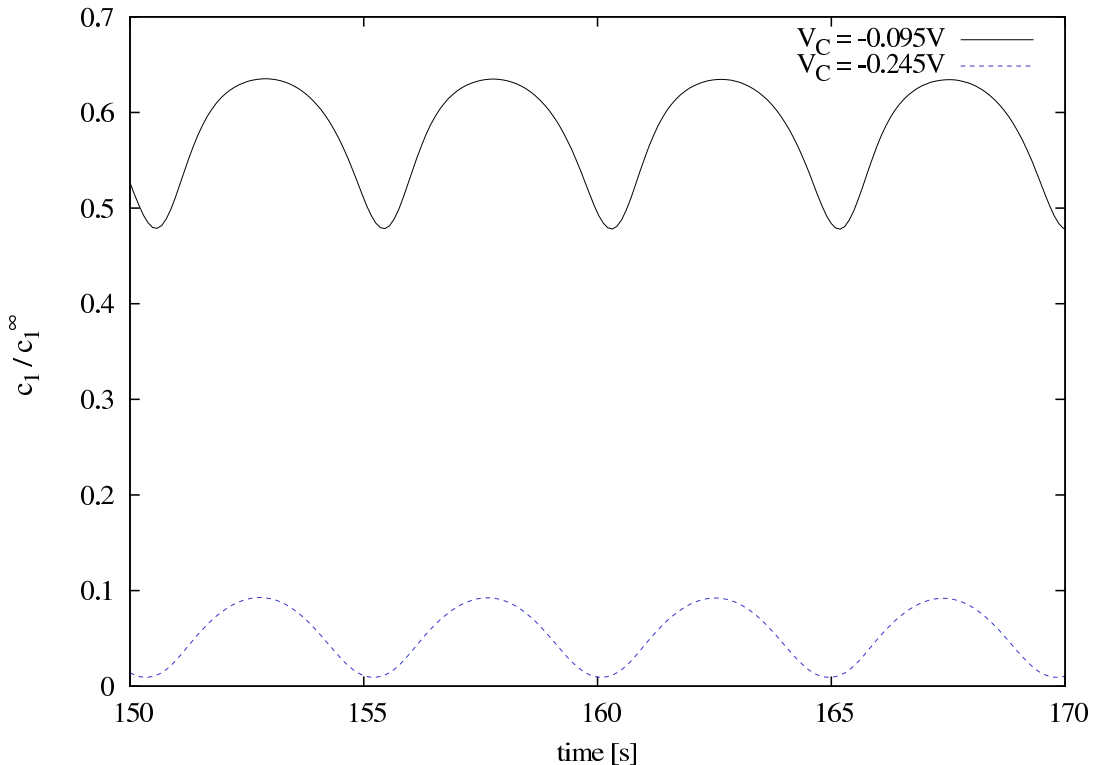


Figure 4.19: Numerical results for the temporal evolution of space-averaged surface concentration of  $\text{Cu}^{2+}$  ions at the cathode.

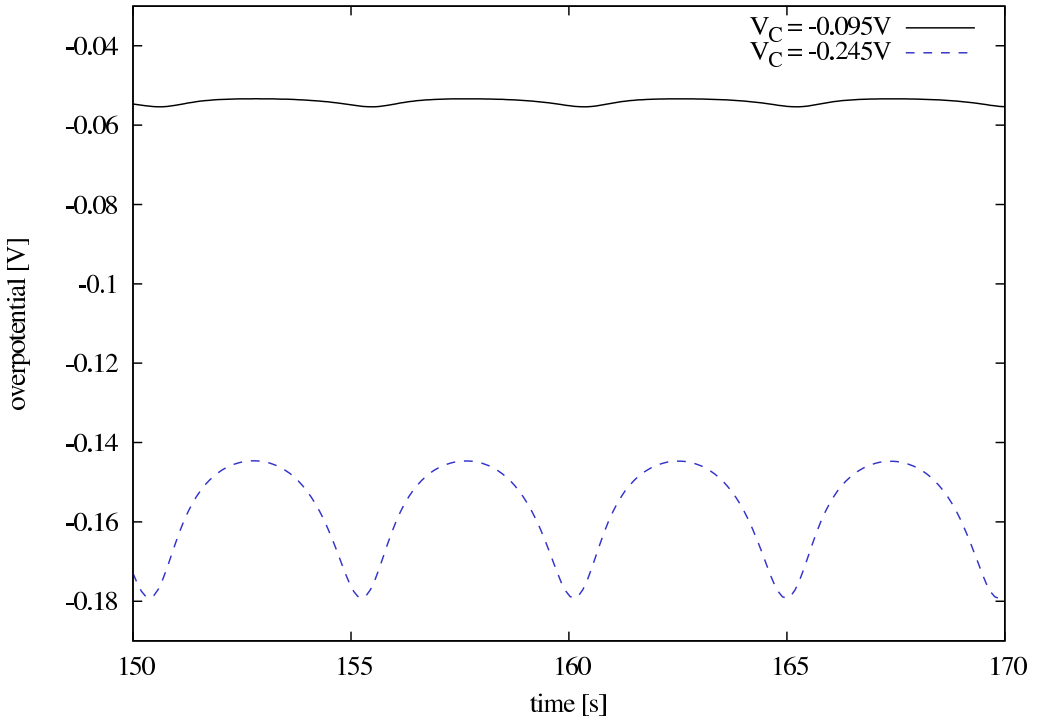


Figure 4.20: Numerical results for the temporal evolution of space-averaged surface overpotential  $\eta_{s,c} = V_c - \Phi$  at the cathode.

between 1% and 10% of the bulk concentration value reflecting that the cell is operating near the limiting current density in the second experiment. For the same time interval as before, the average surface overpotential  $\eta_{s,c} = V_c - \Phi$  is finally plotted in Fig. 4.20 for both experiments.

### 4.3 Natural convection in a rectangular electrolytic cell

In the following numerical example, galvanostatic copper deposition from a binary electrolyte solution coupled to buoyancy-driven flow is investigated. In this context, the advantage of the proposed general galvanostatic boundary condition combined with a Butler-Volmer formulation is demonstrated. The considerations below are a summary of the simulation results presented recently in Ehrl et al. [56]. A rectangular electrolytic cell with parallel vertical electrodes is considered. In Fig. 4.21, the exact geometrical setup is illustrated. The electrodes of the cell are directly embedded into an insulator. The simulations are conducted in a two-dimensional domain to be comparable to respective results of Kawai et al. [113, 114].

Here, two different modeling approaches are compared. In the computational model M1, the ENP system of equations is considered. A Butler-Volmer condition (2.44) for the reacting ionic species is used at the electrode surfaces. This boundary condition is combined with the proposed approach to galvanostatic simulations (see section 3.5.2). For comparative reasons also a second computational model is investigated, denoted as model M2, for which the single scalar transport equation (3.89) including a Neumann boundary condition for the reacting ionic species on the electrode is used. In this simplified

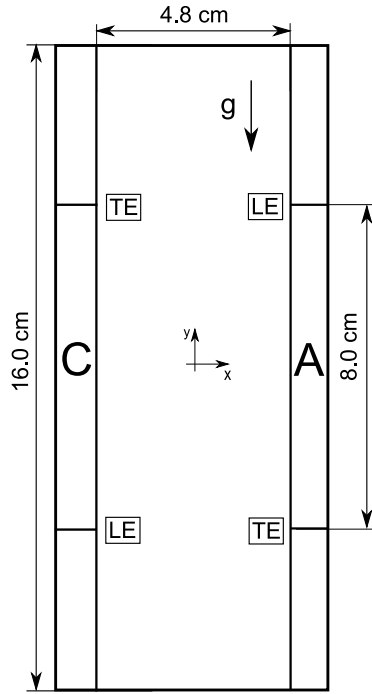


Figure 4.21: Rectangular electrochemical cell with vertical electrodes (C: cathode, A: anode, LE: leading edge, TE: trailing edge).

model M2 applicable only for binary electrolyte solutions, the potential is not a solution variable, but the migration effect is included in the diffusion coefficient of the electrolyte solution  $D$  defined in (3.90). The influence of the ionic surface concentration and the surface overpotential on the local current density is neglected when using a Neumann boundary condition.

For all inert ionic species, no-flux boundary conditions are applied at the electrode surface. No-flux boundary conditions are also used for all ionic species at the remaining boundary parts, which are representing insulating surfaces or a free surface at the top of the cell. The latter is modeled using a free-slip boundary condition for the flow problem. All other boundaries represent rigid walls. Thus, no-slip boundary conditions are applied there. In order to obtain a unique solution, a zero value for the pressure is prescribed at the left lower corner of the cell. The Boussinesq approximation is utilized to account for natural convection in the electrolytic cell. Standard gravity acceleration  $g = 9.81 \text{ m/s}^2$  is assumed.

The required physical properties of the aqueous  $\text{CuSO}_4$  solution considered here are provided in Table 4.3. Complete dissociation is assumed for this binary electrolyte. Consequently, the valences of the two ionic species are  $z_{\text{Cu}^{2+}} = 2$  and  $z_{\text{SO}_4^{2-}} = -2$ . According to Ehrl et al. [56], the two ionic diffusion coefficients  $D_{\text{Cu}^{2+}}$  and  $D_{\text{SO}_4^{2-}}$  are calculated from the diffusion coefficient of the electrolyte solution  $D_{\text{CuSO}_4}$  using definition (3.90) and the transference number for binary electrolyte solutions given by (see, e.g., Newman and

aqueous electrolyte solution (Kawai et al. [113]):	0.05 M CuSO <sub>4</sub>
applied current densities $i_{\text{tot}}$ [mA cm <sup>-2</sup> ]	1.96, 3.65
$D_{\text{CuSO}_4}$ [cm <sup>2</sup> s <sup>-1</sup> ]	$6.50 \times 10^{-6}$
$D_{\text{Cu}^{2+}}$ [cm <sup>2</sup> s <sup>-1</sup> ]	$5.08 \times 10^{-6}$
$D_{\text{SO}_4^{2-}}$ [cm <sup>2</sup> s <sup>-1</sup> ]	$9.03 \times 10^{-6}$
$t_{\text{Cu}^{2+}}^*$ [-]	0.36
$\nu$ [cm <sup>2</sup> s <sup>-1</sup> ]	$1.0 \times 10^{-2}$
$\rho_0$ [g cm <sup>-3</sup> ]	0.99
$\alpha_{\text{CuSO}_4}$ [cm <sup>3</sup> mmol <sup>-1</sup> ]	0.16
parameters for Butler-Volmer law (Kawai et al. [116]):	
$i_0$ [mA cm <sup>-2</sup> ]	3.73
$\beta$ [-]	0.75
$\alpha_a$ [-]	1.5
$\alpha_c$ [-]	0.5

Table 4.3: Physical properties and model parameters.

Thomas-Alyea [137] and Appendix A)

$$t_{\text{Cu}^{2+}}^* = \frac{z_{\text{Cu}^{2+}} \mu_{\text{Cu}^{2+}}}{z_{\text{Cu}^{2+}} \mu_{\text{Cu}^{2+}} - z_{\text{SO}_4^{2-}} \mu_{\text{SO}_4^{2-}}}. \quad (4.19)$$

Strictly speaking, this approach is only valid in the bulk of the electrolyte solution, since definition (4.19) is only valid for binary electrolyte solutions in the absence of concentration gradients. The densification factor  $\alpha_{\text{CuSO}_4}$  can be used instead of the densification factors of single ionic species, since the electroneutrality requires the same amount of cations as anions to be at each point of the domain. The parameters for the Butler-Volmer condition (2.44) are taken from Kawai et al. [116] and are listed in Table 4.3. According to Kawai et al. [113, 114], a temperature value of  $T = 293$  K is assumed.

The computational domain is discretized by 180x640 bilinearly-interpolated quadrilateral elements. Towards both electrode surfaces the element length  $h_x$  is reduced to fully resolve the concentration boundary layers. The minimal element length adjacent to the electrode is  $h_{x,\min} = 20 \mu\text{m}$ . The element length  $h_y$  is reduced towards the leading and trailing edges, since concentration gradients and current densities are higher in these regions. A minimal element length in y-direction of  $h_{y,\min} = 70 \mu\text{m}$  is used. The element size is similarly refined towards the free surface and the bottom of the cell. For discretization in time, a generalized trapezoidal rule with  $\theta = 0.67$  is utilized here. A constant time step  $\Delta t = 0.05$  s is used for all simulations.

The numerical results obtained with the present computational approach are compared to numerical and experimental results published by Kawai et al. [113, 114]. In Fig. 4.22(a), the Cu<sup>2+</sup> concentration field including streamlines is plotted at  $t = 600$  s. Therein, the black rectangles at the left and right hand side indicate the electrodes of the electrolytic cell, whereas the dark-gray areas represent the insulators above and below the vertical electrodes. The lighter electrolyte solution with a decreased ion-concentration level accumulates at the top, the heavier at the bottom. In the center of the cell, the electrolyte solution rotates in clockwise direction. This flow pattern is slightly disturbed at the top

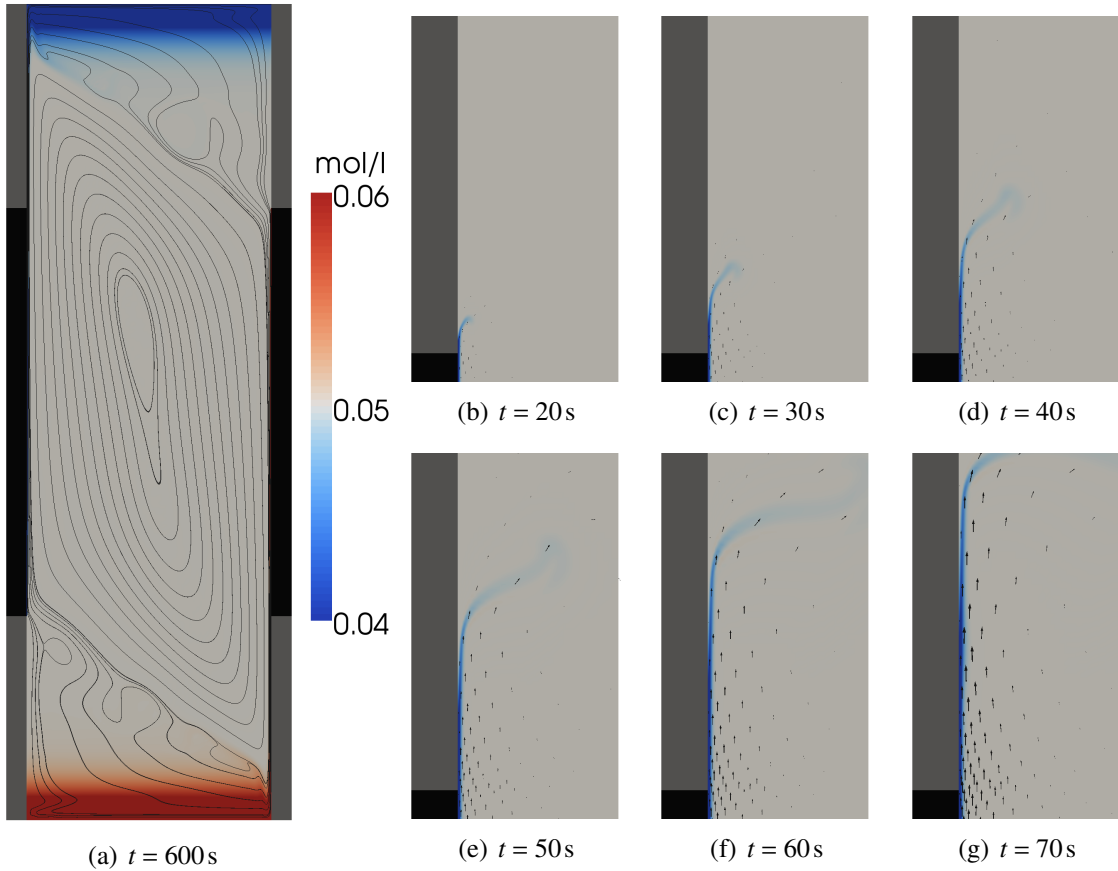


Figure 4.22: (a)  $\text{Cu}^{2+}$  concentration field including the velocity field displayed by streamlines and (b)-(g) detailed views of the  $\text{Cu}^{2+}$  concentration field in the vicinity of the cathodic trailing edge including the velocity field vectors at different time steps.

and bottom of the cell as shown in Fig. 4.22(a). The thin ionic diffusion layers at the electrodes can only be observed in a more detailed depiction. As an example, the trailing edge of the cathode is shown in Fig. 4.22(b)–4.22(g). This series of figures illustrates the development of the concentration boundary layer at the cathode while being carried away by the self-induced buoyancy-driven flow field. The presented computational approach (referred to as model M1 in this numerical example) is able to represent the three effects of ohmic overpotential, concentration overpotential and surface overpotential (see section 2.5.3). The surface overpotential is a result of the Butler-Volmer model for electrode kinetics, whereas ohmic and concentration overpotentials are accounted for automatically by the coupled ion-transport equations, as it can be observed in Fig. 4.23. In this figure, the electric potential is depicted along the horizontal line  $y = 0$ , which almost corresponds to an electric field line directed from the middle of one electrode to the other. Along such a line, the ohmic overpotential causes a linear potential profile behavior in the bulk electrolyte solution, since the uniform concentration levels lead to a constant conductivity. In the vicinity of the electrodes, that is inside the ionic boundary layer, the additional concentration overpotential causes a nonlinear potential profile which differs from the linear curve (black dotted line) obtained when assuming solely ohmic losses and a constant con-

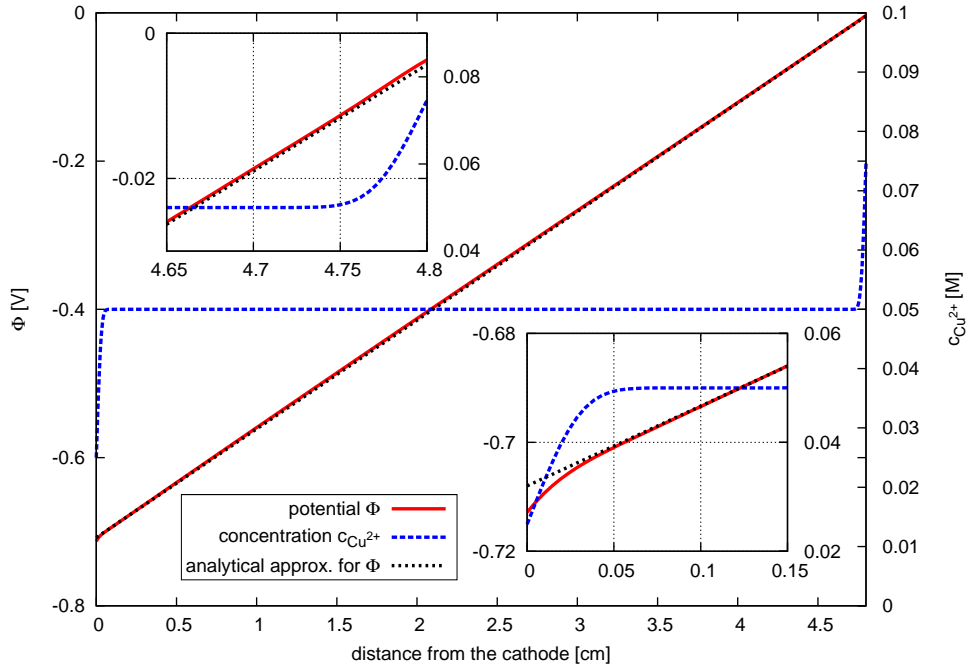


Figure 4.23: Electric potential along the horizontal line  $y=0$  at time  $t = 600\text{ s}$  ( $i_{\text{tot}} = 1.96\text{ mA/cm}^2$ ).

ductivity. It is emphasized that the influence of the concentration overpotential is much smaller at the anode.

The natural convection effects observed for the present cell configuration are caused by density variations inside the thin ionic diffusion layers. The latter are a result of the ongoing electrochemical reactions at the electrodes. Here, the electrochemical reaction (1.6) is considered here, where copper deposition takes place at the cathode and a corresponding dissolution process is occurring at the anode surface. A comparison of computed vertical velocities  $u_y$  (model M1 and M2) with experimental and numerical values from Kawai et al. [114] is presented in Fig. 4.24(a). Additionally, the temporal evolution of the maximal vertical velocity  $u_{y,\text{max}}$  is depicted in Fig. 4.24(b). Both simulation results agree very well with the numerical results of Kawai et al. [114], with the maximal velocity values being slightly higher, though. The higher value of  $u_{y,\text{max}}$  predicted by model M2 is in the range of the velocity fluctuations, as shown in Fig. 4.24(b). According to Kawai et al. [114], these fluctuations are the result of interacting upward and downward natural convection. However, in the present simulation, the fluctuations are not as distinct as the fluctuations reported by Kawai et al. [114]. The higher maximal velocity computed with model M1 is probably the result of different electrode surface concentrations (and therefore boundary-layer thicknesses), leading to different buoyancy effects. Additionally, the maximal velocity determined experimentally also confirms both numerical results.

Ionic surface concentrations can be expressed analytically in the case of an unsteady one-dimensional diffusion equation in a semi-infinite medium by the equation

$$c_{\text{Cu}^{2+}}(t) = c_{\text{Cu}^{2+}}^{\infty} + \frac{2(1-t^*_{\text{Cu}^{2+}})i_{\text{tot}}}{z_{\text{Cu}^{2+}}F} \sqrt{\frac{t}{\pi D_{\text{CuSO}_4}}},$$

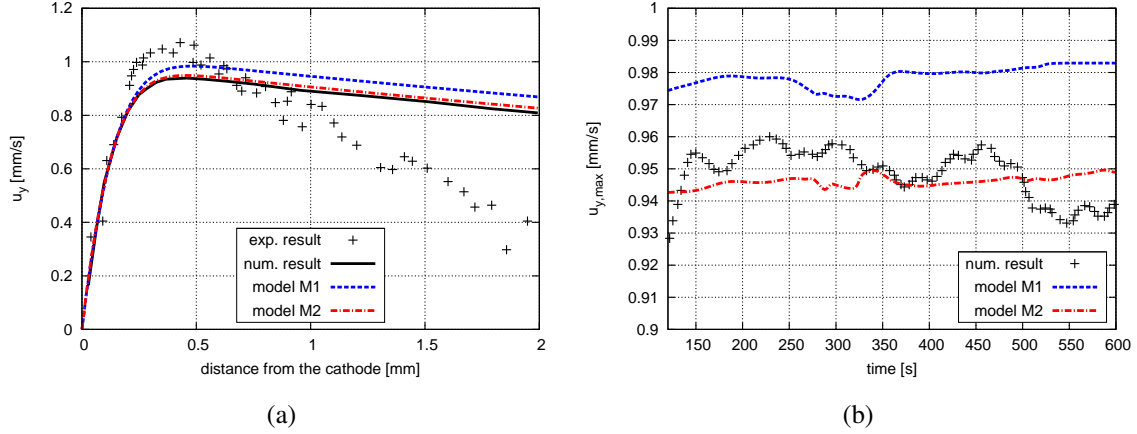


Figure 4.24: (a) Vertical velocity  $u_y$  for  $i_{\text{tot}} = 1.96 \text{ mA/cm}^2$  in the vicinity of the cathode along a horizontal line at  $y = 0$  at time  $t = 600\text{s}$  and (b) maximal vertical velocity component  $u_{y,\max}$  for  $i_{\text{tot}} = 1.96 \text{ mA/cm}^2$  along a line at  $y = 0$  over time  $t$ .

where  $i_{\text{tot}} = I_{\text{tot}}/A$  is the total applied current per electrode surface  $A$  (see, e.g., Bard and Faulkner [7]). The analytical solution fits very well to the present numerical results based on model M2, as may be observed in Fig. 4.25. Analytical, experimental and numerical (model M1 and M2) results are depicted against the square root of time in Fig. 4.25.

Initially, diffusion and migration are the dominating ion-transport phenomena. As shown in Fig. 4.25, the ionic concentration  $c_{\text{Cu}^{2+}}$  decreases proportional to the square root of time. Later on, the emerging buoyancy force becomes dominant and causes the surface concentration to converge to a quasi-steady state. From then on, numerical results deviate from the analytical solution, which does not account for convection effects. After the quasi-steady state has been reached, fluctuations can be observed in the ionic surface concentrations, which are due to the velocity fluctuations. In the case of  $i_{\text{tot}} = 1.96 \text{ mA/cm}^2$ , the solution resulting from model M2 is almost identical to the numerical results presented by Kawai et al. [114]. For a higher current density  $i_{\text{tot}} = 3.65 \text{ mA/cm}^2$ , the numerical results match very well until the beginning of the quasi-static state ( $t = 100\text{s}$ ). At this point, a jump in the surface concentration curve provided by Kawai et al. [114] is observable in Fig. 4.25, which is probably related to the specific boundary condition used by Kawai et al. [114], which includes a correction factor for the limiting current condition that is activated at a concentration limit of  $c_{\text{Cu}^{2+}} = 0.0025 \text{ mmol/cm}^3$  (cf. Kawai et al. [113]). This specific boundary condition in combination with the galvanostatic constraint condition leads to a non-uniform current density distribution at the cathode as shown by Kawai et al. [114]. In contrast to model M2, the galvanostatic constraint condition for model M1 leads to a slower reduction of the ionic surface concentration from the beginning on for both current densities considered. After the quasi-steady state has been reached, the observed concentration level is about 0.0025 M lower compared to the simulation with model M2, whereas the influence on the concentration is larger in the case of the lower current density. The galvanostatic constraint condition does not prescribe a local fixed current density at the single nodes of the electrode but allows a variable current density constrained by equation (2.48) and (2.49) at the cathode and the anode, respectively. As indicated in (2.44), the

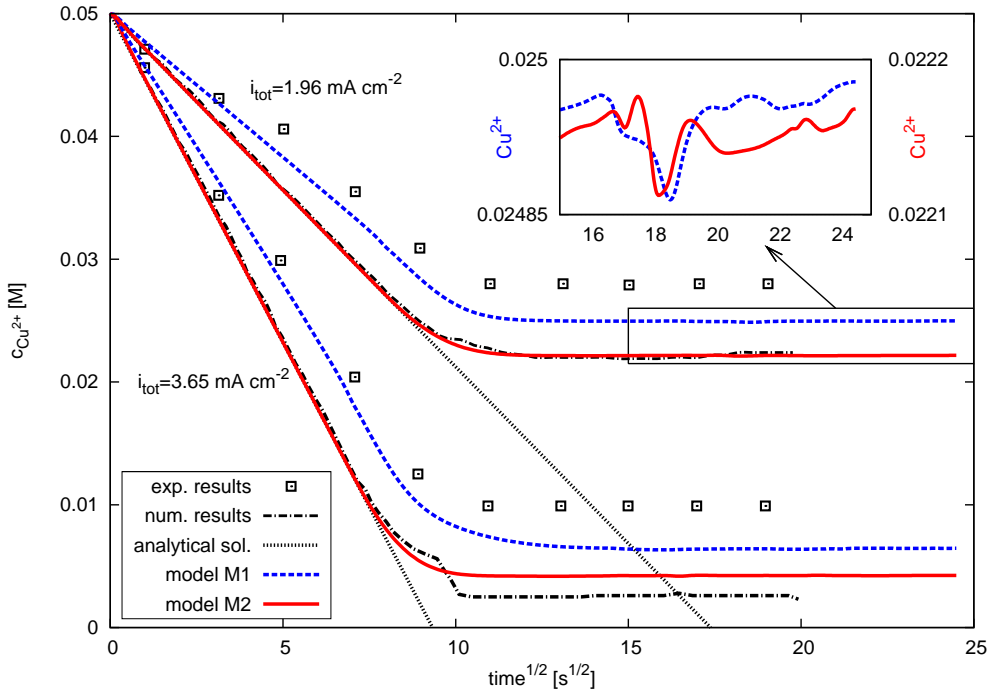


Figure 4.25: Surface concentration of  $\text{Cu}^{2+}$  ions in the middle of the cathode at  $y = 0$  plotted against the square root of time.

local current density  $i_n$  depends on the ionic surface concentration  $c_k(y)$  and the surface overpotential  $\eta_s(y) = V_E - \Phi(y)$ .

The effect of the galvanostatic Butler-Volmer boundary condition is demonstrated in Fig. 4.26 and 4.27. In Fig. 4.26, the cathodic current density  $i_n$  normalized by the applied current density  $i_{\text{tot}}$  is shown along the cathode. The solid black line indicates a uniform current distribution as it is imposed in the case of a Neumann boundary condition (model M2). In Fig. 4.27(a), the molar concentration of  $\text{Cu}^{2+}$  along the electrode is depicted. The solid lines represent the numerical solution obtained from model M2, whereas the dashed lines correspond to the application of galvanostatic Butler-Volmer conditions. In the case of  $i_{\text{tot}} = 3.65 \text{ mA/cm}^2$ , model M2 results in negative ionic concentrations at the trailing edge of the cathode, since a uniform current density distribution is prescribed along the whole electrode via a Neumann condition. In Kawai et al. [113], negative concentrations are avoided by introducing a specific boundary condition for limiting current conditions. For model M1, no negative concentration values occur and the zero concentration level for limiting currents is automatically fulfilled, as shown in Fig. 4.27(a).

In Fig. 4.27(b), the distribution of the electric potential  $\Phi$  normalized by the applied cell voltage  $U = V_c - V_a$  is depicted. The applied cell potentials are  $U = 0.72 \text{ V}$  for  $i_{\text{tot}} = 1.96 \text{ mA/cm}^2$  and  $U = 1.45 \text{ V}$  for  $i_{\text{tot}} = 3.65 \text{ mA/cm}^2$ . These values are a result of the proposed galvanostatic simulation approach. In particular, for each prescribed electric current required, values for the cathodic potential  $V_c$  are determined based on the choice  $V_a = 0 \text{ V}$ . The difference between the applied cathodic potential  $V_c$  and the potential  $\Phi$  at the electrolyte solution side of the electrode represents the cathodic surface overpotential  $\eta_{s,c} = V_c - \Phi$  (cf. section 2.5.3). Its non-uniform distribution along the cathode can be also

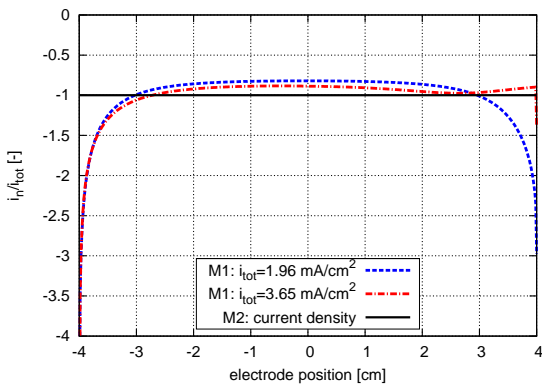


Figure 4.26: Non-uniform current density distribution for  $i_{\text{tot}} = 1.96 \text{ mA/cm}^2$  and  $i_{\text{tot}} = 3.65 \text{ mA/cm}^2$  along the cathode surface at  $t = 600 \text{ s}$ .

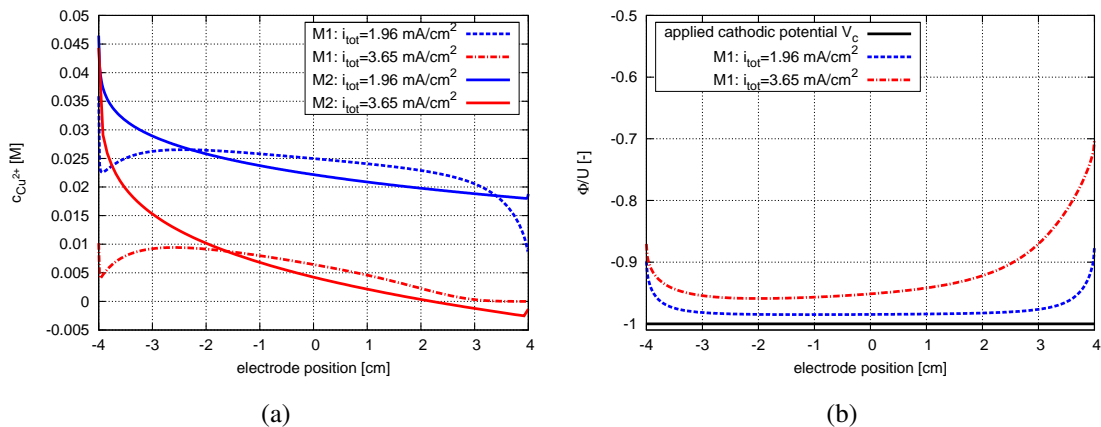


Figure 4.27: (a) Concentration and (b) normalized potential distribution  $\Phi/U$  for  $i_{\text{tot}} = 1.96 \text{ mA/cm}^2$  and  $i_{\text{tot}} = 3.65 \text{ mA/cm}^2$  along the cathode surface at  $t = 600 \text{ s}$ .

be observed in Fig. 4.27(b).

The current density computed with the galvanostatic condition exhibits a characteristic distribution dominated by the ohmic drop ( $i_{\text{tot}} = 1.96 \text{ mA/cm}^2$ ) and by convection and diffusion ( $i_{\text{tot}} = 3.65 \text{ mA/cm}^2$ ). In the latter case, the higher current density causes a lower ionic concentration at the cathode (see Fig. 4.27(a)). Consequently, higher buoyancy forces and vertical velocities arise in this case. Thus, unconsumed electrolyte solution is brought faster to the electrode at the leading edge, resulting in a very thin diffusion layer and locally very high, but finite, current densities. The finite value is a result of the non-uniform potential distribution at the electrode, particularly by the jump in the overpotential at the leading edge, as shown in Fig. 4.27(b). In contrast, the value would be infinite in the case of an equipotential surface on the electrolyte solution side of the electrode (primary current density distribution), as discussed in Newman and Thomas-Alyea [137]. The  $\text{Cu}^{2+}$  concentration declines to zero at the trailing edge (see Fig. 4.27(a)), since the majority of the cupric ions has already been consumed in the electrodeposition process further upstream. In the case of the lower current density, i.e.,  $i_{\text{tot}} = 1.96 \text{ mA/cm}^2$ , the

influence of convection can be observed in the declining concentration downstream (see, Fig. 4.27(a)), which has obviously a minor influence on the current distributions, since the concentration level does not decline to zero. Anyway, the current density peak at the leading edge is more distinct than the peak at the trailing edge. Both peaks are finite as a result of an increased surface overpotential at leading and trailing edge (see, Fig. 4.27(b)), whereas it is almost uniform in the middle of the electrode.

As discussed, e.g. in Newman and Thomas-Alyea [137], concentration variations along the electrode are usually ignored for the evaluation of current distributions in electrochemical systems with strong convection; it is emphasized that this is not the case for natural convection. Besides the surface overpotential, the ion-concentration level at the electrode influences the current density distribution. As a result, one observes non-uniform current density distributions exhibiting a characteristic U-shaped form as also described, e.g., by Wallgren et al. [176].

When the CNP system of equations (3.83)-(3.84) is utilized for this challenging two-way-coupled problem instead of the standard ENP model, identical results for all unknown fields are obtained. This is a very important observation, since it confirms the theoretical expectations. As a consequence, the number of iterations in the outer and inner loops of the two-way coupled partitioned scheme are identical as well.

Nevertheless, an increase in computational efficiency is observed, since within the CNP model the inert ionic species  $\text{SO}_4^{2-}$  is eliminated from the system of equations by means of electroneutrality. Consequently, it has only to be solved for the nodal values of  $c_1$  and  $\Phi$  within the electrochemistry subproblem. For the structured mesh with 115,200 quadrilateral elements considered here, the corresponding number of nodes is  $n_{\text{nod}} = 116,383$ . Thus, for the CNP model only  $2n_{\text{nod}} = 232,766$  degrees of freedom arise, while a number of  $3n_{\text{nod}} = 348,063$  degrees of freedom have to be determined for the ENP formulation. Furthermore, the CNP formulation does not lead to a saddle-point matrix system which is in general difficult to solve. This preliminary result demonstrates the benefit of the CNP formulation and encourages further investigations of this promising approach in the future.

## 4.4 Rotating cylinder electrodes

Another particularly important electrochemical cell configuration is the rotating cylinder electrode (RCE), where a cylinder-shaped cathode is rotating in the center of an electrolytic cell. A series of review articles by Gabe [66], Gabe and Walsh [67] and Gabe et al. [68] documented the research and development of RCE configurations. In the present context, the RCE also serves as an important model problem for electrodeposition applications, since rotationally-symmetric parts to be plated are usually rotated to achieve more uniform plating results.

Several different RCE configurations and physical phenomena are addressed in the following three examples. In section 4.4.1, primary and secondary current density distributions subject to galvanostatic conditions are computed for a rotating cylinder Hull cell. Natural convection induced by local density variations in the vicinity of a RCE is considered in section 4.4.2. Finally, coupled multi-ion transport in turbulent Taylor-Couette flow is studied in section 4.4.3. It is successfully demonstrated that the proposed computational approach is capable to provide accurate results for all of these challenging electrochemical configurations.

#### 4.4.1 Primary and secondary current density distribution

The first numerical example devoted to RCE configurations is based on the study by Madore et al. [129], who investigated primary and secondary current density distributions in a rotating cylinder Hull cell. In this reference also experimental results are provided, which enables a sophisticated comparison of experiment and simulation.

The basic experimental setup is depicted in Fig. 4.28(a), while the geometrical definitions are provided in Fig. 4.28(b). The cathode with height 6 cm and diameter 1.5 cm is part of the inner cylinder which is rotating around its own axis with 1250 rpm. The rotating cylinder is located in concentric position within a cylindrical insulating tube made of plexiglass with diameter 5.5 cm. The planar, circular counter electrode (anode) is located at the bottom of the vessel and has a diameter of 8 cm. Further details on the geometrical configuration are given in Fig. 4.28(b). The volume outside the insulating tube is not considered in the numerical simulations, since this region is assumed to be completely shielded by the insulating components of the cell. An illustration of the final computational domain is provided in Fig. 4.28(c).

Copper deposition from an aqueous 0.5 M CuSO<sub>4</sub> – 1.0 M H<sub>2</sub>SO<sub>4</sub> electrolyte solution is considered at a temperature of 25 °C ( $T = 298.15\text{ K}$ ). The specific conductivity of the electrolyte solution is  $\sigma = 0.286\text{ S/cm}$ , which is derived based on data provided by Madore et al. [129]. Four galvanostatic copper electrodeposition experiments with average cathodic current densities  $i_{\text{avg}} = 2, 10, 35$  and  $75\text{ mA/cm}^2$  were performed by Madore et al. [129]. Since the surface area of the cathode is  $28.27\text{ cm}^2$ , the four corresponding values for the total electric current are  $I_{\text{tot}} = 56.54, 282.7, 989.5$  and  $2120.3\text{ mA}$ .

According to Madore et al. [129], the highest applied current density corresponds to about 20% of the limiting current density. Thus, mass transfer effects can still be neglected and the simple model for the electric potential (2.53)-(2.57) is applicable. For both cathode and anode, the Butler-Volmer law (2.44) with parameters  $i_0 = 2.0\text{ mA/cm}^2$ ,  $\beta = 0$ ,  $\alpha_a = 1.285$  and  $\alpha_c = 0.571$  is used for modeling electrode kinetics. For the anode, the electrode potential is set to  $V_a = 0\text{ V}$ , while the cathode potential  $V_c$  is a further unknown of the galvanostatic problem, which has to be adjusted in order to reach the prescribed current values  $I_{\text{tot}}$ . For this purpose, the solution approach for current-controlled problems as presented in section 3.5.2 is utilized here.

The computational setup described here for modeling the secondary current density distribution can also be used to compute the primary current density distribution subject to a galvanostatic control. For this purpose, the value for the exchange current density is simply set to a very high value. In the present example, a value of  $i_0 = 1000.0\text{ mA/cm}^2$  is used. As a result, the influence of the surface overpotential  $\eta_s$  in the Butler Volmer equation (2.44) is artificially reduced to a negligible value and the ohmic resistance of the electrolyte solution becomes the only relevant dissipative effect. For a justification of obtained results, the computed values for  $V_c$  and  $V_a$  can be applied as Dirichlet boundary conditions (2.55) at the electrodes within a subsequent simulation run.

Owing to the radial symmetry of the present setup, the computations are actually performed only on one quarter of the cylindrical volume. The natural boundary condition  $\nabla\Phi \cdot \mathbf{n} = 0$  is used at all arising artificial boundaries. Except the electrodes, all other remaining boundaries are regarded as insulators, and homogeneous Neumann boundary conditions  $\nabla\Phi \cdot \mathbf{n} = 0$  are applied there as well. For all simulations, a very fine structured mesh consisting of 1,033,320 trinilearly-interpolated hexahedral elements is used.

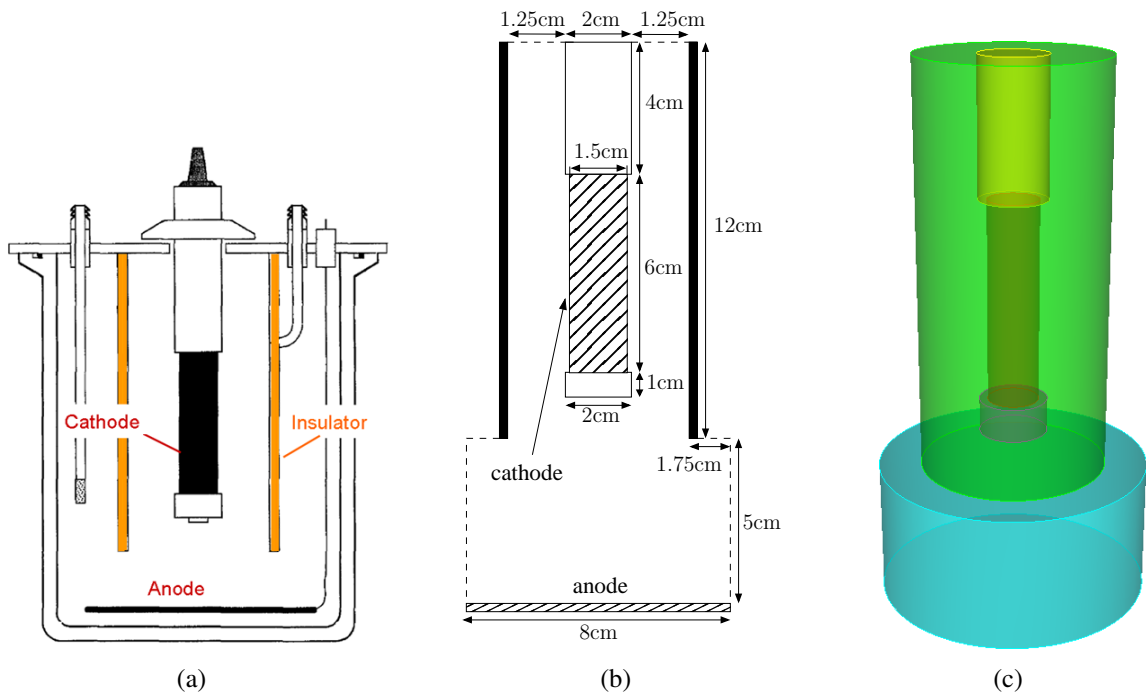


Figure 4.28: Problem setup for a rotating cylinder Hull cell: experimental setup (adapted from Madore et al. [129]) (a), geometric definitions (b) and three-dimensional visualization of the computational domain (c).

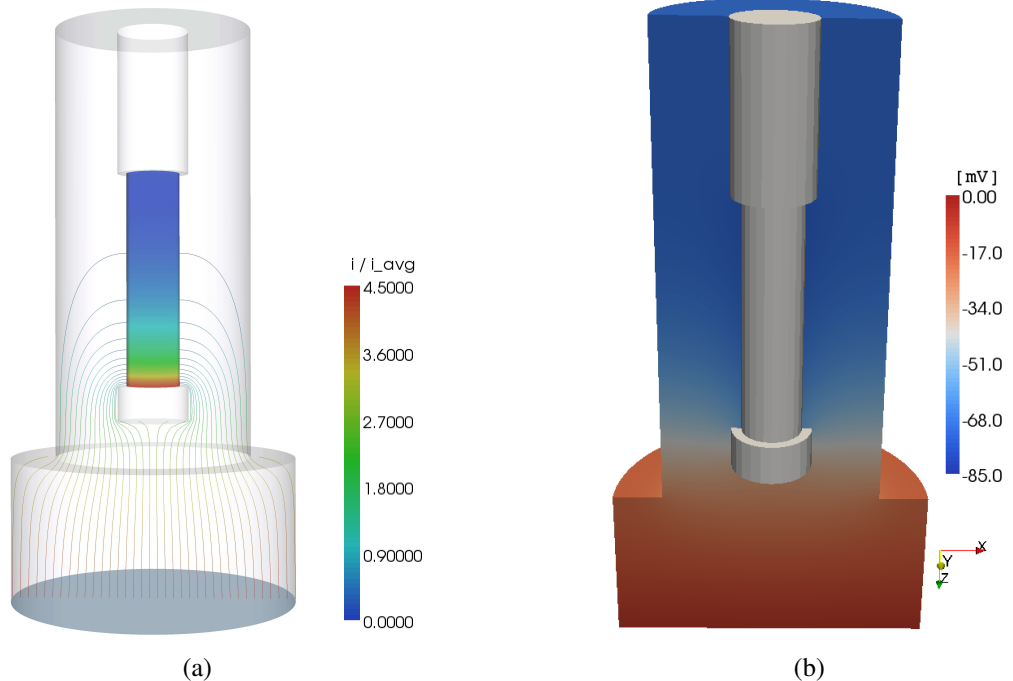


Figure 4.29: Visualization of the primary current density distribution at the cathode with electric field lines between the electrodes (a) and the electric potential field inside the electrolyte solution (b) .

$i_{\text{avg}}$ [mA/cm <sup>2</sup> ]	2	10	35	75
$V_c$ [mV] (primary current density)	-55.38	-276.9	-969.2	-2076.8
$V_c$ [mV] (secondary current density)	-84.56	-389.3	-1162.9	-2319.6

Table 4.4: Calculated cathodic electrode potentials required for reaching the four prescribed average current densities.

In Fig. 4.29(a), the computed primary current density distribution at the cathode surface is illustrated. Additionally, some characteristic field lines between the electrodes are shown. A visualization of the electric potential field inside the electrolyte solution is provided in Fig. 4.29(b). The depicted result is obtained from the model for the secondary current density distribution with an applied electric current of  $I_{\text{tot}} = 56.54 \text{ mA}$ .

The calculated current density distributions for the four experimental conditions are depicted in Fig. 4.30. Owing to the geometrical setup of the cell, non-uniform current density distributions are obtained along the cathode surface. For the primary current density distribution, the presented curves for  $i/i_{\text{avg}}$  are independent from the actual value of the electric current. Thus, the primary current density distribution is identical for all of the four simulations as shown in Fig. 4.30, reflecting that the cell geometry is governing the electric potential field in this case. Only for the higher applied currents the primary current density distribution comes close to the experimentally determined profiles, while the approximation at low currents is rather poor. In contrast, the secondary current density distribution shows very good agreement with the experimental data for all of the four applied currents. This example clearly demonstrates the importance of including the effects of surface overpotential into the model.

The cathodic electrode potentials  $V_c$  required to achieve the four prescribed mean currents are listed in Tab. 4.4 for both modeling approaches considered here. Unfortunately, no values for electrode or cell potentials are provided by Madore et al. [129]. Hence, a comparison of computed cell voltages with experimentally determined values is not possible for this example. In general, a combined comparison of current density distributions *and* corresponding cell voltages is important to validate a given computational model on a rigorous basis.

As a summary, the modeling approach for the secondary current density distribution provides an adequate model for the range of electric currents studied here. It is clearly demonstrated that it is important to take into account the surface overpotential at electrode surfaces. However, for higher current densities, an *a priori* assumption of negligible ionic mass transfer as done here is not valid anymore. For such situations, the full multi-ion transport model has to be solved. Since the inner cylinder is rotating with 1250 rpm, a turbulent flow problem has to be considered. A numerical example addressing such a challenging situation is presented below in section 4.4.3.

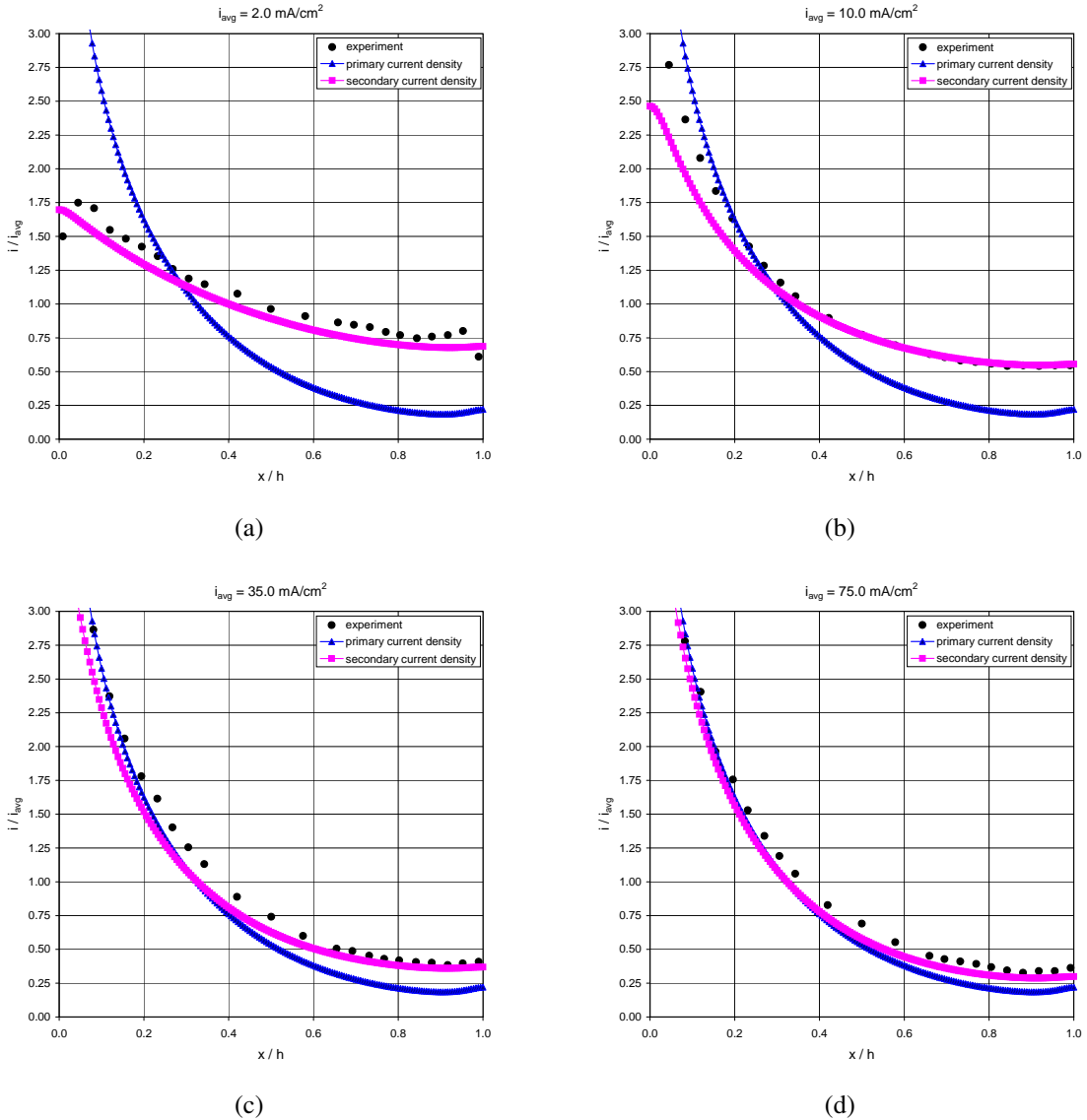


Figure 4.30: Numerical results for primary and secondary current density distributions along the cathode in comparison to the experimental values provided by Madore et al. [129].

### 4.4.2 Natural convection at a rotating cylinder electrode

The rotation of a RCE mainly induces so-called forced convection, which in turn influences the rate of electrochemical reaction (e.g., the deposition process in the present context of electroplating). When the rotational speed is low enough and concentration gradients are present, natural convection phenomena can become important as well. For a RCE configuration as considered by Mandin et al. [130], tertiary current density distributions influenced by natural convection are investigated below. Parts of the following example were published in Ehrl et al. [56]. In this reference further numerical examples for natural convection in electrolytic cells are provided.

For details on the present RCE setup, the reader is referred to Mandin et al. [130] as well as literature referenced therein. Mandin et al. [130] used a two-dimensional, rotationally-symmetric model to solve a stationary, conservative formulation of the Navier-Stokes equations. A single transport equation for the copper ion concentration was solved in a stationary and convective form for investigating the system at limiting current. Only convection and diffusion of copper ions was considered resulting in a “single-ion model”. Such a neglect of migration was justified by the high electric conductivity of the electrolyte solution due to an excess of supporting electrolyte (sulfuric acid) and the solely consideration of limiting current conditions. For a thorough discussion of this single-ion model for the electrolytic cell at limiting current and a validation of the present numerical method based on numerical results provided by Mandin et al. [130], the reader is referred to Ehrl et al. [56].

In contrast to that simplified ion-transport model, three-dimensional time-dependent simulations are performed here using the proposed two-way-coupled computational approach to account for natural convection. The limiting current value referenced in Mandin et al. [130] was determined experimentally by a linear voltammetry measurement presented in Mandin et al. [132]. Thus, time-dependent simulations are performed here in order to reproduce that voltammetry experiment. In addition, the full multi-ion transport problem is considered in the following, including a Butler-Volmer law for the reacting cupric ion at the cathode. The proposed stabilized finite element formulation for the ENP system of equations is utilized in this example.

In Fig. 4.31, the three-dimensional computational domain is illustrated. The rotating inner cylinder has a diameter of  $d_i = 2r_i = 12\text{ mm}$ . The part of the cylinder that is immersed in the electrolyte solution has a length of  $l_i = 60\text{ mm}$ . Only a part with length  $l_c = 4\text{ mm}$  of the total cylinder surface is an electro-active area (cathode) with a surface area of  $A = l_c\pi d_i = 150\text{ mm}^2$ . The center position of the cathode surface is located 38 mm below the free surface of the electrolyte solution. The entire outer cylindrical boundary surface (height  $l_o = 135\text{ mm}$  and diameter  $d_o = 76\text{ mm}$ ) is acting as anode. According to Mandin et al. [130], the inner cylinder is rotating with  $\omega = 1.0\text{ rad s}^{-1}$  and a constant temperature of  $T = 337\text{ K}$  ( $64^\circ\text{C}$ ) is assumed for the electrolyte solution. For these conditions, the hydrodynamic regime is considered mixed, i.e., both natural and forced convection are important effects for the given problem setup.

In accordance to Mandin et al. [130], a value of  $\nu = 6.6 \cdot 10^{-7}\text{ m}^2\text{s}^{-1}$  is used for the kinematic viscosity of the electrolyte solution at the given temperature. Furthermore, the density of the bulk electrolyte solution is given as  $\rho^\infty = 1158.7\text{ kg m}^{-3}$ . For the present setup, the Reynolds number is computed as  $\text{Re} = \omega r_i(r_o - r_i)/\nu = 290$ . Therefore, a laminar flow regime without any physical instabilities can be considered for this particular rotat-

ing cylinder configuration, as pointed out in Mandin et al. [130] and the previous studies referenced therein. Additionally, the laminar character of the developing flow field is also confirmed by a fully three-dimensional simulation not presented here. Assuming a laminar flow regime, the efficiency of the simulations can be enhanced by performing calculations only for a segment of the three-dimensional domain utilizing the rotational symmetry of the considered problem setup. Here, a wedge-shaped domain with an angle of  $\alpha = 15^\circ$  is chosen. This reduction of the domain size is only possible when imposing rotationally-symmetric boundary conditions at the same time, as described in more detail in Appendix C.

Copper electrodeposition from an aqueous electrolyte solution consisting of 0.567 M CuSO<sub>4</sub> and 1.63 M H<sub>2</sub>SO<sub>4</sub> as additional supporting electrolyte is studied. Complete dissociation is assumed, resulting in a multi-ion transport problem involving three different ionic species. These are given as Cu<sup>2+</sup> ( $k=1$ ), SO<sub>4</sub><sup>2-</sup> ( $k=2$ ), and H<sup>+</sup> ( $k=3$ ). The corresponding bulk concentration values are set to be

$$c_{\text{Cu}^{2+}}^{\infty} = 0.567 \text{ mol/l}, \quad c_{\text{SO}_4^{2-}}^{\infty} = 2.197 \text{ mol/l}, \quad c_{\text{H}^+}^{\infty} = 3.26 \text{ mol/l}.$$

In the experimental study by Moats et al. [134], the diffusion coefficient for cupric ions is given as  $D_{\text{Cu}^{2+}} = 1.07 \cdot 10^{-9} \text{ m}^2/\text{s}$  for a temperature of 60°C and  $D_{\text{Cu}^{2+}} = 1.23 \cdot 10^{-9} \text{ m}^2/\text{s}$  for 65°C for a very similar bath composition as the one considered here. It is important to note that these values are significantly lower than the value  $D_{\text{Cu}^{2+}} = 1.62 \cdot 10^{-9} \text{ m}^2 \text{s}^{-1}$  which was used by Mandin et al. [130]. For a thorough discussion and comparison of results concerning these different diffusion coefficients the reader is referred to Ehrl et al. [56]. In the following, two characteristic cupric diffusion coefficients given as  $D_{\text{Cu}^{2+}} = 1.1 \cdot 10^{-9} \text{ m}^2/\text{s}$  (DC1) and  $D_{\text{Cu}^{2+}} = 1.2 \cdot 10^{-9} \text{ m}^2/\text{s}$  (DC2) are considered, which are in accordance to the range of values experimentally determined by Moats et al. [134]. The Schmidt number of the problem is computed as  $\text{Sc} = \nu/D_{\text{Cu}^{2+}}$  = 660 in case of DC1. A value of  $\text{Sc} = 550$  is obtained when the diffusion coefficient DC2 is considered. Corresponding values for diffusivities of inert ionic species at 64°C are derived from so-called ionic equivalent conductances reported in the literature (for details, see, e.g., Newman and Thomas-Alyea [137]):  $D_{\text{SO}_4^{2-}} = 2.73 \cdot 10^{-9} \text{ m}^2/\text{s}$  and  $D_{\text{H}^+} = 2.38 \cdot 10^{-8} \text{ m}^2/\text{s}$ . The density of the electrolyte solution is correlated to the ionic concentrations via (2.65). The molar mass of each ionic species scaled by the density of the bulk electrolyte solution  $M_k/\rho^{\infty}$  serves as the basis for individual densification coefficients, resulting in  $\alpha_{\text{Cu}^{2+}} = 5.48 \cdot 10^{-5} \text{ m}^3/\text{mol}$ ,  $\alpha_{\text{SO}_4^{2-}} = 8.29 \cdot 10^{-5} \text{ m}^3/\text{mol}$  and  $\alpha_{\text{H}^+} = 8.63 \cdot 10^{-7} \text{ m}^3/\text{mol}$ .

At the inner cylinder surface, the velocity resulting from the rotation with  $\omega = 1.0 \text{ rad s}^{-1}$  is prescribed via

$$u_x = \omega y, \quad u_y = -\omega x, \quad u_z = 0. \quad (4.20)$$

The outer cylinder and the bottom of the cell are at rest. As done by Mandin et al. [130], the free surface at the top of the computational domain is modeled by free-slip boundary conditions for the flow problem. Based on experimental data provided by Mandin et al. [132], appropriate coefficients for the Butler-Volmer law (2.44) applied at the cathode surface were determined as:  $i_0 = 5.0 \text{ A/m}^2$ ,  $\alpha_c = 1.0$ ,  $\alpha_a = 1.0$  and  $\beta = 1.0$ . This parameter choice was found by a parameter study performing a series of simulations. A curve fitting without simulation is not possible in the present case since polarization curves are a result of the coupled ion-transport problem natural convection. At the outer cylinder surface

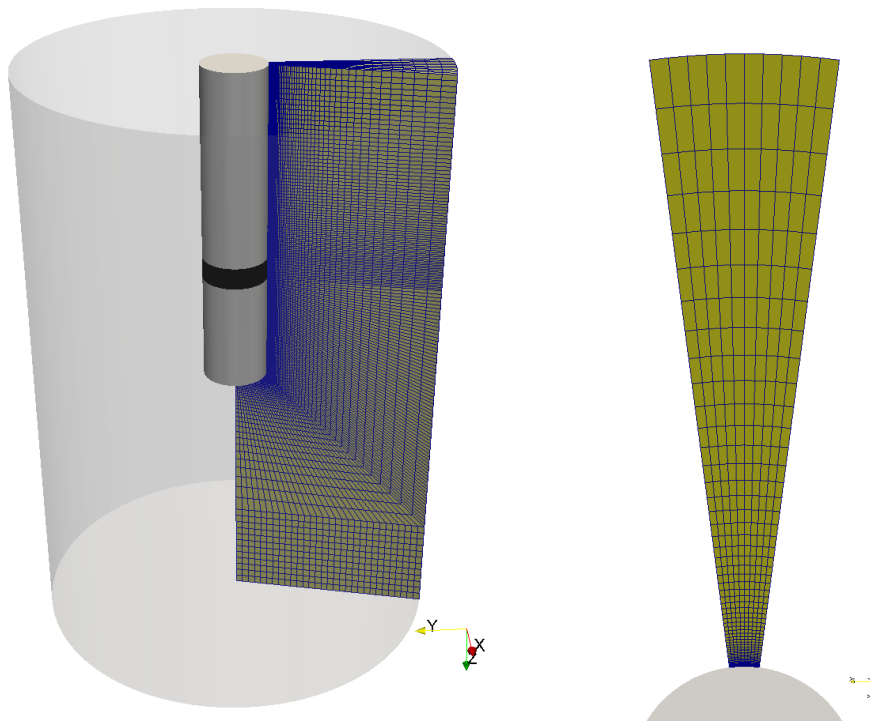


Figure 4.31: Computational domain and locally refined mesh towards the inner cylinder (left) and top view of the 15° segment (right).

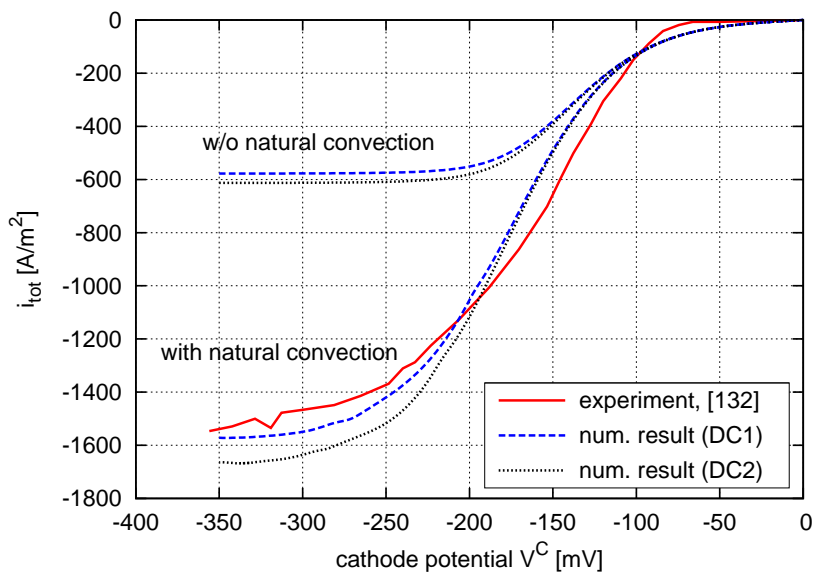


Figure 4.32: Linear voltammetry experiment for the considered RCE setup: comparison of present numerical results and experimental data provided by Mandin et al. [132].

the individual ionic concentrations and a reference level for the electric potential are prescribed reading  $c_k = c_k^\infty$  and  $\Phi = 0\text{mV}$ . For the free surface, the bottom of the cell as well as the insulating parts of the inner cylinder, no-flux boundary conditions are applied for all ionic species.

In total, the mesh consists of 260,085 trilinearly-interpolated hexahedral elements. The spatial discretization is refined towards the rotating cylinder in radial direction, with additional local refinement near the cathode surface. In Fig. 4.31, the wedge-shaped computational domain including the discretization is depicted. For illustration, the cathode surface on the inner cylinder is marked by a black area. In accordance to the experimental procedure referenced by Mandin et al. [132], the cell voltage  $U = V_a - V_c$  is linearly increased from  $U = 0\text{mV}$  to  $U = 350\text{mV}$  with a rate of  $1\text{mV/s}$ . Since  $V_a = 0\text{mV}$  is kept fixed, the cathode potential  $V_c$  is decreased from  $V_c = 0\text{mV}$  to  $V_c = -350\text{mV}$ . For this time-dependent simulation, a generalized trapezoidal rule ( $\theta = 0.66$ ) with a constant time-step size  $\Delta t = 1.0\text{s}$  is used. Before starting the linear decrease of  $V_c$ , a number of 30 time steps is used to compute a developed flow field induced by the rotation of the inner cylinder.

In Fig. 4.32, the numerically determined mean current densities are shown against the cathode potential  $V_c$  for the two considered diffusion coefficients DC1 and DC2. Both graphs match the experimental curve presented by Mandin et al. [132] quite well. The importance of including buoyancy effects is demonstrated by the two curves obtained from a one-way coupled simulation neglecting the effect of density variations. In this case, the obtained mean current densities are significantly lower compared to both the experiment and the simulations including natural convection. In general, the experimental curve used by Mandin et al. [132] to determine the value of  $1544\text{A/m}^2$  for the limiting current does not show a complete horizontal slope around  $V_c = -350\text{mV}$ , as shown in Fig. 4.32. This may represent an uncertainty for the experimentally determined limiting current value.

In Fig. 4.33, simulation results for velocity, cupric ion concentration and density fields for the cell operating at limiting current ( $U = 350\text{mV}$ ) are displayed. Cupric ion concentration profiles towards the cathode surface are depicted in Fig. 4.34. These are evaluated for the electrode center position at  $z = 38\text{mm}$ . With increasing cell voltage  $U$ , the surface concentration declines due to the increased consumption of ions in the electrochemical reaction. Finally, as shown for the case  $U = 350\text{mV}$ , the ionic concentration at the cathode surface approaches to zero and the limiting current condition is reached. Computed current density profiles along the RCE are presented in Fig. 4.35 for several intermediate states during the linear voltammetry experiment. In all curves, an increased current value at the leading edge of the electrode at  $z = 40\text{mm}$  is observed. From there towards the trailing edge, located at  $z = 36\text{mm}$ , the current density is decreasing, since the concentration boundary-layer thickness is increasing in vertical direction. In summary, the current density profiles exhibit a characteristic shape dominated by vertical convection. The difference in the diffusion coefficients DC1 and DC2 leads to slightly different results w.r.t. the current density. This difference is maximum when the limiting current is reached.

Limiting factors of the present numerical simulation are general inaccuracies in determining exact diffusion coefficients for individual ions, the concentration dependence of the diffusion coefficients, particularly for such concentrated electrolyte solutions, and unknown parameters for the phenomenological Butler-Volmer law. Finally, especially for such high temperatures as considered here, the temperature dependence of diffusion coefficients becomes important, as indicated above and also stated by Moats et al. [134].

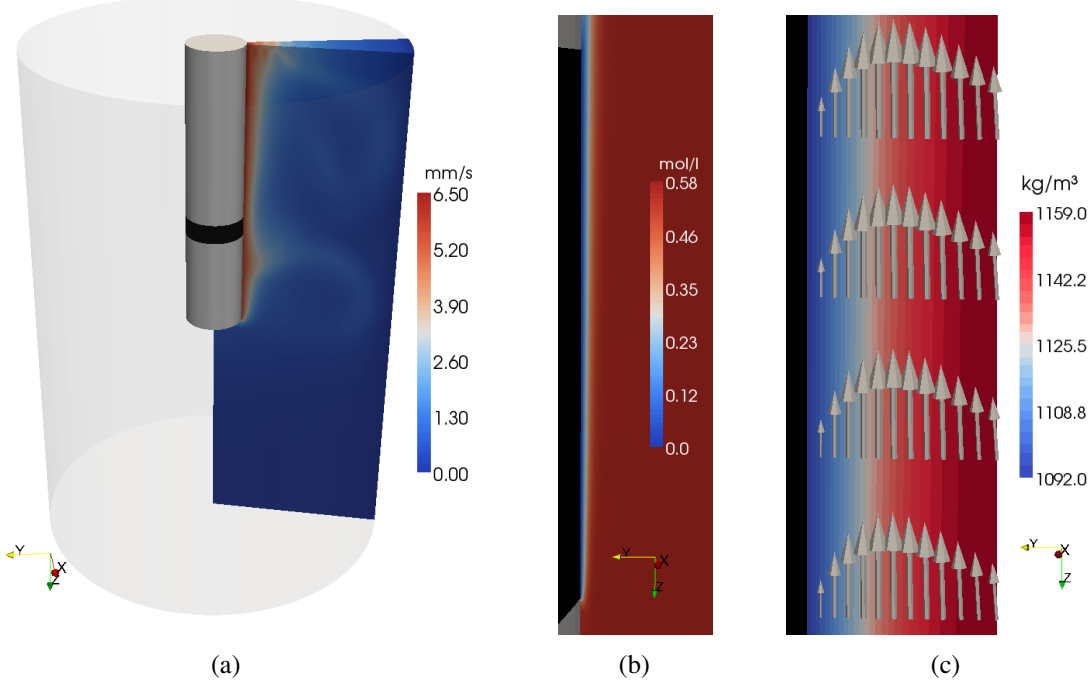


Figure 4.33: Simulation results at  $t = 380\text{ s}$  ( $U = 350\text{ mV}$ ) for the considered RCE configuration: (a) velocity magnitude  $\|\mathbf{u}\|$ , (b) zoom to the concentration boundary layer of cupric ions at the surface of the cathode and (c) detailed view of the density field including the vertical velocity component  $u_z$  near the cathode.

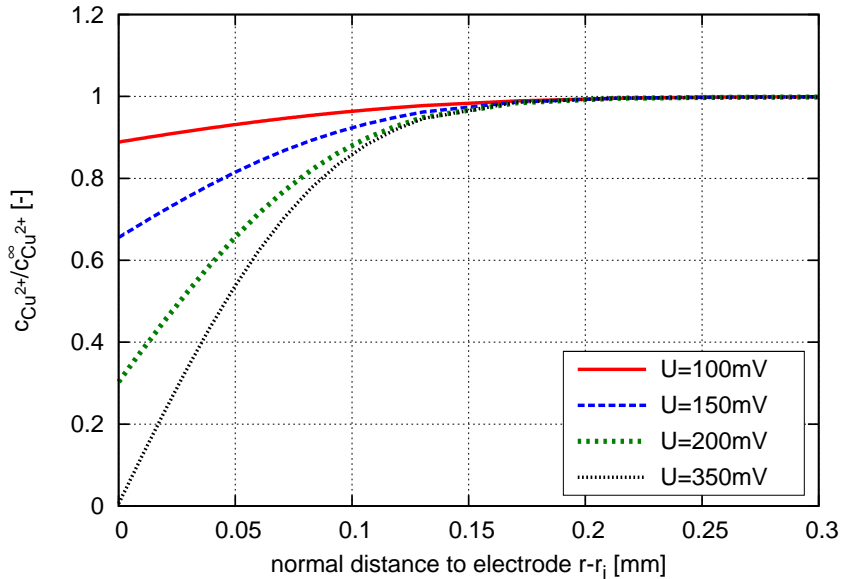


Figure 4.34: Concentration profiles near the cathode in radial direction for the case DC1 (evaluated at the cathode center position at  $z = 38\text{ mm}$ ).

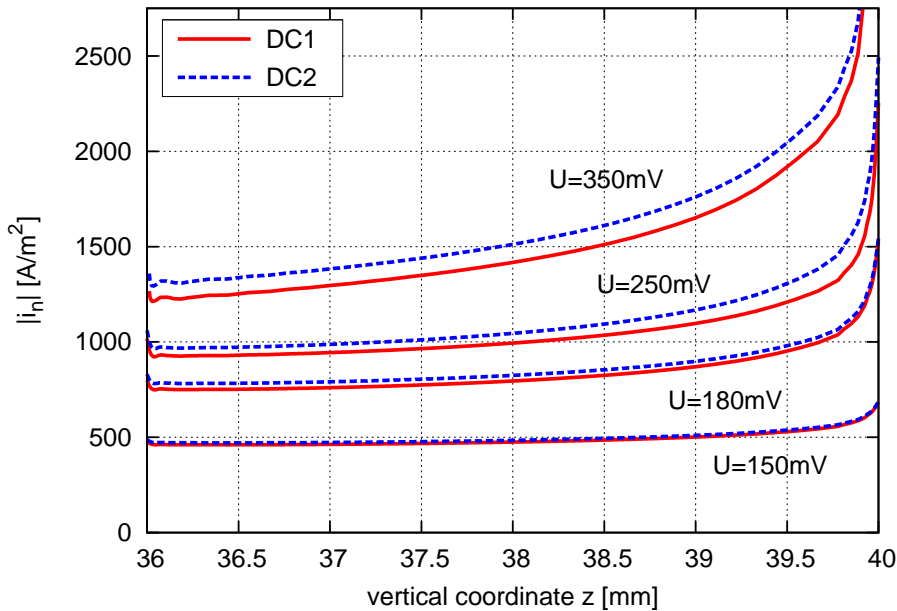


Figure 4.35: Computed current density distributions along the cathode surface in axial direction.

#### 4.4.3 Multi-ion transport in turbulent Taylor-Couette flow

In this numerical example, multi-ion transport in turbulent incompressible flow within the gap between two concentric cylinders is considered. The problem setup described in the following is a model problem for the well-known electrochemical configuration of a rotating cylinder electrode (RCE), which is usually used under turbulent flow conditions. The rotating inner cylinder surface acts as cathode, while the outer cylinder represents the anode of the electrolytic cell. The present geometric configuration is taken from Dong [52] and illustrated in the left part of Fig. 4.36. The dimensionless problem formulation of the ENP model as introduced in section 2.8.5 is used here. In the following, dimensionless quantities are marked with an asterisk.

The inner cylinder with radius  $R_i^* = 1$  is rotating about the  $z$ -axis with constant angular velocity  $\omega^* = 1$ . Based on the radius  $R_o^* = 2$  of the fixed outer cylinder a gap of width  $d^* = R_o^* - R_i^* = 1$  results. The space between the cylinder surfaces is filled by a dilute electrolyte solution. The height of the computational domain is set to  $H^* = \pi$ . For the flow solver, no-slip boundary conditions are prescribed on inner and outer cylinder surface, respectively. In the direction of the rotation axis, periodic boundary conditions are assumed.

The Reynolds number definition used by Dong [52] as well as Bazilevs and Akkerman [15] reads  $Re = U_i d / \nu$ , where  $U_i = \omega \cdot R_i$  is the imposed rotation velocity of the inner cylinder surface and  $\nu$  the kinematic viscosity of the electrolyte solution. In the following, the case  $Re = 8000$  is considered. According to Dong [52], the Taylor-Couette flow at this Reynolds number is fully turbulent. For the corresponding pure flow problem, DNS and LES data for comparison are provided in Dong [52], Bazilevs and Akkerman [15]. Other definitions for the Reynolds number were proposed in literature for the present geometrical configuration. For instance, in Eisenberg et al. [58], the diameter of the inner cylinder was

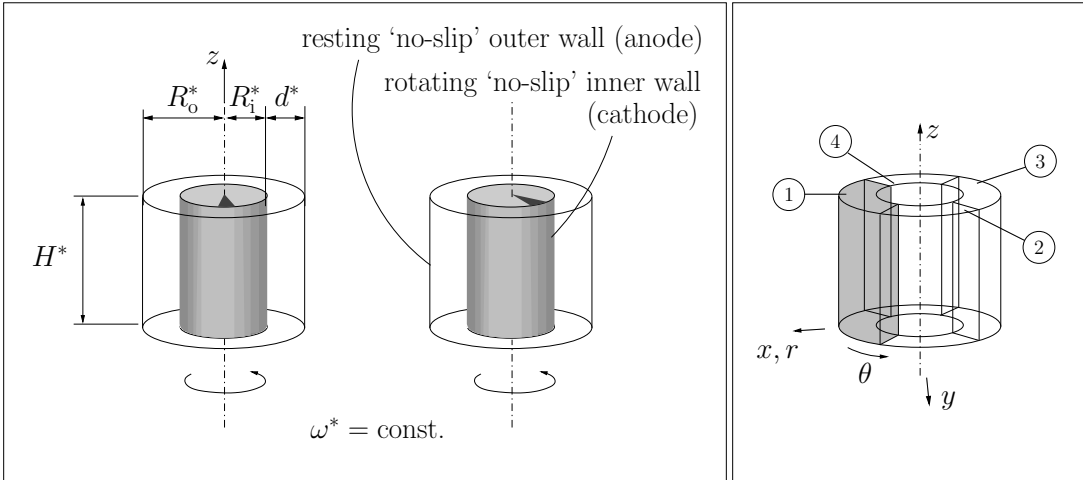


Figure 4.36: Problem setup (left) and patches for isogeometric discretization approach (right).

taken as the characteristic length, instead of the inter-electrode gap width. For the present geometry, this alternative definition yields a Reynolds number  $\text{Re}_D = 16,000$ .

In an experimental realization, all aforementioned dimensionless parameters describing the geometry and flow for  $\text{Re} = 8000$  would correspond, for instance, to  $U_i = 32 \text{ cm/s}$ ,  $R_i = 2.5 \text{ cm}$ ,  $R_o = 5.0 \text{ cm}$ ,  $d = 2.5 \text{ cm}$  and  $\nu = 10^{-2} \text{ cm}^2/\text{s}$ . Consequently, rotation of the inner cylinder takes place with about 122 rpm. These dimensional values are obtained from the non-dimensional setting based on the reference quantities  $L_{\text{ref}} = 2.5 \text{ cm}$ ,  $U_{\text{ref}} = 32 \text{ cm/s}$  and  $t_{\text{ref}} = L_{\text{ref}}/U_{\text{ref}}$ . Compared to the experimental settings used by Eisenberg et al. [58], it is evident that the present numerical model is indeed justified as an example for real applications.

As an example for multi-ion transport in this flow, potentiostatic copper electrodeposition from an aqueous 0.003 M CuSO<sub>4</sub> – 0.1 M H<sub>2</sub>SO<sub>4</sub> electrolyte solution is considered. A reasonable constant temperature value of  $T = 298 \text{ K}$  is assumed. Most of the required model parameters correspond to those used by Yang and West [182], who simulated copper deposition for a different geometry. As done by Yang and West [182], complete dissociation of the electrolyte is assumed, resulting in a multi-ion transport problem involving three different ionic species [ $\text{Cu}^{2+}$  ( $k=1$ ), SO<sub>4</sub><sup>2-</sup> ( $k=2$ ), H<sup>+</sup> ( $k=3$ )]. The specific properties and bulk concentration values are listed in Table 4.5 in non-dimensional form. Dimensional molar concentrations are obtained by multiplying with the reference concentration  $c_{\text{ref}} = 0.003 \text{ mmol/cm}^3$ , leading to  $c_k = c_{\text{ref}} \cdot c_k^*$ . Values for the molecular diffusion constants are taken from Newman and Thomas-Alyea [137]:  $D_1 = 0.72 \cdot 10^{-5} \text{ cm}^2/\text{s}$ ,  $D_2 = 1.065 \cdot 10^{-5} \text{ cm}^2/\text{s}$  and  $D_3 = 9.312 \cdot 10^{-5} \text{ cm}^2/\text{s}$ . The Peclet numbers are defined as  $\text{Pe}_k = U_i d / D_k$ . Values for the inverse of the Peclet number  $1/\text{Pe}_k$  required for the non-dimensional problem formulation are specified in Table 4.5. The reference flux is defined by  $N_{\text{ref}} = U_{\text{ref}} c_{\text{ref}}$ . The Schmidt number of the problem with respect to the reactive species is  $\text{Sc} = \nu / D_1 = 1389$ . Consequently, the Peclet number of the problem is  $\text{Pe} = \text{Re} \cdot \text{Sc} \approx 1.1 \cdot 10^7$ .

The electrode-kinetics boundary condition for both cathode and anode is based on the

following nonlinear relationship for the normal current density:

$$i_n^*(c_1, \Phi) = i_0^* \left[ \exp\left(\frac{\alpha_a F}{RT} (V_{\{c,a\}} - \Phi)\right) - \left(\frac{c_1}{c_1^\infty}\right)^\gamma \exp\left(\frac{-\alpha_c F}{RT} (V_{\{c,a\}} - \Phi)\right) \right],$$

where  $\gamma = 0.5$ ,  $\alpha_a = 1.5$ ,  $\alpha_c = 0.5$  and  $i_0^* = i_0 / (L_{\text{ref}} \cdot U_{\text{ref}})$ , with  $i_0 = 40.0 \text{ mA/cm}^2$  (see Yang and West [182] as well as Bauer et al. [11]). As a consequence of (2.40), the expression  $i_n^*/z_k F$  defines a non-dimensional current density. The electric potential  $V_c$  at the metal side of the cathode is linearly decreased from 0V down to  $V_c = -0.2V$  within the time period [0;0.2]. Afterwards, the potential is kept constant at value  $V_c = -0.2V$ . The anode potential defines the reference level for  $\Phi$  and is set to zero ( $V_a = 0V$ ) at the outer cylinder surface. The resulting total cell voltage difference of  $U = 0.2V$  is chosen high enough to reach limiting current conditions, where  $c_1^*$  tends to zero at the inner cylinder surface. As a result, diffusive mass transfer becomes the limiting factor of the electrochemical reaction and prevents further increase of current density with increasing cell voltage. Note that  $\Phi^* = F\Phi/RT$  provides a natural definition for a non-dimensional electric potential, since  $F/RT$  has the unit 1/V (cf. section 2.8.5).

For the spatial discretization of the present RCE configuration, an isogeometric representation consisting of 300,000 quadratic NURBS elements is used, constructed from four patches as displayed in the right part of Fig. 4.36. The computational domain is constructed geometrically exact, using a minimal number of control points and NURBS functions, which are first-order in  $u$  and  $w$  direction and second-order in  $v$  direction. Here, the directions  $u$ ,  $v$ , and  $w$  refer to the Cartesian coordinates of the knot space defined by the patches knot vector. Each patch is order-elevated geometrical exact to second-order in each direction and furthermore refined by knot insertion to  $60 \times 25 \times 50$  elements in  $r$ -,  $\theta$ - and  $z$ - direction, respectively.

In radial direction, the knot insertions were performed based on the mesh-stretching relationship  $h : [0, 1] \rightarrow [0, 1]$ :

$$u \mapsto h(u) = \frac{1}{2} \left( \frac{\tanh(C_{\text{stretch}}(2u - 1))}{\tanh(C_{\text{stretch}})} + 1.0 \right),$$

with  $C_{\text{stretch}} = 2.3$ . This mesh-stretching ensures a proper resolution of both flow and ion-concentration boundary layers close to both cylinder surfaces. For further details on the present spatial discretization and the required periodic coupling of basis functions in  $z$ -direction, the reader is referred to Bauer et al. [9].

ionic species	$\text{Cu}^{2+}$	$\text{SO}_4^{2-}$	$\text{H}^+$
$k$	1	2	3
$z_k$	+2	-2	+1
$1/\text{Pe}_k$	$9.0 \cdot 10^{-8}$	$1.33 \cdot 10^{-7}$	$1.164 \cdot 10^{-6}$
$c_k^{*,\infty}$	1.0	34.33	66.66

Table 4.5: Parameters for the multi-ion transport model (in non-dimensional form).

With four degrees of freedom per node (i.e., control point) for the fluid subproblem (velocity vector  $\mathbf{u}^*$ , pressure  $p^*$ ) and four degrees of freedom per node for the electrochemical subproblem (ionic concentrations  $c_1^*, c_2^*, c_3^*$ , electric potential  $\Phi^*$ ), in total, it has to be solved for more than 2.7 million degrees of freedom, as a result of a total number of control points of 339,456.

A generalized-alpha scheme with  $\rho_\infty = 0.5$  (i.e.,  $\alpha_m = 5/6$ ,  $\alpha_f = 2/3$ ,  $\gamma = 2/3$ ) is used here for time integration. As initial flow field, the steady-state radial-symmetric solution is applied, which holds for laminar flow conditions at low Reynolds number. For Cartesian coordinates, the analytical solution is given as

$$u_x^* = -\frac{y^*}{r^*} \left( \frac{4}{3r^*} - \frac{r^*}{3} \right), \quad u_y^* = \frac{x^*}{r^*} \left( \frac{4}{3r^*} - \frac{r^*}{3} \right), \quad u_z^* = 0,$$

with the (dimensionless) radial position  $r^* = \sqrt{(x^*)^2 + (y^*)^2}$  (for elaboration see, e.g., Spurk [161]). For the ionic concentrations, constant initial fields according to their respective bulk concentration values given in Table 4.5 are used. Note that, for isogeometric discretizations, in general, a least-squares problem has to be solved to determine the correct control point values for representing the prescribed initial fields.

The results shown in the following are obtained by running the simulation for more than 5000 time steps with  $\Delta t^* = 0.1$ . This non-dimensional value corresponds to a time-step size of about  $\Delta t = 7.81\text{ms}$ , when converted to dimensional units based on  $t_{\text{ref}} = L_{\text{ref}}/U_{\text{ref}}$ . Statistical sampling is performed over the last 3000 time steps, after a turbulent state of flow has been achieved. This sampling period corresponds to about 48 full rotations of the inner cylinder, providing a sufficiently large statistical data basis. First, the results obtained for a pure turbulent flow problem are evaluated. An isosurface for instantaneous pressure is provided in the left part of Fig. 4.37. The norm of the velocity field  $\|\mathbf{u}^*\|$  obtained at time  $t^* = 500$  is depicted in the right part of Fig. 4.37. Mean azimuthal velocity and corresponding fluctuations of the turbulent Taylor-Couette flow are presented in Fig. 4.38. For comparison, DNS results reported in Dong [52] are included, marked by ‘‘Dong DNS’’. The computed velocity results are in very good accordance with those DNS results. When neglecting the cross- and Reynolds-stress terms within the fluid problem formulation, a slightly larger deviation of the obtained mean velocity profile from the DNS results is observed as shown in Fig. 4.38. For the root-mean-square profiles there are not any notable differences, such that only one result curve is depicted in Fig. 4.38.

Second, the results obtained for multi-ion transport in turbulent flow are presented. Statistical results for mean and root-mean-square concentration profiles for  $c_1^*$  ( $\text{Cu}^{2+}$  concentration) are depicted in Fig. 4.39. Owing to the very high Schmidt number of the problem ( $\text{Sc} = 1389$ ), the concentration boundary layer of  $c_1^*$  is found to be much smaller than the flow boundary layer. The formation of the boundary layer at the inner cylinder is caused by the consumption of ions due to the electrodeposition process at the cathode, while the anodic oxidation reaction occurring at the outer cylinder surface establishes a source for  $c_1^*$ . Turbulent velocity fluctuations govern the boundary-layer thickness for ionic concentration species. Resolving these layers, typically forming inside the flow boundary layers, is one of the most challenging issues in the simulation of turbulent multi-ion transport. By choosing an isogeometric spatial discretization, the variation diminishing properties of NURBS are exploited to accurately represent the sharp boundary layers. It is emphasized that no  $\alpha$

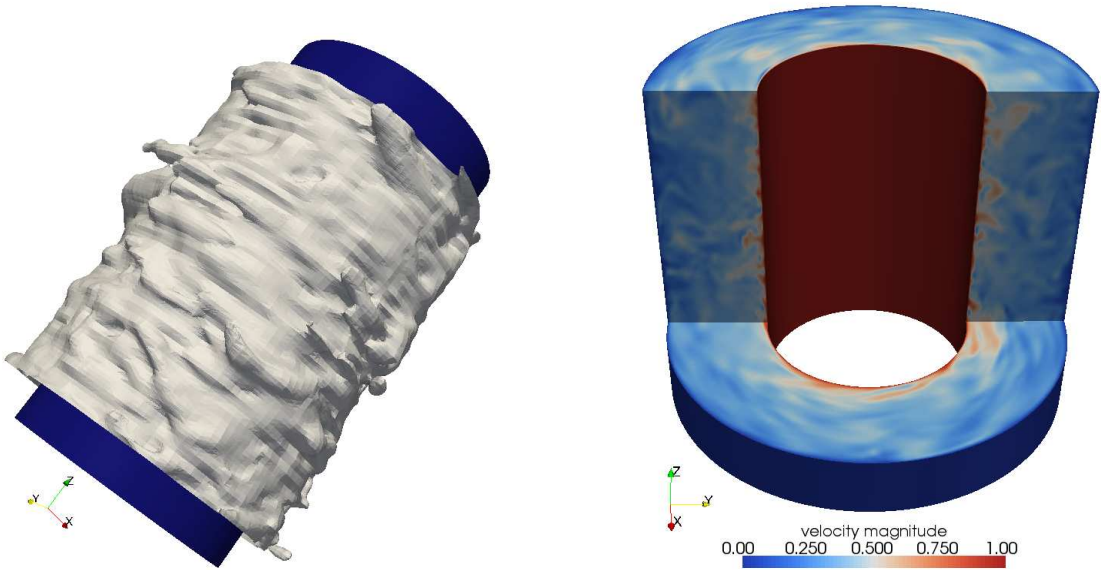


Figure 4.37: Pressure isosurface  $p^* = -0.025$  (left) and velocity magnitude  $\|\mathbf{u}^*\|$  (right) at time  $t^* = 500$ .

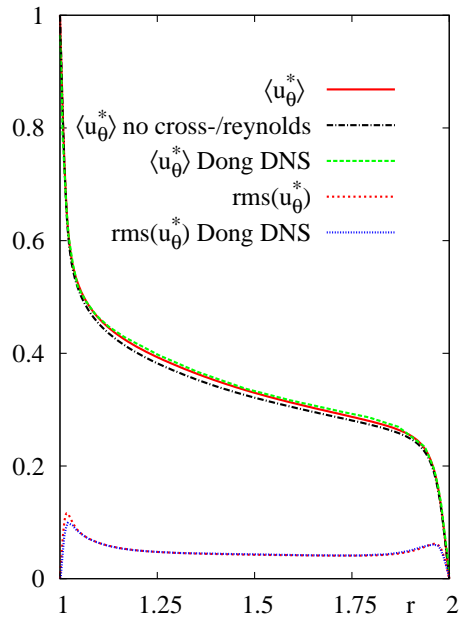


Figure 4.38: Mean azimuthal velocity and corresponding fluctuations.

*a priori* knowledge of the boundary-layer thickness is put into the model. The obtained mean and root-mean-square concentration profiles are qualitatively in good accordance with typical curves obtained for simulations of high-Schmidt-number mass transfer in turbulent channel flow (see, e.g., Dong et al. [53]). With increasing Schmidt number, the concentration profile typically flattens in the bulk volume, whereas the boundary-layer thickness decreases, and concentration gradients close to the boundaries increase. An isosurface for the instantaneous concentration  $c_1^*$  at  $t^* = 500$  is depicted in Fig. 4.40. Mean concentration

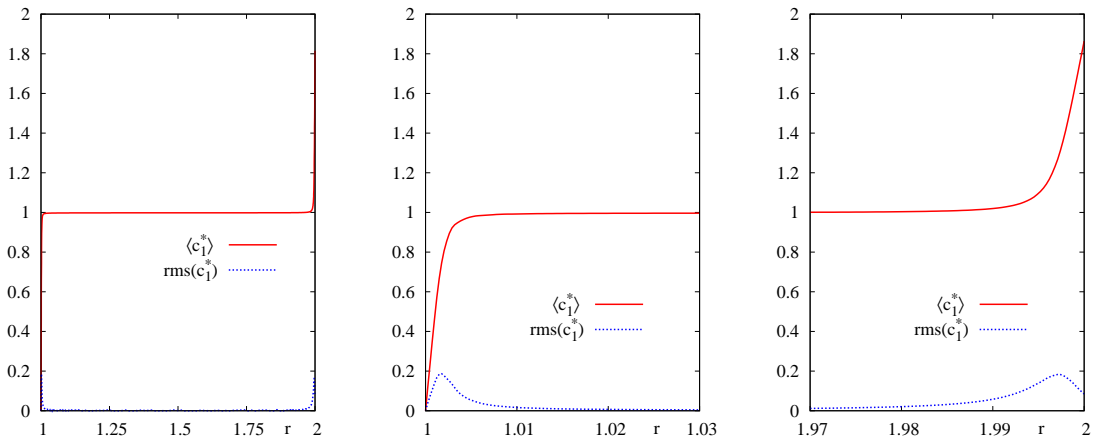


Figure 4.39: Mean and root-mean-square concentration profile for  $c_1^*$  ( $\text{Cu}^{2+}$  concentration). For better illustration, additional zooms of the regions next to the cylinder surfaces are provided.

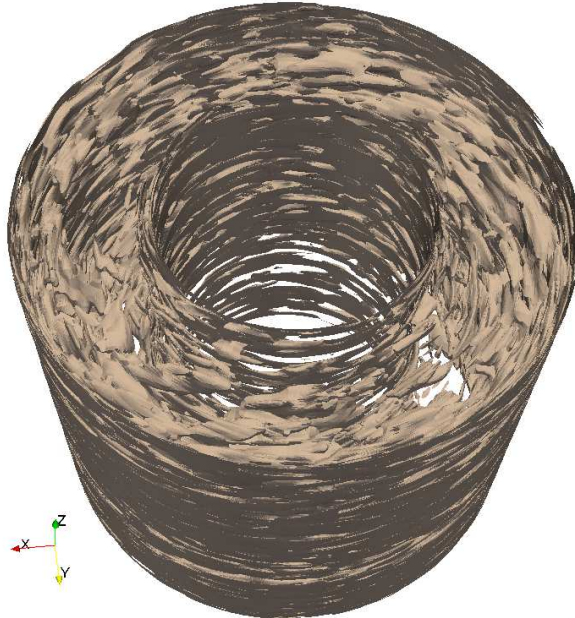


Figure 4.40: Concentration isosurface for  $c_1^* = 1.0$  at time  $t^* = 500$ .

profiles for  $c_2^*$  and  $c_3^*$  are provided in Fig. 4.41, while corresponding root-mean-square profiles for the normalized quantities  $c_2^*/c_2^{*,\infty}$ ,  $c_3^*/c_3^{*,\infty}$  are depicted in Fig. 4.42. In the bulk volume (i.e., the volume in the center of the gap), all concentration fields remain merely constant at their original bulk values.

Although ion species 2 and 3 are inert at the boundaries, they also form boundary layers, in order to maintain local electroneutrality. Thus, fluctuations in  $c_1^*$  always cause fluctuations in  $c_2^*$  and  $c_3^*$ , as well, and vice versa. In Fig. 4.43, computed results for the mean and root-mean-square electric potential field are shown. Fluctuations in the ionic concentrations also give rise to temporal and spatial variations in the electric potential field inside

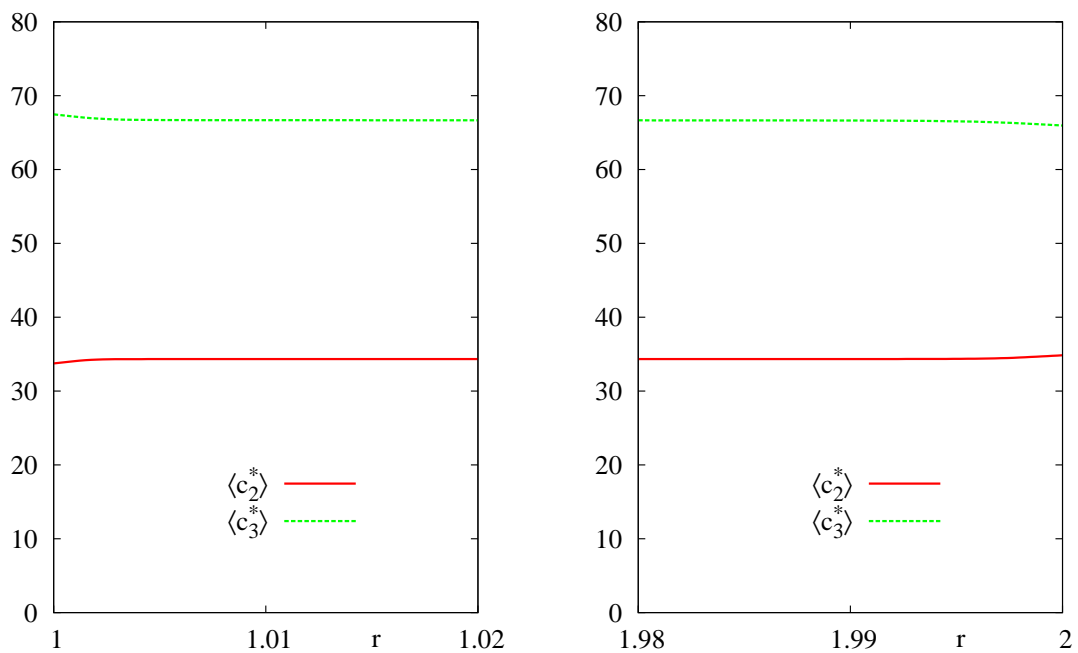


Figure 4.41: Mean concentration profiles for the inert ionic species  $\text{SO}_4^{2-}$  ( $c_2^*$ ) and  $\text{H}^+$  ( $c_3^*$ ) in the regions close to the cylinder surfaces.

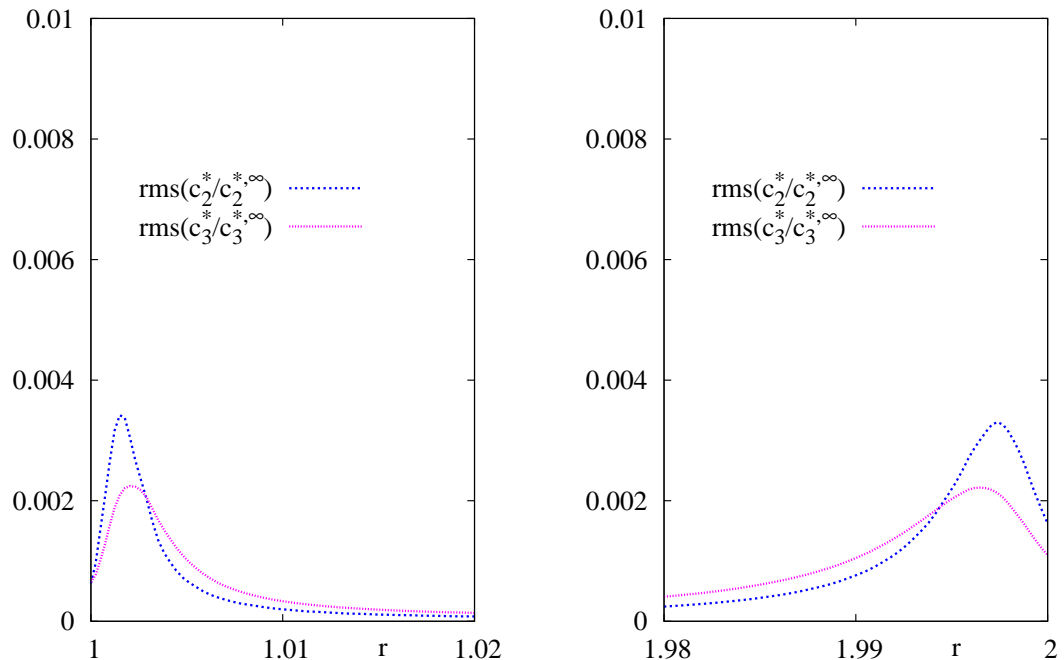


Figure 4.42: Root-mean-square concentration profiles for the inert ionic species  $\text{SO}_4^{2-}$  ( $c_2^*$ ) and  $\text{H}^+$  ( $c_3^*$ ) in the regions close to the cylinder surfaces.

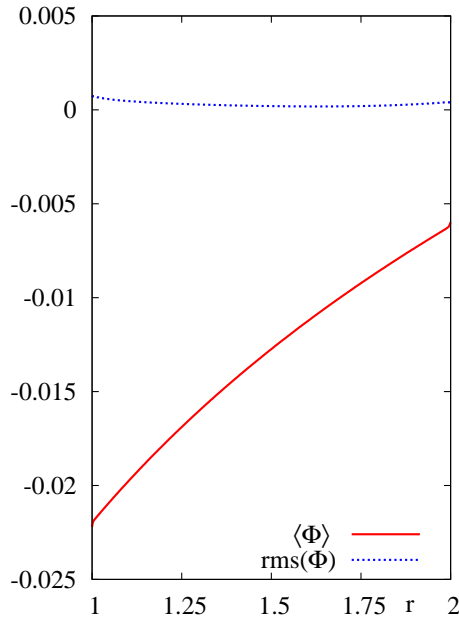


Figure 4.43: Mean and root-mean-square electric potential field inside the electrolytic cell.

the electrolytic cell. From the mean electric potential field, the mean voltage drop due to ohmic resistance of the electrolyte solution between the electrodes is computed to be 0.0162V.

Furthermore, the observed fluctuations in all physical fields occurring near the electrode surfaces also result in temporal and spatial fluctuations in the boundary mass fluxes of the reacting ionic species. Thus, due to the relation of mass and charge transfer, local current densities and the total measured current are fluctuating values, as well. In Fig. 4.44, the temporal evolution of the total current across the inner cylinder surface is compared to the total current across the outer cylinder electrode. Conservation of charge is obviously ensured, since the electric current entering the domain and leaving the cell are always identical in the simulations. This is a natural consequence of the full electrochemical model, which ensures mass conservation and also charge conservation (see section 2.4), since ions are both mass and charge carriers at the same time.

Simplified models for ionic transport at limiting current, which typically solve only a convection-diffusion equation for a single reactive ionic species, cannot ensure this property. For such models, the mass flux at inner and outer cylinder surface are not automatically coupled and may in principle evolve independent from each other, as a result. As a further effect of mass conservation and the balanced deposition and dissolution of copper ions, the overall mass of each ionic species contained in the closed electrolytic cell remains constant over time. This conservation of mass is also observed from the numerical results.

Finally, the obtained simulation results are compared with the well-known empirical correlation proposed by Eisenberg et al. [58]. Therein, the limiting current density  $i_L$  for RCE configurations is correlated to the Reynolds number  $\text{Re}_D$  characterizing the flow and

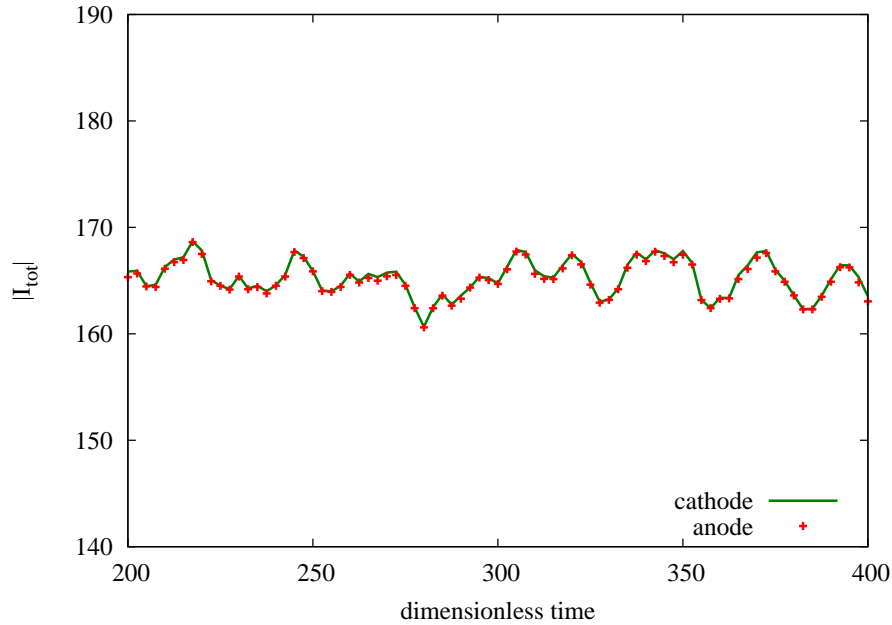


Figure 4.44: Temporal evolution of total current at cathode and anode.

the Schmidt number  $\text{Sc}$  characterizing the electrolyte solution via

$$i_L = 0.0791 \frac{nFD_1 c_1^\infty}{2R_i} \text{Re}_D^{0.7} \text{Sc}^{0.356}. \quad (4.21)$$

For the present problem with  $n = z_1 = 2$ ,  $\text{Re}_D = 16,000$  and  $\text{Sc} = 1389$ , a dimensional value of  $i_L = 0.76 \text{ mA/cm}^2$  is predicted by (4.21). Statistical evaluation of the results shown in Fig. 4.44 provides a value of  $I_L^{*,\text{sim}} = 165.03$  for the mean total current and  $i_L^{*,\text{sim}} = I_L^{*,\text{sim}}/A_c^* = 8.36$  for the mean current density at the inner rotating electrode with (dimensionless) surface area  $A_c^* = 2\pi R_i H = 2\pi^2$ . Transferred to dimensional values by multiplication with  $(U_{\text{ref}} \cdot c_{\text{ref}})$ , a value of  $i_L^{\text{sim}} = 0.803 \text{ mA/cm}^2$  is obtained from the simulation, which is in good accordance with the predicted value from the empirical correlation (4.21), since the relative difference  $(i_L^{\text{sim}} - i_L)/i_L$  is only 5.7%. Hence, the proposed comprehensive computational approach appears to provide the opportunity to verify empiric correlations, such as the famous Eisenberg correlation (4.21) in the present context, by means of numerical simulation. It is emphasized that the present model is not restricted to the consideration of limiting current densities, but provides a rather general problem formulation. In addition, it is successfully demonstrated that the proposed computational approach is able to correctly simulate coupled multi-ion transport in turbulent incompressible flow.

## 4.5 Copper pulse plating at a rotating disk electrode

The rotating disk electrode (RDE) is probably the most popular electrochemical device. A sketch of a basic RDE configuration is provided in Fig. 4.45. According to the definition given by Bard et al. [8], a RDE is a small metal disk inlaid into an insulating cylinder which

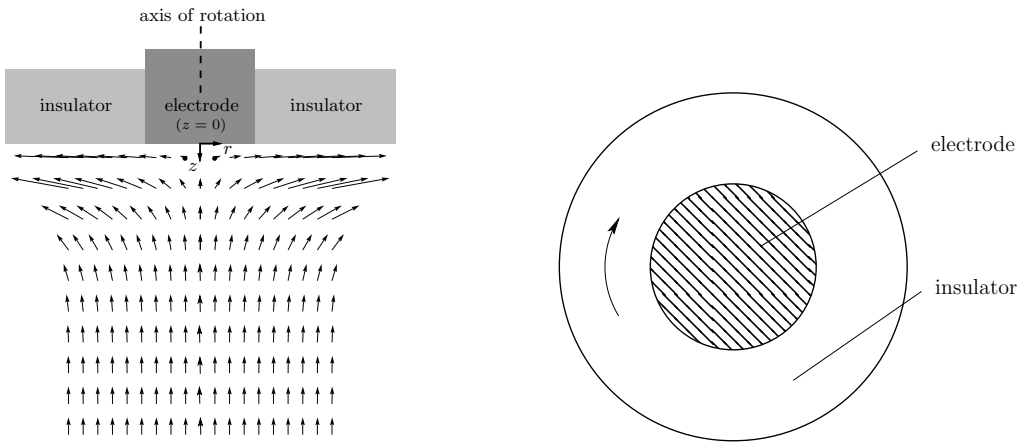


Figure 4.45: Rotating disk electrode (RDE): side view (left, according to Kontturi et al. [117]) and bottom view (right).

has a large base. The disk is flush-mounted in concentric position and represents the working electrode (cathode). The insulating cylinder is immersed into an electrolyte solution and rotated around its own axis. The counter electrode (anode) of the electrochemical cell is usually placed at a sufficiently large distance to the cathode. Since the flow properties near the rotating disk are well-known, experiments can be conducted under controlled hydrodynamic properties. This is one reason why the RDE cell-configuration is well-suited as a laboratory device for investigating electrolyte solutions and electrochemical reactions.

The rotation of the disk electrode causes local centrifugal forces that accelerate the electrolyte solution in radial direction away from the axis of rotation. The induced radial velocity generates a suction effect, which leads to a flow of electrolyte solution from the bulk towards the electrode surface. As a result, a nonzero velocity component normal to the cylindrical surface is observed. The arising characteristic flow field is also sketched in Fig. 4.45. In a generally accepted approximation (see, e.g., Newman and Thomas-Alyea [137]), the velocity component  $u_z$  normal to the electrode surface (located at  $z = 0$ ) is given by a polynomial expression reading

$$u_z = \sqrt{\omega\nu} \left( a \left( \frac{\omega}{\nu} \right) z^2 + \frac{1}{3} \left( \frac{\omega}{\nu} \right)^{\frac{3}{2}} z^3 + \frac{b}{6} \left( \frac{\omega}{\nu} \right)^2 z^4 + \dots \right), \quad (4.22)$$

together with  $a = -0.51023$  and  $b = -0.601$ . Here,  $\nu$  denotes the kinematic viscosity of the electrolyte solution and  $\omega$  is the angular velocity of the RDE.

This normal velocity component is responsible for the transport of fresh electrolyte from the bulk towards the electrode surface. It is emphasized that  $u_z$  given by (4.22) is independent of the radial position, i.e., from the distance to the axis of rotation. This property allows the commonly performed reduction to a one-dimensional problem considering only the normal direction to the electrode. For larger distances from the electrode surface the exponential approximation

$$u_z = \sqrt{\nu\omega} \left( -A + \frac{2B}{A} e^{-A\omega^{0.5}\nu^{-0.5}z} + \dots \right) \quad (4.23)$$

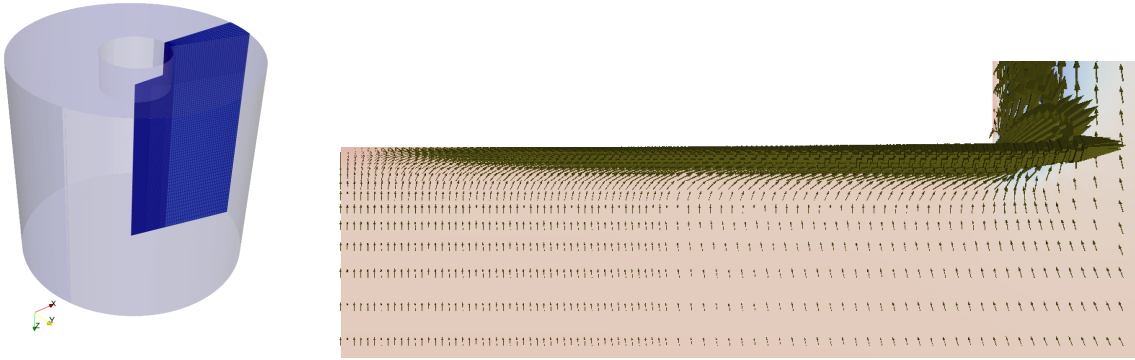


Figure 4.46: Computational domain (segment of  $15^\circ$ ) (left) and computed secondary velocity field close to the RDE (right).

holds (see, e.g., Newman and Thomas-Alyea [137]). The required constants are given as  $A = 0.88447$  and  $B = 0.934$ .

The following example is based on the experimental investigations and corresponding numerical computations presented by Tsai et al. [168]. All required input parameters are taken from that reference. In contrast to the one-dimensional model utilized by Tsai et al. [168], a complete three-dimensional model is considered here. This approach allows to actually compute the arising three-dimensional flow field and compare the results with the theoretical velocity predictions specified in (4.22) and (4.23). In the context of a RDE, the Reynolds number for characterizing the flow is usually defined as

$$\text{Re} = \frac{\omega r^2}{\nu}, \quad (4.24)$$

where  $r$  denotes the radius of the rotating disk. For the present example, the kinematic viscosity of the considered copper electrolyte solution is given as  $\nu = 1.43 \cdot 10^{-3} \text{ cm}^2/\text{s}$ , the angular velocity is set to  $\omega = 52.4 \text{ rad/s}$  and the radius of the rotating cylinder containing the cathode is  $r = 1 \text{ cm}$ . Thus, the flow induced by the RDE is characterized by a Reynolds number of  $\text{Re} = 36,650$ . According to Newman and Thomas-Alyea [137], the flow in the boundary layer at the surface of a rotating disk remains laminar for Reynolds numbers up to a value of about  $2 \cdot 10^5$ . Thus, the flow can still assumed to be laminar for the current problem setting. Furthermore, a stationary flow solution is obtained, after initial transients vanished. Thus, first the laminar, stationary flow field is computed. Afterwards, the transient pulse-plating problem is considered taking into account the result for the velocity field.

In order to enhance the efficiency of the numerical simulations, rotationally-symmetric periodic boundary conditions are used (see Appendix C for details). Here, the computational domain is chosen to be a segment of angle  $15^\circ$ , which is discretized using in total 101,179 trilinearly-interpolated hexahedral finite elements (see Fig. 4.46). The mesh is locally refined towards the working electrode to resolve the concentration boundary layer adjacent to the electrode surface. It is emphasized that the elements adjacent to the cathode surface have a height of only  $7 \mu\text{m}$ . The free surface at the top of the computational domain is modeled by free-slip boundary conditions and the rotation of the RDE is imposed via Dirichlet conditions for the velocity.

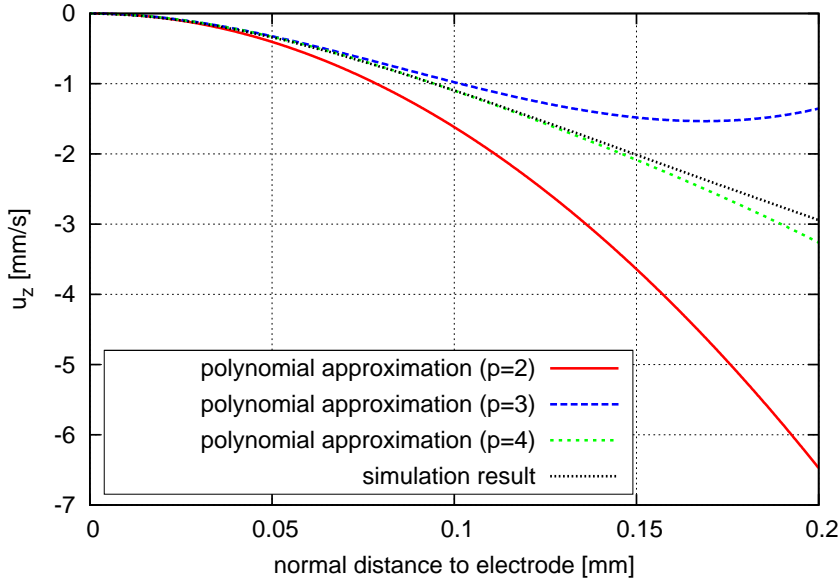


Figure 4.47: Comparison of the computed vertical velocity component  $u_z$  with different polynomial approximations obtained from (4.22).

The computed results for the vertical velocity component  $u_z$  depicted in Fig. 4.47 are in very good agreement with the polynomial approximations obtained from (4.22). The higher the polynomial degree used in (4.22), the better the accordance of analytical and computed results. For polynomial degree four, good accordance is found up to a normal distance to the electrode of about 0.15mm. The exponential approximation (4.23) for  $u_z$  matches the numerical solution for vertical distances to the electrode within the range 0.4mm to 1.3mm. In Fig. 4.49, the vertical velocity component  $u_z$  is depicted for different normal distances  $d$  to the surface of the RDE. The independence of  $u_z$  from the radial position is clearly visible and is in very good accordance with the theory. Of course, close to the outer edge of the rotating cylinder further flow effects become important as illustrated in Fig. 4.49. Since the expressions (4.22), (4.23) have been derived analytically, the observed agreement of numerical results and theoretical predictions serves also as a validation of the flow solver.

The computed stationary velocity field is used for the following time-dependent simulation of copper pulse plating. The plating bath is made of 0.348 M CuSO<sub>4</sub> with 2.06 M H<sub>2</sub>SO<sub>4</sub> and has a temperature of  $T = 300\text{ K}$ . Complete dissociation is assumed leading to a multi-ion transport problem with three ionic species. The physical properties and Butler-Volmer parameters for the cathode surface are chosen according to Tsai et al. [168]. For this example, the stabilized finite element formulation of the ENP system of equations is considered. Following Tsai et al. [168], an equal duration of 4ms is chosen for the pulse ( $t_{\text{on}} = 4\text{ ms}$ ) as well as for the pulse pause ( $t_{\text{off}} = 4\text{ ms}$ ). Thus, the so-called duty cycle is computed as  $t_{\text{on}}/(t_{\text{on}} + t_{\text{off}}) = 0.5$  for the present case. The intensity of the current pulses corresponds to a mean current density of  $i_p = 0.05\text{ A/m}$ . The pulse curve is numerically applied using the general algorithm for current-controlled problems introduced in section 3.5.2. Since the area of the RDE is  $A = 2\pi r_E \approx 3.14\text{ cm}^2$ , where  $r_E = 0.5\text{ cm}$  is the diameter of the cathode, a total current of  $I_{\text{tot}} = i_p A = 0.157\text{ A}$  has to be achieved during the pulse.

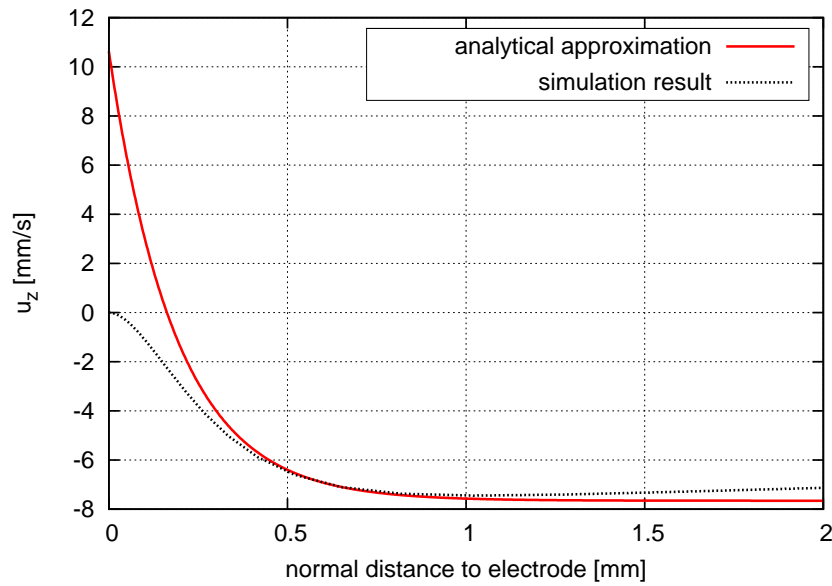


Figure 4.48: Comparison of the computed vertical velocity component  $u_z$  with the exponential approximation (4.23) for larger distances to the electrode surface.

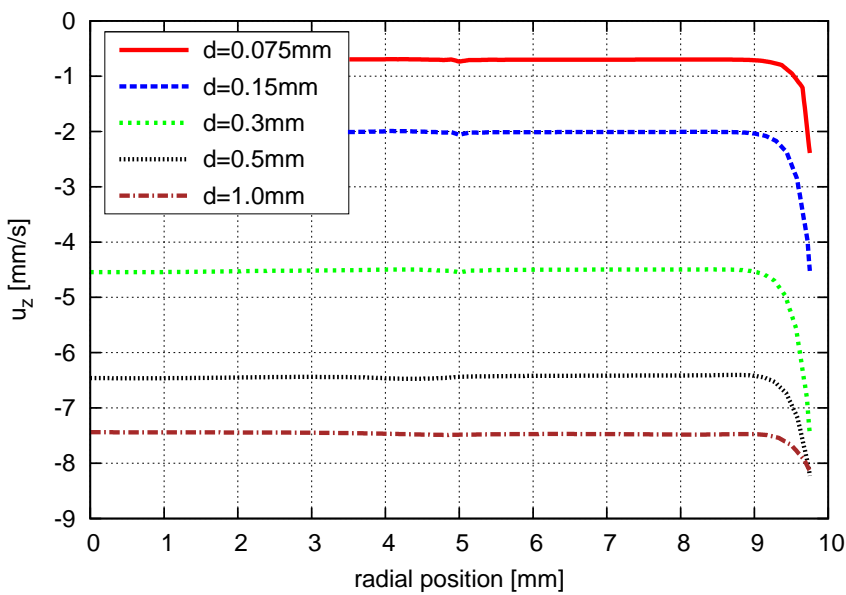


Figure 4.49: Vertical velocity component  $u_z$  depicted for different normal distances  $d$  to the surface of the RDE.

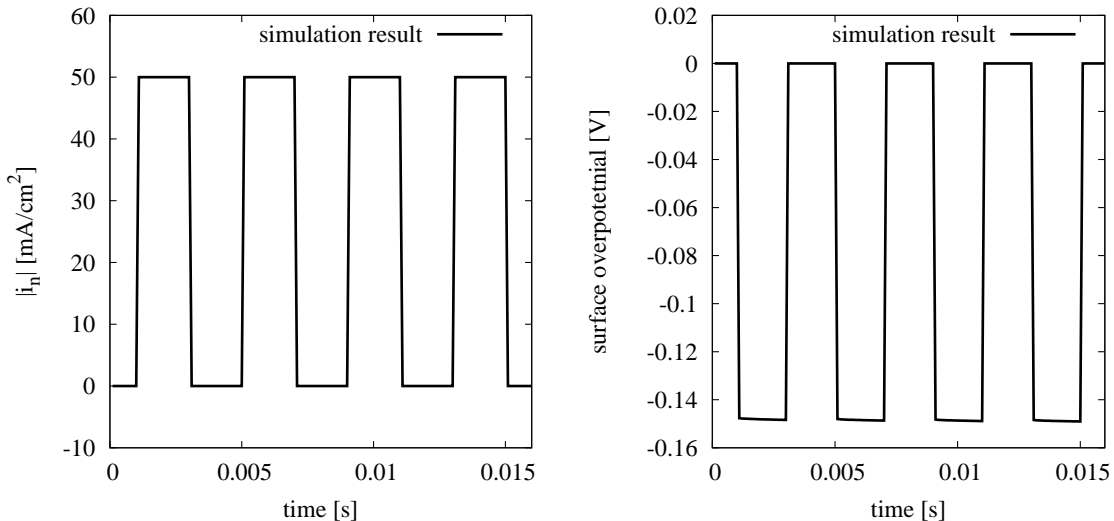


Figure 4.50: Obtained simulation results for the current density (left) and the surface overpotential (right), both evaluated at the center of the RDE.

For time integration, a generalized trapezoidal rule with  $\theta = 0.66$  is used.

In the following, a brief summary of the simulation results obtained from the transient multi-ion transport simulation is presented. In the left part of Fig. 4.50, the temporal evolution of the current density evaluated at the center of the cathode is depicted. As can be clearly seen, the current density follows the prescribed current curve enforced by the galvanostatic control algorithm. In the right part of Fig. 4.50, the corresponding values for the surface overpotential at the center of the RDE are shown. Note that during the current pulse, the overpotential is not constant but slightly varies in time. This is a result of the ion-transport processes at the electrode surface and the continuous adjustment of the cell voltage within the galvanostatic control.

As final important result, the temporal evolution of the  $\text{Cu}^{2+}$  ion concentration at the surface of the RDE is depicted in Fig. 4.51. The effect of the applied current pulses on the ionic concentration is clearly visible. During the pulse, the cupric ions are consumed within the electrochemical reaction. Consequently, the surface concentration decreases during this period of time. During the pulse pause, actually no current passes the electrolytic cell. The observed increase in the  $\text{Cu}^{2+}$  ion concentration is solely caused by a diffusion of  $\text{Cu}^{2+}$  ions towards the electrode.

In summary, copper PP is successfully simulated for a three-dimensional RDE configuration. The consideration of double-layer charge and discharge phenomena (see, e.g., Puijpe and Leaman [146]) remains as a future extension of the present computational model. In general, the normal component of the total current density at an electrode surface is a sum of a faradaic current  $i_f$  and a second current contribution denoted by  $i_{dl}$  (see, e.g., Puijpe and Leaman [146]):

$$i_n = i_f + i_{dl}. \quad (4.25)$$

The faradaic current density  $i_f$  represents the partial current caused by the electrodeposition process. Thus,  $i_f$  is usually determined by an electrode kinetics law such as the Butler-Volmer equation, for example. The partial current  $i_{dl}$  is related to the charging and

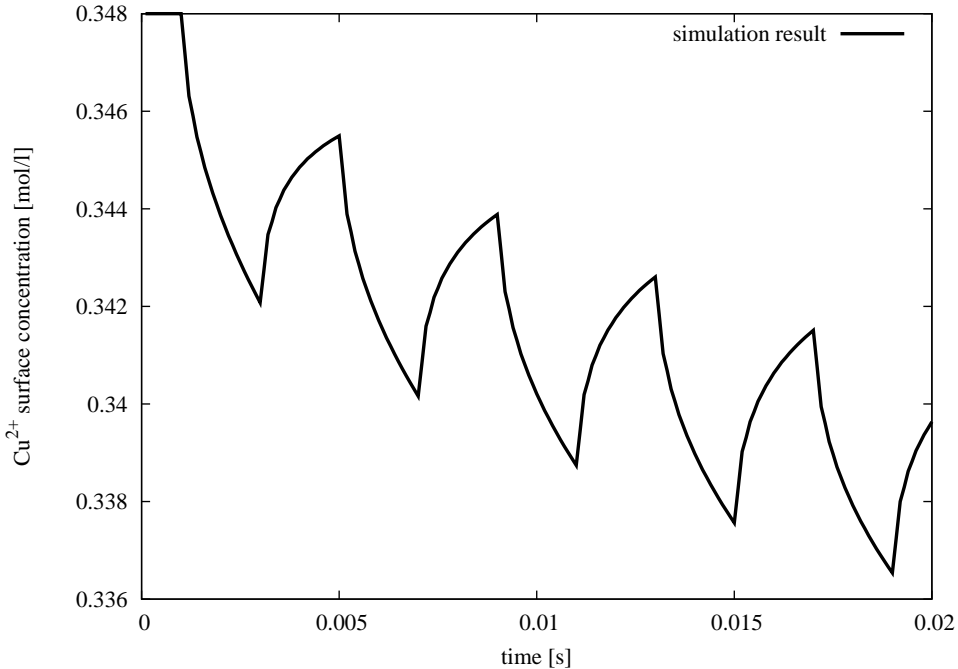


Figure 4.51: Computed surface concentration of cupric ions at the center of the RDE.

discharging of the electric double layer and is typically modeled by a simple macroscopic relationship reading

$$i_{\text{dl}} = C_{\text{dl}} \frac{\partial \eta_s}{\partial t}. \quad (4.26)$$

Here,  $\eta_s$  is the electrode surface overpotential and  $C_{\text{dl}}$  denotes the double-layer capacitance. For rapid changes in the surface overpotential  $\eta_s$ , the total normal current density  $i_n$  is partially consumed by the charging (or discharging) current  $i_{\text{dl}}$ . This is an important phenomenon in the context of PP and PRP methods when short pulse durations are used.

However, when an ideal (step-wise) pulse curve for the electric current is considered, the applied current is formally discontinuous which leads to  $\frac{\partial \eta_s}{\partial t} \rightarrow \infty$ . Thus, for a sophisticated modeling of double layer charging and discharging in the context of PP and PRP methods, deeper knowledge on the actual form of the pulse imposed by the external pulse rectifier is required, since real current curves deviate from the ideal step-wise profile. This is a limitation not mentioned by Tsai et al. [168] in the context of their simulations devoted to the double-layer effect.

An alternative to (4.26) appears also to actually simulate the electric double layer using the PNP system of equations as a nanoscale model (see, e.g., Bazant et al. [14]). This more sophisticated approach to charging and discharging of the electric double layer could then be incorporated into the continuum-based models considered here.

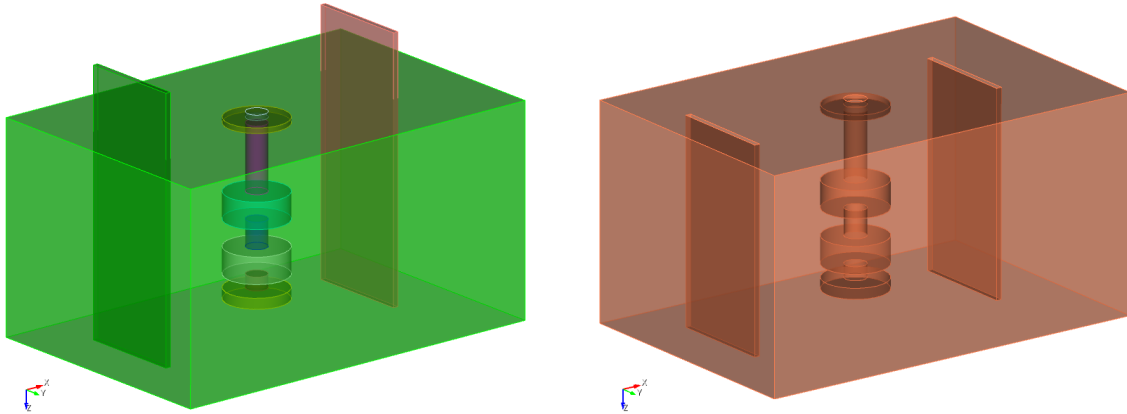


Figure 4.52: Geometric setup of a laboratory nickel electroplating cell (left) and corresponding computational domain (right).

## 4.6 Numerical simulation of a nickel pulse-reverse plating experiment

The work presented in this section was performed during the project “Numerische Simulation von galvanischen Beschichtungsvorgängen” supported by the Space Agency of the German Aerospace Center (DLR). In the following, the numerical simulation of a nickel pulse-reverse plating (PRP) experiment is addressed. The experimental work was carried out by the contractor Happy Plating of the industrial partner EADS Astrium. This experiment serves as an important validation example for the developed computational methods in the context of industrial electrodeposition applications. Below, a brief summary of the utilized modeling approach and the obtained simulation results is given. Although not all details can be provided here, this numerical example illustrates the challenges to be faced when considering real electroplating baths. For the present problem setup, three different modeling approaches are compared. In particular, primary, secondary and tertiary current density distributions (cf. section 2.8.4) are computed using the proposed computational approach. Finally, the predicted results for the nickel deposit thickness distribution are compared with experimental data.

The electroplating bath consists of a 50L basin filled with an aqueous nickel electrolyte solution. In Fig. 4.52, the basic geometric setup of the electrolytic cell is illustrated. Two vertical anodes made of nickel are immersed into the solution. In the center of the basin, a rotation unit is positioned. This rotationally-symmetric part consists of three cylindrical cathodic areas (stainless steel) with identical diameter but different heights. These three cathodes are separated by cylindrical insulators, which have a larger diameter than the electrodes. During the electroplating process, the central unit is rotating with 34 rpm. It is emphasized that the proposed computational approach allows for the consideration of two anodes and three cathodes without any special modifications. In the present model, only the flow induced by the rotation of the central unit is investigated, since it dominates the velocity field close to the cathodes. A well-mixed electrolyte solution is assumed for the bulk. Hence, additional bath agitation and filtering systems present in the experimental

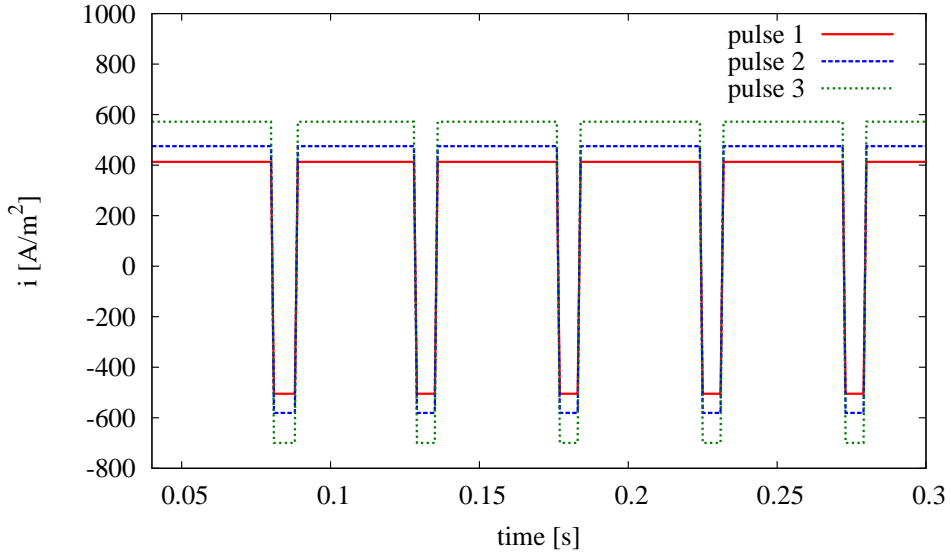


Figure 4.53: Pulse curves used within the nickel PRP experiments.

setup are neglected here. The computational domain is confined to the volume occupied by the electrolyte solution, as depicted in the right part of Fig. 4.52.

For a general overview of recent developments regarding the electrodeposition of nickel and nickel-based alloys the interested reader is referred to Orinakova et al. [138]. Here, a nickel electrolyte solution of Watts bath type is considered at a temperature of 55°C. Physicochemical properties of different nickel electrolytes are reported in the study of Imamura and Toguri [104], for instance. The present electroplating bath is made from two different nickel salts (nickel(II)-sulfate-hexahydrate, nickel(II)-chloride-hexahydrate) dissolved into water. Additionally, boric acid is added. Since the latter is a very weak acid, its degree of dissociation is quite low. Thus, the effect of the corresponding ions is assumed to be negligible for the ion-transport model. In summary, the following three ionic species are considered in the ion-transport model:  $\text{Ni}^{2+}$ ,  $\text{SO}_4^{2-}$  and  $\text{Cl}^-$ .

The nickel ion  $\text{Ni}^{2+}$  represents the reacting ionic species, while the two anions are inert. Phenomenological boundary conditions of Butler-Volmer type are used at all electrode surfaces. Adequate parameters for the Butler-Volmer law (2.44) were determined from measured polarization curves considering the relevant range of current densities. Three different pulse forms are investigated for this PRP experiment as shown in Fig. 4.53. As a preliminary investigation, PRP is simulated for an essentially one-dimensional model problem, considering a flat nickel cathode in contact with a stagnant electrolyte solution. The proposed approach for current-controlled electrochemical systems (see section 3.5.2) is used to impose the three different pulse curves.

The computed temporal evolution of the  $\text{Ni}^{2+}$  surface concentration is presented in Fig. 4.54. During the cathodic pulse, electrodeposition takes place at the cathode and the nickel ion concentration decreases. During the short, but intense reverse pulse, a small amount of deposited material is dissolved again. Consequently, the ion concentration is increasing in this time period as shown in Fig. 4.54. Essentially this leveling effect leads to more uniform plating results in the case of complex geometries, which is one of the advantages of PRP methods compared to conventional DC plating. In Fig. 4.55, the temporal

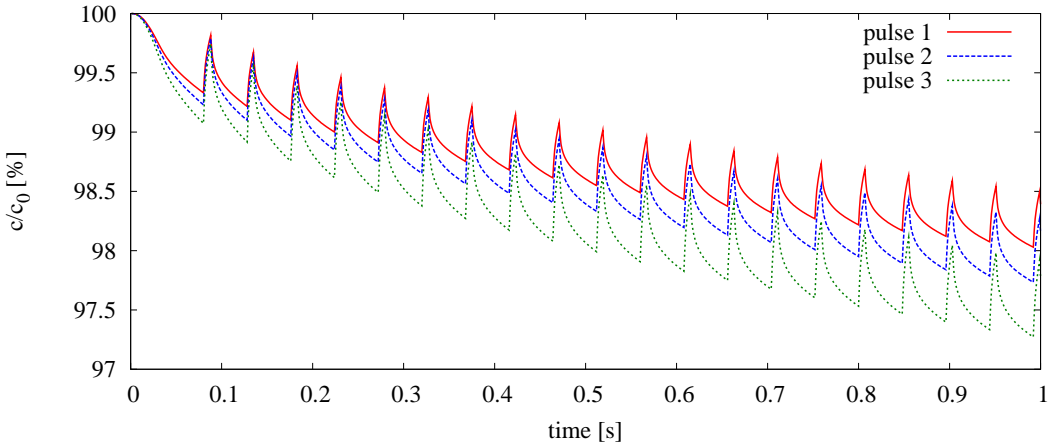


Figure 4.54: Temporal evolution of  $\text{Ni}^{2+}$  surface concentration at a cathode.

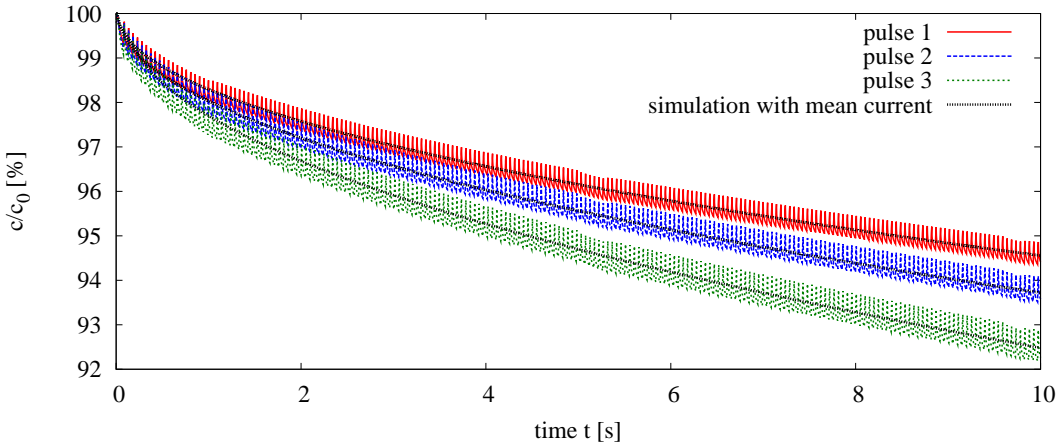


Figure 4.55: Temporal evolution of  $\text{Ni}^{2+}$  surface concentration at a cathode. Comparison of results obtained for applying pulsating current and a corresponding DC with the same mean current density.

evolution of  $\text{Ni}^{2+}$  surface concentration as obtained for applying either pulsating current or the corresponding DC with the same mean current density is shown. As a result, both modeling approaches yield the same mean behavior in time. This observation justifies the consideration of the corresponding DC within the three-dimensional simulations, which are addressed in the following. This observation is important to account for the multiscale character with respect to time, since typical pulse durations are in the order of milliseconds, but characteristic times for flow phenomena are in the order of seconds.

For the three-dimensional model, the ENP system of equations is considered here including a one-way coupling to incompressible flow. For time integration, the generalized trapezoidal rule ( $\theta = 2/3$ ) with a constant time step of  $\Delta t = 0.05\text{s}$  was used. The computational domain is discretized using a hexahedral-dominant (hex-dominant) mesh and trilinearly-interpolated elements. In total, 1,420,429 elements are used for the spatial discretization. In particular, the hybrid mesh consists of hexahedral, pyramidal, wedge-shaped and tetrahedral elements. The corresponding number of nodes is 1,063,025. An

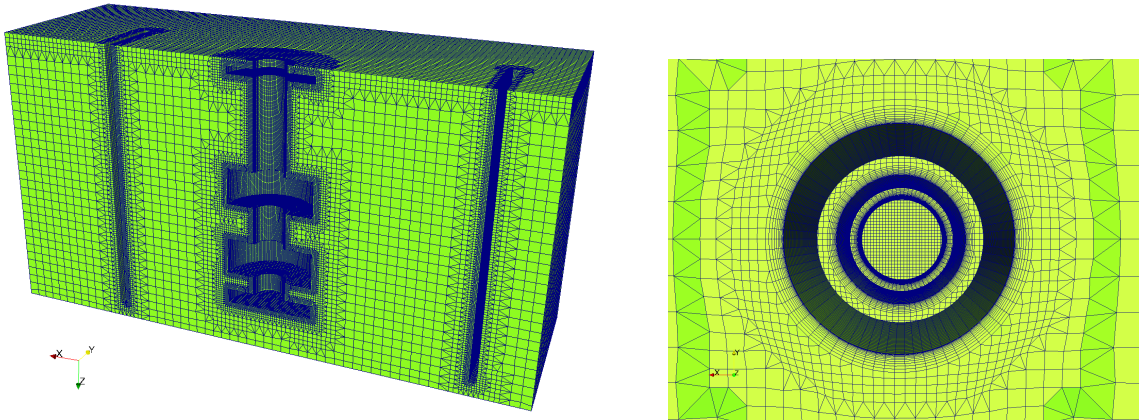


Figure 4.56: Details of the spatial discretization.

illustration of the spatial discretization is provided in Fig. 4.56. Adjacent to the three cathode surfaces, a very fine mesh resolution with element sizes of only about  $7\text{ }\mu\text{m}$  is utilized. Given the total bath volume of  $50\text{L}$ , the creation of an appropriate mesh is already a challenging task. Owing to the large number of unknowns, parallel computations are mandatory. For this example, up to 32 processors are used for the parallel solution of the coupled multi-ion transport problem.

The electric potential field and corresponding electric field lines are depicted in the left part of Fig. 4.57 as obtained for the primary current density distribution. In the right part of Fig. 4.57, the corresponding current density distribution on the three cathodes is illustrated. As expected from the design of the experiment, the current density already increases from the top to the bottom due to purely geometrical reasons. This is an effect of the cylindrical insulators separating the cathodes. Snapshots of the unsteady complex flow field induced by the rotation of the central unit are given in Fig. 4.58. It is noted that the free surface at the top of the computational domain is modeled by free-slip boundary conditions.

From the computed current density distributions, a deposit thickness distribution for the copper layer is predicted using equation (2.51). The plating time for each experiment was within the range  $13 - 20\text{ min}$  depending on the chosen current pattern. The efficiency factor  $\lambda$  introduced in section 2.5.5 is important for reflecting the non-ideal plating behavior, taking into account side reactions such as hydrogen reduction. It is emphasized that values for  $\lambda$  were determined *a priori*, based on a comparison of experimental measurements and theoretical expectations. Thus, no “fitting” of numerical results to experimentally determined data is performed here.

In Fig. 4.59, the numerical predictions for the copper thickness distribution are compared to the provided measurements. Overall, a good accordance is observed for all of the three modeling approaches and all of the three investigated current patterns. The simpler potential models utilized to compute the primary and secondary current density distribution perform quite well, since still low current densities are considered here, which in turn leads to an almost negligible importance of ionic mass transport. Furthermore, the effect of ohmic losses between the electrodes is the dominating the electric potential field.

In summary, a successful numerical simulation of a nickel PRP experiment is presented. In particular, multi-ion transport coupled to a complex flow field is simulated within a re-

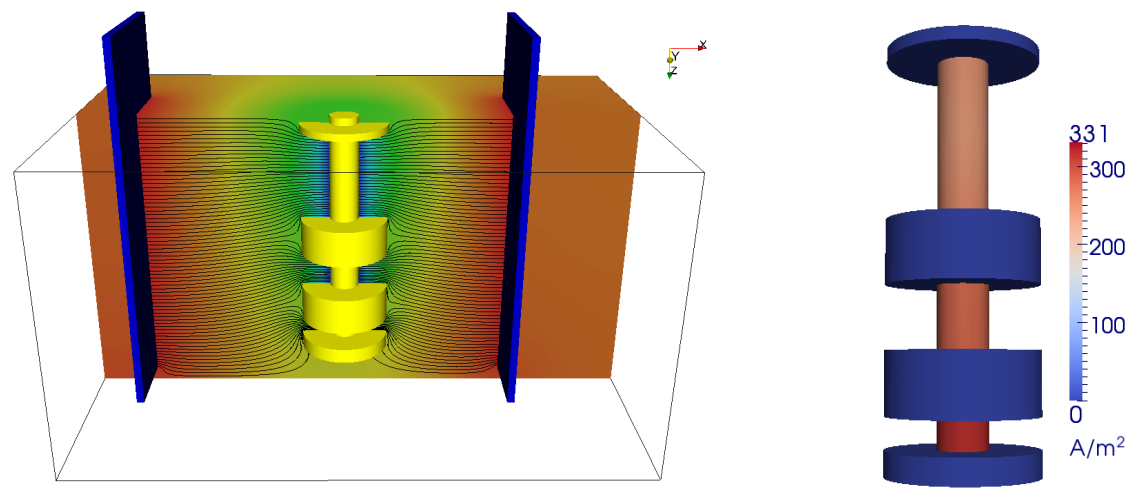


Figure 4.57: Visualization of electric field lines and electric potential (left) and corresponding primary current distribution at the rotation unit (right).

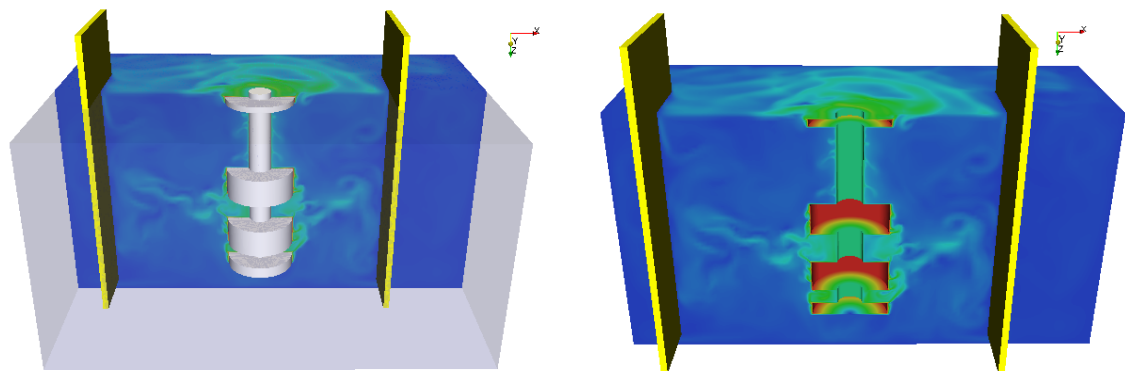


Figure 4.58: Snapshots for the velocity magnitude  $\|u\|$ , depicted on vertical cuts through the computational domain.

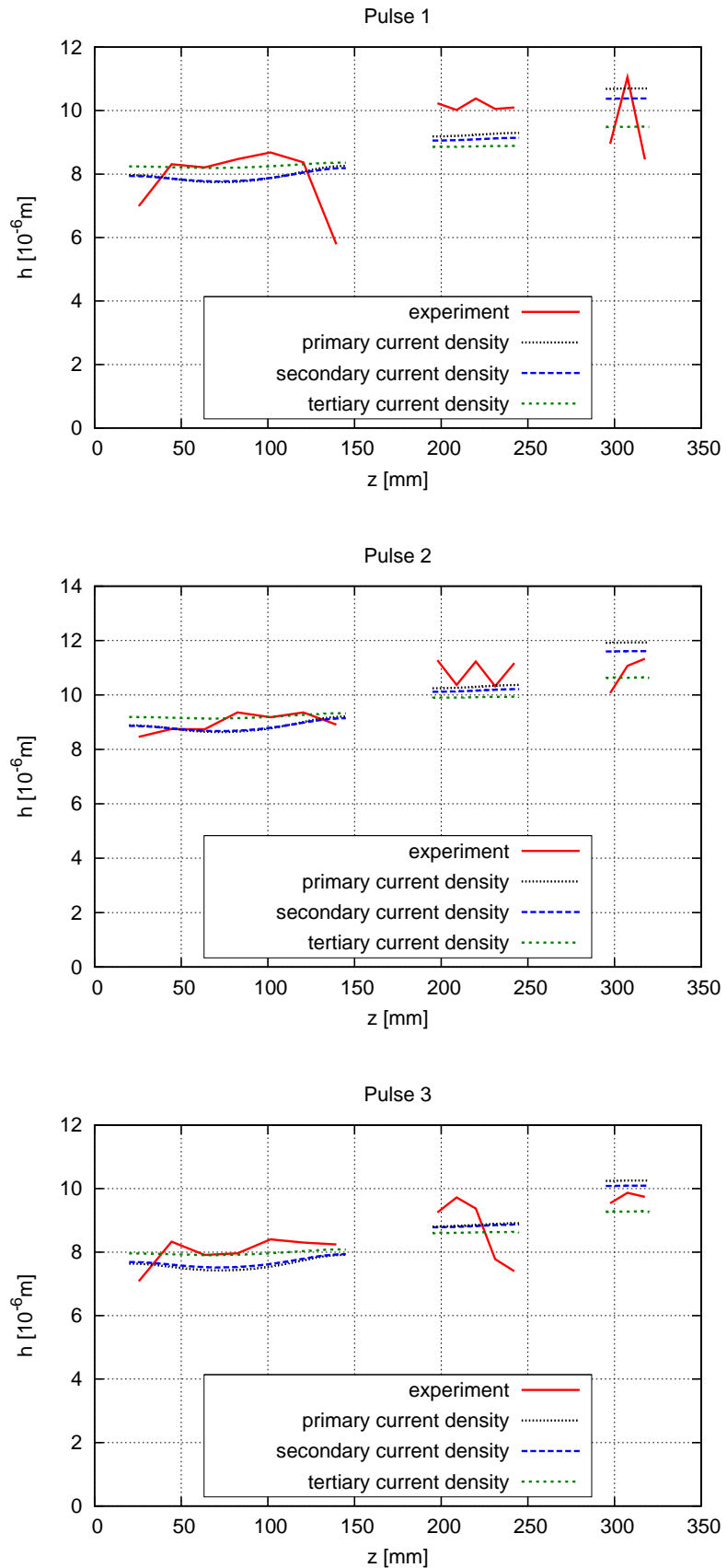


Figure 4.59: Comparison of numerical predictions and measured values for the copper deposit thickness distributions.

alistic three-dimensional geometry. The numerical predictions for the deposit-thickness measurements are in good accordance. For comparison, also simpler potential models for computing primary and secondary density distributions are considered. Although in this specific situation these simpler approaches perform comparable well, the proposed ion-transport model represents the much more general approach. Especially when a given configuration of an electroplating bath is investigated for the first time, the more comprehensive model can be used to either justify the use of simpler models in subsequent numerical studies or to show that such approaches are not applicable due to the importance of ion-transport processes.

# 5 Conclusions and outlook

*“At the end, one realizes that a manuscript is never finished.  
It is just abandoned.”*

D. P. Telionis [165, p. ix]

## 5.1 Conclusions

In this work, a comprehensive computational approach for the coupled numerical simulation of electrochemical systems is proposed. The focus is on electrolytic cells in general and on electrodeposition of metals in particular. Based on a continuum hypothesis, a macroscopic mathematical model is established, which accounts for all three ion-transport phenomena in dilute electrolyte solutions, that is, convection, diffusion and migration. The latter effect describes the movement of ions caused by an electric field. A coupled set of Nernst-Planck equations subject to an electroneutrality constraint is used for describing multi-ion transport in electrolyte solutions. For an appropriate modeling of electrode kinetics, nonlinear phenomenological boundary conditions such as the Butler-Volmer law are applied at electrode surfaces.

In the context of electrodeposition processes, ion transport is typically coupled to a complex, often turbulent flow field. Taking into account this inherent coupling due to convection represents one of the key aspects of this thesis. Besides incompressible flow of an electrolyte solution induced by a rotation of electrodes or other bath agitation techniques, the proposed model additionally accounts for buoyancy-driven flow (natural convection). As a result, a challenging two-way-coupled problem has to be solved. Finally, a general approach for the simulation of current-controlled (galvanostatic) electrochemical problems completes the comprehensive model.

In this work, a novel residual-based variational multiscale finite element method is proposed as the unique discretization approach to all governing equations. It is successfully demonstrated that the proposed stabilization techniques for the coupled ion-transport problem contribute to the robustness of electrochemical simulations when convection plays a significant role. In particular, the importance of correctly defining both stabilization term and parameter for the coupled system of ion-transport equations is emphasized, and the special case of a binary electrolyte solution is highlighted. Important surface-related quantities such as ionic boundary mass fluxes and current densities at electrode surfaces are computed from the finite element representation in a consistent manner including the influence of possible subgrid-scale terms.

Since the variational multiscale method can also be exploited for developing an approach to large eddy simulation of turbulent flows, the proposed computational framework is capable of simulating coupled multi-ion transport in laminar, transitional and turbulent

flow of electrolyte solutions. Besides the classical finite element method, where piecewise polynomial approximations to the unknown solutions are computed, an isogeometric discretization approach utilizing NURBS basis functions is also considered. In this work, the concepts of isogeometric discretization and variational multiscale methods are successfully combined in the challenging context of coupled multi-ion transport in turbulent flow. As an example, ionic mass transfer in turbulent Taylor-Couette flow is investigated, an important model problem for rotating cylinder-electrode configurations. Moreover, for natural convection phenomena in electrochemical cells, a partitioned solution scheme is proposed in this work. This algorithmic approach is successfully used for the simulation of electrolytic processes coupled to buoyancy-driven flow.

For time discretization, a generalized-alpha scheme is utilized here, which includes a broad spectrum of common implicit schemes. The capability of simulating transient electrochemical processes is mandatory for the numerical modeling of many electrochemical applications. One such example, which is addressed in this study, is the simulation of pulse and pulse-reverse plating methods. The developed algorithmic approach to current-controlled simulations used for this kind of applications is an important further contribution to the provided portfolio of numerical methods.

The proposed computational approach is successfully tested for several numerical examples, demonstrating that the method is robust and provides accurate results. Among others, realistic problem configurations with complex three-dimensional geometries are considered. This illustrates its geometrical flexibility, allowing for the consideration of complex geometries, an important property for simulating real laboratory devices or industrial facilities. The diversity of numerical examples presented in this thesis illustrates the broad spectrum of capabilities.

In summary, the present work represents an important contribution concerning the development of a predictive tool for industrial electroplating applications in particular and the numerical simulation of electrochemical systems in general.

## 5.2 Outlook

The proposed computational framework provides a valuable basis for future research and development in the field of computational electrochemistry. Open questions and remaining issues were emphasized at several points in the main part of this thesis. Based on the current implementation, possible model extensions or alternative numerical techniques can be investigated in the future. In the following, some of these potential future research topics are briefly addressed.

Further investigations of the residual-based variational multiscale method for multi-ion transport seem necessary. The current work has to be seen as a first promising step, which raises a couple of interesting questions. One aspect that needs further detailed analysis is the investigation of the additional terms in the coupled ion-transport model emanating from the general variational multiscale method and not being considered up to now. As stated above, the variational multiscale method utilized here also represents an approach to developing numerical methods for large-eddy simulation (LES) of turbulent flows. Hence, the present work is also a first step towards future development of canonical numerical methods for electrochemical systems with ionic mass transfer coupled to turbulent flow.

Especially for this type of problems, which are typically linked with high computational

costs, efficiency of the computational method is a further important requirement. In this work, the electroneutrality condition is primarily used to close the system of ion-transport equations. The use of this algebraic constraints leads to linear systems with a saddle-point matrix, which are difficult to solve. An alternative closing equation derived from the electroneutrality constraint was provided here in addition. As indicated in this work, the use of this closing equation represents a very promising alternative, since it is linked with lower computational costs and does not lead to linear systems with a saddle-point matrix. Since this alternative approach was developed quite recently, further investigations will be required in the future.

In this work, matching spatial discretizations for both the flow and the ion-transport model are used. The consideration of different meshes for each subproblem might be advantageous to account for the different characteristic length scales related to incompressible flow and ion-transport processes. At the moment, the spatial resolution requirements of the ion-transport model govern the element sizes, especially near the electrode surfaces, where very thin concentration boundary layers arise. A volume-coupled problem formulation with non-matching computational grids would further enhance the flexibility and numerical efficiency of the method, since the computational cost for solving the flow problem could be reduced. Mortar-type methods for mesh tying (see, e.g., Wohlmuth [180]) are promising techniques that might be extended to establish a volume coupling of computational grids. In addition, mesh-tying techniques as recently proposed by Ehrl et al. [57] could be utilized to improve mesh creation by a flexible connection of regions with different resolutions. An even more important option of this method is to apply different modeling approaches in different regions of the domain. Thus, close to electrodes, the full ion-transport model is solved, while a simpler model for the electric potential (e.g., the Laplace equation) is sufficient in the bulk of the electrolyte solution. It is expected that computational cost can be significantly decreased by means of such techniques.

From a numerical point of view, several extensions or alternative methods are worth being considered in the future. Monolithic solution schemes are promising alternatives to the partitioned schemes proposed here for the two-way coupling in case of natural convection and also for current-controlled (galvanostatic) problems. In the context of fluid-structure interaction, for example, monolithic solution strategies showed considerably improved numerical efficiency compared to conventional partitioned schemes (see, e.g., Gee et al. [73]).

Computational techniques might also be instrumental for determining values of required model parameters from experimental measurements. Examples are the parameters of electrode kinetics laws or other physical properties such as ionic diffusion coefficients. Numerical methods for inverse analysis (see, e.g., Rausch et al. [150]) offer a powerful systematic approach within a combined experimental and numerical research. In addition, computational methods for uncertainty quantification might perhaps also be valuable in the context of electrochemical systems.

Besides the use of phenomenological boundary conditions for describing electrode kinetics, more sophisticated modeling based on a multiscale approach offers a promising alternative. Within a microscopic model for the electrode surface, electrode kinetics and electric double layer effects can be simulated. The relevant effects of the microscale are integrated into the simulation on the macroscale. This will result in a kind of “enhanced” boundary conditions directly based on the results for the simulated microscale model. This “bridging the scales” is definitely one of the future topics in computational electrochem-

istry (see, e.g., Alkire [2]).

In the context of electrodeposition applications, a natural extension of the proposed method is to actually incorporate the electrode shape changes into the simulations. One simple possibility to account for the arising moving-boundary problem is to use an Arbitrary Lagrangian-Eulerian (ALE) approach (see, e.g., Donea et al. [51]). The eXtended finite element method (X-FEM) represents a promising alternative for the numerical simulation of such moving-boundary problems. Methods such as those recently developed for the simulation of premixed combustion (see, e.g., van der Bos and Gravemeier [170]) and two-phase flow (Rasthofer et al. [149]) employ level-set approaches to treat the respective interfaces. Thus, these methods are able to account for large, complex interface deformations and even topological changes. This is an important requirement for the simulation of typical electrodeposition applications in semiconductor industries and of electrochemical machining processes. A modeling of surface growth including a prediction of the developing surface roughness of deposits might also be important for the investigation of laminar and especially turbulent flow along such boundaries. Certainly one of the ultimate goals is the prediction of material properties of the deposited metal layers, such as hardness, porosity, brightness, ductility, and the distribution of internal stresses.

The developed computational approach may also serve as a basis for numerical simulation of other electrochemical phenomena, such as they arise in the context of other types of electrolytic or galvanic cells. Applications in the context of batteries and fuel cells, bio-electrochemistry, electrophysiology (heart, cerebral system) and corrosion of metals are some examples. However, it is emphasized that each electrochemical application poses its own requirements for both the mathematical modeling and the computational methods.

As a conclusion, computational electrochemistry represents a challenging, but at the same time fascinating scientific field, offering a broad variety of aspects to focus on. Especially the future needs for renewable energy supply and electromobility will further increase the demand for research and development in electrochemistry. Certainly, numerical simulation represents one important approach to contributing to these efforts.

# A Binary electrolyte solutions

For the special case  $m = 2$ , commonly referred to as binary electrolyte, the electroneutrality condition enables further analytic considerations. The following analysis is an excerpt from Bauer et al. [11], extended by additional remarks. The basic ideas can also be found in Newman and Thomas-Alyea [137] and Kontturi et al. [117], for example.

In the following, a transient convection-diffusion-migration problem for a binary electrolyte solution enclosed in a bounded  $d$ -dimensional domain  $\Omega \subset \mathbb{R}^d$  with  $d \leq 3$  is considered. For the time interval  $[0, T_e]$ , the solutions for the molar concentration  $c_1$  of cations with charge number  $z_1 > 0$  and anion concentration  $c_2$  with  $z_2 < 0$  are sought as well as the electric potential denoted by  $\Phi$ . Using the notation as introduced in the main part of this thesis, the complete problem formulation is given as follows. For a given velocity field  $\mathbf{u}$ , find  $c_1, c_2, \Phi$  such that in  $\Omega \times (0, T_e)$  it holds

$$\frac{\partial c_1}{\partial t} + \mathbf{u} \cdot \nabla c_1 - z_1 \mu_1 F \nabla \cdot (c_1 \nabla \Phi) - D_1 \Delta c_1 = 0, \quad (\text{A.1})$$

$$\frac{\partial c_2}{\partial t} + \mathbf{u} \cdot \nabla c_2 - z_2 \mu_2 F \nabla \cdot (c_2 \nabla \Phi) - D_2 \Delta c_2 = 0, \quad (\text{A.2})$$

$$z_1 c_1 + z_2 c_2 = 0, \quad (\text{A.3})$$

together with the following boundary and initial conditions for  $k = 1, 2$ :

$$c_k = g_k \quad \text{on } \Gamma_{D,k} \times (0, T_e), \quad (\text{A.4})$$

$$(z_k \mu_k F c_k \nabla \Phi + D_k \nabla c_k) \cdot \mathbf{n} = h_k \quad \text{on } \Gamma_{N,k} \times (0, T_e), \quad (\text{A.5})$$

$$c_k = c_k^0 \quad \text{in } \overline{\Omega} \times \{0\}, \quad (\text{A.6})$$

and the constraints

$$c_k > 0 \quad \text{in } \Omega \times [0, T_e]. \quad (\text{A.7})$$

Owing to the electroneutrality condition (A.3), the anion concentration  $c_2$  is already uniquely determined by  $c_1$  via

$$c_2 = -\frac{z_1}{z_2} c_1. \quad (\text{A.8})$$

Consequently,  $c_2^0 = -\frac{z_1}{z_2} c_1^0$  is required to be satisfied by the initial conditions (A.6). Furthermore,  $c_2$  can be eliminated from (A.2) by multiplication with  $-z_2/z_1$  and application of (A.8). Subtraction of the resulting equation from (A.1) then yields:

$$(z_2 \mu_2 - z_1 \mu_1) F \nabla \cdot (c_1 \nabla \Phi) + (D_2 - D_1) \Delta c_1 = 0. \quad (\text{A.9})$$

From the expression for the current density,

$$\mathbf{i} = F \sum_{k=1}^2 z_k \mathbf{N}_k^{d+m} = F \sum_{k=1}^2 z_k (-z_k \mu_k F c_k \nabla \Phi - D_k \nabla c_k), \quad (\text{A.10})$$

as introduced in (2.30), the following integrated form of (A.9) is deduced by using (A.8):

$$\frac{\mathbf{i}}{z_1 F} = (z_2 \mu_2 - z_1 \mu_1) F c_1 \nabla \Phi + (D_2 - D_1) \nabla c_1. \quad (\text{A.11})$$

For problems where no current  $\mathbf{i}$  is passing the electrochemical cell, a solution formula for the electric potential  $\Phi$  can be deduced by integration, which is applicable once  $c_1$  is known:

$$\Phi(\mathbf{x}, t) - \Phi(\mathbf{x}_0, t) = \frac{D_2 - D_1}{(z_1 \mu_1 - z_2 \mu_2) F} \ln \left( \frac{c_1(\mathbf{x}, t)}{c_1(\mathbf{x}_0, t)} \right). \quad (\text{A.12})$$

Here,  $\mathbf{x}_0 \in \bar{\Omega}$  is an arbitrary point with  $c_1(\mathbf{x}_0, t) > 0 \forall t \in [0, T_e]$ . For the case  $\mathbf{i} \neq \mathbf{0}$ , an explicit knowledge of the current density  $\mathbf{i}$  is required for integrating (A.11). For one-dimensional problems this requirement is typically fulfilled since the current density is a constant function due to charge conservation. As a result, the solution formula (A.12) will be extended by an additional linear term representing the ohmic voltage drop caused by the passage of electric current. An example for this situation is provided in section 4.1.1.

Finally, using (A.9) in (A.1) reveals that the concentration  $c_1$  is governed by a transient convection-diffusion equation of the form

$$\frac{\partial c_1}{\partial t} + \mathbf{u} \cdot \nabla c_1 - D \Delta c_1 = 0 \quad \text{in } \Omega \times (0, T_e), \quad (\text{A.13})$$

with a resulting diffusion coefficient

$$D := \frac{z_1 \mu_1 D_2 - z_2 \mu_2 D_1}{z_1 \mu_1 - z_2 \mu_2} \quad (\text{A.14})$$

depending on the properties of *both* ionic species of interest. It is important to note that (A.13) holds also in the case when an electric current is passing the considered electrochemical system.

In the same manner as above, one can eliminate  $c_2$  and  $\Phi$  from the flux boundary conditions (A.5), resulting in a new boundary condition

$$D \nabla c_1 \cdot \mathbf{n} = \tilde{h} \quad \text{on } \Gamma_{N,1} \times (0, T_e), \quad (\text{A.15})$$

with

$$\tilde{h} := \frac{(-z_2)(\mu_2 h_1 + \mu_1 h_2)}{z_1 \mu_1 - z_2 \mu_2}, \quad (\text{A.16})$$

which has to be fulfilled by the solution of (A.13). For the case  $h_2 = 0$ , i.e., the anion is an inert ionic species, one can also write

$$\tilde{h} = (1 - t_+) h_1 = t_- h_1, \quad (\text{A.17})$$

---

where  $t_+$ ,  $t_-$  denote the two transference numbers of the binary electrolyte (see, e.g., Newman and Thomas-Alyea [137]). In particular, the two transference numbers are given as

$$t_+ = \frac{z_1\mu_1}{z_1\mu_1 - z_2\mu_2}, \quad t_- = \frac{-z_2\mu_2}{z_1\mu_1 - z_2\mu_2}, \quad (\text{A.18})$$

and fulfill the relation  $t_+ + t_- = 1$ . It is important to note that due to (A.8) also  $c_2$  is fulfilling the convection-diffusion equation (A.13). In addition, the boundary condition (A.15) changes to  $D\nabla c_2 \cdot \mathbf{n} = -z_1 \tilde{h}/z_2$ , when concentration  $c_2$  is considered instead of  $c_1$ .

In summary, the task of solving the coupled nonlinear ion-transport problem (A.1)-(A.7) has been reduced to solving a linear convection-diffusion problem for  $c_1$  governed by equation (A.13) with boundary conditions (A.4), (A.15) and initial condition (A.6). The analysis presented above holds for an arbitrary number of space dimensions and is the basis for the construction of analytical solutions for ion-transport problems in binary electrolyte solutions. In the context of computational methods the knowledge of exact solution formulae is a very important aspect for code-validation purposes. In addition, the convergence behavior of numerical methods can be investigated on the basis of error calculations.



# B Flux calculation for finite element approaches

In the following, appropriate methods for a consistent calculation of nodal fluxes from finite element solutions are presented. Since interfacial phenomena are of special interest in the context of electrochemistry, an accurate computation of surface-related quantities is especially important. Examples for such data are the normal mass flux densities of reacting ionic species and the corresponding normal current density distribution at electrode surfaces. In addition, vector-valued representations for mass fluxes and electric current inside the whole computational domain are sometimes required for visualization purposes. Besides, such a flux reconstruction is also of importance in the context of low-order stabilized finite element methods as shown below. An appropriate method to calculate such vector-valued data from finite element solutions is outlined in the second part of this section.

## B.1 Consistent boundary-flux calculation

On coarse meshes, the method outlined in the following and originally proposed by Gresho et al. [86] typically results in better numerical approximations for derived boundary quantities compared to those gained from simple differentiation of the finite element representation of the solution. Furthermore, possible subgrid-scale contributions are included in a natural way. A comprehensive overview of such methods for consistent flux calculation is provided by Gresho and Sani [85], including a survey of related literature.

As shown by Bauer et al. [12], the basic idea can also be applied to ion-transport equations to compute the normal mass fluxes for each ionic species on respective boundaries and, based on that, normal current density distributions as specified in (2.28). The reader is also referred to Hennigan et al. [95] for current-density calculation from finite element solutions in the context of semiconductor device modeling.

The weak form (3.81) can be rewritten as

$$\int_{\partial\Omega} w_k^h \mathbf{N}_k^{d+m} (c_k^{h,n+\alpha_f}, \Phi^{h,n+\alpha_f}) \cdot \mathbf{n} dS = - \mathcal{B}_k (w_k^h, c_k^{h,n+1}, \Phi^{h,n+1}, \mathbf{u}^{h,n+1}) - \sum_{e=1}^{n_{el}} (\mathbf{v}_k^{h,n+\alpha_f} \cdot \nabla w_k^h, \tau_k^{n+\alpha_f} \mathcal{R}_k^h)_{\Omega_e}. \quad (\text{B.1})$$

together with

$$\mathbf{v}_k^{h,n+\alpha_f} = \mathbf{u}^{h,n+\alpha_f} + \mathbf{u}_{\text{mig},k}^{h,n+\alpha_f}. \quad (\text{B.2})$$

The right-hand side of (B.1) is easily evaluated once the solution fields are determined,

and it already contains all necessary information about the normal boundary fluxes: it is essentially the residual of the weak problem formulation without boundary terms. For each ion species  $k = 1, \dots, m$ , a finite element representation of the normal boundary flux of the form

$$q_k^h = \sum_{i=1}^{n_{\text{bdry}}} N_i^h \Big|_{\partial\Omega} \bar{q}_{k,i} \quad (\text{B.3})$$

is sought, where  $n_{\text{bdry}}$  denotes the number of associated boundary nodes. Each representation has to fulfill the relation

$$\int_{\partial\Omega} w_k^h q_k^{h,n+\alpha_f} dS = \int_{\partial\Omega} w_k^h \mathbf{N}_k^{d+m} (c_k^{h,n+\alpha_f}, \Phi^{h,n+\alpha_f}) \cdot \mathbf{n} dS \quad \forall w_k \in \mathcal{T}_{c_k} \quad k = 1, \dots, m. \quad (\text{B.4})$$

After inserting (B.3) into the left term of (B.4) and substituting the right-hand side via relation (B.1), one obtains

$$\begin{aligned} \int_{\partial\Omega} w_k^h q_k^{h,n+\alpha_f} dS &= -\mathcal{B}_k (w_k^h, c_k^{h,n+1}, \Phi^{h,n+1}, \mathbf{u}^{h,n+1}) \\ &\quad - \sum_{e=1}^{n_{\text{el}}} (\mathbf{v}_k^{h,n+\alpha_f} \cdot \nabla w_k^h, \tau_k^{n+\alpha_f} \mathcal{R}_k^h)_{\Omega_e} \quad \forall w_k \in \mathcal{T}_{c_k}. \end{aligned} \quad (\text{B.5})$$

Consequently, the solution of a small linear system of the form

$$\mathbf{M} \mathbf{q}_k^{n+\alpha_f} = \mathbf{r}_k^{n+\alpha_f} \quad (\text{B.6})$$

will be required to determine the nodal normal flux values  $\bar{q}_{k,i}^{n+\alpha_f}$  arranged in the vector  $\mathbf{q}_k^{n+\alpha_f}$ . The arising boundary mass matrix  $\mathbf{M}$  is given by

$$\mathbf{M}_{ij} = \int_{\partial\Omega} N_i^h N_j^h dS, \quad (\text{B.7})$$

where  $N_i^h$  denotes the shape function associated to node  $i$ . The nodewise contributions to the right-hand side  $\mathbf{r}_k^{n+\alpha_f}$  of (B.6) are computed as

$$\bar{r}_{k,i}^{n+\alpha_f} = -\mathcal{B}_k (N_i^h, c_k^{h,n+1}, \Phi^{h,n+1}, \mathbf{u}^{h,n+1}) - \sum_{e=1}^{n_{\text{el}}} (\mathbf{v}_k^{h,n+\alpha_f} \cdot \nabla N_i^h, \tau_k^{n+\alpha_f} \mathcal{R}_k^h)_{\Omega_e}. \quad (\text{B.8})$$

However, according to Gresho et al. [86], in most situations a lumping strategy for the arising boundary mass matrix  $\mathbf{M}$  in (B.6) provides sufficient accuracy and saves computational time. In the present work, a simple lumping strategy of the form

$$\bar{q}_{k,i}^{n+\alpha_f} \approx \bar{r}_{k,i}^{n+\alpha_f} / \bar{s}_i \quad (\text{B.9})$$

with

$$\bar{s}_i = \int_{\partial\Omega} N_i^h dS \quad (\text{B.10})$$

is used. The required values for the integrated shape functions  $\bar{s}_i$  can be computed once and simply reused for executing the nodewise division specified in (B.9). Note that the approach outlined here provides nodal boundary-flux values for the time level  $t^{n+\alpha_f}$ . For the case  $\alpha_f \neq 1$ , the present method can be combined with an extrapolation technique to obtain flux values for the time level  $t^{n+1}$ .

It is emphasized that the proposed method can also be used for consistent flux calculation at a subset of  $\partial\Omega$ , e.g., only at electrode surfaces. One important feature of the consistent flux calculation method is that it provides exactly the value  $h_k$  that is prescribed at the Neumann boundary part  $\Gamma_{N,k}$  (see Gresho et al. [86]).

## B.2 Flux approximation in the computational domain

The following method enables a consistent calculation of nodal flux vector fields in the whole computational domain  $\Omega$ . This is often required for visualization purposes, but is also important in the context of stabilized finite element methods as explained below. Examples in the present context of electrochemistry are vector field representations of the electric current density  $\mathbf{i}$ , as well as individual mass flux vector fields, such as  $\mathbf{N}_k$  or  $\mathbf{N}_k^{d+m}$ . Again, the most natural approach to simply evaluate the definition of these quantities is not recommended, since it requires the computation of derivatives of the finite element approximation at nodes.

As a remedy, a consistent flux reconstruction method by means of an  $L^2$ -projection is utilized here. The basic idea outlined in the following is identical to the technique presented by Jansen et al. [109] for improving consistency of stabilization terms in case of low-order finite element discretizations. Thus, the reader is encouraged to consult Jansen et al. [109] for further details. As a consequence, an implementation of the following flux calculation procedure can be utilized for two different purposes. First, as an improvement for low-order stabilized finite element methods and, second, as a valuable postprocessing feature.

Here, the aim is to globally reconstruct a continuous approximation to the ionic mass flux due to diffusion and migration by means of an  $L^2$ -projection. Thus, a finite element representation  $\mathbf{q}_k^h$  with the components

$$q_{k,a}^h = \sum_{i=1}^{n_{\text{nod}}} N_i^h \bar{q}_{k,i,a} \quad a = 1, \dots, d \quad (\text{B.11})$$

is sought, which approximates the  $d$ -dimensional flux vector field. The corresponding governing equations emanate from the idea of  $L^2$ -projection and read for the present case

$$\int_{\Omega} N_i^h \mathbf{q}_k^h \, d\mathbf{x} = \int_{\Omega} N_i^h \mathbf{N}_k^{d+m} (c_k^h, \Phi^h) \, d\mathbf{x} \quad \forall i = 1, \dots, n_{\text{nod}}, \quad k = 1, \dots, m. \quad (\text{B.12})$$

As a result, for each spatial component  $q_{k,a}$  of the nodewise flux-vector representation a linear system of the form

$$\mathbf{M} \mathbf{q}_{k,a} = \mathbf{r}_{k,a} \quad (\text{B.13})$$

has to be solved for  $a = 1, \dots, d$ . The mass matrix  $\mathbf{M}$  is given by

$$\mathbf{M}_{ij} = \int_{\Omega} N_i^h N_j^h \, d\mathbf{x}, \quad (\text{B.14})$$

and the right-hand-side  $\mathbf{r}_{k,a}$  of (B.13) is computed from the nodewise contributions

$$\bar{r}_{k,a,i} = \int_{\Omega} N_i^h \left( -D_k [\nabla c_k^h]_a - z_k \mu_k F c_k^h [\nabla \Phi^h]_a \right) \, d\mathbf{x}. \quad (\text{B.15})$$

Again, instead of actually solving the global linear system (B.13), lumping strategies are commonly used (Jansen et al. [109]). For an overview of different lumping strategies the reader is referred to Hughes [100].

Note that the procedure outlined above is not restricted to any specific time level. Typically, for the purpose of postprocessing, values for the time  $t^{n+1}$  will be of primary interest. For improving stabilized finite element methods as proposed by Jansen et al. [109], an evaluation at  $t^{n+\alpha_f}$  appears reasonable in the context of a generalized-alpha method, since the approximated flux terms are required at the intermediate time level  $t^{n+\alpha_f}$ .

Finally, it is emphasized that also other vector-valued quantities such as the total ionic mass flux  $\mathbf{N}_k$  or the electric current density  $\mathbf{i}$  can be inserted into (B.4) in order to compute a nodewise vector representation of these fields.

## C Rotationally-symmetric periodic boundary conditions

When a given problem setting shows rotational symmetry with respect to both the geometric setup as well as for the unknown physical fields, efficiency of simulations can be enhanced by performing calculations only on a segment of the computational domain. Several electrochemical cells exhibit such a symmetry, such as rotating disk or rotating cylinder electrodes. A confinement of the calculations to a wedge-shaped segment with angle  $\alpha$  is only applicable for stagnant electrolyte solutions or laminar, rotationally-symmetric flow conditions. In contrast, the symmetry assumption is not valid for turbulent flow. The required conditions for master and slave boundary read

$$\mathbf{u}_s = \mathbf{R}(\alpha)\mathbf{u}_m, \quad (C.1)$$

$$\{p, c_k, \Phi\}_s = \{p, c_k, \Phi\}_m. \quad (C.2)$$

For the case of rotational symmetry with respect to the z-axis, the rotation matrix  $\mathbf{R}(\alpha)$  required in (C.1) is given by

$$\mathbf{R}(\alpha) = \begin{bmatrix} \cos \alpha & -\sin \alpha & 0 \\ \sin \alpha & \cos \alpha & 0 \\ 0 & 0 & 1 \end{bmatrix}.$$

Since the matrix  $\mathbf{R}$  is orthogonal, it holds that  $\mathbf{R}^T = \mathbf{R}^{-1}$ . Scalar-valued degrees-of-freedom (i.e., pressure  $p$ , ionic concentrations  $c_k$  and electric potential  $\Phi$ ) take on the same values on master and slave boundary, as stated in (C.2). Vector-valued degrees-of-freedom, such as the fluid velocity  $\mathbf{u}$  on slave and master side are related through a linear transformation (C.1) defined by the rotation matrix  $\mathbf{R}$ . The situation for rotationally-symmetric periodic boundary conditions is also sketched in Fig. C.1.

For the implementation of rotationally-symmetric periodic boundary conditions standard master-slave relationships can be used. The evaluation of a finite element adjacent to the slave boundary necessitates the implementation of two additional operations. For the calculation of element contributions to element right-hand-side vectors and Jacobian matrices the current nodal velocity field is required. Thus, for element nodes belonging to the slave boundary, the velocity vector values received from the corresponding master node have to be rotated according to (C.1) before an interpolation to integration points is performed. This rotation is required for both the fluid and the electrochemistry subproblem. In general, if the problem formulation depends on further vector-valued data, such as displacements, for example, an analogous procedure has to be executed for that data.

The second action to be implemented is only required for the Navier-Stokes equations. During the assembly process, at slave boundary nodes, nodal contributions w.r.t. the momentum equation are rotated backwards using  $\mathbf{R}^T$  before assembling to the set of degree-

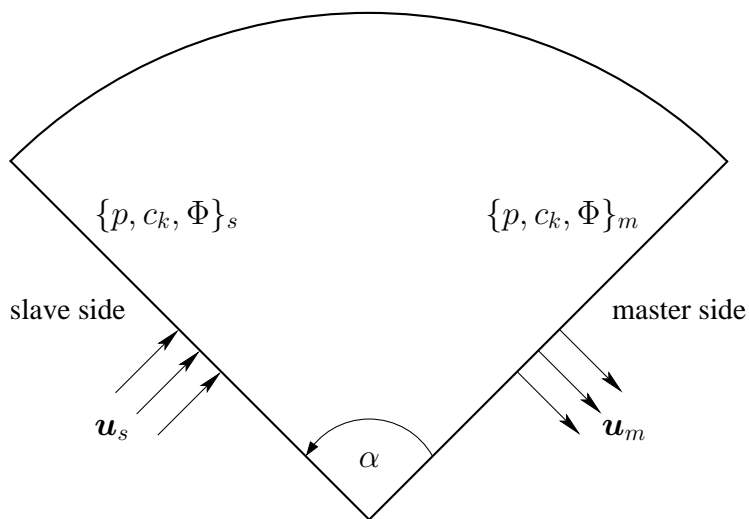


Figure C.1: Rotationally-symmetric periodic boundary conditions.

of-freedom of the corresponding master node takes place.

# Bibliography

- [1] R. A. ADAMS, J. J. F. FOURNIER, Sobolev Spaces, 2nd Edition. Vol. 140 of *Pure and Applied Mathematics*. Academic Press, Oxford, 2003.
- [2] R. ALKIRE, Processing nanostructured materials: the need to integrate experimental data with multiscale continuum/non-continuum simulations, *Journal of Electroanalytical Chemistry* **559** (2003) 3 – 12.
- [3] ASM INTERNATIONAL HANDBOOK COMMITTEE (Ed.), ASM Handbook, Volume 05 - Surface Engineering. ASM International, 1994.
- [4] V. S. BAGOTSKY, Fundamentals of Electrochemistry, 2nd Edition. Wiley, Hoboken, 2006.
- [5] D. BARAK-SHINAR, M. ROSENFELD, S. ABOUD, Numerical simulations of mass-transfer processes in 3D model of electrochemical sensor, *Journal of The Electrochemical Society* **151** (2004) H261–H266.
- [6] O. E. BARCIA, N. MANGIAVACCHI, O. R. MATTOS, J. PONTES, B. TRIBOLLET, Rotating disk flow in electrochemical cells: A coupled solution for hydrodynamic and mass equations, *Journal of The Electrochemical Society* **155** (2008) D424–D427.
- [7] A. J. BARD, L. R. FAULKNER, Electrochemical Methods, 2nd Edition. John Wiley & Sons, New York, 2001.
- [8] A. J. BARD, G. INZELT, F. SCHOLZ (Eds.), Electrochemical Dictionary. Springer, Berlin and Heidelberg, 2008.
- [9] G. BAUER, P. GAMNITZER, V. GRAVEMEIER, W. A. WALL, An isogeometric variational multiscale method for large-eddy simulation of coupled multi-ion transport in turbulent flow, *Preprint, submitted for publication in Journal of Computational Physics* (2012).
- [10] G. BAUER, V. GRAVEMEIER, W. A. WALL, Modeling and numerical simulation of electroplating facilities: coupling ion transport, electric field and fluid flow. In: Proceedings of the International Conference on Computational Methods for Coupled Problems in Science and Engineering – Coupled Problems, 2009.
- [11] G. BAUER, V. GRAVEMEIER, W. A. WALL, A 3D finite element approach for the coupled numerical simulation of electrochemical systems and fluid flow, *International Journal for Numerical Methods in Engineering* **86** (2011) 1339–1359.
- [12] G. BAUER, V. GRAVEMEIER, W. A. WALL, A stabilized finite element method for the numerical simulation of multi-ion transport in electrochemical systems, *Computer Methods in Applied Mechanics and Engineering* **223–224** (2012) 199–210.

## Bibliography

---

- [13] G. BAUER, V. GRAVEMEIER, W. A. WALL, A 3D finite element method for the coupled numerical simulation of electrochemical systems and fluid flow: ion transport in electrodeposition. In: J. C. F. Pereira, A. Sequeira, J. M. C. Pereira (Eds.), Proceedings of the V European Conference on Computational Fluid Dynamics (ECCOMAS CFD 2010), Lisbon, Portugal, June 14-17, 2010.
- [14] M. Z. BAZANT, K. T. CHU, B. J. BAYLY, Current-voltage relations for electrochemical thin films, *SIAM Journal on Applied Mathematics* **65** (2005) 1463–1484.
- [15] Y. BAZILEVS, I. AKKERMANN, Large eddy simulation of turbulent Taylor-Couette flow using isogeometric analysis and the residual-based variational multiscale method, *Journal of Computational Physics* **229** (2010) 3402–3414.
- [16] Y. BAZILEVS, V. M. CALO, J. A. COTTRELL, T. J. R. HUGHES, A. REALI, G. SCOVAZZI, Variational multiscale residual-based turbulence modeling for large eddy simulation of incompressible flows, *Computer Methods in Applied Mechanics and Engineering* **197** (2007) 173–201.
- [17] M. BENZI, G. H. GOLUB, J. LIESEN, Numerical solution of saddle point problems, *Acta Numerica* **14** (2005) 1–137.
- [18] P. BERG, J. FINDLAY, Analytical solution of the Poisson-Nernst-Planck-Stokes equations in a cylindrical channel, *Proceedings of the Royal Society A: Mathematical, Physical and Engineering Science* **467** (2011) 3157–3169.
- [19] P. BOCHEV, R. B. LEHOUCQ, On finite element solution of the pure Neumann problem, *SIAM Review* **47** (2001) 50–66.
- [20] L. BORTELS, J. DECONINCK, B. VAN DEN BOSSCHE, The multi-dimensional upwinding method as a new simulation tool for the analysis of multi-ion electrolytes controlled by diffusion, convection and migration. Part 1. Steady state analysis of a parallel plane flow channel, *Journal of Electroanalytical Chemistry* **404** (1996) 15–26.
- [21] L. BORTELS, B. VAN DEN BOSSCHE, J. DECONINCK, Analytical solution for the steady-state diffusion and migration. Application to the identification of Butler-Volmer electrode reaction parameters, *Journal of Electroanalytical Chemistry* **422** (1997) 161–167.
- [22] L. BORTELS, B. VAN DEN BOSSCHE, J. DECONINCK, S. VANDEPUTTE, A. HUBIN, Analytical solution for the steady-state diffusion and migration involving multiple reaction ions. Application to the identification of Butler-Volmer kinetic parameters for the ferri-/ferrocyanide redox couple, *Journal of Electroanalytical Chemistry* **429** (1997) 139–155.
- [23] M. BRAACK, E. BURMAN, V. JOHN, G. LUBE, Stabilized finite element methods for the generalized Oseen problem, *Computer Methods in Applied Mechanics and Engineering* **196** (2007) 853–866.
- [24] S. C. BRENNER, L. R. SCOTT, The Mathematical Theory of Finite Element Methods. Springer, New York, 1994.

- [25] D. BRITZ, Digital Simulation in Electrochemistry (Lecture Notes in Physics). Springer, Berlin and Heidelberg, 2005.
- [26] A. N. BROOKS, T. J. R. HUGHES, Streamline upwind/Petrov-Galerkin formulations for convection dominated flows with particular emphasis on the incompressible Navier-Stokes equations, *Computer Methods in Applied Mechanics and Engineering* **32** (1982) 199–259.
- [27] M. BUONI, L. PETZOLD, An efficient, scalable numerical algorithm for the simulation of electrochemical systems on irregular domains, *Journal of Computational Physics* **225** (2007) 2320–2332.
- [28] M. BUONI, L. PETZOLD, An algorithm for simulation of electrochemical systems with surface-bulk coupling strategies, *Journal of Computational Physics* **229** (2010) 379–398.
- [29] G. C. BURTON, The nonlinear large-eddy simulation method applied to  $\text{Sc} \approx 1$  and  $\text{Sc} \gg 1$  passive-scalar mixing, *Physics of Fluids* **20** (2008) 035103.
- [30] I. CALMET, J. MAGNAUDET, Large-eddy simulation of high-Schmidt number mass transfer in a turbulent channel flow, *Physics of Fluids* **9** (1997) 438–455.
- [31] V. M. CALO, Residual-based multiscale turbulence modeling: Finite volume simulations of bypass transition. Ph.D. thesis, Stanford University, 2005.
- [32] M. S. CHANDRASEKAR, M. PUSHPAVANAM, Pulse and pulse reverse plating – Conceptual, advantages and applications, *Electrochimica Acta* **53** (2008) 3313–3322.
- [33] Y. S. CHOI, K.-Y. CHAN, Exact solutions of transport in a binary electrolyte, *Journal of Electroanalytical Chemistry* **334** (1992) 13–23.
- [34] Y. S. CHOI, Z. HUAN, R. LUI, Global existence of solutions of a strongly coupled quasilinear parabolic system with applications to electrochemistry, *Journal of Differential Equations* **194** (2003) 406–432.
- [35] Y. S. CHOI, R. LUI, Uniqueness of steady-state solutions for an electrochemistry model with multiple species, *Journal of Differential Equations* **108** (1994) 424–437.
- [36] Y. S. CHOI, R. LUI, Global stability of solutions of an electrochemistry model with multiple species, *Journal of Differential Equations* **116** (1995) 306–317.
- [37] Y. S. CHOI, R. LUI, Multi-dimensional electrochemistry model, *Archive for Rational Mechanics and Analysis* **130** (1995) 315–342.
- [38] Y. S. CHOI, X. YU, Steady-state solution for electroplating, *IMA Journal of Applied Mathematics* **51** (1993) 251–267.
- [39] J. CHUNG, G. M. HULBERT, A time integration algorithm for structural dynamics with improved numerical dissipation: The generalized-alpha method, *Journal of Applied Mechanics* **60** (1993) 371–375.

## Bibliography

---

- [40] M.-H. CHUNG, A numerical method for analysis of tertiary current distribution in unsteady natural convection multi-ion electrodeposition, *Electrochimica Acta* **45** (2000) 3959–3972.
- [41] R. CODINA, J. PRINCIPE, O. GUASCH, S. BADIA, Time dependent subscales in the stabilized finite element approximation of incompressible flow problems, *Computer Methods in Applied Mechanics and Engineering* **196** (2007) 2413–2430.
- [42] S. S. COLLIS, Monitoring unresolved scales in multiscale turbulence modeling, *Physics of Fluids* **13** (2001) 1800–1806.
- [43] B. DAMASKIN, O. PETRII, Historical development of theories of the electrochemical double layer, *Journal of Solid State Electrochemistry* **15** (2011) 1317–1334.
- [44] C. DAN, B. VAN DEN BOSSCHE, L. BORTELS, G. NELISSEN, J. DECONINCK, Numerical simulation of transient current responses in diluted electrochemical ionic systems, *Journal of Electroanalytical Chemistry* **505** (2001) 12–23.
- [45] M. DATTA, D. LANDOLT, Fundamental aspects and applications of electrochemical microfabrication, *Electrochimica Acta* **45** (2000) 2535–2558.
- [46] T. A. DAVIS, Algorithm 832: UMFPACK V4.3 – an unsymmetric-pattern multifrontal method, *ACM Transactions on Mathematical Software* **30** (2004) 196–199.
- [47] T. DE MULDER, The role of bulk viscosity in stabilized finite element formulations for incompressible flow: A review, *Computer Methods in Applied Mechanics and Engineering* **163** (1998) 1–10.
- [48] E. DICKINSON, J. LIMON-PETERSEN, R. COMPTON, The electroneutrality approximation in electrochemistry, *Journal of Solid State Electrochemistry* **15** (2011) 1335–1345.
- [49] C. R. DOERING, The 3D Navier-Stokes problem, *Annual Review of Fluid Mechanics* **41** (2009) 109–128.
- [50] J. DONEA, A. HUERTA, Finite Element Methods for Flow Problems. John Wiley & Sons, Chichester, 2003.
- [51] J. DONEA, A. HUERTA, J. PONTHOT, A. RODRÍGUEZ-FERRAN, Arbitrary Lagrangian-Eulerian methods. In: The Encyclopedia of Computational Mechanics. Vol. 1. Wiley, pp. 413–437, 2004.
- [52] S. DONG, Direct numerical simulation of turbulent Taylor-Couette flow, *Journal of Fluid Mechanics* **587** (2007) 373–393.
- [53] Y.-H. DONG, X.-Y. LU, L.-X. ZHUANG, Large eddy simulation of turbulent channel flow with mass transfer at high-Schmidt numbers, *International Journal of Heat and Mass Transfer* **46** (2003) 1529–1539.
- [54] J. O. DUKOVIC, Computation of current distribution in electrodeposition, a review, *IBM Journal of Research and Development* **34** (1990) 693–705.

- [55] A. EHRL, Numerical simulation of natural convection in electrochemical systems. Master's thesis, Technische Universität München, 2009.
- [56] A. EHRL, G. BAUER, V. GRAVEMEIER, W. A. WALL, A computational approach for the simulation of natural convection in electrochemical cells, *Preprint, submitted for publication in Journal of Computational Physics* (2012).
- [57] A. EHRL, A. POPP, V. GRAVEMEIER, W. A. WALL, A mortar approach with dual Lagrange multipliers for mesh tying within a variational multiscale method for incompressible flow, *Preprint, submitted for publication in Computer Methods in Applied Mechanics and Engineering* (2012).
- [58] M. EISENBERG, C. W. TOBIAS, C. R. WILKE, Ionic mass transfer and concentration polarization at rotating electrodes, *Journal of The Electrochemical Society* **101** (1954) 306–320.
- [59] Electrochemical Science and Technology Information Resource (ESTIR). <http://electrochem.cwru.edu/estir/>, 2011.
- [60] H. ELMAN, V. E. HOWLE, J. SHADID, R. SHUTTLEWORTH, R. TUMINARO, A taxonomy and comparison of parallel block multi-level preconditioners for the incompressible Navier-Stokes equations, *Journal of Computational Physics* **227** (2008) 1790–1808.
- [61] W. FANG, K. Ito, An electrochemistry model with nonlinear diffusion: steady-state solutions, *IMA Journal of Applied Mathematics* **66** (2001) 195–213.
- [62] G. E. FARIN, NURBS: From Projective Geometry to Practical Use. A.K. Peters, Ltd., Natick, 1999.
- [63] S. W. FELDBERG, On the dilemma of the use of the electroneutrality constraint in electrochemical calculations, *Electrochemistry Communications* **2** (2000) 453–456.
- [64] S. W. FELDBERG, C. AUERBACH, Model for current reversal chronopotentiometry with second-order kinetic complications, *Analytical Chemistry* **36** (1964) 505–509.
- [65] C. FÖRSTER, Robust methods for fluid-structure interaction with stabilised finite elements. Ph.D. thesis, Universität Stuttgart, 2007.
- [66] D. R. GABE, The rotating cylinder electrode, *Journal of Applied Electrochemistry* **4** (1974) 91–108.
- [67] D. R. GABE, F. C. WALSH, The rotating cylinder electrode: a review of development, *Journal of Applied Electrochemistry* **13** (1983) 3–21.
- [68] D. R. GABE, G. D. WILCOX, J. GONZALEZ-GARCIA, F. C. WALSH, The rotating cylinder electrode: its continued development and application, *Journal of Applied Electrochemistry* **28** (1998) 759–780.
- [69] P. GAMNITZER, Residual-based variational multiscale methods for turbulent flows and fluid-structure interaction. Ph.D. thesis, Technische Universität München, 2010.

- [70] P. GAMNITZER, V. GRAVEMEIER, W. A. WALL, Time-dependent subgrid scales in residual-based large eddy simulation of turbulent channel flow, *Computer Methods in Applied Mechanics and Engineering* **199** (2010) 819–827.
- [71] D. K. GANJOO, T. E. TEZDUYAR, Petrov-Galerkin formulations for electrochemical processes, *Computer Methods in Applied Mechanics and Engineering* **65** (1987) 61–83.
- [72] D. K. GANJOO, T. E. TEZDUYAR, W. D. GOODRICH, A new formulation for numerical simulation of electrophoresis separation processes, *Computer Methods in Applied Mechanics and Engineering* **75** (1989) 515–530.
- [73] M. W. GEE, U. KÜTTLER, W. A. WALL, Truly monolithic algebraic multigrid for fluid-structure interaction, *International Journal for Numerical Methods in Engineering* **85** (2010) 987–1016.
- [74] M. GEORGIADOU, Finite-difference simulation of multi-ion electrochemical systems governed by diffusion, migration and convection, *Journal of The Electrochemical Society* **144** (1997) 2732–2739.
- [75] M. GEORGIADOU, Modeling current density distribution in electrochemical systems, *Electrochimica Acta* **48** (2003) 4089–4095.
- [76] M. GEORGIADOU, R. MOHR, R. C. ALKIRE, Local mass transport in two-dimensional cavities in laminar shear flow, *Journal of The Electrochemical Society* **147** (2000) 3021–3028.
- [77] S. GHOSAL, Z. CHEN, A nonlinear equation for ionic diffusion in a strong binary electrolyte, *Proceedings of the Royal Society A* **466** (2010) 2145–2154.
- [78] V. GRAVEMEIER, The variational multiscale method for laminar and turbulent incompressible flows. Ph.D. thesis, Universität Stuttgart, 2003.
- [79] V. GRAVEMEIER, The variational multiscale method for laminar and turbulent flow, *Archives of Computational Methods in Engineering — State of the Art Reviews* **13** (2006) 249–324.
- [80] V. GRAVEMEIER, M. KRONBICHLER, M. W. GEE, W. A. WALL, An algebraic variational multiscale-multigrid method for large-eddy simulation: generalized-alpha time integration, Fourier analysis and application to turbulent flow past a square-section cylinder, *Computational Mechanics* **47** (2011) 217–233.
- [81] V. GRAVEMEIER, S. LENZ, W. A. WALL, Towards a taxonomy for multiscale methods in computational mechanics: building blocks of existing methods, *Computational Mechanics* **41** (2008) 279–291.
- [82] V. GRAVEMEIER, W. A. WALL, An algebraic variational multiscale-multigrid method for large-eddy simulation of turbulent variable-density flow at low Mach number, *Journal of Computational Physics* **229** (2010) 6047–6070.

- [83] V. GRAVEMEIER, W. A. WALL, Residual-based variational multiscale methods for laminar, transitional and turbulent variable-density flow at low Mach number, *International Journal for Numerical Methods in Fluids* **65** (2011) 1260–1278.
- [84] V. GRAVEMEIER, W. A. WALL, Variational multiscale methods for premixed combustion based on a progress-variable approach, *Combustion and Flame* **158** (2011) 1160–1170.
- [85] P. GRESHO, R. SANI, Incompressible Flow and the Finite Element Method, Isothermal Laminar Flow. Vol. 2. Wiley, Chichester, 1998.
- [86] P. M. GRESHO, R. L. LEE, R. L. SANI, M. K. MASLANIK, B. E. EATON, The consistent Galerkin FEM for computing derived boundary quantities in thermal and or fluids problems, *International Journal for Numerical Methods in Fluids* **7** (1987) 371–394.
- [87] M. E. GURTIN, An introduction to continuum mechanics. In: Mathematics in Science and Engineering. Vol. 158. Academic Press, 1981.
- [88] E. HACHEM, B. RIVAUT, T. KLOCZKO, H. DIGONNET, T. COUPEZ, Stabilized finite element method for incompressible flows with high Reynolds number, *Journal of Computational Physics* **229** (2010) 8643–8665.
- [89] E. HAIRER, S. P. NØRSETT, G. WANNER, Solving Ordinary Differential Equations I: Nonstiff Problems, 2nd Edition. Vol. 8 of *Springer Series in Computational Mathematics*. Springer, Berlin/Heidelberg/New York, 2000.
- [90] E. HAIRER, G. WANNER, Solving Ordinary Differential Equations II, Stiff and Differential-Algebraic Problems, 2nd Edition. Vol. 14 of *Springer Series in Computational Mathematics*. Springer, Berlin/Heidelberg/New York, 2004.
- [91] C. H. HAMANN, A. HAMNETT, W. VIELSTICH, Electrochemistry, 2nd Edition. Wiley-VCH, Weinheim, 2007.
- [92] G. HAUKE, A simple subgrid scale stabilized method for the advection-diffusion-reaction equation, *Computer Methods in Applied Mechanics and Engineering* **191** (2002) 2925–2947.
- [93] X. HE, N. LI, Lattice Boltzmann simulation of electrochemical systems, *Computer Physics Communications* **129** (2000) 158–166.
- [94] I. E. HENLEY, A. C. FISHER, Computational electrochemistry: The simulation of voltammetry in microchannels with low conductivity solutions, *The Journal of Physical Chemistry B* **107** (2003) 6579–6585.
- [95] G. L. HENNIGAN, R. J. HOEKSTRA, J. P. CASTRO, D. A. FIXEL, J. N. SHADD, Simulation of neutron radiation damage in silicon semiconductor devices. Technical Report SAND2007-7157, Sandia National Laboratories, 2007.

- [96] M. A. HEROUX, R. A. BARTLETT, V. E. HOWLE, R. J. HOEKSTRA, J. J. HU, T. G. KOLDA, R. B. LEHOUCQ, K. R. LONG, R. P. PAWLOWSKI, E. T. PHIPPS, A. G. SALINGER, H. K. THORNQUIST, R. S. TUMINARO, J. M. WILLENBRING, A. WILLIAMS, K. S. STANLEY, An overview of the trilinos project, *ACM Transactions on Mathematical Software* **31** (2005) 397–423.
- [97] G. HINDS, J. M. D. COEY, M. LYONS, Influence of magnetic forces on electrochemical mass transport, *Electrochemistry Communications* **3** (2001) 215–218.
- [98] M. HUGHES, N. STRUSSEVITCH, C. BAILEY, K. McMANUS, J. KAUFMANN, D. FLYNN, M. P. Y. DESMULLIEZ, Numerical algorithms for modelling electrodeposition: Tracking the deposition front under forced convection from megasonic agitation, *International Journal for Numerical Methods in Fluids* **64** (2010) 237–268.
- [99] T. J. R. HUGHES, Multiscale phenomena: Green's functions, the Dirichlet-to-Neumann formulation, subgrid scale models, bubbles and the origins of stabilized methods, *Computer Methods in Applied Mechanics and Engineering* **127** (1995) 387–401.
- [100] T. J. R. HUGHES, The Finite Element Method – Linear Static and Dynamic Finite Element Analysis. Dover Publications, Mineola, 2000.
- [101] T. J. R. HUGHES, L. MAZZEI, K. E. JANSEN, Large eddy simulation and the variational multiscale method, *Computing and Visualization in Science* **3** (2000) 47–59.
- [102] T. J. R. HUGHES, G. SCOVAZZI, L. FRANCA, Multiscale and stabilized methods. In: E. Stein, R. de Borst, T. Hughes (Eds.), Encyclopedia of Computational Mechanics. John Wiley & Sons, Chichester, pp. 5–59, 2004.
- [103] J.-Y. HWANG, K.-S. YANG, K. BREMHORST, Direct numerical simulation of turbulent flow around a rotating circular cylinder, *Journal of Fluids Engineering* **129** (2007) 40–47.
- [104] M. IMAMURA, J. TOGURI, Physicochemical properties of nickel electrolytes, *Metallurgical and Materials Transactions B* **25** (1994) 637–644.
- [105] H. IMMICH, J. ALTING, J. KRETSCHMER, D. PRECLIK, Technology developments for thrust chambers of future launch vehicle liquid rocket engines, *Acta Astronautica* **53** (2003) 597–605.
- [106] F. P. INCROPERA, D. P. DEWITT, Fundamentals of Heat and Mass Transfer, 5th Edition. Wiley, New York, 2001.
- [107] G. INZELT, Milestones of the development of kinetics of electrode reactions, *Journal of Solid State Electrochemistry* **15** (2011) 1373–1389.
- [108] J. D. JACKSON, Classical Electrodynamics, 3rd Edition. Wiley, New York, 1998.
- [109] K. E. JANSEN, S. S. COLLIS, C. WHITING, F. SHAKI, A better consistency for low-order stabilized finite element methods, *Computer Methods in Applied Mechanics and Engineering* **174** (1999) 154–170.

- [110] K. E. JANSEN, C. H. WHITING, G. M. HULBERT, A generalized-alpha method for integrating the filtered Navier-Stokes equations with a stabilized finite element method, *Computer Methods in Applied Mechanics and Engineering* **190** (2000) 305–319.
- [111] N. KANANI, Electroplating: Basic Principles, Processes and Practice. Elsevier Science, Oxford and Amsterdam, 2005.
- [112] S. KANG, H. G. CHOI, J. Y. YOO, Investigation of fluid-structure interactions using a velocity-linked P2/P1 finite element method and the generalized- $\alpha$  method, *International Journal for Numerical Methods in Engineering* **90** (2012) 1529–1548.
- [113] S. KAWAI, Y. FUKUNAKA, S. KIDA, Numerical simulation of ionic mass-transfer rates with natural convection in CuSO<sub>4</sub>–H<sub>2</sub>SO<sub>4</sub> solution, I. Numerical study on the developments of secondary flow and electrolyte stratification phenomena, *Journal of The Electrochemical Society* **156** (2009) F99–F108.
- [114] S. KAWAI, Y. FUKUNAKA, S. KIDA, Numerical simulation of ionic mass-transfer rates with natural convection in CuSO<sub>4</sub>–H<sub>2</sub>SO<sub>4</sub> solution, II. Comparisons between numerical calculations and optical measurements, *Journal of The Electrochemical Society* **156** (2009) F109–F114.
- [115] S. KAWAI, Y. FUKUNAKA, S. KIDA, Numerical calculation of transient current density distribution along vertical plane electrode in CuSO<sub>4</sub>–H<sub>2</sub>SO<sub>4</sub> electrolyte solution, *Journal of The Electrochemical Society* **157** (2010) F40–F48.
- [116] S. KAWAI, M. OGAWA, K. ISHBASHI, Y. KONDO, T. MATSUOKA, T. HOMMA, Y. FUKUNAKA, S. KIDA, Transient mass transfer rate of Cu<sup>2+</sup> ion caused by copper electrodeposition with alternating electrolytic current, *Electrochimica Acta* **55** (2010) 3987–3994.
- [117] K. KONTURI, L. MURTOMÄKI, J. A. MANZANARES, Ionic Transport Processes – In Electrochemistry and Membrane Science. Oxford University Press, Oxford and New York, 2008.
- [118] P. K. KUNDU, I. M. COHEN, Fluid Mechanics, 4th Edition. Academic Press, 2008.
- [119] Y.-K. KWOK, C. C. K. WU, Fractional step algorithm for solving a multi-dimensional diffusion-migration equation, *Numerical Methods for Partial Differential Equations* **11** (1995) 389–397.
- [120] Y.-K. KWOK, C. C. K. WU, Numerical simulation of electrochemical diffusion-migration model with reaction at electrodes, *Computer Methods in Applied Mechanics and Engineering* **132** (1996) 305–317.
- [121] A. LA ROCCA, H. POWER, Free mesh radial basis function collocation approach for the numerical solution of system of multi-ion electrolytes, *International Journal for Numerical Methods in Engineering* **64** (2005) 1699–1734.
- [122] W. M. LAI, D. RUBIN, E. KREML, Introduction to Continuum Mechanics, 4th Edition. Butterworth-Heinemann, Burlington, 2009.

## Bibliography

---

- [123] J. LEE, J. B. TALBOT, A model of electrocodeposition on a rotating cylinder electrode, *Journal of The Electrochemical Society* **154** (2007) D70–D77.
- [124] J.-M. LEE, A. C. WEST, Impact of pulse parameters on current distribution in high aspect ratio vias and through-holes, *Journal of The Electrochemical Society* **152** (2005) C645–C651.
- [125] P. T. LIN, J. N. SHADID, M. SALA, R. S. TUMINARO, G. L. HENNIGAN, R. J. HOEKSTRA, Performance of a parallel algebraic multilevel preconditioner for stabilized finite element semiconductor device modeling, *Journal of Computational Physics* **228** (2009) 6250–6267.
- [126] P. T. LIN, J. N. SHADID, R. S. TUMINARO, M. SALA, Performance of a Petrov-Galerkin algebraic multilevel preconditioner for finite element modeling of the semiconductor device drift-diffusion equations, *International Journal for Numerical Methods in Engineering* **84** (2010) 448–469.
- [127] C. T. J. LOW, E. P. L. ROBERTS, F. C. WALSH, Numerical simulation of the current, potential and concentration distributions along the cathode of a rotating cylinder Hull cell, *Electrochimica Acta* **52** (2007) 3831–3840.
- [128] K. LUDWIG, I. MORALES, B. SPEISER, EChem++ – an object-oriented problem solving environment for electrochemistry. Part 6. Adaptive finite element simulations of controlled-current electrochemical experiments, *Journal of Electroanalytical Chemistry* **608** (2007) 102–110.
- [129] C. MADORE, M. MATLOSZ, D. LANDOLT, Experimental investigation of the primary and secondary current distribution in a rotating cylinder Hull cell, *Journal of Applied Electrochemistry* **22** (1992) 1155–1160.
- [130] PH. MANDIN, J. M. CENSE, C. FABIAN, C. GBADO, D. LINCOT, Electrodeposition process modeling using continuous and discrete scales, *Computers and Chemical Engineering* **31** (2007) 980–992.
- [131] PH. MANDIN, C. FABIAN, D. LINCOT, Mean and unsteady hydrodynamic and mass transport properties at a rotating cylinder electrode: From laminar to transitional flow regime, *Journal of Electroanalytical Chemistry* **586** (2006) 276–296.
- [132] PH. MANDIN, C. FABIAN, D. LINCOT, Numerical simulation of hydrodynamic and mass-transport properties at a laminar rotating cylinder electrode, *Journal of The Electrochemical Society* **153** (2006) D40–D50.
- [133] N. MANGIAVACCHI, J. PONTES, O. E. BARCIA, O. R. MATTOS, B. TRIBOLLET, Rotating disk flow stability in electrochemical cells: Effect of the transport of a chemical species, *Physics of Fluids* **19** (2007) 114109 (15 pages).
- [134] M. S. MOATS, J. HISKEY, D. W. COLLINS, The effect of copper, acid, and temperature on the diffusion coefficient of cupric ions in simulated electrorefining electrolytes, *Hydrometallurgy* **56** (2000) 255–268.

- [135] Á. MOLINA, F. MARTÍNEZ-ORTIZ, E. LABORDA, R. G. COMPTON, Analytical solution for reverse pulse voltammetry at spherical electrodes: A remarkably sensitive method for the characterization of electrochemical reversibility and electrode kinetics, *Journal of Electroanalytical Chemistry* **648** (2010) 67–77.
- [136] G. NELISSEN, A. VAN THEEMSCHE, C. DAN, B. VAN DEN BOSSCHE, J. DECONINCK, Multi-ion transport and reaction simulations in turbulent parallel plate flow, *Journal of Electroanalytical Chemistry* **563** (2004) 213–220.
- [137] J. NEWMAN, K. E. THOMAS-ALYE, Electrochemical Systems, 3rd Edition. John Wiley & Sons, Hoboken, 2004.
- [138] R. ORINAKOVA, A. TURNOVA, D. KLADEKOVA, M. GALOVA, R. SMITH, Recent developments in the electrodeposition of nickel and some nickel-based alloys, *Journal of Applied Electrochemistry* **36** (2006) 957–972.
- [139] J. H. PARK, J. W. JEROME, Qualitative properties of steady-state Poisson–Nernst–Planck systems: Mathematical study, *SIAM Journal on Applied Mathematics* **57** (1997) 609–630.
- [140] S. V. PATANKAR, D. B. SPALDING, A calculation procedure for heat, mass and momentum transfer in three-dimensional parabolic flows, *International Journal of Heat and Mass Transfer* **15** (1972) 1787–1806.
- [141] M. PAUNOVIC, M. SCHLESINGER, Fundamentals of Electrochemical Deposition, 2nd Edition. The Electrochemical Society Series. John Wiley & Sons, Hoboken, 2006.
- [142] L. PIEGL, W. TILLER, The NURBS book, 2nd Edition. Monographs in Visual Communication. Springer, Berlin/Heidelberg/New York, 1997.
- [143] J. PONTES, N. MANGIAVACCHI, A. R. CONCEICAO, O. E. BARCIA, O. R. MATTOS, B. TRIBOLLET, Rotating disk flow stability in electrochemical cells: Effect of viscosity stratification, *Physics of Fluids* **16** (2004) 707–716.
- [144] D. PRICE, W. DAVENPORT, Physico-chemical properties of copper electrorefining and electrowinning electrolytes, *Metallurgical and Materials Transactions B* **12** (1981) 639–643.
- [145] A. PROHL, M. SCHMUCK, Convergent finite element discretizations of the Navier-Stokes-Nernst-Planck-Poisson system, *ESAIM: Mathematical Modelling and Numerical Analysis* **44** (2010) 531–571.
- [146] J.-C. PUIPPE, F. LEAMAN, Theory and Practice of Pulse Plating. American Electroplaters and Surface Finishers Society, Orlando, 1986.
- [147] M. PURCAR, L. BORTELS, B. VAN DEN BOSSCHE, J. DECONINCK, 3D electrochemical machining computer simulations, *Journal of Materials Processing Technology* **149** (2004) 472–478.

## Bibliography

---

- [148] M. PURCAR, J. DECONINCK, B. VAN DEN BOSSCHE, L. BORTELS, Electroforming simulations based on the level set method, *The European Physical Journal - Applied Physics* **39** (2007) 85–94.
- [149] U. RASTHOFER, F. HENKE, W. A. WALL, V. GRAVEMEIER, An extended residual-based variational multiscale method for two-phase flow including surface tension, *Computer Methods in Applied Mechanics and Engineering* **200** (2011) 1866–1876.
- [150] S. M. K. RAUSCH, C. MARTIN, P. B. BORNEMANN, S. UHLIG, W. A. WALL, Material model of lung parenchyma based on living precision-cut lung slice testing, *Journal of the Mechanical Behavior of Biomedical Materials* **4** (2011) 583–592.
- [151] M. REHMAN, C. VUIK, G. SEGAL, SIMPLE-type preconditioners for the Oseen problem, *International Journal for Numerical Methods in Fluids* **61** (2009) 432–452.
- [152] I. RUBINSTEIN, *Electro-Diffusion of Ions*. Society for Industrial and Applied Mathematics, Philadelphia, 1990.
- [153] Y. SAAD, M. H. SCHULTZ, GMRES: A generalized minimal residual algorithm for solving nonsymmetric linear systems, *SIAM Journal on Scientific Computing* **7** (1986) 856–869.
- [154] E. SAMSON, J. MARCHAND, J.-L. ROBERT, J.-P. BOURNAZEL, Modelling ion diffusion mechanisms in porous media, *International Journal for Numerical Methods in Engineering* **46** (1999) 2043–2060.
- [155] M. SCHLESINGER, M. PAUNOVIC, *Modern Electroplating*, 4th Edition. Wiley, New York, 2000.
- [156] F. SCHWERTFIRM, M. MANHART, DNS of passive scalar transport in turbulent channel flow at high Schmidt numbers, *International Journal of Heat and Fluid Flow* **28** (2007) 1204–1214.
- [157] J. A. SETHIAN, Y. SHAN, Solving partial differential equations on irregular domains with moving interfaces, with applications to superconformal electrodeposition in semiconductor manufacturing, *Journal of Computational Physics* **227** (2008) 6411–6447.
- [158] R. SEVILLA, S. FERNÁNDEZ-MÉNDEZ, A. HUERTA, NURBS-enhanced finite element method (NEFEM), *International Journal for Numerical Methods in Engineering* **76** (2008) 56–83.
- [159] R. SEVILLA, S. FERNÁNDEZ-MÉNDEZ, A. HUERTA, 3D NURBS-enhanced finite element method (NEFEM), *International Journal for Numerical Methods in Engineering* **88** (2011) 103–125.
- [160] A. V. SOKIRKO, F. H. BARK, Diffusion-migration transport in a system with Butler-Volmer kinetics, an exact solution, *Electrochimica Acta* **40** (1995) 1983–1996.
- [161] J. H. SPURK, *Fluid Mechanics*. Springer, Berlin/Heidelberg/New York, 1997.

- [162] T. SUBBAIAH, S. DAS, Physico-chemical properties of copper electrolytes, *Metallurgical and Materials Transactions B* **20** (1989) 375–380.
- [163] N. TANTAVICHET, M. D. PRITZKER, Low- and high-frequency pulse current and pulse reverse plating of copper, *Journal of The Electrochemical Society* **150** (2003) C665–C677.
- [164] C. A. TAYLOR, T. J. R. HUGHES, C. K. ZARINS, Finite element modeling of blood flow in arteries, *Computer Methods in Applied Mechanics and Engineering* **158** (1998) 155–196.
- [165] D. P. TELIONIS, Unsteady Viscous Flows. Springer, Berlin/Heidelberg/New York, 1981.
- [166] T. E. TEZDUYAR, Stabilized finite element formulations for incompressible flow computations. Vol. 28 of *Advances in Applied Mechanics*. Elsevier, pp. 1–44, 1991.
- [167] P. THUM, T. CLEES, G. WEYNs, G. NELISSEN, J. DECONINCK, Efficient algebraic multi-grid for migration-diffusion-convection-reaction systems arising in electrochemical simulations, *Journal of Computational Physics* **229** (2010) 7260–7276.
- [168] W.-C. TSAI, C.-C. WAN, Y.-Y. WANG, Pulsed current and potential response of acid copper system with additives and the double layer effect, *Journal of The Electrochemical Society* **149** (2002) C229–C236.
- [169] B. VAN DEN BOSSCHE, G. FLORIDOR, J. DECONINCK, P. VAN DEN WINKEL, A. HUBIN, Steady-state and pulsed current multi-ion simulations for a thallium electrodeposition process, *Journal of Electroanalytical Chemistry* **531** (2002) 61–70.
- [170] F. VAN DER Bos, V. GRAVEMEIER, Numerical simulation of premixed combustion using an enriched finite element method, *Journal of Computational Physics* **228** (2009) 3605–3624.
- [171] D. VARADARAJAN, C. Y. LEE, A. KRISHNAMOORTHY, D. J. DUQUETTE, W. N. GILL, A tertiary current distribution model for the pulse plating of copper into high aspect ratio sub-0.25  $\mu\text{m}$  trenches, *Journal of The Electrochemical Society* **147** (2000) 3382–3392.
- [172] V. VOLGIN, A. DAVYDOV, Natural-convective instability of electrochemical systems: A review, *Russian Journal of Electrochemistry* **42** (2006) 567–608.
- [173] V. M. VOLGIN, O. V. VOLGINA, D. A. BOGRACHEV, A. D. DAVYDOV, Simulation of ion transfer under conditions of natural convection by the finite difference method, *Journal of Electroanalytical Chemistry* **546** (2003) 15–22.
- [174] W. A. WALL, Fluid-Struktur-Interaktion mit stabilisierten Finiten Elementen. Ph.D. thesis, Universität Stuttgart, 1999.
- [175] W. A. WALL, M. W. GEE, BACI: A parallel multiphysics simulation environment. Technical report, Institute for Computational Mechanics, Technische Universität München, 2010.

- [176] C. F. WALLGREN, F. H. BARK, R. ERIKSSON, D. S. SIMONSSON, J. PERSSON, R. I. KARLSSON, Mass transport in a weakly stratified electrochemical cell, *Journal of Applied Electrochemistry* **26** (1996) 1235–1244.
- [177] G. WEYNs, G. NELISSEN, J. PEMBERY, P. MACIEL, J. DECONINCK, H. DECONINCK, M. PATRICK, A. WRAGG, Turbulent fluid flow and electrochemical mass transfer in an annular duct with an obstruction, *Journal of Applied Electrochemistry* **39** (2009) 2453–2459.
- [178] C. H. WHITING, K. E. JANSEN, A stabilized finite element method for the incompressible Navier-Stokes equations using a hierarchical basis, *International Journal for Numerical Methods in Fluids* **35** (2001) 93–116.
- [179] D. WITTMANN, Erweiterte Reaktionsmodelle für die numerische Simulation von elektrochemischen Systemen. Bachelor thesis, Technische Universität München, 2011.
- [180] B. WOHLMUTH, Discretization Techniques and Iterative Solvers Based on Domain Decomposition. Vol. 17 of *Lecture Notes in Computational Science and Engineering*. Springer, Berlin, 2001.
- [181] M. R. WRIGHT, An Introduction to Aqueous Electrolyte Solutions. Wiley, Hoboken, 2007.
- [182] J. D. YANG, A. C. WEST, Current distributions governed by coupled concentration and potential fields, *AICHE Journal* **43** (1997) 811–817.
- [183] K.-M. YIN, R. E. WHITE, A mathematical model of pulse plating on a rotating disk electrode, *AICHE Journal* **36** (1990) 187–196.
- [184] D.-H. YOON, K.-S. YANG, K. BREMHORST, Effects of Schmidt number on turbulent mass transfer around a rotating circular cylinder, *Journal of Fluids Engineering* **133** (2011) 081204.1–081204.11.
- [185] R. ZIENKIEWICZ, R. TAYLOR, The Finite Element Method, Vol. 1 - The Basis, 5th Edition. Butterworth-Heinemann, Oxford, 2000.
- [186] R. ZIENKIEWICZ, R. TAYLOR, The Finite Element Method, Vol. 3 - Fluid Dynamics, 5th Edition. Butterworth-Heinemann, Oxford, 2000.